

NOTE TO USERS

The original manuscript received by UMI contains pages with slanted print. Pages were microfilmed as received.

This reproduction is the best copy available

UMI



**HYDROCARBON YIELD OF PYROLYTIC GRAPHITE DUE TO LOW-ENERGY
HYDROGEN IRRADIATION**

by

Brian Vernon Mech

A thesis submitted in conformity with the requirements
for the degree of Doctor of Philosophy
Graduate Department of Aerospace Studies
University of Toronto

© Copyright by Brian Vernon Mech (1997)



National Library
of Canada

Acquisitions and
Bibliographic Services

395 Wellington Street
Ottawa ON K1A 0N4
Canada

Bibliothèque nationale
du Canada

Acquisitions et
services bibliographiques

395, rue Wellington
Ottawa ON K1A 0N4
Canada

Your file Votre référence

Our file Notre référence

The author has granted a non-exclusive licence allowing the National Library of Canada to reproduce, loan, distribute or sell copies of this thesis in microform, paper or electronic formats.

L'auteur a accordé une licence non exclusive permettant à la Bibliothèque nationale du Canada de reproduire, prêter, distribuer ou vendre des copies de cette thèse sous la forme de microfiche/film, de reproduction sur papier ou sur format électronique.

The author retains ownership of the copyright in this thesis. Neither the thesis nor substantial extracts from it may be printed or otherwise reproduced without the author's permission.

L'auteur conserve la propriété du droit d'auteur qui protège cette thèse. Ni la thèse ni des extraits substantiels de celle-ci ne doivent être imprimés ou autrement reproduits sans son autorisation.

0-612-27698-8

Canadä

Hydrocarbon yield of pyrolytic graphite due to low-energy hydrogen irradiation

by Brian Vernon Mech, Department of Aerospace Studies, University of Toronto

submitted in conformity with the requirements for the degree of Ph.D. (1997).

ABSTRACT

Recent developments with gaseous divertors in tokamaks have led to prospects of less energetic ion bombardment (10's of eV) in the divertor region. Previous low-energy results indicate that an H-ion induced chemical erosion process is occurring which is distinct from that observed for high impact energies (300 eV - 3 keV). Furthermore, there is some discrepancy in the literature as to the magnitude of the isotopic effect due to H⁺ and D⁺ impact at these low energies.

In the present experiments, mass spectrometry in the residual gas is used to perform a systematic study of hydrocarbon formation rates as a function of pyrolytic graphite temperature (300 - 1000 K) and ion energy (10 - 200 eV) for mass-analysed H⁺ and D⁺ beams (10^{18} ions/m²s). This provides a unique opportunity to also investigate isotopic effects. The results can be used to optimize operating conditions in a tokamak fusion reactor.

The present results indicate that, as the ion impact energy is reduced, there is a reduction in the maximum chemical yield (Y_m) and that broadening of the temperature dependence for hydrocarbon formation does, in fact, lead to significant erosion for low-energy impact at room temperature. These room-temperature methane and total chemical

yields display maxima at about 50 eV and decrease as the ion energy is further reduced. Within experimental errors the isotopic effect on the chemical yield was not significant and was generally less than a factor of 1.7. Furthermore, there was strong evidence for changes in the dominating erosion mechanism(s) as the ion energy was reduced below 100 eV.

A semi-empirical model has been developed, based on previously identified atomistic processes, with some modifications and additional processes incorporated. In general, this model agrees very well with the present results for methane production due to H⁺ and D⁺ impact. The additional processes, which account for the kinetic effects of the energetic particles, can be used to explain many of the observed erosion features.

ACKNOWLEDGMENTS

I would like to thank my supervisor, Professor A.A. Haasz, for his invaluable guidance and support throughout this project. In addition, I am indebted to Dr. J. W. Davis for his direction and encouragement and to Professor P.C. Stangeby for his assistance. To Charles Perez, a special thanks for his incomparable technical abilities which produced the ion deceleration lens. I am also appreciative of the assistance provided by Dr. S. Tanner in running the ion trajectory code, SimIon. I would also like to recognize the contributions of the other members of the Fusion Materials Research Group at UTIAS.

The financial support provided by the National Sciences and Engineering Research Council, the Canadian Fusion Fuels Technology Project, and the University of Toronto is gratefully acknowledged.

Finally, I would like to thank my family for their total support, and Jo-Anne for her unwavering patience, understanding and friendship.

TABLE OF CONTENTS

	Page
Abstract	ii
Acknowledgements	iv
List of Symbols	viii
1. INTRODUCTION	1
1.1 Nuclear Fusion	1
1.2 Tokamaks	2
1.3 ITER	3
1.4 Technological Issues	4
1.5 Plasma-surface Interactions	4
1.6 Objectives of this Thesis	6
2. LITERATURE REVIEW	9
2.1 Chemical Erosion in Tokamaks	10
2.2 Chemical Erosion in Plasma Experiments	11
2.3 Chemical Erosion in Low-energy Ion Beam Experiments	12
2.4 Summary	16
3. A REVIEW OF RECENT MODELS	19
3.1 The Atomic Interaction of Hydrogen and Carbon	19
3.1.1 Thermally activated release of hydrogen and hydrocarbons	20
3.1.2 Hydrogenation	21
3.1.3 Dehydrogenation	22
3.1.4 Atom-induced chemical erosion	22
3.1.5 Summary of the atomistic model	23
3.2 Applications of the Atom Model to Energetic Ion Impact on Graphite	24
3.2.1 Application of the atom model to ASDEX-U	24
3.2.2 Application of the atom model to energetic ion beam experiments	27
4. A MODEL FOR THE CHEMICAL EROSION OF PYROLYTIC GRAPHITE DUE TO LOW-ENERGY H⁺ AND D⁺ IMPACT	31
4.1 Processes Associated with Energetic Hydrogen Impact	31

4.1.1 Energy deposition	31
4.1.2 Low-energy hydrogen ion impact	32
4.2 Modifications to the Processes Associated with Atomic Impact	34
4.2.1 Distributed activation energies	34
4.2.2 Activated abstraction	35
4.2.3 Surface treatment	36
4.3 Model System for Methane Erosion due to Energetic Hydrogen Ion Impact	37
5. EXPERIMENT	40
5.1 Experimental Facility	40
5.1.1 UHV system	40
5.1.2 Ion gun	41
5.1.3 Mass filter	42
5.1.4 Electrostatic deceleration lens	43
5.1.4.1 Background	43
5.1.4.2 Design	44
5.1.4.3 Charcterization	45
5.1.5 Graphite Specimen	46
5.1.6 Tritium Lab Simulation	47
5.2 Experimental Procedure	48
5.2.1 Matrix analysis of measured erosion signals	50
5.2.2 Wall contribution to erosion signals	52
6. EXPERIMENTAL RESULTS	56
6.1 Methane Erosion Yields	56
6.1 Heavy Hydrocarbon Yields	57
6.1 Total Chemical Erosion Yields	60
7. DISCUSSION OF RESULTS	61
7.1 Methane Erosion Yields	61
7.2 Heavy Hydrocarbon Erosion Yields	63
7.3 Total Chemical Erosion Yields	66
7.4 General Discussion	66
7.5 Isotopic Effects in the Chemical Erosion of Pyrolytic Graphite	70
7.5.1 Isotopic effects in the methane yield	71
7.5.2 Isotopic effects in the heavy hydrocarbon yields	73
7.5.3 Isotopic effects in the total chemical erosion yield	74
7.6 A Comparison of the present Methane and Total Chemical Yields with Previously Published Results	75

8. FITTING OF THE MODEL FOR METHANE EROSION DUE TO LOW-ENERGY HYDROGEN ION IMPACT TO THE EXPERIMENTAL RESULTS	79
8.1 Results and Energy Dependence of fitting parameters	79
8.2 Energy Dependence of the Methane Yield	83
8.3 Flux Dependence of the Methane Yield	83
8.4 Summary of Methane Yield Model and Possible Improvements	84
9. CONCLUSIONS	87
REFERENCES	90
FIGURES	95
APPENDIX A: MODEL FITTING	154

LIST OF SYMBOLS

- f_{CE} : beam fraction which undergoes charge exchange
- k : Boltzmann constant
- k : frequency constant for thermal release of hydrogen and methane
- k_D : abstraction prefactor
- k_x : frequency constant for atom-induced thermal release of methane
- k_{H} : frequency constant for atom-induced thermal H-atom splitoff
- m : mass
- m_{CH_4} : QMS sensitivity to methane
- n : plasma density
- n_{H_2} : neutral hydrogen density
- s : erosion signal vector divided by ion flux
- sp^1 : hybridization state of carbon which results in triple bonding with adjacent carbon
- sp^2 : hybridization state of carbon which results in double bonding with adjacent carbon
- sp^3 : hybridization state of carbon which results in single bonding with adjacent carbon
- sp^x : radical hybridization state of carbon
- sp^x_{CH} : radical hybridization state of carbon involved in atom-induced thermal release of methane
- sp^x_{H} : radical hybridization state of carbon which does not lead to thermal release of methane
- y : erosion yield vector
- B : magnetic field magnitude
- C : cracking pattern matrix
- C_{chem} : the total chemical yield = $[(\text{CH}_4 + 2 \times \sum \text{C}_2\text{H}_x + 3 \times \sum \text{C}_3\text{H}_y)/\text{H}^+]$
- C_{heavy} : the total heavy hydrocarbon chemical yield = $C_{\text{chem}} \cdot \text{CH}_4/\text{H}^+$
- D : multiplicative constant which depends on ion mass in [64]
- E : electric field magnitude
- E : ion energy
- E_0 : ion energy in [64]

- E_D : activation energy for abstraction
 E_H : activation energy for atom-induced H-atom splitoff
 E_{th} : activation energy for thermal release of hydrogen
 E_m : activation energy for thermal release of methane
 E_x : activation energy for atom-induced methane release
 R : QMS relative sensitivity matrix
 T : temperature
 T_e : electron temperature
 T_i : ion temperature
 T_m : temperature at which maximum yield occurs
 U : ion energy
 Y : erosion yield
 Y_{chem} : total chemical yield as predicted by the model of García-Rosales and Roth [64]
 Y_{phys} : physical sputtering yield
 Y_{surf} : chemical erosion yield due to kinetic ejection of surface hydrocarbons [64]
 Y_{therm} : chemical erosion yield in [64] resulting from application of Küppers atomistic model [63]
 Y_{phys}^* : modified physical sputtering yield shifted towards lower threshold energies [64]
 Y_m : maximum erosion yield
 Y_{RT} : erosion yield at room temperature
 Y_{1000} : erosion yield at 1000 K
 W_D : FWHM for the abstraction activation energy
 W_H : FWHM for the atom-induced H-atom splitoff activation energy
 W_x : FWHM for the atom-induced methane release activation energy
 σ_{CE} : cross-section for charge exchange
 σ_D : cross-section for abstraction
 σ_E : cross-section for damage deposition
 σ_H : cross-section for hydrogenation
 σ_i : cross-section for kinetic ejection of methane

ω_c : cyclotron frequency

Φ : particle flux

τ_E : energy confinement time

1. INTRODUCTION

At current growth rates the world-wide energy demands are expected to double every 35 years. Fossil fuels and nuclear fission currently provide most of the world's energy supply, but the former is not inexhaustible and both represent sources which are becoming less acceptable environmentally, and so, much effort has been invested in the development of alternative centralized energy sources. Nuclear fusion, with its nearly inexhaustible fuel supply and significant environmental advantages, has been investigated as an alternative energy concept for nearly five decades. Significant progress has been made during that span so that controlled fusion as a source of electricity is within sight of current researchers.

1.1 NUCLEAR FUSION

Nuclear fusion is a reaction in which two light nuclei combine to produce a heavier nucleus while releasing a large amount of energy. It is the same process which powers the Sun and all stars. When two atoms approach very close together it is only their positively charged nuclei which take part in this reaction and so they are naturally repelled. In order to overcome this Coulomb barrier the atoms must be traveling at very high relative velocities. Heating the atoms to very high temperatures, such that the tail of the Maxwellian velocity distribution coupled with quantum tunneling effects allow enough of the atoms to fuse, is one of the preferred methods of overcoming this barrier. This is called thermo-nuclear fusion.

There are several candidate fusion reactions involving light isotopes, but D-T fusion is the one most intensely investigated mainly because it should be most easily achieved. This reaction proceeds as



In order to provide the incident atoms with enough energy so that enough of them fuse they must be heated to temperatures in excess of 100 million °C. This poses several challenges but this reaction actually has the highest cross-section for fusion at such 'low' temperatures. Furthermore, this reaction has a high power density and natural energy exhaust (via the neutrons) which are both advantageous. On the other hand, D-T fusion

uses tritium which is both a rare and radioactive isotope of hydrogen and the high energy neutrons lead to activation of most materials in the neighbourhood of the fusing atoms.

It is quite possible that, when D-T fusion will have been fully developed, alternative fusion concepts will be explored including D-D, which avoids much of the tritium and activation problems [1], and D-³He which produces only charged particles [2].

1.2 *TOKAMAKS*

When a gas is heated to the temperatures required for D-T fusion it becomes nearly perfectly ionized forming a plasma of ions and electrons with very high thermal kinetic energies. These particles would escape the plasma in millionths of a second if not contained by some means. In the Sun this confinement is achieved by gravitational forces, but on Earth we are restricted to either inertial or magnetic confinement and much of the current research effort is concentrated on the latter.

Fortunately, the very fact that the fuel atoms are fully ionized means that they can be influenced by externally applied magnetic fields. A charged particle will orbit a magnetic field line under the Lorentz force with a cyclotron frequency of $\omega_c = eB/m$. Along the field line the particle may move freely thus executing a net helical motion. Clearly, if all of the magnetic field lines can be forced to close on themselves then it should be possible, ideally, to nearly contain the plasma and prevent it from reaching the reactor vessel walls.

Several confinement schemes have been proposed based on this principle, but that most commonly used is the tokamak. In this scheme the reactor vessel is shaped like a torus with many toroidal field coils surrounding the vessel and running through its center. These constant current coils provide a magnetic field in the axial, or toroidal, direction of the torus. A set of transformer coils, using the plasma as the secondary winding, are used to generate an electrical field in the axial direction by time-varying currents in the primary. This field induces an axial current in the plasma (while also heating it ohmically) which, in turn, produces a poloidal magnetic field. Thus the net magnetic field lines are helically screwed around the torus producing excellent confinement of both the plasma and its energy.

Unfortunately, the confinement in a tokamak is not perfect. Self diffusion through Coulombic collisions and anomalous transport through microinstabilities lead to escape of particles from the plasma. Furthermore, the requirement for exhausting helium ash from the plasma to prevent dilution of the fuel necessitates active removal of some plasma from the core to a more remote part of the vessel. The question arises then; how good must - or should - the confinement be?

Several criteria have been developed in order to quantify the required confinement in a tokamak. Generally such criteria arise from the balance of the energy given up by the helium in heating the plasma against the many mechanisms of energy loss (conduction, diffusion, and radiation). Typically, n , the plasma density, T , the plasma temperature, and τ_E the energy confinement time are used to quantify the result and the balance equation results in the following triple product criteria for ignition [3]

$$nT\tau_E \equiv 6 \times 10^{28} \text{ m}^{-3}\text{sK}$$

Progress in fusion research can be measured by the evolution of this factor achieved in various machines. In 1971, an achievable triple product was 25,000 times smaller than that required, whereas in 1991 that factor had been reduced to just 6 [3]. This rate of improvement is remarkable, but there are several hurdles still blocking the route to ignition.

1.3 *ITER*

The International Thermonuclear Experimental Reactor (ITER) is an international collaboration whose mission , “to demonstrate the scientific and technological feasibility of fusion power...”, emerged from the 1985 summit meeting. To this end an immense effort has been undertaken to design and eventually construct a D-T machine which can demonstrate ignition and extended burn for periods of up to 1000 s while producing 1500 MW of fusion power.

The engineering design phase began in 1992 and will last until 1998. At that point construction may or may not be undertaken due to both technical and political issues. A brief review of some technological issues facing ITER, however, would help summarize the current state and focus of fusion research.

1.4 TECHNOLOGICAL ISSUES

Generally, the scientific challenges facing fusion research today can be classified as either plasma physics issues, or engineering issues, although many fall into both categories.

Many of the pressing issues were raised by Sessler and Stix [4] and these include the tremendous structural damage that would ensue in the event of a disruption, microscopic and macroscopic plasma instabilities, and the ability to produce the large superconducting magnets on site which will meet stringent field tolerances. Longer range issues brought up by the same authors included difficulties in profile control, burn control, heat exchange, steady-state operation and helium ash removal.

Still there are other pressing decisions which must be made. One is the method of heating the plasma. Ohmic heating can only provide a fraction of that required since the plasma resistivity drops as temperature increases. Auxiliary sources include rf waves and energetic neutral beam injection both of which decrease the confinement time while representing engineering challenges in a reactor environment. Also, the effects of the 14.1 MeV neutrons and other radiation sources on the first-wall and structure still need to be fully assessed. A significant portion of the fusion energy produced will be deposited here and more materials research is required to develop a sound ITER first-wall design.

Most of the unresolved issues mentioned above are concerned with either the core plasma and its control or the macroscopic structure and its maintenance and feasibility. A whole new category of problems arise when one considers the interface of the plasma and the reactor vessel.

1.5 PLASMA-SURFACE INTERACTIONS

As mentioned already the confinement in a tokamak is not perfect. Escaping particles can enter the region outside the last closed magnetic flux surface or scrape-off layer (SOL) where the magnetic field lines end on some part of the vessel wall. Also some flux bundles are intentionally diverted away from the main plasma to a more remote part of the machine where the resulting plasma flux impinges on a small area of material so that helium ash may be pumped away (divertor machines). In either case, plasma particles

reach parts of the plasma facing components at fluxes and energies which can vary greatly by location.

Many processes occur in the plasma edge region and Reiter offers an excellent summary of these [3]. Of principal concern here, however, is what happens when the plasma reaches the wall.

Hydrogenic particles striking the surface can either be reflected or penetrate it. Typically, the impinging particles can erode the plasma facing material. This eroded material may then enter the SOL and possibly be transported into the main plasma where it can both dilute the fuel and cool the plasma through radiation. Impurity tolerance in the core plasma is a critical constraint and may not exceed a few percent depending on the impurity Z. Hydrogenic particles may also be retained in the wall until saturation is reached when they subsequently begin to recycle. Recycling, while reducing the energy of the ions reaching the wall, increases the ion flux.

In the case of divertors, very large fluxes of particles are directed to relatively small areas on the divertor plates. Not only does this cause a large efflux of impurities in this region which may reach the main plasma, but it also represents a high power load on the divertor material. ITER calls for average power loads of $\leq 1\text{MW/m}^2$ and peak loads of $\leq 5\text{MW/m}^2$ with particle impact energies of $< 20 \text{ eV}$. None of the existing methods for reducing power flow to divertors can meet these requirements and work is continuing on this aspect (gas target divertors).

Many of the processes occurring during the plasma-surface interaction are still not understood and so cannot be adequately controlled. Yet they can have a tremendous impact on not only the plasma edge, but on the core plasma as well, and so identification and experimental validation of many of these elementary processes is essential to the successful design of ITER. Consequently, the role of plasma-surface interactions has become a principal focus. This represents one of the more pressing issues facing the design of ITER.

1.6 OBJECTIVES OF THIS THESIS

As the focus on plasma-surface interactions has increased, more effort has been expended in determining hydrogen retention in, and erosion of, various candidate plasma facing materials. These are not simple tasks since it is difficult to determine these quantities in a reactor and impossible to truly simulate a reactor environment in the laboratory. Nevertheless, since these interactions have a great influence on the core plasma performance, it is imperative that a clear understanding of the plasma-surface interface is developed in order to effect suitable materials choices.

Candidate ITER reference materials for plasma facing components include beryllium, tungsten, and carbon-based materials, such as graphite and carbon-carbon composites. The main advantage of Be and C is their low Z (reduced radiation losses) and, in the case of carbon, excellent thermo-mechanical properties. This thesis focuses on carbon as a candidate plasma facing material. One of the main disadvantages of carbon is its susceptibility to erosion under plasma particle bombardment reducing component lifetimes and increasing impurity levels in the plasma. Graphite can be physically sputtered through momentum transfer from energetic impinging particles which can eject lattice carbon atoms. This process has been studied extensively in both the laboratory environment and in existing tokamaks and several reviews are available [5,6,7,8]. For temperatures exceeding 1200 K, radiation enhanced sublimation (RES) leads to erosion yields which increase monotonically with graphite temperature [8]. In addition to physical sputtering and RES, the erosion of graphite, under hydrogen ion and atom irradiation, is enhanced at temperatures between 300 and 1000 K due to the formation of volatile hydrocarbon molecules, producing maximum yields more than 10 times greater than those due to physical sputtering alone [5]. This phenomenon is called chemical erosion.

Many studies of the chemical erosion of graphite by energetic hydrogen ions, in the range of 100 eV - 3 keV, and thermal hydrogen atoms have been conducted in laboratory environments. An extensive review of these results is beyond the scope of this forum and the reader is referred to recent reviews [9,10]. Briefly, the chemical erosion of graphite under energetic hydrogen bombardment is characterized by a pronounced temperature dependence with the hydrocarbon yield maxima (Y_m) occurring between 725 - 850 K (T_m).

The absolute magnitude of Y_m depends on the ion energy and flux [11]. Energy deposition, in the form of broken carbon bonds [12], and volatile molecule formation at the end of ion range (following thermalization) [13,14,15] play key roles in explaining the observed features [9].

As the energy of the impacting hydrogen ions is decreased, the relative contributions of the heavier hydrocarbons, C_2H_x and C_3H_y , to the total carbon erosion yield become significant [16,17]. For 3 keV H^+ impact on carbon, methane comprises 90% of the total carbon yield. This drops to 50% for 50 eV impact [16,18] and only 5-10% for thermal H atom impact [16,19]. Some discrepancies exist in these studies with regards to the magnitude of the C_2H_x contributions [16,17,20].

Recent developments with gaseous divertors have lead to the prospects of high neutral densities and consequently low temperatures and ion energies in the divertor region. There has been a corresponding shift in research focus towards the interaction of lower energy hydrogen ions (10's of eV) with graphite (and other plasma-facing materials). Comparatively little work in the field of chemical erosion of graphite has been done for ion energies below ~ 100 eV. Some interesting features of this low-energy regime have been observed, including significant chemical erosion of carbon even at room temperature [21,22], and a large isotopic effect on the carbon yield [22]. The remarkable feature of this observed low-energy chemical erosion is that it occurs for hydrogen energies below the threshold (~ 40 eV for H^+ and ~ 33 eV for D^+ [23]) for physical sputtering of carbon which seemingly precludes the role of damage deposition used to explain the high-energy results. Producing relatively intense beams of low-energy ions represents a challenge that has limited experimental research in this area and so it has been difficult to verify these results.

It is the increased focus on the need for low-energy hydrogen erosion yields of carbon-based materials like graphite that provides the motivation for the current work. A body of empirical data is required for engineering applications and furthermore an understanding of the underlying physical mechanisms is required in order to enable the selection of optimal materials for a machine like ITER. From this perspective the objectives of this thesis can be listed as:

- (1) Experimental determination of the hydrocarbon yields of pyrolytic graphite (including methane and heavier hydrocarbons) under low-energy hydrogen impact as a function of both energy (10 - 200 eV) and temperature (300 - 1000 K).
- (2) Experimental determination of the isotopic effect on the hydrocarbon yields of graphite due to protium and deuterium ion impact in the same energy range.
- (3) Development of a semi-empirical model which will fit the observed data and help to indicate many of the underlying mechanisms involved in the low-energy erosion of graphite by hydrogen.

In the following section (Section 2) a brief review of the previous results obtained for the erosion of carbon materials due to low-energy hydrogen impact is presented.

A recently developed atomic hydrogen impact model and it's applications to energetic hydrogen ion impact will be reviewed in section 3. In section 4, a revised semi-empirical model is developed, based on these previous efforts.

A significant amount of design, construction, and characterization of the experimental facility and its components was required for this thesis. Principally, a well characterized compact source of low-energy ions which could be implemented in an ultra-high vacuum environment equipped with suitable diagnostics was required. The development and characterization of this system, and the experimental procedure, will be discussed in detail in section 5.

The results of the chemical erosion experiments are presented in section 6 followed by a detailed discussion of these results in section 7.

In section 8, the revised model developed in section 4 is fitted to our new experimental data for the methane yields of pyrolytic graphite due to H^+ and D^+ impact. The nature of the fitting parameters is discussed in detail.

The conclusions and contributions of this thesis are then presented in section 9.

2. LITERATURE REVIEW

When discussing the chemical erosion of graphite due to low-energy hydrogen impact, it is important to consider the differences between laboratory and reactor environments which can affect the measured erosion yields and their interpretation.

In a reactor there are several species which will participate in the plasma-surface interactions. Of principal concern are the energetic fuel ion species which will have an impact energy of $\sim 2kT_i + 3kT_e$ [24], which, for the low electron temperatures reported for ALCATOR C-mod [25] and the low ion temperatures found in ASDEX-U [26], may correspond to impact energies of a few 10's of eV. There are other edge species to consider, however. These include energetic impurity and helium ash ions, energetic charge exchange neutrals, Franck-Condon atoms with energies of $\sim 3\text{eV}$, as well as neutrons and electrons. All of these edge species can play a role in the chemical erosion of graphite. In fact, the total chemical yield is not simply the linear sum of the yields due to each species acting alone, but rather, the simultaneous impact of several edge species can lead to synergistic enhancement of the yield. Such enhancements have been observed in laboratory experiments for simultaneous ion/H-atom impact [16,27,28,29,30,31] as well as other combinations of impacting species, e.g. C^+ and H^+ [30, 32], or nonreactive He^+ , Ne^+ or Ar^+ with 100-eV H^+ [32].

The fluxes of each species reaching reactor components can vary by several orders of magnitude depending on the geometric location within the machine. For instance, fuel ion fluxes of $\sim 3 \times 10^{23} \text{ H}^+/\text{m}^2\text{s}$ are expected at the divertor plates [33,34], whereas wall fluxes are expected to be in the range of $10^{20} - 10^{22} \text{ H}^+/\text{m}^2\text{s}$ [7] and energetic neutral fluxes are in the range of $\sim 5 - 20 \times 10^{18} \text{ H}/\text{m}^2\text{s}$ [35].

Such a complicated plasma-surface environment can only truly be reproduced in an experimental tokamak where only remote techniques are available for determining both particle fluxes and erosion yields and it is very difficult to obtain well calibrated data. Furthermore, although information on the net erosion is obtained from a reactor, it is nearly impossible to separate the contributions of individual species and so identify the main reaction processes. In order to study the chemical erosion due to a single species, or

limited multi-species impact, experiments are carried out within better controlled environments like ion accelerators and plasma generators.

In the following sections we will briefly review the tokamak evidence for chemical erosion and the chemical erosion observed for low-energy hydrogen impact in plasma experiments. A more detailed discussion of the chemical erosion due to low-energy well-defined ion-beam experiments will ensue.

2.1 *CHEMICAL EROSION IN TOKAMAKS*

Optical emission spectroscopy (OES) has clearly demonstrated hydrocarbon formation in several tokamaks. CD line emission has been observed for deuterium discharges in JET [36], ASDEX [36,37,38], DITE [39], TEXTOR [40], and TORE SUPRA [41] under different plasma conditions. Despite the difficulties in calibrating measurements and the differences in the discharges, the experimentally determined methane yields showed good agreement and were found to be between 0.01 - 0.05 CD₄/D at the corresponding T_m.

Sniffer probe experiments in TEXTOR [42], where the plasma in the SOL was diverted onto a remotely located graphite specimen and hydrocarbon products were monitored in the residual gas, showed methane yields from deuterium impact at ~ 60 eV to be 0.01 CD₄/D at room temperature (RT) and 0.02 CD₄/D at T_m. The same experiment showed evidence for heavier hydrocarbon production (~0.005 C₂D₄/D) although the spectrum analysis was only approximate. For higher impact energies (~ 260 eV) the authors noted that the RT yield dropped while the yield at T_m (Y_m) increased leading to a more significant difference between the yields at these two temperatures. The authors further noted an isotopic decrease in the methane and total erosion yields of a factor of ~ 2 for H⁺ impact at the same energies.

The amount of carbon observed near the divertor strike points can be largely explained by physical sputtering suggesting that a strong flux dependence is reducing the chemical erosion yield or that there is prompt redeposition of the hydrocarbons produced [7]. Nevertheless, there is strong evidence that chemical erosion occurs in tokamaks (at

least for lower flux regions) and so many laboratory studies of this phenomenon are in progress. For more comprehensive reviews of the chemical erosion observed in tokamaks the reader is referred to [7,9].

2.2 CHEMICAL EROSION IN PLASMA EXPERIMENTS

Laboratory plasma experiments bridge the gap of fluxes available in ion-beam experiments (up to 10^{20} H⁺/m²s) and the highest fluxes expected in a tokamak like ITER. Some control is lost over the exact nature of the bombarding species, but as plasma characterization improves this becomes less of a concern [7].

Chemical erosion of graphite has been observed in plasma facilities like PISCES [43,44]. In an experiment where several different graphites (POCO, ATJ, and pyrolytic) were bombarded by 100 eV D⁺ no differences were found in the chemical yield of the different graphites [45] indicating that damage in the implantation zone leads to rapid amorphization. These graphites were subjected to H⁺ and D⁺ impact between 50 and 200 eV, at fluxes of 2×10^{22} ions/m²s, and the hydrocarbon products were monitored by OES and mass loss. The authors found that, for the case of 100 eV impact of D⁺, $Y_m = 0.043$ C/D and $Y_{RT} = 0.012$ C/D where the yield at T_m was dominated by methane production. Of course, since mass loss was used to determine these yields contributions from physical sputtering are also included. For 100 eV D⁺ impact on carbon the physical sputtering yield is ~ 0.01 C/D⁺ [8, 23] and so the yield observed at room temperature may be entirely due to this process. The authors further noted an isotopic reduction of a factor of ~ 2 for H⁺ impact at the same energy and that the total yield, at room temperature, did not depend on the energy of the impacting species over the energy range studied (50 - 200 eV). Since the contribution from physical sputtering drops dramatically for ion energies below ~ 100 eV ($\sim 1 \times 10^{-3}$ C/D⁺ at 50 eV [8, 23]) much of the yield observed at room temperature for ion impact at 50 eV must be due to chemical erosion processes. For 50 eV D⁺ impact, Y_m was reduced to 0.025 C/D and the chemical yield was observed to drop off quickly for $T > T_m$. Comparing these results with those obtained in ion-beam experiments at fluxes

three orders of magnitude lower, the reduction in chemical erosion at the higher flux was only a factor of ~ 2 [45,46].

A more recent study conducted at the PSI-1 plasma generator for H^+ fluxes of 4×10^{20} to $1.2 \times 10^{22} H/m^2 s$ and energies ≤ 30 eV used residual gas analysis (RGA) to determine that the maximum total chemical erosion yields for carbon fiber composites (CFC's) were between 0.01 and 0.02 C/ H^+ depending on the type of CFC [47]. The authors also found a much larger difference between Y_{RT} and Y_m that exceeds a factor of 10 and a constant ratio of hydrocarbon species $CH_4:C_2H_4:C_2H_6 \equiv 85:11:4$ independent of temperature and flux. The degree to which methane dominates and the fact that no other heavier hydrocarbons were observed for such low impact energies is in direct contrast with ion-beam experiments [16,18,48]. This may be due to the different substrate, the much higher ion flux, or, more likely, dissociation of the heavier hydrocarbons by the plasma prior to detection by RGA.

Differences between chemical yields under high flux impact, such as found in plasma experiments and divertor regions of tokamaks (where multi-species impact also occurs), and the comparatively low flux and limited-species impact of ion-beam experiments raise questions about the validity of the latter for application to reactor design. Ion-beam experiments, however, are essential in that they provide a relatively 'clean' environment in which identification of specific physical mechanisms becomes more realistic.

2.3 CHEMICAL EROSION IN LOW-ENERGY ION-BEAM EXPERIMENTS

Regardless of the nature of the ion source used in an ion-beam experiment it is relatively difficult to extract a high flux of low-energy ions because the current density goes as the extraction voltage to the $3/2$'s power. Thus one is often forced to extract the ions at high energy and subsequently decelerate the beam. A significant amount of charge exchange may occur, however, seeding the beam with a quantity of energetic neutrals which is difficult to measure. Synergistic erosion studies have already indicated that a small fraction of energetic particles can significantly enhance the yield due to thermal atoms [16]. Furthermore, deceleration of ion-beams can lead to rapid expansion, due to

space charge effects, reducing the particle flux density. Thus it is difficult to produce a relatively intense beam of low-energy hydrogen ions without much charge exchange and so fewer low-energy (< 100 eV) ion-beam studies on the chemical erosion of graphite have been conducted. Here the findings of the limited number of such investigations will be reviewed.

Roth and Bohdansky [22] decelerated hydrogen ion-beams down to 20 eV/ion using a double cylinder arrangement surrounding the specimen to prevent secondary electron interference and reduce beam spreading. For H^+ and D^+ flux densities of $\sim 5 \times 10^{19}$ ions/m²s they determined a beam neutral content of 1-2%. Using in situ weight loss and line of sight (LOS) mass spectrometry they measured both the methane and total erosion yields for pyrolytic graphite under low-energy hydrogen impact as a function of temperature and energy (see fig. 1). The key feature to note is the reduction of the peak yield and the broadening of the temperature dependence as the energy is reduced (fig. 1a) such that there is significant chemical erosion (methane and total yield) occurring, even at room temperature, which is nearly independent of the ion energy over the range of 20 - 80 eV (fig. 1b). For 50 eV D^+ impact, the total yield at room temperature is ~ 0.03 C/D and the methane yield is ~ 0.02 CD₄/D. The methane yield rises to ~ 0.05 CD₄/D at T_m (800 K) which agrees well with the factor of 2 increase over Y_{RT} observed in the TEXTOR sniffer probe experiments [42] and in PISCES [45]. For all energies below 80 eV, methane comprises 50-70% of the total yield. In the case of H^+ impact for energies below ~ 100 eV there is a remarkable isotopic effect on the total erosion yield of about a factor of 5 reduction over that due to D^+ impact which is considerably more than the factor of ~ 2 observed in TEXTOR [42] and PISCES [45]. The source of this discrepancy is unclear. The authors observed that the reduction in Y_m with energy was a logical consequence of the reduced radiation damage deposited in the surface layer, but that the increased yield at room temperature was inconsistent with this. They suggested that knock-on processes resulting in the emission of hydrocarbon precursors from the near-surface were possibly occurring.

Wu, Davis and Haasz [49] investigated the chemical erosion of pyrolytic graphite for H⁺ impact between 20 and 300 eV and fluxes of 3×10^{17} to 4×10^{18} H⁺/m²s. In this experiment the ions were simply extracted at 10 keV and slowed at a deceleration stage resulting in the lower flux densities. The methane produced from the sample was monitored by RGA with the methane signal calibrated in situ against a known leak. The methane yield was determined as a function of graphite temperature (425 - 1000 K) and ion energy (20 - 300 eV/ion). The authors again noted a reduction in Y_m with energy, from ~ 0.072 CH₄/H⁺ at 300 eV to ~ 0.014 CH₄/H⁺ at 50 eV. The authors also noted the broadening of the temperature dependence, but did not extend their results down to room temperature. Furthermore, they noted a pronounced dependence of T_m on energy. In fact, T_m shifted from 625 K to 775 K over the energy range of 20 to 300 eV. The authors further observed that T_m was tending towards the limit expected for thermal atoms, ~ 500 K [50], as the ion energy was reduced. This shift in T_m was not observed by Roth and Bohdansky and may be attributable to the lower flux density. The authors also noted that Y_m, T_m, and activation energies shift strongly between the 100 and 50 eV impact cases suggesting that there is a change in the dominating reaction mechanism for ion energies below 100 eV which may be due to the reduction in energy deposited in the near-surface.

In a subsequent investigation [16], the contribution of methane to the total hydrocarbon yield was determined as a function of energy down to 50 eV for H⁺ impact on pyrolytic graphite. The authors found that the methane contribution at 50 eV was slightly greater than 50% of the total chemical yield, in fair agreement with the results of Roth and Bohdansky [22], and this value increased to $\sim 90\%$ at 3 keV. They further noted that, for sub-eV H^o impact, the total chemical yield was dominated by the contributions from C₂H_x and C₃H_y species and was only five times smaller than that obtained at 50 eV impact. Spectrum analysis indicated that, for 300 eV impact which produces an amorphous hydrogenated carbon layer with many C=C double bonds, C₂H₆ and C₂H₄ were the dominant heavier hydrocarbons while, for sub-eV impact on the polycrystalline pyrolytic graphite with predominantly single carbon-carbon bonds, C₂H₆ alone was the dominant heavy hydrocarbon. In both cases the contribution from C₂H₂ , presumably due

to triple bonded carbon, was more than an order of magnitude lower than that of the dominant heavy hydrocarbons. The authors proposed a relationship between the bond structure of the graphite and the spectrum of hydrocarbons produced.

García-Rosales and Roth [21] investigated the chemical erosion of pyrolytic graphite and boron-doped graphite (USB15) for D^+ impact down to 10 eV. Using a similar deceleration technique as Roth and Bohdansky [22] along with in situ mass loss and LOS they measured the total chemical yield and methane yield as a function of ion energy and specimen temperature for fluxes of $\sim 2.8 \times 10^{19} D^+/\text{m}^2\text{s}$ (see figure 2). A reduction in Y_m for methane with decreasing energy was again observed (Y_m at 200 eV $\sim 0.08 \text{ CD}_4/D^+$ and Y_m at 50 eV $\sim 0.03 \text{ CD}_4/D^+$) for pyrolytic graphite. This was accompanied by the broadening of the temperature dependence previously noted which may be associated with near-surface reactions favouring the out-diffusion of hydrocarbon molecules. For 50 eV D^+ impact, a room temperature methane yield of $\sim 0.008 \text{ CD}_4/D^+$ was observed which is a factor of ~ 2.5 lower than that previously determined by Roth and Bohdansky [22]. The maximum methane yield for 50 eV impact was a factor of ~ 3.5 higher than the room temperature yield. The authors did not observe a strong dependence in T_m on ion energy for pyrolytic graphite, but did observe a 100 K shift (600 - 700 K) in T_m for USB15 as the energy was increased from 50 to 1 keV. They also noted that, for $T \leq 600 \text{ K}$, the methane yields for USB15 and pyrolytic graphite were essentially the same, especially for low-energy impact, whereas the yield of the boron-doped graphite was significantly reduced at higher temperatures suggesting that dopants may have little effect on the chemical erosion at low temperatures. The authors further noted that, between 10 and 40 eV, the total chemical yield of USB15 is nearly energy independent ($\sim 0.017 \text{ C/D}$) at room temperature, and methane formation accounts for $\sim 50\%$ of the total yield in this energy range. Thermal desorption spectroscopy (TDS) experiments were also performed which showed that, while erosion is observed at room temperature during ion irradiation below 100 eV, temperatures in excess of 600 K were required to desorb methane after low-energy irradiation. This indicates that the low-energy, low-temperature chemical erosion of graphite is radiation enhanced and involves some sort of energy transfer.

2.4 SUMMARY

The most obvious conclusion that can be drawn from the published data, with regards to low-energy hydrogen impact on graphite, is that broadening of the temperature dependence as the energy is reduced leads to significant erosion even at room temperature ($E < 100$ eV). Both the room temperature methane and total erosion yields appear to be independent of the ion energy over the range of ~ 30 - 80 eV.

Table 1. Experimentally Determined results for the erosion of Graphite by 50 eV Hydrogen Impact

Experimental Description				Methane Yield		Total Yield		Methane Fraction
Source	Species	Sample	Flux $\text{m}^{-2}\text{s}^{-1}$	Y_{RT}	Y_m	Y_{RT}	Y_m	
Ion-beam [22]	D ⁺	pyrolytic	5.0×10^{19}	0.02	0.05	0.03	0.075	65
Ion-beam [21]	D ⁺	pyrolytic	2.8×10^{19}	0.008	0.03	-	-	-
Ion-beam [21]	D ⁺	USB15	2.8×10^{19}	0.009	0.016	0.025	-	40
TEXTOR* [42]	D ⁺	pyrolytic	1.1×10^{22}	0.01	0.018	0.017	0.033	60
PISCES [45]	D ⁺	Poco	2.0×10^{22}	-	-	0.012	0.025	-
Ion-beam [22]	H ⁺	pyrolytic	5.0×10^{19}	-	-	0.005	-	-
Ion-beam [49,16]	H ⁺	pyrolytic	3.0×10^{17}	-	0.014	-	0.027	50
TEXTOR* [42]	H ⁺	pyrolytic	5.0×10^{21}	0.005	0.01	0.008	0.017	60
PSI-1 [47]	H ⁺	CFC's	1.2×10^{22}	-	-	<0.001	0.01-0.02	-

* TEXTOR results obtained for 60 eV impact.

In Table 1, data for the methane and total chemical erosion yields, from the experiments outlined here for 50 eV H⁺ and D⁺ impact, is summarized. This table also includes the measured fraction of the total chemical yield which methane represents. The experimentally determined yields of Roth and Bohdansky [22] due to D⁺ impact seem high and perhaps this is due to a synergistic contribution from the 1-2% estimated energetic charge exchange neutrals in their ion-beam. If these data are excluded we note that there is good agreement, in general for all of the results. For D⁺ impact at room temperature, the methane yields vary between 0.008 and 0.01 CD₄/D⁺ and the total yields are in the range of 0.012 - 0.025 C/D⁺. The values of Y_m show similar agreement (0.016 - 0.03 CD₄/D⁺ and 0.025 - 0.033 C/D⁺). That is, even for a flux which varies over 4 orders of magnitude, all of the experimentally determined yields for D⁺ impact agree within a factor of ~ 2. For H⁺ impact at room temperature the methane yield was found to be 0.005 CH₄/H⁺ in

TEXTOR [42] and the total chemical yield was between 0.005 and 0.008 C/H⁺ (excluding CFC results). The experimentally determined values for Y_m of 0.01 - 0.014 CH₄/H⁺ and 0.017 - 0.027 C/H⁺ also show good agreement. In general, we observe that the room temperature yield (methane or total) is approximately 1/2 the value of the corresponding peak yield and that the flux dependence, if it exists, appears to be quite small. We also note that methane composes between 40 and 60 % of the total chemical yield for graphite under 50 eV hydrogenic impact. The fact that consistent results can be obtained by a number of different investigators is encouraging.

There are a number of other key points to note. The exact magnitude of the isotopic effect on the total chemical yield is unclear. In PISCES, H⁺ impact at 100 eV resulted in total chemical yields a factor of ~ 2 lower than those for D⁺ impact at the same energy [45] and a similar isotopic factor was observed in TEXTOR [42]. Roth and Bohdansky, however, observed a total yield due to H⁺ impact which was a factor of ~ 5 less than that due to D⁺ impact over the energy range of 20 - 100 eV [22]. The reason for this discrepancy is unclear and one would not expect such a large isotopic effect based on elementary chemical and kinetic considerations. Furthermore, a dependence in T_m on ion energy was noted in some cases [16,49] and not in others [21,22,42,45]. The ion flux in the former case was between 2 and 4 orders of magnitude lower than those where no dependence in T_m on energy was observed, indicating a possible explanation for the disagreement. In general, we note that there are significant changes in Y_m, and the contributions from heavier hydrocarbons as the impact energy is reduced below 100 eV. As well, TDS results indicate that the low-energy room temperature chemical erosion of graphite is radiation induced which, along with the isotopic evidence, suggests that energy transfer plays a key role, perhaps in knock-on ejection of weakly bound hydrocarbon precursors.

It is remarkable that such consistent erosion yields have been determined by vastly different experimental facilities and yet there are some peculiar discrepancies. To date there has been no systematic study of the chemical erosion of graphite due to low-energy H⁺ and D⁺ impact as a function of graphite temperature and ion energy and the contribution of heavy hydrocarbons over the energy range of 10 - 200 eV. Tokamak

evidence indicates that erosion of graphite due to low-energy fuel ion impact may be significant and so, such a systematic study is warranted.

3. A REVIEW OF RECENT MODELS

There have been many efforts made at modelling the chemical erosion due to energetic ion impact and thermal atom impact [10,15,35,51,52,53]. Generally, these semi-empirical models have been successful at explaining many of the experimentally observed features. Comparatively little work has been done on modelling of chemical erosion due to low-energy ion impact. Recently, however, there has been a detailed experimental investigation [54-63] of the atomic erosion of amorphous C:H films which has provided insight into what may be going on in the case of more energetic impact. Modelling efforts by those investigators [60,63] and others [64], based on these results, have shown promise in explaining the chemical erosion of graphite due to low-energy hydrogen impact. This body of work [54-64] will be reviewed here in some detail.

3.1 THE ATOMIC INTERACTION OF HYDROGEN AND CARBON

Küppers and co-workers have undertaken an intensive analysis of the atomistic processes occurring under H-atom impact on amorphous hydrogenated carbon (a-C:H) films [54-63]. Films of several monolayers in thickness were formed by ion-beam deposition of 160 eV hydrocarbons onto a suitable substrate (typically platinum with a graphite interface). H/C ratios for the films typically ranged from 0.3 to 0.5 as determined by TDS. Various other spectroscopic methods were subsequently used to monitor the evolution of the films under thermal hydrogen atom impact and as a function of the film temperature. In particular, High Resolution Electron Energy Loss Spectroscopy (HREELS) was used to provide chemical information about the film surface.

Amorphous C:H films formed in this manner exhibit essentially the same features as carbon irradiated by hydrogen. That is a carbon network partially terminated by hydrogen and are considered to be appropriate models for the study of the interaction of H atoms and surfaces of partially or fully hydrogenated carbon materials [62]. Using this model system and spectroscopic techniques, Küppers et al. have been able to identify five elementary processes, induced by heating the a-C:H films and exposing them to thermal H-atoms, which will be discussed below.

3.1.1 Thermally Activated Release of Hydrogen and Hydrocarbons

In the absence of H atom irradiation the films were investigated by TDS [54,55]. It was found that H₂ desorption began at 400 K and peaked near 910 K and 1150 K. As well, desorption of hydrocarbons (both C₁ and C₂) occurred between 600 and 1040 K peaking near 850 K. Several hydrocarbons were observed, but methyl was the dominant radical and methane the dominant molecule. Furthermore, the CH₃/CH₄ ratio decreased with increasing film thickness suggesting that methyl produced at greater depths combines more effectively with hydrogen prior to escaping the film and that radical desorption occurs primarily at the surface.

The temperature evolution of methyl and methane production were identical, as were those of the C₂-containing molecules and radicals suggesting the breaking of a carbon network-C_iH_j bond was the rate determining step.

Subsequent vibrational analysis of the surface as a function of temperature [55,56] using HREELS revealed that the as-deposited films exhibited about equal amounts of carbon in the sp² and sp³ hybridization states with a much smaller component of carbon in the sp hybridization state. Carbon atoms in the sp² hybridization state are part of the graphitic network with sp³ and sp groups attached as ligands [55]. As the temperature of the film was increased, however, changes in the vibrational spectra were noted. The complete removal of sp carbon centers by 600 K was observed as was the subsequent removal of sp³ carbon centers between 600 and 1040 K. Removal of carbon in the sp² hybridization state was noted for temperatures in excess of 1040 K. The conclusion was that the sp³ hybridization state was associated with the thermal desorption of H₂ and most of the hydrocarbons (with some acetylene desorption above 1040 K attributed to carbon in the sp² hybridization state).

The authors proposed two rate equations for the thermal release of hydrogen and methane, in the absence of H° irradiation, from these films:

$$\text{H}_2 \text{ release: } d[\text{sp}^3]/dt = -[\text{sp}^3]k \exp(-E_{\text{th}}/RT)$$

$$\text{CH}_4 \text{ release: } d[\text{sp}^3]/dt = -[\text{sp}^3]k \exp(-E_{\text{th}}/RT)$$

where [sp³] is the concentration of sp³ carbon centers (m⁻³), k is the frequency factor ~ 10¹³ s⁻¹, E_{th} is the activation energy for the thermal release of hydrogen ~ 264 kJ/mol, and

E_{tm} is the activation energy for the thermal release of methane ~ 234 kJ/mol [63]. It is worth noting that these activation energies exhibit a fairly broad normal distribution of ~ 40 kJ/mol.

3.1.2 Hydrogenation

In subsequent experiments the authors exposed the a-C:H films to thermal hydrogen atoms [57-59]. Again HREELS spectroscopy was used to examine the surface and the authors noted that there was a decrease in the concentration of sp^2 hybridization states accompanied by an increase in the concentration of sp^3 centers with increasing atom exposure [57,58]. Furthermore, if a different isotope of hydrogen was used as the impacting ion, then the spectra showed that it was exclusively bound to carbon in the sp^3 hybridization state [57,58].

In another experiment they produced a film where all the hydrogen was exclusively bound to the sp^2 carbon centers (by flashing the films to 1040 K). Subsequent exposure of the film to deuterium atoms resulted in an increase in the $\nu(\text{CH})$ sp^3 intensity and the appearance of a $\nu(\text{CD})$ sp^3 stretch region. When this modified film was subsequently flashed to 1040 K the network returned to carbon exclusively in the sp^2 hybridization state, but now with both hydrogen and deuterium attached.

The authors concluded that the exposure of a-C:H films to thermal hydrogen atoms results in the hydrogenation of unsaturated CH groups in the near surface region. They proposed a reaction whereby hydrogenation of an sp^2 carbon center produces carbon in the sp^3 hybridization state and a neighbouring carbon with a radical electronic structure (sp^\times). The rate equation is given by:

$$d[\text{sp}^2]/dt = -[\text{sp}^2]\sigma_H\Phi$$

where σ_H is the cross-section for hydrogenation $\sim 4.5 \times 10^{-20}$ m² and Φ is the flux of thermal atoms to the surface (/m²s). The radical sp^\times bond may be further hydrogenated to produce another sp^3 hybridization state according to the rate equation:

$$d[\text{sp}^\times]/dt = -[\text{sp}^\times]\sigma_H\Phi$$

where the value of σ_H remains the same.

3.1.3 Dehydrogenation

The investigators completely hydrogenated an a-C:H film by exposing it to 10 monolayers of hydrogen atoms so that only stretch modes due to carbon in the sp^3 hybridization state remained. Upon subsequent exposure of these treated films to deuterium atoms they found that, not only did a $\nu(CD)$ sp^3 stretch mode appear, but the existing $\nu(CH)$ sp^3 modes were isotopically shifted. This suggested that a dehydrogenation reaction followed by hydrogenation was occurring [59].

This reaction involving hydrogen, where the gas-phase species reacts directly with the adsorbed species, showed a small activation. Furthermore, when hydrogen atoms impinged on a fully deuterated a-C:D film no isotopic effect on the abstraction process was noted.

The authors concluded that an Eley-Rideal type abstraction process was occurring which produces a hydrogen molecule and a carbon in the intermediate radical electronic state with the rate equation given by:

$$d[sp^3]/dt = -[sp^3]\sigma_D\Phi$$

where σ_D is the cross-section for dehydrogenation $\sim 0.05 \times 10^{-20} m^2$ [59].

3.1.4 Atom Induced Chemical Erosion

In the same experiment the authors noted that when the temperature of the films was raised to 500 K in the presence of a thermal atom flux, auger electron spectroscopy (AES) revealed that the films were thinning. This effect was more pronounced at 600 K. Yet if the flux of atoms was halted the films kept a constant thickness. They concluded that an erosion step, which is distinct from the thermally activated release described in 3.1.1, and proceeds by thermal atom impact, is involved [59].

This phenomenon was investigated more thoroughly in a subsequent experiment [60]. A fully hydrogenated a-C:H film was subjected to a flux of atoms at different temperatures. The investigators found that the erosion was most pronounced at 600 K and had nearly stopped by 700 K. Using HREELS they analyzed the film surfaces. At 400 K they found that all of the hydrogen was exclusively bound to carbon in the sp^3

hybridization state indicating a fully hydrogenated surface. As the temperature of the surface was raised, still in the presence of atomic hydrogen, the concentration of sp^3 carbon centers was reduced and the concentration of sp^2 carbon centers increased until, at 700 K, the latter hybridized states dominated. They concluded that H° impact induces de-excitation of the radical carbon hybridization state (sp^x) produced by abstraction, via split-off of the methyl group attached to the neighbouring hybridized carbon (sp^3) producing two sp^2 hybridized carbons. This process is endothermic and the reaction rate is given by:

$$d[sp^x]/dt = -[sp^x]k_x \exp(-E_x/kT)$$

where k_x is the frequency factor $\sim 10^{13} s^{-1}$, and E_x is the activation energy for atom induced release of methyl ~ 142 kJ/mol [63].

The authors also note that, if such a reaction is permissible then, a similar de-excitation of the radical center (sp^x), produced by hydrogenation, via H-atom split-off from a neighbouring carbon in the sp^3 hybridization state must also be allowed. The reaction rate for this process is given by:

$$d[sp^x]/dt = -[sp^x]k_H \exp(-E_H/kT)$$

where k_H is the frequency factor $\sim 10^{13} s^{-1}$ and E_H is the activation energy for atom-induced H-atom split-off ~ 167 kJ/mol [63].

3.1.5 Summary of the Atomistic Model

The key steps leading to the chemical erosion of amorphous C:H films by thermal atomic hydrogen are summarized in figure 3. Starting from the bottom and working clockwise we note that hydrogenation of carbon in the sp^2 hybridization state occurs creating a radical sp^x hybridization state with a neighbouring hydrogen containing carbon in the sp^3 hybridization state. At higher temperatures split-off of this hydrogen can return the two carbon atoms to their original sp^2 electronic state.

The radical and sp^3 carbon centers can be further hydrogenated to form two carbons in the sp^3 hybridization state, some fraction of which will have a methyl group attached. Abstraction of a singly bound H can produce another carbon in the radical sp^x configuration with a neighbouring methyl containing carbon in the sp^3 hybridization state.

Hydrogenation can return the sp^x center to its previous sp^3 state or, at higher temperatures, it can de-excite by split-off of the neighbouring methyl group producing two carbons in the sp^2 hybridization state.

Note that the purely thermally activated release of hydrogen and methane is not included in this model diagram. In the presence of thermal hydrogen atoms, most of the release of methane has occurred before 700 K and the higher activation energies of these two processes means they will have a negligible effect.

Thus, at low temperatures, exposure of the film to thermal hydrogen atoms results in the conversion of carbon from the sp^2 to the sp^3 hybridization state with some fraction of radical centers, determined by the ratio of σ_D/σ_H . At higher temperatures (400 - 650 K) an equilibrium balance, between the supply of sp^x radical carbon centers from hydrogenation and abstraction and their loss through thermal decomposition due to methyl and H-atom split-off, is established leading to measurable erosion rates. At even higher temperatures, however, the rapid decomposition of the radical states by H-atom split-off prevents significant hydrogenation to sp^3 . This, in turn, means there is little or no abstraction occurring and so no significant production of carbon in the radical electronic state. Thus, chemical erosion is suppressed at high temperatures.

Logistically and numerically, the model works very well at explaining the chemical erosion of a-C:H films by thermal hydrogen atom impact [60,63]. Given that, for energetic hydrogen ion impact on graphite, the ions must thermalize before forming hydrocarbons at the end of range, the question becomes whether or not this model can be applied to the case of more energetic hydrogen impact. At least two such attempts have been made [63,64] and these will be discussed next.

3.2 APPLICATIONS OF THE ATOM MODEL TO ENERGETIC ION IMPACT ON CARBON

3.2.1 Application of the Atom Model to ASDEX-U

Wittmann and Küppers used this model to try to calculate the chemical erosion yields encountered in ASDEX upgrade [63]. In this case, one is forced to deal with a flux

of ions and charge exchange neutrals both of which have distinct energy distributions and can be implanted to depths of several 10's of nm. Since the model applies only to the reaction of thermalized hydrogen with carbon, one may calculate the distribution of thermalized hydrogen as a function of depth in the carbon substrate. From this it is possible to extract the effective flux of thermal hydrogen as a function of depth and then apply the model to successive layers of the carbon substrate.

In the present application the authors selected a Maxwellian distribution of ion energies determined by a sheath potential of 150V and a distribution of neutral energies approximated by $1/E$ in order to simulate the energy distributions of hydrogen particles found at the target plates of ASDEX upgrade. The authors note that the presence of energetic particles will result in the production of an amorphous carbon layer several 10's of nm in depth. Such a layer is well modelled by an a-C:H film and so application of the model is justified. Using TRIDYN code, based on the binary collision model, they were able to calculate depth distributions of mono-energetic particles impinging on a carbon target at normal incidence. Then, given the energy distributions of the particles outlined above and a total flux density, they were able to calculate the effective flux density of thermal hydrogen as a function of depth. For the case of a total flux density of 10^{23} H⁺/m²s, the effective flux of thermal hydrogen ranged from $\sim 2 \times 10^{22}$ H/m²s at a 2nm depth to $\sim 10^{16}$ H/m²s at 50 nm.

The carbon substrate was then mathematically analysed, depth-wise, on the basis of 1 nm layers parallel to the surface and, using the experimentally determined model parameters and the flux calculated from TRIDYN, the chemical reaction scheme outlined in sections 3.1.1 to 3.1.4 was applied. This involved formulating the complete set of three differential equations for the concentrations of the three carbon hybridization states (sp², sp³, sp^x) and solving them numerically using the Rosenbrock method. For several total hydrogen flux densities the set of equations was solved for each layer, over the temperature range of 500 - 1100 K at 10 K intervals, and allowed to run to steady state where the concentrations of the three hybridized carbon species and the rate of methane formation were determined. The results of this calculation are shown in figure 4. It is important to note that no modification was made to the equations for the role of energy

deposition in the substrate. Furthermore, no distinction is made between carbon in the radical hybridization state with neighbouring methyl terminated, or hydrogen terminated carbons in the sp^3 hybridization state.

In figure 4a it is clear that the lower the effective flux of thermal hydrogen (i.e. the greater the depth of implantation) the lower the temperature at which thermally activated processes become important. For example, at the surface where the flux of thermal H is 10^{22} H/m²s the concentration of sp^3 carbon centers equals that of sp^2 at 900 K, however, at a depth of 40 nm where the flux of thermal H is 10^{18} H/m²s these two concentrations are equal at 700 K. In figure 4b, we note that the consequence is a methyl production rate which depends strongly on the thermal hydrogen flux. The maximum erosion rate always occurs near the surface where the effective flux is highest, but the temperature at which the maximum occurs depends on the total flux. T_m for a total flux of 10^{21} H/m²s was 870 K and this rose to 1050 K for a total flux of 10^{23} H/m²s. This latter value seems too high since plasma experiments, at fluxes of up to 2×10^{22} H/m²s suggest that T_m never exceeds ~ 950 K [45]. The authors note that it is impossible to give the absolute yields since the concentration of methyl groups neighbouring a radical carbon atom is not known.

Again, the authors note that, at low temperature, hydrogenation leads to a large population of carbon in the sp^3 hybridization states. At high temperatures the thermally activated processes dominate and so the fractional concentration of sp^2 carbon centers is nearly 1. The intermediate temperature range, which depends on the effective flux of thermal hydrogen, exhibits a smooth transition from sp^3 carbon center dominance to sp^2 carbon center dominance. In order to have methyl production there must be a population of carbon in the sp^3 configuration with attached methyl groups, but their release is thermally activated. At the temperatures where this release becomes effective, this and other thermally activated processes serve to reduce the population of these sp^3 hybridized carbon bonds. It is this trade-off which results in the temperature optimum observed in theory and experiment.

Application of the atom model works quite well at explaining many of the experimentally observed features of the more energetic impact of hydrogen on carbon. Unfortunately, due to the limits imposed by an unknown methyl group concentration, the

authors can do little to compare their yields to those observed in ASDEX-U and so it is difficult to quantify the accuracy of this model. Furthermore, although the authors have considered the effective flux of atoms introduced by energetic impact, they have not accounted for the effects of energy deposition which are likely to be significant, and they have not distinguished between the two populations of carbons in the sp^x hybridization state which clearly affects the methane yield since one population leads to thermal release of methyl radicals and the other does not. Also, the low-energy erosion of graphite at low temperatures is not explained by this model. Another modelling attempt, discussed in 3.2.2, has considered these aspects.

3.2.2 Application of the Atom Model to Energetic Ion-Beam experiments

Roth and García-Rosales applied the model developed by Küppers et al., with additional terms for radiation damage, low-energy erosion, and a modified flux dependence, to the erosion of graphite by mono-energetic hydrogen and deuterium ions [64]. The authors felt that this atom model was applicable since the energetic hydrogen does not react chemically until it is thermalized. While they did distinguish between the two populations of sp^x hybridized carbon centers they did not apply the model to successive layers as did Wittmann and Küppers, but, in effect, treated the entire deposition zone as one surface. Here we will review their formulation.

The series of steps which lead to chemical erosion of carbon, as described by Küppers et al., are referred to here as the thermal process and the carbon yield due to this process is designated Y_{therm} . The authors, using the steps outlined in sections 3.1.2 to 3.1.4 (i.e. excluding the purely thermally activated release of methane and hydrogen), set up a system of four time based differential equations in the four unknown carbon center concentrations sp^2 , sp^3 , sp^x_H , and sp^x_{CH} , where the latter two designations refer to the two radical carbon center populations; the first of which does not lead to atom-induced thermal release of methyl groups and the second which does. An additional equation is provided by the fact that the sum of the concentrations equals one.

In steady-state, it is possible to set the differential equations equal to zero and solve for the analytic expressions which give the concentrations of the four carbon atom species. Doing so, one obtains for the thermal yield,

$$Y_{therm} = \frac{[sp^x_{CH}]}{\Phi} K_x = \frac{\sigma_D K_x}{\sigma_H \Phi + \sigma_D \Phi + (1 + 2 \frac{\sigma_D}{\sigma_H} + \frac{\sigma_D K_{-H}}{\sigma_H^2 \Phi}) K_x}$$

where $K_x = k_x \exp(-E_x/kT)$ and $K_{-H} = k_{-H} \exp(-E_{-H}/kT)$.

Now the authors argue that, since the absolute concentration of carbon in the sp^3 hybridization state with attached methyl groups is unknown, it is reasonable to use the values of k_x , k_{-H} , E_x , E_{-H} as adjustable fit parameters. The authors also note that the steady-state solution to the differential equations leads to a very weak dependence in Y_m and a very strong dependence in T_m on the flux density, Φ . Such dependencies are not observed experimentally and so they include a term accounting for the annealing and graphitization of carbon that occurs at high temperatures (> 900 K). Thus they obtain,

$$Y_{therm} = \frac{0.033 \exp(-1.7/kT)}{2 \cdot 10^{-32} \Phi + \exp(-1.7/kT)} [sp^3]$$

$$[sp^3] = \frac{C(2 \cdot 10^{-32} \Phi + \exp(-1.7/kT))}{2 \cdot 10^{-32} \Phi + (1 + \frac{2 \cdot 10^{29}}{\Phi} \exp(-1.8/kT)) \exp(-1.7/kT)}$$

$$C = \frac{1}{1 + 10^{13} \exp(-2.45/kT)}$$

where the activation energies are now in eV and $E_x = 1.7$ eV, $E_{-H} = 1.8$ eV.

In addition to Y_{therm} , a term is required which accounts for radiation damage resulting from energetic impact. For ions with energies above the threshold for physical sputtering, energy deposition in the carbon substrate results in atomic displacements and C-C bond breaking which creates active sites increasing the chemical erosion yield. The authors argue that this enhancement can be well described by a multiplicative term which is proportional to physical sputtering such that the energetic chemical yield is given by

$$Y_{chem} = Y_{therm}(1 + DY_{phys})$$

where D is a constant dependent on the mass of the impinging isotope and Y_{phys} is the physical sputtering yield given by the revised Bohdansky formula [23].

In the case of low-energy hydrogen ion impact on carbon, hydrocarbon production is observed at room temperature which is not explained by the atom impact model where higher temperatures are required. The isotopic effect on the yield which has been observed for this low-energy impact [22], as well as TDS results [21], suggest that physical sputtering of weakly bound sp^3 centers with attached hydrocarbon ligands may be occurring at the surface. This seems reasonable since the concentration of these carbon atoms is high at room temperature. The authors argue that the dependence of this kinetic ejection process on energy should be similar to physical sputtering, but shifted towards lower threshold energies in the range of 1-2 eV, and that, for hydrogenic impact at energies greater than ~ 90 eV, hydrogenation occurs at the end of range, away from the surface and so the erosion yield from this surface process is reduced. Furthermore, as the temperature of the carbon increases the sp^3 hybridization state concentration drops, limiting the effect of this surface process to temperatures below T_m . The authors propose an additional term, Y_{surf} , to describe this process such that

$$Y_{\text{surf}} = \frac{Y^*_{\text{phys}}(E_o)}{1 + \exp(\frac{E_o - 90}{50})} [\text{sp}^3]$$

where $Y^*_{\text{phys}}(E_o)$ is the yield given by the modified Bohdansky equation with the lower threshold energies. Note that the term in the denominator restricts the process to energies below 90 eV.

So the authors have incorporated radiation effects, low-energy impact, and a modified flux dependence into the atomic impact model in order to model the erosion due to energetic ions. The total chemical erosion yield for this case is given by

$$Y_{\text{chem}} = Y_{\text{surf}} + Y_{\text{therm}}(1 + DY_{\text{phys}})$$

This model was used to calculate the yields of pyrolytic graphite under energetic hydrogen and deuterium ion bombardment as a function of energy and temperature, at fluxes of $3-6 \times 10^{19} \text{ H}^+/\text{m}^2\text{s}$ and the results are shown in figures 5 and 6. It is notable that, for temperatures near T_m , an energy independent total yield is predicted for ion energies

below the threshold for physical sputtering. At room temperature however, where Y_{surf} dominates, the model predicts a drop in the total yield at these low energies towards a threshold of a few eV.

The term C included in Y_{therm} incorporates the suspected annealing of graphite at higher temperatures and has the effect of changing the flux dependence of Y_m , and T_m as predicted by the atomic impact model. Y_m now drops off more rapidly at higher fluxes and T_m increases less rapidly at higher fluxes and does not exceed 950 K. Note from the figures that, for a fixed flux density, T_m shows no strong dependence on the energy of the impinging ion.

Comparison of the predicted yields to the experimentally determined values, generally shows good agreement. There are some possible problems, however, with the implementation of the processes omitted from the Wittmann and Küppers model. Firstly, the new terms are outside of the framework of the atomistic model. The authors have chosen the forms of the equations to fit the data, rather than allowing the individual reactions to proceed in the model system. To illustrate this point, Y_{surf} clearly depends on the concentration of sp^3 carbon atoms, but it also affects this concentration as the methyl groups are removed by kinetic interactions. Since this process is not included in the system of differential equations this effect is not represented.

It seems that it may be possible to set up a system of equations within the confines of the model system as defined by Küppers et al. in which other processes, introduced by the energy of the impinging particles, may be accounted for. Such an attempt is made in this thesis and is discussed in section 4.

4. A MODEL FOR THE CHEMICAL EROSION OF PYROLYTIC GRAPHITE DUE TO LOW-ENERGY H⁺ AND D⁺ IMPACT

Since energetic hydrogen ions do not form hydrocarbons in graphite until they reach the end of their range (i.e. after they have thermalized), it seems that, in principle, it should be possible to apply the atom model developed by Küppers et al. to the case of energetic ion impact. Of course, modifications to include the effects of energy deposition and low-energy kinetic ejection of near-surface hydrocarbon groups should be incorporated, preferably within the confines of the model system. That is, the atomistic processes resulting from energy deposition and low-energy impact should be identified, and their effects on the populations of the four hybridized carbon populations determined. It should be possible then, to develop a set of differential equations which include the terms developed by Küppers et al., as well as the new terms associated with energetic impact, which may be used to model the chemical erosion of pyrolytic graphite due to low-energy hydrogen ion impact.

In this section, such a semi-empirical model is developed for the methane yield of pyrolytic graphite under low-energy hydrogen irradiation. The new processes associated with the energetic impact of hydrogen will be introduced and their effects discussed. Modifications to the atomistic model of Küppers et al. will also be considered. Once the model has been fully developed, the system of equations will be solved, in steady state, for the methane yield of pyrolytic graphite under low-energy hydrogen impact. Fitting of the model to the present experimentally determined methane yields is left until section 8, where possible extensions of the model to include heavier hydrocarbons and total chemical erosion yields will also be discussed.

4.1 PROCESSES ASSOCIATED WITH ENERGETIC HYDROGEN IMPACT

4.1.1 Energy Deposition

One of the primary effects of the energy associated with incident hydrogen ions is the breaking of carbon-carbon bonds in graphite which, for ions with sufficient energy, leads to amorphization of the graphite throughout the implantation zone. It is this process

which renders the a-C:H films studied by Küppers et al. as suitable model systems for graphite under energetic hydrogen impact [57].

In the context of the atomistic model already developed, an energetic incoming hydrogen ion could break one of the double covalent bonds linking carbon in the sp^2 hybridization state, which has a bond strength of somewhat less than 5 eV [65], resulting in a bond rearrangement producing sp^3 and neighbouring sp^x carbon centers. In this case, the net effect is the same as the hydrogenation of sp^2 carbon centers to form an sp^3 and neighbouring radical sp^x carbon configuration described in section 3.1.2. Such a process should be independent of the graphite temperature and so a rate equation describing this process is given by:

$$d[sp^2]/dt = -[sp^2]\sigma_E\Phi$$

where σ_E is now the effective cross-section (m^2) for the breaking and rearrangement of one of the double covalent bonds in the C=C network by an incident energetic hydrogen ion. Clearly, such a cross-section depends on the energy and isotope of the hydrogen ion. This cross-section will be used as a fit parameter in the model.

4.1.2 Low-energy Hydrogen Ion Impact

Roth and García-Rosales postulated that the room temperature chemical erosion observed for low-energy hydrogen impact on graphite was due to the kinetic ejection of loosely bound hydrocarbons attached as ligands to sp^3 hybridized electronic configurations [64]. This seems to be a reasonable conclusion considering that the observed yield depends on the hydrogen isotope [22] and that the surface concentration of these sp^3 carbon centers is high at low temperatures [63].

Such a process can be incorporated in the model system rather easily by allowing an energetic incoming hydrogen ion to kinetically eject a methyl group which is attached to a carbon in the sp^3 hybridization state creating an sp^x radical configuration. In the Küppers model there are only two sp^3 populations with attached methyl groups, one which is neighboured by another carbon in the sp^3 hybridization state and one which is neighboured by a radical sp^x_{CH} carbon center. The incorporation of the kinetic ejection will, in the first case, lead to a reversal of the hydrogenation reaction, producing

neighbouring carbons in the sp^3 and sp^x configurations while, in the latter case, the neighbouring radical carbon centers will simply form another covalent bond to return to a C=C state. These two processes can be described by their respective rate equations:

$$d[sp^3]/dt = -[sp^3]\sigma_i\Phi$$

$$d[sp^x_{CH}]/dt = -[sp^x_{CH}]\sigma_i\Phi$$

where σ_i is the effective cross-section for kinetic ejection of methyl groups by energetic hydrogen ions (m^2) and is both energy and isotope dependent. This cross-section will also be used as a fit parameter.

Strictly speaking, it is not correct to use the entire concentration of sp^3 hybridization states in the kinetic ejection reaction (or any reaction involving an sp^3 center) since they do not all contain attached methyl groups. It would be more correct to consider two populations of sp^3 configurations, one with an attached methyl group and another with only hydrogen attached, but there are no data available on the relative concentrations of these two populations and so a fifth independent equation cannot be generated to solve for another carbon center population. An implicit assumption involved here (and also in the work of Küppers et al. [60,63] and Roth and Garcia-Rosales [64]), is that the ratio of sp^3 carbon centers with attached methyl groups to sp^3 carbon centers without methyl groups is a constant regardless of the graphite temperature. It is not immediately evident that such an assumption must be true, though it does not seem unreasonable.

This assumption, in essence, provides a fifth independent equation which is linear:

$$[sp^3_{CH3}] = f[sp^3]$$

where $[sp^3_{CH3}]$ is the concentration of sp^3 hybridized carbon with attached methyl groups, and f is a fraction which is ≤ 1 . So the kinetic ejection reaction described above would be more correctly written as:

$$d[sp^3]/dt = -f[sp^3]\sigma_i\Phi$$

The cross-section σ_i however, is simply a constant fit parameter and so the fraction, f , can be incorporated in one step, avoiding the need of a fifth population of carbon centers and the required use of another independent equation.

This argument, which hinges on the assumption that the fraction f is independent of temperature, can be applied to all of the reactions involving carbon in the sp^3 hybridization state. The reader should be aware that this unknown constant is thus incorporated into the fitted cross-sections associated with these processes. Furthermore, if this fraction, f , is energy dependent, such a dependence would also be incorporated in the process of fitting these cross-sections to the experimental data.

In summary, we propose the addition of two new processes associated with the energy of the hydrogen ion to the Küppers model; these are the breaking of one of the C=C double bonds, and the kinetic removal of a methyl group attached to a sp^3 carbon center. These processes are described, in the revised model system, by their cross-sections, σ_E and σ_i respectively, which are used as fitting parameters in the model. It is quite likely that other processes are also occurring, but these two seem to be the most obvious, intuitively, for incorporating energy deposition and explaining low-energy erosion at room temperature. In the next section some modifications to the processes identified by Küppers et al. are suggested and discussed.

4.2 MODIFICATIONS TO THE PROCESSES ASSOCIATED WITH ATOMIC IMPACT

Küppers and his co-workers identified many of the atomistic processes which occur for atomic hydrogen impact on amorphous hydrogenated carbon films as discussed in 3.1. In order to incorporate these fundamental processes into the energetic impact model some small modifications are required. In general, these modifications are included because they will lead to better agreement between the energetic impact model and the present experimental results, but they are also justifiable on a mechanistic level. These modifications and their consequences are discussed here.

4.2.1 Distributed Activation Energies

It has been found previously that the purely thermally activated release of methane and hydrogen (i.e. in the absence of atomic hydrogen impact) from a-H:C films was normally distributed about a central activation energy, with a distribution width of ~ 40 kJ/mol [55,56]. No such distributions were employed for the thermally activated processes

induced by atomic hydrogen impact, namely methane release and H-atom splitoff, in the work of Wittmann and Küppers [63] or Roth and García-Rosales [64]. Horn et al. argued that the heterogeneity of C-C bond strengths in the carbon network led to a precise activation barrier [60], but it is not clear why this matters. The same C-CH₃ bond which must be broken for the purely thermal release of methane must also be broken in the release of methane which is induced by atomic exposure. Similarly, for H-atom splitoff a C-H bond must be broken. One would expect that these bond strengths are distributed. This precise activation barrier led to a very rapid reduction in the methane yield for temperatures below T_m in the modelling of the ASDEX-U erosion results [63] described in 3.2.1, while this problem was alleviated by the Y_{surf} term in the ion erosion model discussed in 3.2.2 [64].

In the present experimental results for energetic hydrogen impact on pyrolytic graphite no such rapid reduction in the methane yield was observed for temperatures below T_m because significant erosion levels occurred even down to room temperature. Furthermore, there was a smooth transition between Y_m and Y_{RT}. Incorporating normal distributions on the activation energies for the atomic hydrogen induced thermal release of methane and hydrogen, E_x and E_H respectively, allows for better modelling of this smooth transition towards the room temperature yield. Since the activation energies for these processes (E_x = 142 kJ/mol and E_H 167 kJ/mol) are on the same order as those for the purely thermal release of methane and hydrogen (234 and 264 kJ/mol, respectively) the use of similar distributions would seem reasonable. In our revised model the best results were obtained for normal distribution widths of 40 and 50 kJ/mol for E_x and E_H, respectively. This is discussed further in section 8.

4.2.2 Activated Abstraction

Lutterloh et al. identified the Eley-Rideal abstraction process using HREELS as described in section 3.1.3 [59]. They noted that, although this abstraction was slightly activated, it could be well approximated by a constant cross-section of $\sigma_D = 5 \times 10^{-22} \text{ m}^2$.

In our revised model better agreement with the experimental results is obtained, for temperatures below T_m, if this abstraction process is slightly activated. That is, instead

of an abstraction process described by a constant cross-section, σ_D , an activated term described by k_D and E_D is used, where k_D is the prefactor and E_D is the activation energy for atom induced abstraction and is normally distributed. The two unknowns, k_D and E_D , were used as fit parameters in the present model with the restriction that, for low-energy impact (10 eV) at high temperatures, the value of $k_D/\Phi \exp(-E_D/kT)$ approaches a constant which is close to the value of σ_D used in the Wittmann-Küppers model [63]. We do not preclude the possibility that these parameters are functions of energy and thereby allow for a kinetic effect on this abstraction process.

4.2.3 Surface Treatment

The hydrogen atom impact model developed by Küppers et al. deals with processes that occur on the surface of a-C:H films. In their extension to energetic hydrogen impact, Wittmann and Küppers mathematically divided the graphite bulk into 1 nm layers and treated each as a surface which was exposed to an energy- and depth-dependent flux of thermal atoms [63]. Roth and García-Rosales, however, do not go to this length, but rather, treat the entire implantation zone as one effective surface exposed to the total flux density of thermalized ions [64]. Although the former method is more rigorous, the latter also has merit and is easier to use.

Exposure of graphite to ions of sufficient energy results in the creation of an amorphous implantation layer which is saturated with hydrogen [9]. Such a layer has many internal surfaces which are well connected to the geometrical surface via ion induced damage pathways. So, for energetic ion impact, one can talk about an ‘effective surface’ which is greater than the geometric surface. The release of methane and hydrogen may occur at any of these internal surfaces and, assuming instantaneous transport, this is equivalent to the release of these molecules at the geometric surface. Of course, for ion impact below say 25 eV, this amorphisation does not occur. Instead, all of the reactions occur on or near the physical surface and it is likely that this graphite surface is still well described by the model system of Küppers.

In our model, this ‘effective surface’ approach has been adopted because it is easier to implement. As in the model of Roth and García-Rosales, the total flux density, as

determined by the geometric surface has been used. Strictly speaking, this is not the correct approach. The total effective surface area should be estimated so that a revised flux density may be determined. This effective surface area depends on the ion impact energy and is difficult to determine. Instead, we have chosen to use the total flux density as measured in the experiments, which was nearly constant for all ion energies, and use the fit parameters σ_E , σ_i , k_D , and E_D as characteristic of the total flux at which the fitting occurs ($10^{18} \text{ H}^+/\text{m}^2\text{s}$). It is not immediately evident if these parameters are strong functions of ion flux.

In brief, our modifications to the atom model of Küppers et al. include (i) the introduction of distributed activation energies for the atom-induced thermal release of hydrogen and methane, (ii) the use of a slightly activated abstraction process instead of a constant abstraction cross-section, and (iii) the treatment of the entire implantation zone as one ‘effective surface’. In all other aspects the model is unchanged. Namely, the values for k_x , k_H , σ_H , E_x , and E_H as determined previously [63], have been used in the present model. In the next section our revised model system is summarized and solved in steady state.

4.3 MODEL SYSTEM FOR METHANE EROSION DUE TO ENERGETIC HYDROGEN ION IMPACT

The model, including the new and modified terms discussed in the previous sections is shown in figure 7. Starting from the bottom and working clockwise we note that hydrogenation (σ_H) and energy deposition (σ_E) lead to a reduction in the surface concentration of sp^2 hybridized carbon centers (state 1) while producing an sp^3 and a neighbouring radical sp^2H center (state 2). An activated release of hydrogen atoms (k_H) may return the electronic configuration to state 1, or further hydrogenation (σ_H) may occur leading to the formation of neighbouring carbon in the sp^3 hybridization state, some unknown fraction of which will contain at least one attached methyl group (state 3). Energetic ion impact may kinetically remove a methyl group (σ_i) returning the sp^3 carbon configuration to state 2 or, activated hydrogen abstraction (k_D) may occur leading to the

formation of a radical sp^x_{CH} carbon configuration neighboured by a methyl containing sp^3 center (state 4). Hydrogenation of the radical bond (σ_H) may return this carbon pair to state 3 or methyl may be released, either by an activated process (k_x) or an ion induced kinetic mechanism (σ_i), leading to a return to state 1.

All of these processes can be described by a set of four time-based differential equations in the four unknown carbon hybridization state populations. This system of equations is summarized in Table 2 below.

Table 2. Revised Model System of differential equations

Reaction	Parameters	$d[sp^2]/dt$	$d[sp^x_H]/dt$	$d[sp^3]/dt$	$d[sp^x_{CH}]/dt$
hydrogenation $sp^2 \rightarrow sp^x_H$	$\sigma_H = 4.5 \times 10^{-20} m^2$ [63]	$-2[sp^2]\sigma_H\Phi$	$[sp^2]\sigma_H\Phi$	$[sp^2]\sigma_H\Phi$	
hydrogenation $sp^x_H \rightarrow sp^3$	$\sigma_H = 4.5 \times 10^{-20} m^2$		$-[sp^x_H]\sigma_H\Phi$	$[sp^x_H]\sigma_H\Phi$	
hydrogenation $sp^x_{CH} \rightarrow sp^3$	$\sigma_H = 4.5 \times 10^{-20} m^2$			$[sp^x_{CH}]\sigma_H\Phi$	$-[sp^x_{CH}]\sigma_H\Phi$
hydrogen abstraction $sp^3 \rightarrow sp^x_{CH}$	E_D $k_D = f(E_n)$			$-[sp^3]K_D$	$[sp^3]K_D$
methyl ejection $sp^3 \rightarrow sp^x_H$	σ_i		$[sp^3]\sigma_i\Phi$	$-[sp^3]\sigma_i\Phi$	
methyl ejection $sp^x_{CH} \rightarrow sp^2$	σ_i	$2[sp^x_{CH}]\sigma_i\Phi$		$-[sp^x_{CH}]\sigma_i\Phi$	$-[sp^x_{CH}]\sigma_i\Phi$
energy deposition $sp^2 \rightarrow sp^x_H$	σ_E	$-2[sp^2]\sigma_E\Phi$	$[sp^2]\sigma_E\Phi$	$[sp^2]\sigma_E\Phi$	
methyl release $sp^x_{CH} \rightarrow sp^2$	$E_x = 142 \text{ kJ/mol}$ $k_x = 10^{13} \text{ s}^{-1}$ [63]	$2[sp^x_{CH}]K_x$		$-[sp^x_{CH}]K_x$	$-[sp^x_{CH}]K_x$
H release $sp^x_H \rightarrow sp^2$	$E_H = 167 \text{ kJ/mol}$ $k_H = 10^{13} \text{ s}^{-1}$ [63]	$2[sp^x_H]K_H$	$-[sp^x_H]K_H$	$-[sp^x_H]K_H$	

In steady-state, these four equations can be set equal to zero and, using the additional equation:

$$[sp^2] + [sp^x_H] + [sp^3] + [sp^x_{CH}] = 1$$

it is possible to solve for the unknown surface concentrations of the four types of carbon centers in terms of the experimentally determined constants and fitting parameters. The resulting solution is presented here:

$$[sp_{CH}^x] = \left\{ \frac{K_x}{\sigma_H \Phi} + \frac{K_x}{\Phi(\sigma_H + \sigma_E)} + I + \frac{K_x K_{-H}}{\sigma_H \Phi^2 (\sigma_H + \sigma_E)} + \frac{\sigma_H \Phi}{K_D} + \frac{K_x}{K_D} + \frac{K_x \sigma_i}{K_D \sigma_H} \left(I + \frac{K_{-H}}{\Phi(\sigma_H + \sigma_E)} \right) \right\}^{-1}$$

$$+ \frac{\sigma_i \Phi}{K_D} \left(I + \frac{\sigma_i}{\sigma_H} \right) + \frac{\sigma_i}{(\sigma_H + \sigma_E)} \left(I + \frac{K_{-H}}{\sigma_H \Phi} \right) + \frac{\sigma_i K_{-H}}{K_D (\sigma_H + \sigma_E)} \left(I + \frac{\sigma_i}{\sigma_H} \right) + \frac{\sigma_i}{\sigma_H} + \frac{\sigma_i \Phi}{K_D}$$

$$[sp^3] = [sp_{CH}^x] \left\{ K_x + \Phi \frac{\sigma_H + \sigma_i}{K_D} \right\}$$

$$[sp_H^x] = [sp_{CH}^x] \left\{ \frac{K_x}{\sigma_H \Phi} + \frac{\sigma_i}{\sigma_H} \left(I + \frac{K_x + \Phi(\sigma_H + \sigma_i)}{K_D} \right) \right\}$$

$$[sp^2] = [sp_H^x] \frac{K_{-H}}{\Phi(\sigma_H + \sigma_E)} + [sp_{CH}^x] \frac{K_x + \sigma_i \Phi}{\Phi(\sigma_H + \sigma_E)}$$

Given these steady-state concentrations, the resulting methane yield is given by:

$$Y_{CH4} = \rho \{ [sp^3] \sigma_i + [sp_{CH}^x] (\sigma_i + K_x / \Phi) \}$$

where ρ is a normalizing constant which is the surface density of carbon atoms, $\sim 6 \times 10^{19} \text{ m}^{-2}$.

Using the fitting parameters described in sections 4.1 and 4.2 it is now possible to compare this methane yield model to the experimentally measured methane yields due to low-energy hydrogen ion impact on pyrolytic graphite. This is discussed in section 8 following the presentation and discussion of the experimental results.

5. EXPERIMENT

Extensive design, development and characterization of the experimental facility and its components was required before the low-energy hydrogen impact erosion experiments could begin. Details of the experimental facility and its operational characteristics are provided here followed by a discussion of the experimental procedures employed in the present chemical erosion experiments.

5.1 EXPERIMENTAL FACILITY

Here we describe the main components of the experimental facility including the vacuum system, ion gun and mass filter characterization, deceleration lens design and testing, graphite specimen properties, quadrupole operation and data acquisition, and a simulation of the tritium lab operation.

5.1.1 UHV System

All experiments were performed in a ultra-high vacuum (UHV) facility depicted schematically in figure 8. The test chamber was equipped with four 203.2 mm ports, two 152.4 mm ports, and twelve 69.85 mm ports. An ion gun was directed towards the center of the main chamber via a wien-type mass filter and a 5-element electrostatic deceleration lens. Gas was supplied to the ionization chamber of the gun via a variable leak valve. Pumping of the ionization chamber and differential pumping of the mass filter was provided by a SAES 50 L/s getter pump. The graphite specimen was positioned normal to the ion-beam, 50 mm from the last electrode of the deceleration lens. The specimen, held in stainless steel jaws, could be heated resistively and its temperature was monitored via optical pyrometry. All reaction products produced at the specimen were monitored in the residual gas using a non-differentially pumped Extranuclear quadrupole mass spectrometer.

The entire UHV facility was pumped by a 360 L/s Leybold-Heraus turbo-molecular pump which was backed by a Leybold Trivac mechanical pump. After exposure to atmosphere the entire system was baked at 220 °C for at least 24 hours. If water levels remained high, a 'hot' (~ 1800 K) tungsten ring filament producing H⁰-atoms in a

hydrogen backfill of $\sim 10^{-4}$ Torr was operated for a further 24 hours. The pressure was monitored, both in the ionization chamber of the ion gun and the main chamber, via Bayard-Alpert type ionization gauges. This system routinely achieved ultimate pressures of $< 5 \times 10^{-10}$ Torr consisting mainly of H₂ and CO, with much smaller contributions from H₂O and CO₂.

5.1.2 Ion Gun

A compact SPECS IQE 12/38 electron-impact extraction type ion gun was used to provide a fairly intense ion beam. This ion source utilizes an iridium ring filament as a cathode which encloses an anode cage. The 100 eV electrons emitted from the cathode traverse the anode cage several times producing a high density of ions in this region. These ions are extracted at selectable energies between 0.2 and 5.0 keV. Two lens elements allow variable focusing of the beam.

Following installation of the ion gun, extensive characterization was carried out using argon, helium, deuterium, and hydrogen. The available ion current for each gas was determined as a function of both the ion energy and the gas pressure in the ionization chamber. In figure 9, the available ion current as a function of energy, at the optimum source pressure, is shown for the three test gases. In the case of deuterium, $\sim 37 \mu\text{A}$ was available at 5 keV and $\sim 6 \mu\text{A}$ at 1 keV. The optimum source pressure depended on the gas, but was always in the narrow range of $2-5 \times 10^{-3}$ Torr.

A 12-pin probe, on an adjustable vertical feedthrough, was used to profile the beam density and a typical profile is shown in figure 10. In general, the beam displayed a Gaussian profile which was slightly elongated in the vertical plane. In the defocused high current mode, spot sizes were still $\leq 2\text{mm}$. Finer focusing could be achieved at the expense of beam current. For the proposed experiments, a higher ion current was advantageous and so further characterization was done in the defocused mode.

5.1.3 Mass Filter

A SPECS wien-type mass filter was installed between the ionization chamber and the dual lens elements of the ion gun. Differential pumping of the filter was provided by a SAES 50 L/s getter pump. A wien filter is a velocity analyzer which uses an $\mathbf{E} \times \mathbf{B}$ force to select ions of a specific velocity. The filter included a bend which acted as a neutrals stop so that, rather than a straight-through analyzer, only ions with a specific radius of curvature imparted by the $\mathbf{E} \times \mathbf{B}$ force exit the filter. The removable magnet had a field strength of ~ 4060 G while the electric field was variable between 0 and 1×10^5 V/m. The equation governing the mass selection is given by

$$m/e = (2UB^2)/E^2$$

where U is the ion energy, and so the maximum transmittable ion energy is determined by the mass of the ion and the maximum available electric field.

With the mass filter installed the transmission through the filter in the defocused mode was in the range of 25 - 30 % of the unfiltered current. For lighter gases an upper limit was imposed on the ion energy by the equation given above. If we specify a minimum required current of $0.7 \mu\text{A}$ then it is possible to define usable energy ranges for both deuterium (900 to 1300 eV D_2^+) and hydrogen (400 to 700 eV H_3^+). Here the different molecular ion species have been selected in order to maximize the ion beam current for each species.

The resolution of the filter was also determined experimentally using nitrogen and carbon dioxide as test gases. In general, the resolution improved as the ion energy was decreased. At 1 keV the resolution was $m/\Delta m = 17$ which was more than sufficient for the proposed experiments (i.e. resolution of HD^+ and D_2^+ was possible). Profiling of the filtered beam showed a similar distribution to that of the unfiltered beam. Since the spot sizes remained about the same the reduction in ion current resulted in reduced current density. It was found that current densities of $2-4 \times 10^{18}$ ions/m²s were available for deuterium and protium. Unfortunately, the available energy ranges were still too high to perform low-energy erosion experiments, characteristic of the plasma species in the divertor region of tokamaks.

5.1.4 Electrostatic Deceleration Lens

5.1.4.1 Background

When working with intense beams of energetic ions it is often difficult to simply decelerate the beam at the target since space-charge effects lead to rapid expansion of the beam and subsequent loss of beam current and current density. A common approach used to overcome this problem is to transmit the beam through an electrostatic deceleration lens in front of the target in order to focus the beam against space-charge forces. If it is not necessary to change the orientation of the target then it is often possible to use the target as the end electrode of the lens. If, however, target orientation will vary, it is necessary to design a lens system which will leave the target in a virtually field free zone [66]. Much work has been conducted on the design and characterization of electrostatic ion lenses and a discussions of commonly used lenses and their design are available [66,67].

Electrostatic lenses need not be complex. The 3-element ‘zoom’ type lens was employed by Liebl et al. [68] and after decelerating a deuterium beam from 6 keV down to 100 eV they obtained current densities of $\sim 100 \mu\text{A}/\text{cm}^2$. On the other hand, a 13-element lens, developed by Herman et al. [69], extended the energy range even lower and allowed for placement of the target in a virtually field free zone. Using this lens they were able to obtain current densities of $8 \mu\text{A}/\text{cm}^2$ down to 30 eV. More recently a 5-element lens using the target as the end electrode was developed by Foo et al. [70] which could decelerate argon from 3 keV to 10 eV while maintaining a current density of $10 \mu\text{A}/\text{cm}^2$. We concluded that such a 5-element system was a good starting point in the design of an electrostatic lens capable of decelerating 600 eV H_3^+ and 1300 eV D_2^+ down to 10’s of eV.

A further concern in the present experiments was the possibility of charge exchange in the lens leading to a significant amount of energetic neutrals in the beam as it strikes the target. The equation governing the fraction of hydrogen ions undergoing charge exchange is given by [71]

$$f_{CE} = 1 - \exp(-n_{H2}\sigma_{CE}x)$$

where n_{H_2} is the density of the background hydrogen (m^{-3}), σ_{CE} is the cross-section for charge exchange due to energetic hydrogen impacting on neutral H_2 (m^2), and x is the distance the ions travel through the hydrogen background (m). This fraction would have to be calculated for any lens design and kept below ~ 0.001 in order to make synergistic effects negligible [16].

5.1.4.2 Design

In general, the design of an electrostatic deceleration lens is aided greatly by software which, given the lens geometry and applied voltages, calculates ion trajectories through the lens system. One such available program is SimIon which uses a technique called successive displacement with over-relaxation [72] to solve Laplace's equation for the potential field distribution in the ion optical array given the required boundary conditions. This code has been modified by Tanner [73] to include space-charge effects in an iterative procedure. The space-charge is calculated from the ion density map and modifications to the potential field distribution are incorporated. The new ion trajectory is then calculated and the procedure is iterated until the calculated trajectory converges to a solution. This software was used to assist in the design of a deceleration lens for the present experiments.

A 5-element cylindrically symmetric lens using the target as an additional end electrode, based on the one developed by Foo et al. [70] with similar lens element dimensions, was chosen as a starting point for our design. For such a design the final ion energy is determined by the difference between the beam energy of the source and the bias voltage applied to the target. Ion trajectories, through the lens array, for 1500 eV T_2^+ ions were calculated, using the space-charge corrected SimIon software, for several applied fields and end ion energies, and a typical trajectory calculation is included in figure 11. Similar trajectory calculations could not be made for D_2^+ and H_3^+ due to limited availability of the computer used for these trials. Several hundred cases were run in order to optimize the lens design with respect to the electrode dimensions and the applied voltages so that maximum transmission at a reasonable current density ($> 5 \mu A/cm^2$) could be achieved without exceeding any applied element voltage of 3 kV.

The final design settled upon showed strong transmission characteristics and is shown in figure 12. The transfer end of the lens sits just downstream (3mm) of the exit aperture of the ion gun and is designed with a bulky support structure which allows mounting and alignment on the inside of a 152.4 mm conflat flange (I.D. = 97.3 mm). Insulating gaps of 5 mm (Macor) were chosen to prevent dielectric breakdown. A high voltage/low current voltage divider circuit was designed so that voltages for all 6 elements (including the target) could be supplied by just 2 power supplies. In general, this lens system accelerates the ions emerging from the gun over the first half of its length and then strongly focuses them using nearly parallel potential fields over the last half.

No exit aperture was used on the lens because no ion current loss could be afforded. This has the drawback of allowing some of the secondary electrons produced in the lens to reach the target specimen making the measurement of ion current more complicated. On the other hand, due to the large conductance of the lens, the volume inside can be maintained at pressures near those of the test chamber, $\sim 1 \times 10^{-7}$ Torr for typical source pressures of 2×10^{-3} Torr in the gun ionizer, which reduces the amount of charge-exchange in the lens. For example, for 600 eV H_3^+ , $\sigma_{CE} \sim 4 \times 10^{-19} m^2$ [71], $x = 0.2$ m, $n_{H_2} = 8 \times 10^{15} m^{-3}$, and so the fraction of the beam undergoing charge exchange in the lens is

$$f_{CE} = 1 - \exp(-n\sigma_{CE}x)$$

$$f_{CE} = 6.5 \times 10^{-4}$$

This value represents an upper limit since neutrals created by charge exchange will continue in the direction they were traveling at the time of creation and, hence, only a fraction of the charge exchange neutrals created will actually strike the specimen. This upper value of 0.07% energetic neutral content in the beam should make synergistic effects negligible [16].

5.1.4.3 Characterization

The lens was installed between the exit aperture of the ion gun and the graphite specimen and was characterized using deuterium and protium. Initially the voltages

applied to the 5 lens elements were based on the results of the SimIon calculations for tritium. A single pin probe was used to profile the transmitted beam as a function of the applied voltages, and the location of the specimen downstream from the last lens element, for several final ion energies. Typical profiles are shown in figure 13. It should be noted that electron-impact ion sources of the type used here have energy spreads of < 1eV [66] and so the decelerated beam was not energy analyzed. In general, voltage settings needed to optimize the transmitted beam current while maintaining spot sizes < 4mm were determined using the single pin probe. Subsequent secondary electron corrections (originating from the lens elements) to the measured ion currents were made on the basis of the negative background observed in the ion beam profiles.

The lens performed very well. Transmission characteristics were good with 100% transmission of the mass-filtered beam at 200 eV/D⁺ and 80% transmission at 10 eV/D⁺. Similar results were obtained for hydrogen transmission. This performance meant that the obtainable current densities were ~ 1- 3 × 10¹⁸ (H⁺ or D⁺)/m²s.

5.1.5 Graphite Specimen

A single graphite specimen was used for all of the low-energy erosion experiments. The as-deposited pyrolytic graphite specimen, HPG99, was manufactured by Union Carbide. This polycrystalline graphite exhibits both micro and macro porosity, has a mosaic spread of ~ 30°, and a density of 2.2×10⁻³ g/mm³. The specimen was held normal to the incident low-energy beam in stainless steel jaws and could be heated resistively. The graphite temperature was monitored with an Ircon optical pyrometer which was calibrated against a type-C tungsten-rhenium thermocouple.

5.1.6 Quadrupole Mass Spectrometer and Data Acquisition

An Extranuclear quadrupole mass spectrometer equipped with a channeltron electron multiplier was used for all of the low-energy experiments. The quadrupole was used to monitor hydrocarbon products in the residual gas (RGA) and was attached to the main UHV chamber via a high-conductance orifice. The quadrupole was not differentially pumped and so care was taken to ensure that the background hydrogen pressure in the test

chamber, and hence the quadrupole sensitivity, were kept nearly constant during erosion experiments. The quadrupole was calibrated *in situ* with known leaks of CH₄, C₂H₄, C₃H₆, CD₄, C₂D₄, and C₃D₆. The quadrupole sensitivity to other hydrocarbons was not measured explicitly, but was calculated. This is discussed further in section 5.2.1.

Data acquisition was done by computer (486 DX33) which employed a 16-bit National Instruments ATMIO data acquisition card. Using software developed in the LabWindows user interface environment it was possible to select the quadrupole mass and read the signal intensity at that mass. The software allowed display, handling, and storage of all of the acquired data and this is discussed further in section 5.2.

5.1.6 Tritium Lab Simulation

One of the reasons that a compact ion gun was chosen for the present investigation was that it could subsequently be installed in the University of Toronto's tritium lab [74] so that the erosion experiments could be continued with tritium. The tritium lab is an oil free facility which uses cryosorption and cryocondensation pumps to provide the vacuum, while getter pumps, which pump isotopes of hydrogen reversibly, are used to control the tritium inventory. Tests which would simulate operation of the gun in the tritium lab were carried out prior to installation of the deceleration lens.

In order to simulate the tritium lab, the turbomolecular pump was isolated, and a source getter (SAES ST. 101/CTAM 4.4D) was loaded with a fixed amount of hydrogen (0.4 TorrL) corresponding to $\sim 2 \mu\text{Ci}$ of tritium. This was done by filling a known volume (0.24 L) with a fixed hydrogen pressure, which was measured by a pirani gauge calibrated against a capacitance manometer. A valve between the fixed volume and the source getter chamber was then opened and the source getter was loaded. This getter was then activated (5 to 11 A) to supply the ionization chamber of the ion gun with hydrogen at a pressure of about 5×10^{-4} Torr. A getter pump (SAES ST707-50) was used to pump both the test chamber and the differential stage of the wien filter, thus retrieving most of the hydrogen. Following operation in this mode, the hydrogen on the getter pump could be regenerated back onto the source getter through a connecting valve. This process could be

repeated until the hydrogen losses in the system (due to wall pumping and getter pump equilibrium pressure) became too great.

Tests were performed according to this procedure and it was found that a 0.4 ± 0.2 TorrL load resulted in stable gun operation at 0.85 to $1.00 \mu\text{A}$ D_2^+ for up to 100 minutes at a time. It took ~ 80 - 120 minutes to regenerate the hydrogen back onto the source getter and subsequent operation yielded run times $\sim 10\%$ shorter. Even though this performance meant experiments would take a long time it was considered acceptable for application in the tritium lab.

5.2 EXPERIMENTAL PROCEDURE

All of the experiments were performed in the UHV facility described in 5.1.1. The graphite specimen used in all of the experiments was the same and was positioned normal to the incident beam. Following exposure to air, the specimen was baked at 1100 K overnight. Annealing at 2000 K for 30 seconds was performed between experiments of different ion energies in order to remove ion induced damage resulting from prior irradiation [75].

Typically, a set of experiments was conducted at each of the selected ion energies (10, 15, 25, 50, 100, and 200 eV), where temperature profiles for the methane and heavy hydrocarbons (C_2H_2 , C_2H_4 , C_2H_6 , C_3H_6 , C_3H_8) yields were determined. The ion energy was determined by the difference between the energy of the extracted beam and the bias potential of the sample. Since the transmitted ions are molecular this energy is divided among the atoms in the molecule. Here we refer to the incident beam particles as H^+ or D^+ even though not all of the atoms in the molecular ion (H_3^+ or D_2^+) are charged. It is also recognized that when low-energy molecular ions break up, upon striking the graphite surface, there may be an uneven sharing of energy between the atoms, on the order of the binding energy, a few eV [76]. Furthermore, it is also possible that, for low-energy impact, the atoms in the molecular ion do not act independently as they interact with the surface atoms, which may affect their chemistry and the hydrocarbon formation process.

At the beginning of each experiment the quadrupole sensitivity was calibrated against in situ known leaks and the graphite specimen was heated to 1200 K for ~ 10 seconds in order to release trapped hydrogen. For a given ion energy, the graphite specimen bias voltage and deceleration lens element voltages were selected and verified with a high impedance voltage probe. When the ion-beam was turned on the ion current was measured at the specimen with small corrections made for the contribution from secondary electrons, originating in the deceleration lens, which reach the specimen.

A typical chemical erosion experiment began with the graphite specimen at room temperature and the temperature was subsequently increased in ~ 100 K increments up to the final temperature of 1000 K. For each graphite specimen temperature the ion-beam impact proceeded for more than an hour prior to signal measurement. Thus the achieved fluence (~ 4×10^{21} H⁺,D⁺/m²) was near the value of ~ 10^{22} H⁺,D⁺/m² required for steady state erosion signals for energetic hydrogen impact [77-79].

Once steady state was achieved the data acquisition system was used to scan and record the QMS signals for masses 15, 16, 24, 25, 26, 27, 28, 29, 30, 39, 41, 42, and 43 a.m.u in the case of H⁺ impact, and 18, 20, 26, 30, 32, 34, 36, 46, 48 a.m.u in the case of D⁺ impact. For each individual mass the quadrupole peak was scanned in a step-wise (150 steps) manner. The peak value was then selected and displayed in a real-time plot as the measured signal for that mass. This peak scan was repeated 10 times for each mass and the average of the 10 peak values was stored as the measured signal for that mass. The ion-beam was subsequently turned off and a plot of the QMS signal intensity at mass 15 for H⁺ impact (mass 20 for D⁺ impact) was observed to determine when the background steady-state was achieved. Other masses were also observed to ensure that steady-state was achieved for the heavier hydrocarbons. The same selected masses were again scanned and stored by the data acquisition system. Typical real-time spectra produced by this technique are shown for 10 and 200 eV D⁺ impact in figures 14 and 15, respectively. The differences in the average peak values of the beam on signals and beam off signals was stored on disk as the measured erosion signals.

The calculation of the erosion yields for the hydrocarbon products monitored in these experiments is complicated by the variance in QMS sensitivity to each of the

hydrocarbon species and the QMS convolution of the measured signals due to hydrocarbon cracking in the ionizer. Furthermore, contributions from hydrocarbon formation on the walls due to reflected hydrogen ion incidence must also be determined and subtracted from the calculated yields. The data analysis required for these experiments is discussed next.

5.2.1 Matrix Analysis of Measured Erosion Signals

When determining the erosion yields for several hydrocarbons one must consider the relative QMS sensitivities to each of these species as well as contributions to the measured erosion signal at a certain mass which may arise from cracking of heavier hydrocarbons in the quadrupole ionizer. One relatively simple way to do this is by the use of matrix analysis of the erosion signals such as that described by Davis et al. [16].

Such a matrix analysis requires an assignment of each hydrocarbon species to its principal analysis mass. The assignments used here for H^+ and D^+ are summarized in Table 3 below.

Table 3. Principal Analysis Masses

<i>Hydrocarbon Product</i>	<i>Analysis Mass (a.m.u.)</i>	
	H^+ impact	D^+ impact
$CH(D)_4$	15	20
$C_2H(D)_2$	26	26
$C_2H(D)_4$	27	30
$C_2H(D)_6$	30	36
$C_3H(D)_6$	41	46
$C_3H(D)_8$	29	34

In order to account for cracking of heavier hydrocarbons it is necessary to determine the contributions from cracking to each of the six principal analysis masses. Since only three in situ leak bottles were used for the experiments it was only possible to determine exact cracking patterns for three of the hydrocarbons, the other three cracking patterns were inferred from the results of Davis et al. [16]. In this way it is possible to form a 6×6

cracking pattern matrix, \mathbf{C} , where the rows are the principal analysis masses in ascending numerical order and the columns are the hydrocarbon species in ascending mass order. A typical example of the cracking pattern matrix for hydrogen ion impact is shown below.

The cracking patterns for the three in situ leak bottles were measured prior to each erosion experiment and the variance was, in general, < 3%. The cracking patterns for the other three gases were not changed.

$$C = \begin{bmatrix} m:gas & CH_4 & C_2H_2 & C_2H_4 & C_2H_6 & C_3H_6 & C_3H_8 \\ 15 & 1 & 0 & 0.011 & 0.21 & 0.073 & 0.06 \\ 26 & 0 & 1 & 0.974 & 1 & 0.158 & 0.083 \\ 27 & 0 & 0 & 1 & 1.47 & 0.58 & 0.38 \\ 29 & 0 & 0 & 0.031 & 1 & 0.011 & 1 \\ 30 & 0 & 0 & 0 & 1 & 0 & 0 \\ 41 & 0 & 0 & 0 & 0 & 1 & 0.095 \end{bmatrix}$$

Using the three in situ leak bottles it was possible to determine the relative QMS sensitivities for ethylene and propylene with respect to methane. Once again, the other three relative sensitivities were estimated based on the results of Davis et al. [16]. A typical set of QMS sensitivities relative to methane for hydrogen ion impact is shown in Table 4 below.

Table 4. QMS Sensitivities relative to methane.

Mass (a.m.u.)	Relative Sensitivity	Hydrocarbon
15	1.0	CH ₄
26	0.30	C ₂ H ₂
27	0.64	C ₂ H ₄
30	1.62	C ₂ H ₆
41	1.05	C ₃ H ₆
29	0.41	C ₃ H ₈

The relative sensitivities for the two in situ heavy hydrocarbon leak bottles were measured prior to each erosion experiment. Although, these values did not change significantly (< 5 %) from day to day, long term trends in the QMS sensitivity were observed. Typically, the measured sensitivities relative to methane for ethylene and propylene were used in the calculations and small adjustments to the other relative sensitivities were made on the basis of their masses.

Given the cracking matrix, C , the measured signal vector divided by incident ion flux, \underline{s} , the relative sensitivities in a diagonal matrix, R , and the constant, m_{CH_4} , which is the QMS sensitivity to methane, then the following equality is true;

$$m_{CH_4} R \underline{s} = C \underline{y}$$

where \underline{y} is the erosion yield vector. Rewriting this one obtains;

$$m_{CH_4} C^{-1} (R \underline{s}) = \underline{y}$$

It is possible then, given the measured erosion signals at each analysis mass, to determine the hydrocarbon erosion yields by solving the left hand side of this equation. This was the method employed in the present data analysis. It should also be mentioned that previous studies show little evidence of significant contributions from even heavier hydrocarbons (C_4H_k etc.), even for thermal atom impact where the relative contributions of these species should be greatest [80,81].

5.2.2 Wall Contribution to Erosion Signals

In general, a fraction of the hydrogen ions incident on graphite are reflected from the specimen to the walls of the vacuum chamber where they can form hydrocarbons which may subsequently be desorbed and detected by RGA. This may be called the wall contribution to the erosion signal and should be subtracted to obtain the true chemical erosion yields. In practice, it is not always necessary to make this correction since, for high energy H^+ , D^+ impact, the reflection coefficient is small [82] and the chemical erosion yield of graphite is high and so the wall contribution to the total signal is negligible. In the present experiments, however, the opposite is true. For low incident ion energies the reflection coefficient is relatively higher [82] and the erosion signals are relatively lower so that the wall contribution may actually dominate the measured signal. It becomes

necessary then to quantify and subtract the wall contribution in order to obtain the true erosion yields.

In the present experiments the wall contribution was determined in the following manner. The graphite specimen was annealed at 1200 K for \sim 10 s, in order to thermally desorb the hydrogen in the specimen, and then allowed to cool to room temperature over a period of \sim 45 minutes. The ion-beam was then turned on while the data acquisition system monitored the methane signal from the QMS. As is shown in figure 16, typically, a very fast rise in the methane signal was observed with a time constant of \sim 3 s followed by a long slower increase with an energy dependent time constant of \sim 20 - 100 s.

For energetic hydrogen impact on graphite there is essentially 100% retention of the non-reflected particles until a fluence corresponding with the saturation of the implantation zone is reached. For 1 keV deuterium impact on carbon this fluence is $\sim 1.5 \times 10^{21} D^+/m^2$ [83,84]. Of course this saturation fluence depends on the ion energy since the depth of the implantation zone is reduced at lower energies. For instance, the saturation fluence for 50 eV D^+ impact on carbon is $\sim 1.4 \times 10^{20} D^+/m^2$ [83]. If we consider 10 eV D^+ impact, the implantation zone is about 3 monolayers and using a D/C ratio of ~ 0.4 we determine that a fluence of $\sim 3.5 \times 10^{19} D^+/m^2$ is required for saturation. For the fluxes employed in the present experiments ($10^{18} D^+/m^2$ s), this corresponds to a saturation time of about 30 seconds which is confirmed, approximately, in figure 16.a. For higher energy bombardment, longer saturation times are expected (fig. 16.b).

Thus, immediately after the beam is turned on the graphite specimen is not hydrogenated and the initial steep rise cannot be due to methane desorbed from the specimen. There is however, an abundance of hydrocarbon precursors found on the vacuum walls, due to the history of particle bombardment resulting in carbon sputtering, and this initial steep rise can be attributed to methane formation resulting from the interaction of the reflected particles with the walls. The subsequent long steadily increasing signal is due to methane originating from the specimen as its hydrogen inventory approaches steady state. It should be noted that this steep signal increase was also observed, to varying degrees, for the heavier hydrocarbons.

Since the reflection coefficient increases and the chemical erosion yield decreases as the hydrogen ion energy is reduced, the wall contribution to the total chemical erosion signal increases. The experimentally determined values for the wall contribution to the methane production as a percentage of the total measured Mass 15 (H^+ impact) signal at T_m are summarized in Table 5.

It is clear that, at low energies, the real methane erosion signal (and that due to heavier hydrocarbons where similar ratios apply) is a small signal on a large background. This is especially true at temperatures removed from T_m where the real methane erosion signals are smaller. The reader should be aware that any systematic errors in determining this wall correction could result in significant errors in the reported yields.

Table 5. Wall Contribution as percentage of Measured Methane Signal at T_m for H^+ impact

<u>Energy (eV)</u>	<u>% of Total Signal</u>
10	75
15	69
25	61
50	50
100	45
200	30

It should be noted that the magnitude of this wall contribution is independent of the graphite specimen temperature within experimental error. That is, even for graphite temperatures of 1100 K, where no significant chemical erosion is expected, the total measured methane signal (and those for heavier hydrocarbons) obtained by turning on the ion-beam was within 5 % of the wall contribution as determined at room temperature. Although heating the specimen induces warming of the vacuum walls, the release of hydrocarbons from the walls seems to be dominated by the kinetic interaction of the reflected beam ions and is not thermally activated for the wall temperatures achieved in these experiments (room temperature to $\sim 60^\circ C$).

Using the experimental procedure and data analysis techniques described here, total chemical erosion yield experiments for H^+ and D^+ impact on pyrolytic graphite were

conducted for ion energies between 10 and 200 eV and the results of these experiments are presented in section 6.

6. EXPERIMENTAL RESULTS

The main objective of this thesis is the study of the chemical erosion of pyrolytic graphite due to low-energy hydrogen ion impact. The study includes, principally, the experimental measurement and determination of methane and heavier hydrocarbon erosion yields as a function of graphite temperature (300 - 1000 K) and ion energy (10 - 200 eV). The use of both protium and deuterium as the impacting ion species also allows an investigation into the isotopic effect on the low-energy chemical erosion of pyrolytic graphite.

In this section we will present the basic data obtained from the present chemical erosion experiments and indicate the significant features. Discussion of these results is, however, left until section 7. Fitting of the revised model, developed in section 4, to the present experimental data for the methane yield of pyrolytic graphite is undertaken in section 8.

Chemical erosion experiments were performed for H^+ and D^+ impact energies between 10 and 200 eV/ion. The presentation of the experimentally determined erosion yields will be divided into methane, heavy hydrocarbon, and total chemical erosion yields. The reader should be aware that previous experimental results on the total chemical erosion of pyrolytic graphite due to H^+ [48], and the methane erosion due to D^+ [48, 85] have been published. The present experiments have been conducted with a more accurate quadrupole mass spectrometer and so these data supersede those previously published.

6.1 Methane Erosion Yields

The methane erosion yields due to H^+ and D^+ impact are shown as a function of temperature for the six selected ion energies in figure 17. In general, it can be seen that the temperature profiles are more peaked at the higher energies and this leads to a strong dependence in Y_m on energy. For H^+ impact at 200 eV a maximum yield of $\sim 3.6 \times 10^{-2}$ CH_4/H^+ was determined. As the energy is reduced, however, Y_m is also reduced so that a maximum yield of $\sim 7.7 \times 10^{-3}$ CH_4/H^+ is observed for 10 eV H^+ impact. For D^+ impact a maximum methane yield of $\sim 6.1 \times 10^{-2}$ CD_4/D^+ was found at 200 eV and this was

reduced to $\sim 8.9 \times 10^{-3}$ CD₄/D⁺ at 10 eV. We note that the methane yield due to 10 eV D⁺ impact appears to exceed that due to 15 eV impact above T_m, but within experimental error these yields are considered to be similar.

For both H⁺ and D⁺ impact, below T_m the temperature dependence curves broaden as the ion energy is reduced so that significant erosion levels are seen at room-temperature for low-energy impact. Furthermore, there is a downwards trend in T_m with decreasing energy from ~ 710 K for energies ≥ 100 eV down to ~ 600 K at 10 eV. Both the broadening of the temperature profile [21,22,49] and the shift in T_m (for similar ion fluxes) [16,49] have been noted before.

In figure 18, the methane erosion yield dependence on ion energy for several isotherms is shown with error bars on selected data. For both H⁺ and D⁺ impact at 300 K, the methane yield exhibits a shallow peak at ~ 50 eV ($\sim 6.6 \times 10^{-3}$ CH₄/H⁺ and $\sim 9.5 \times 10^{-3}$ CD₄/D⁺) and decreases as the energy is reduced ($\sim 1.4 \times 10^{-3}$ CH₄/H⁺ and 3.3×10^{-3} CD₄/D⁺ at 10 eV), suggesting that the methane yield is not energy independent at room-temperature, for ion energies below 100 eV. At 500 K, although the methane yield appears to be increasing between 10 and ~ 50 eV it is relatively insensitive to ion energy. It is noteworthy that the 500 K yield is consistently higher than that observed at room-temperature. For temperatures near the peak for the methane yield due to energetic ion impact (~ 700 K for > 100 eV) a dramatic decrease in the methane yield of a factor of ~ 8 for H⁺ and ~ 9 for D⁺ is observed as the ion energy is decreased from 200 to 10 eV. At 1000 K, the methane yield for H⁺ impact appears to increase with ion energy over most of the energy range while the D⁺ induced methane yield exhibits a peak near 50 eV. However, within the error bars this difference is not significant. We note that below ~ 100 eV for H⁺ and ~ 50 eV for D⁺ the methane yield is smaller than that observed at room-temperature by a factor of up to 3.

6.2 Heavy Hydrocarbon Yields

The hydrocarbon spectra presented in figures 19 to 24 show that, over the energy range of 10 to 200 eV, heavier hydrocarbons do contribute significantly to the total

chemical erosion yield. It should be noted that the actual heavy hydrocarbon signals are a factor of $\sim 3\text{-}70$ smaller than the methane signals leading to greater relative errors in the data. In general, it can be seen that the C_2H_2 and C_3H_8 contributions to the total chemical erosion yield are the smallest throughout most of the temperature and energy range investigated while the contributions from the other heavy hydrocarbons (C_2H_4 , C_2H_6 , and C_3H_6) are more significant. The small C_2H_2 yield may be due to a relatively small concentration of triply bonded carbon atoms in the implantation zone while the relatively minor C_3H_8 contribution may be due to the size of the molecule or preferential formation of other hydrocarbons. Methane is always the dominant reaction product, but one must consider the number of carbon atoms in each molecule when determining the relative contribution to C erosion.

The temperature profiles for the C_2 -containing hydrocarbon contributions [$2 \times (\text{Y}_{\text{C}_2\text{H}_2} + \text{Y}_{\text{C}_2\text{H}_4} + \text{Y}_{\text{C}_2\text{H}_6})$] to the total chemical erosion yield for H^+ and D^+ impact are shown in figure 25. In general, the behaviour of the C_2 -containing hydrocarbon yields is similar to that of methane. Namely, there is a decrease in Y_m , $\sim 0.011 \text{ C/H}^+$ at 200 eV to $\sim 7.0 \times 10^{-3} \text{ C/H}^+$ at 10 eV for H^+ impact and $\sim 0.021 \text{ C/D}^+$ down to $8.3 \times 10^{-3} \text{ C/D}^+$ in the case of deuterium impact at the same respective energies. While T_m shows the characteristic shift downwards with ion energy for D^+ impact ($\sim 670 \text{ K}$ at 200 eV down to $\sim 580 \text{ K}$ at 10 eV) there is little variation in T_m with H^+ energy. It is curious to note that the contribution from C_2 -containing deutero-hydrocarbons at 50 eV exceeds that at 100 eV over most of the temperature range. Equally important, however, is the fact that even for low-energy impact below say 25 eV, significant production of heavy hydrocarbons is observed even though there is little damage deposition resulting in carbon-carbon bond rearrangement.

In figure 26, the energy dependence of the C_2 -containing hydrocarbon yield due to H^+ and D^+ impact is shown for four isotherms, with error bars on selected data. For H^+ impact we note that the room-temperature yield increases between 10 eV ($\sim 8.0 \times 10^{-4} \text{ C/H}^+$) and 50 eV ($\sim 2.7 \times 10^{-3} \text{ C/H}^+$), but levels off between 50 and 200 eV, while for D^+ impact at this temperature the yield does not drop off at energies below ~ 50 eV resulting

in a C₂-yield which is relatively independent of energy (< a factor of 2) over the range of 10 to 200 eV. At 500 K, the profiles are relatively independent of energy, although the yield due to H⁺ impact does increase between 10 and 50 eV by less than a factor of 2. At 700 K, we observe an increasing yield with energy, but now the increase between 10 and 200 eV is less than a factor of 2 for H⁺ impact and ~ 4 for D⁺ impact, whereas with methane these factors were nearer 8 and 9, respectively. At 1000 K, the yields are peaked in the region of 50 eV and fall off sharply as the ion energy is reduced.

The temperature profiles for C₃-containing hydrocarbon contributions [3×(Y_{C₃H₆} + Y_{C₃H₈})] to the chemical erosion yield for H⁺ and D⁺ impact are shown in figure 27. Again, for H⁺ impact, we observe a reduction in Y_m with decreasing ion energy from a value of ~ 8.5×10^{-3} C/H⁺ at 200 eV impact to ~ 4.3×10^{-3} C/H⁺ at 10 eV impact. For D⁺, the maximum yields for 50, 100 and 200 eV impact are nearly indistinguishable, Y_m ~ 9.0×10^{-3} C/D⁺ and this falls to ~ 5.5×10^{-3} C/D⁺ for 10 and 15 eV impact. While there is little discernible shift in T_m with ion energy for H⁺ impact there is a downwards shift in T_m for D⁺ impact from ~ 660 to ~ 600 K as the energy is reduced from 200 to 10 eV. Similar behaviour was noted for the C₂ molecular yields due to H⁺ and D⁺ impact.

In figure 28, the energy dependence of the C₃-containing hydrocarbon yield is shown for four isotherms, with error bars on selected data. As was the case with the C₂-containing hydrocarbon yields we note different behaviour for H⁺ and D⁺ impact at room-temperature. For protium impact at 300 K the yield increases between 10 and 50 eV where it levels off while for deuterium impact the yield is nearly independent of temperature. The 500 K yields are still relatively energy independent. At 700 K the H⁺ induced yield increases by a factor of about 2 between 10 and 200 eV while for D⁺ impact the yield increases by a factor of ~ 3 between 10 and 50 eV after which it levels off. At 1000 K, again there is evidence of a peak near 50 eV for both H⁺ and D⁺ impact. Except for D⁺ impact near ~ 60 eV these yields are smaller than those at room-temperature throughout the energy range .

6.3 Total Chemical Erosion Yields

The temperature dependence of the total chemical erosion yield due to H^+ and D^+ impact is shown in figure 29. Here we note a net behaviour which is similar to that of methane alone in that the profiles broaden and Y_m and T_m decrease as the ion energy is decreased, but is also moderated by the heavy hydrocarbon contribution which is generally less dependent on impact energy than the methane production is. The highest chemical yields are $\sim 0.056 \text{ C}/H^+$ for 200 eV H^+ impact near 700 K and $\sim 0.089 \text{ C}/D^+$ for D^+ impact at the same energy and temperature, while 10 eV impact results in $Y_m \sim 0.018 \text{ C}/H^+$ and $0.023 \text{ C}/D^+$. Furthermore, T_m shifts downwards with decreasing ion energy from ~ 700 to 640 K for H^+ impact and ~ 700 to 600 K for D^+ impact. For protium impact this shift is only due to the shift observed in the methane yields since for the heavier hydrocarbons no such variation in T_m was evidenced. For deuterium impact this shift was observed for methane and the C_2^- - and C_3^- containing hydrocarbon yields.

In figure 30, the energy dependence of the total chemical erosion yield is shown for 4 isotherms and error bars are shown for selected data. For both H^+ and D^+ impact, the room-temperature yield is peaked near 50 eV and 40 eV respectively. This yield decreases by a factor of ~ 3.5 for H^+ impact and ~ 2 for D^+ impact as the ion energy is reduced down to 10 eV. The 500 K profiles are quite broad, and exhibit only a slight energy dependence over the energy range investigated. The energy profiles at 700 K are increasing over the energy range so that the yield at 200 eV is ~ 4 times that at 10 eV for H^+ impact, while for D^+ impact this factor is about 5.5. At 1000 K the yields exhibit a peak near 50 eV. For protium impact this energy curve is similar in shape to that observed at room-temperature, but is smaller by a factor of 1.4 to 2. For deuterium impact the 1000 K yield approaches that observed at room-temperature near 50 eV. Below this energy it falls off dramatically so that it is ~ 4.5 times smaller than the room-temperature yield at 10 eV.

Having presented the these data on the chemical erosion of pyrolytic graphite due to H^+ and D^+ impact we will discuss, in section 7, the significance of the results.

7. DISCUSSION OF RESULTS

In this section we undertake to explain many of the key features of the experimental results for the chemical erosion of pyrolytic graphite by low-energy hydrogen and deuterium ion impact. In many cases, we will invoke the concepts introduced in the models of section 3 and those used to develop our revised model of section 4 in order to formulate a coherent physical picture. This discussion will be divided into methane, heavy hydrocarbon and total chemical erosion yields based on the data already presented. Subsequently, we will present the data in new ways in order to conduct a more general discussion on the chemical erosion process. Finally we will discuss the isotopic effects on chemical erosion and compare the present experimentally determined erosion yields to previously published low-energy data.

7.1 METHANE EROSION YIELDS

Here we discuss the key features of the methane erosion yield of pyrolytic graphite due to H^+ and D^+ impact.

In figure 17 a and b we noted a characteristic increase in Y_m with ion energy, between 10 and 200 eV, by a factor of ~ 4.7 for H^+ and ~ 6.8 for D^+ . This likely indicates the role that damage deposition plays in enhancing the methane yield. In our model this process is described by σ_E , the cross-section for breaking one of the carbon-carbon double bonds in the graphitic lattice, which we expect to increase with ion energy. The increase in damage deposition leads to a higher concentration of methyl groups attached as ligands to the graphite network and, hence, a greater methane yield. We must also acknowledge the possibility that the abstraction process, described by k_D (the prefactor for this low-activation thermal process), may be enhanced at higher energies which would also lead to higher methane yields.

We further observed an increase in T_m with ion energy which suggests that damage deposition and/or an enhanced abstraction process delay the effect of the thermal process which reduces our concentration of carbon atoms in the sp^x and sp^3 hybridization states (ultimately required for methane production), namely thermal H-atom splitoff described by k_H . It is not readily apparent from the model equations developed in section 4 that this

must be true and we leave further discussion until section 8 where the model is fitted to the present experimental results.

If we consider the methane yield as a function of energy (figure 18 a and b) we note a moderate peak in the area of 50 eV for both H^+ and D^+ impact at room temperature. Certainly at low energies, say < 25 eV, where we expect little or no damage deposition, and at 300 K, where thermal release of methane is not significant, the observed methane yield must be due to kinetic ejection of near-surface methyl ligands formed via hydrogenation of the sp^2 hybridized carbon to sp^3 . Within our model system this process is described by the cross-section for kinetic ejection, σ_i . One might expect an increase in the rate of kinetic ejection with ion energy as more energy is transferred to these surface methyl groups. As the ion energy is further increased, however, it seems likely that implantation of the ions reduces their interaction with these surface groups. This offers a possible explanation for the energy optimum observed in the room-temperature methane yield observed for low-energy impact. Of course, for higher energy impact, damage deposition occurs which should enhance the methane yield, but this does not seem to compensate for the reduction in energy transferred to the surface groups.

At 700 K we noted a reduction in the methane yield of a factor of ~ 8 for H^+ and ~ 9 for D^+ as the ion energy was decreased from 200 to 10 eV (fig.18 a and b). Such results have been viewed previously as an indication that the high-temperature methane erosion mechanism, which dominates for energetic ion impact (> 100 eV), is nearly suppressed at lower energy incidence [9] and have led investigators to postulate a new erosion mechanism which dominates for hydrogen ion impact below 100 eV [49] at graphite temperatures approaching room temperature or lower [9]. Based on our model this low-energy, low-temperature process is simply the kinetic ejection of near-surface methyl groups formed as a consequence of hydrogenation. At 700 K, however, this is not the only process resulting in methane production for low-energy hydrogen impact. We note that the methane yields are greater than those at 300 K even for 10 eV impact. Clearly the thermally enhanced abstraction process leading to greater thermal release of methyl also plays a very important role. We may say that low-energy H^+ and D^+ ions kinetically eject

surface methyl groups and, for higher temperatures, enhance the thermal release of these groups whose concentration depends almost solely on temperature.

Of course, as the ion energy is increased we must also consider the effects of increased damage deposition, $\sigma_E(E)$, and possibly enhanced abstraction, $k_D(E)$, which will serve to increase the concentration of methyl ligands, for a fixed temperature, over the low-energy case. At 700 K this concentration is still relatively high, the thermal release of these groups (k_x) is effective, and the thermally induced H-atom splitoff (k_{-H}) has not yet served to dramatically reduce the population of sp^3 carbon centers. That is, although the energetic ions are kinetically ejecting methyl groups at this temperature, it is the energy deposition and abstraction processes which lead to an enhancement of the methyl concentration and its thermal release. This results in a larger methane yield than is the case for low-energy impact.

For graphite temperatures of 1000 K, the thermally induced splitoff of H-atoms is dominating and restricting the concentrations of the sp^x and sp^3 carbon centers which are required for methyl formation. Consequently the methane production rate is dramatically reduced. This is especially true at low impact energies where the methane yield is measurably smaller than that determined at room-temperature (fig 18). Damage deposition at higher energies seems to offset this effect slightly.

The various kinetic and chemical processes outlined in sections 3 and 4 can be used to explain most of the observed features of the methane yield of pyrolytic graphite in the range of 10 to 200 eV and 300 to 1000 K. For low-energy impact at room temperature it is σ_i and σ_H which largely determine the methane yield, but for higher energy impact at elevated temperatures it is the complex interaction of σ_H , σ_E , k_D , k_x and k_{-H} which govern the methane erosion yield.

7.2 HEAVY HYDROCARBON EROSION YIELDS

Here we discuss the main features of the heavy hydrocarbon production resulting from H^+ and D^+ impact on pyrolytic graphite. This discussion will cover both the C_2 - and C_3 -containing hydrocarbon yields shown in figures 25 to 28.

The temperature dependence of the heavy hydrocarbon (HHC) yields shown in figures 25 and 27 shows that, as with methane, Y_m increases with ion energy. The increase in Y_m between 10 and 200 eV, however, is more modest than that observed for methane. For instance the C₂-containing hydrocarbon yield increases over this energy range by a factor of ~ 1.5 for H⁺ and ~ 2.5 for D⁺. This implies that the ion energy does not play as important of a role in determining the heavy hydrocarbon yield as it does for methane. There are three processes in our model system which depend directly on ion energy, namely, physical ejection (σ_i), damage deposition (σ_E), and abstraction (k_D). It may be that one, two or all three of these processes are responsible for the reduced energy dependence.

A peculiar feature of the HHC yields shown in figures 25 and 27 is the shift in T_m with ion energy observed for deuterio-heavy hydrocarbon production and a T_m which is apparently energy independent for H⁺ induced hydrocarbon production. Apart from experimental errors we can offer no explanation for this behaviour.

For ion impact below 25 eV, where there is little damage deposition occurring, we see significant heavy hydrocarbon production for nearly all temperatures suggesting that there is a complex spectrum of hydrocarbons attached as ligands to the graphitic network. The removal of these complexes, by kinetic ejection or thermal release, is governed by their concentrations which, for a fixed temperature, are determined by ion energy and mass. In figures 26 and 28 the energy dependence for the heavy hydrocarbon production is shown. If we consider H⁺ impact at 300 K (figs. 26a and 28a), we note an increase in the heavy hydrocarbon yield between ~ 15 and 50 eV which would suggest that damage deposition plays a role in determining this yield. For D⁺ impact however (figs. 26b and 28b), the heavy hydrocarbon yield is relatively high already at 10 eV so that no such transition is observed. This would seem to refute the role that damage deposition plays at 300 K. Instead, we may infer that, as was the case for methane production, it is kinetic ejection which is principally responsible for the heavy hydrocarbon production at room-temperature and that this process is less efficient for low-energy (< 25 eV) protium impact.

At 700 K (figs 26 and 28), we observe that the heavy hydrocarbon yields are increasing between 10 and 200 eV by a factor of ~ 2 for H⁺ and ~ 3 - 4 for D⁺ impact. Such increases are more modest than those observed for methane at the same temperature which were closer to factors of 8 and 9 for H⁺ and D⁺, respectively. This raises several possibilities; i) the frequency constant for the thermal process leading to the release of heavy hydrocarbons, k_x is different for each hydrocarbon group (i.e. generally lower for heavier hydrocarbons), ii) the heavy hydrocarbon groups produced at greater depths are broken up as they move to the surface and/or fractions of these groups are kinetically ejected (i.e. a methyl radical is removed from a C₃H₇ ligand) or iii) damage deposition leads to preferential formation of methyl ligands compared with hydrogenation alone. Each of these three possibilities, or some combination of them, may account for the more moderate energy dependence observed in the heavy hydrocarbon production compared with methane.

At 1000 K (figs. 26 and 28), we see again that thermal H-atom splitoff has resulted in a dramatic reduction in the heavy hydrocarbon yields. The yields, however, also exhibit a peculiar maximum near 50 eV so that they approach the room-temperature yield near this energy. This maximum is difficult to reconcile since both hydrogenation and damage deposition, resulting in the production of carbon in the sp^x and sp³ hybridization states, are rapidly negated by the H-atom splitoff which returns the carbon bonds to their graphitic sp² form and so we expect very small yields regardless of the impacting ion energy. This behaviour may indicate that the distributions of both the damage deposition and the implanted ions play a role in hydrocarbon production. For ion energies producing the greatest overlap of these distributions, significant HHC formation and release may still be possible, even at 1000 K. We note that such an effect is not included in the model developed in section 4 which assumes a constant hydrogenation cross-section regardless of the distribution of thermalized ions.

Once again, most of the heavy hydrocarbon erosion features observed for the impact energies and graphite temperatures employed in the present experiments can be well described by the kinetic and chemical processes outlined in sections 3 and 4. Although kinetic ejection and hydrogenation govern the behaviour at low energies and

temperatures, damage deposition, activated abstraction, and thermal release of hydrocarbons and H-atoms become important at higher energies and temperatures. In this latter regard we infer that, for heavy hydrocarbon production, σ_E and possibly k_D , are less dependent on ion energy than they are for methane production.

7.3 TOTAL CHEMICAL EROSION YIELDS

Of course, the total chemical erosion yield is just the sum of the methane and heavier hydrocarbon yields and, having thoroughly examined these two contributions, we comment here only briefly on figures 29 and 30.

In figure 29 we note that the net behaviour of the total chemical yield as a function of temperature is very much like that due to methane in that we have a shift upwards in Y_m and T_m with increasing ion energy. Both of these shifts are largely due to an increase in damage deposition, and possibly abstraction, with ion energy. By increasing the concentration of sp^x and sp^3 carbon centers these two processes delay the effect of the thermal H-atom splitoff which serves to reduce the yield at high temperature. When compared to methane, however, the total chemical yield curves are moderated by the contributions from heavy hydrocarbons which exhibit less of a dependence on ion energy than those of methane (see fig. 30).

The consequence, from a reactor point of view, is that over the energy range of 10 to 200 eV the temperature of the graphite plasma facing material will, in general, have more of an effect on the net erosion yield than will the impacting energy. If it is desirable to have chemical yields of $\leq 0.01 C/H(D)^+$ then one is better served to keep the plasma-facing graphite at room temperature or near 1000 K than in striving to reduce the ion impact energy. Of course, there are still gains to be made in reducing ion energy. For example, 10 eV impact at 1000 K results in chemical yields approaching 0.1 %.

7.4 GENERAL DISCUSSION

Here we will use new presentations of the experimental data to further our understanding of the chemical erosion of pyrolytic graphite by low-energy protium and deuterium ions.

In figures 31 (H^+ impact) and 32 (D^+ impact) we look at the methane, heavy hydrocarbon, and total chemical erosion yields as a function of ion energy on the same scale for each of the selected isotherms. We also include for comparison the total chemical erosion yields predicted by the RG-R model described in section 3.2.2 for the ion fluxes used in the present experiment ($10^{18} H(D)^+/\text{m}^2\text{s}$). At 300 K, we note that the heavy hydrocarbon contribution is significant for all energies between 10 and 200 eV, ranging from $\sim 30\%$ of the total yield for D^+ impact near 50 eV to almost 70% of the total yield for H^+ impact at 200 eV. We also note that the total yield does not drop very much at higher energies, as was expected based on methane results, due to the heavy hydrocarbon contribution. The RG-R model agrees fairly well with the present H^+ results up to ~ 100 eV, but is a factor of ~ 2 larger than the deutero-methane yields over the same energy range. This likely arises from a larger isotopic effect observed in the data used to fit their model than is seen here (see section 7.5).

For ion impact proceeding at 500 K (figs. 31b and 32b), we note that, within experimental error the methane and heavy hydrocarbon yields are virtually coincident and relatively independent of energy over the range studied here. The RG-R model predicts essentially no increase over the yields at room temperature while experimentally a measurable increase is observed. Thus, the agreement with the H^+ results is generally poor while the agreement with the D^+ induced yield is quite good up to ~ 100 eV, where the increase in the yield over room temperature observed experimentally nearly compensates for the higher isotopic effect incorporated in the RG-R model.

At temperatures close to T_m for energetic impact, 700 K, we note that heavy hydrocarbons become more important as the ion energy is reduced. In the case of H^+ impact (fig. 31c), heavy hydrocarbons account for $\sim 35\%$ of the total chemical yield at 200 eV, and this increases to $\sim 50\%$ at 50 eV and $\sim 70\%$ at 10 eV. For D^+ impact (fig. 32c), the heavy hydrocarbon yield again accounts for $\sim 30\%$ of the total yield at 200 eV and $\sim 50\%$ for all energies ≤ 50 eV. The slight difference between the isotopes for energies below 50 eV falls within experimental errors. Similar hydrocarbon ratios have been noted previously [16,18,19,22] and have prompted investigators to conclude that the

contribution from heavy hydrocarbons becomes more important as the ion energy is reduced. The present experimental results for ion impact between 10 and 200 eV indicate that, while this may be true near T_m , heavy hydrocarbons can make significant contributions (up to 50% or greater) to the total yield at other temperatures regardless of ion energy. The RG-R model, although consistently higher, agrees fairly well with present experimental data at 700 K except at low energies where it predicts yields more than a factor of 2 greater than are observed.

For impact at 1000 K (figs 31d and 32d), the trends for H^+ , where the heavy hydrocarbon production exceeds that of methane between 10 and 80 eV, and D^+ , where methane dominates for all energies (10 to 200 eV), is puzzling. Given the large relative errors in this region, though, we may say that the HHC and methane yields are indistinguishable. At this temperature the predictions of the RG-R model are more than an order of magnitude too low.

In general, figures 31 and 32 effectively indicate the consequence of the more moderate energy dependence in heavy hydrocarbon production than that of methane production. Namely, that although the methane contribution to the total chemical yield increases with ion energy near T_m , this is not necessarily true at other temperatures. Estimating the total chemical yield for a given ion energy and graphite temperature, based on the methane yield and the methane fractions determined at T_m , may not be accurate.

We have suggested, in section 6.1.2, that, based on the low C_3H_8 yield, the size of the hydrocarbon molecule may affect its release rate since momentum transfer to heavier hydrocarbon ligands becomes less efficient. In figures 33 (H^+) and 34 (D^+) we have plotted the yields as a function of ion energy on the same scale based on the number of carbon atoms in the molecule. Any significant effects arising from molecular size should become apparent in these figures.

At 300 K (figs. 33a and 34a), we note that the C_2 - and C_3 -containing hydrocarbon yields are nearly coincident over the entire energy range, and that for ion energies approaching 200 eV the magnitude of their contribution approaches that of methane. For this low temperature it is principally kinetic ejection from the near-surface which determines the hydrocarbon yields, as discussed in sections 7.1 and 7.2. One would

expect, based on energy transfer considerations, this ejection to depend on the size and mass of the ejected group, with the lighter methyl radical being favoured, and this is the case over most of the energy range. The coincidence of the two heavier hydrocarbon curves likely reflects that the increased cross-section for the ejection of C₂-containing hydrocarbons is offset by the increased number of carbon atoms in the C₃-containing molecules.

At higher temperatures, we note that the C₂-containing hydrocarbon yields are consistently higher than those due to C₃-containing hydrocarbons by a nearly constant factor of ~ 1.5 regardless of the energy and isotope, but this factor falls within the range of experimental error. We do observe, however, that for impact at 700 K (figs. 33c and 34c), the methane yield, which is comparable to the heavier hydrocarbon yields at low energies, is measurably higher at 200 eV. Since the latter energy corresponds to the greatest implantation depth this may offer some support for chemical yields favouring smaller molecules at higher energies. One cannot discount the possibility, however, that either the thermal release of molecules (k_{\star}) is dependent on the radical and favours methyl, and/or that damage deposition (σ_E) leads to a higher relative concentration of methyl ligands on the surface than would result simply from hydrogenation. Having no information on the relative surface concentrations of the various radicals we cannot verify this.

We do know that C₃H₆ and C₃D₆ are among the more dominant heavy hydrocarbon products (figs 19 to 24) regardless of the impact energy and, since their mass and size are not much different from the minor products C₃H₈ and C₃D₈, respectively, it is unlikely that molecular size (at least for molecules containing 3 or fewer carbon atoms) is the deciding factor in hydrocarbon production. Based on the low C₂H₂ yields observed in the present experiments it is possible that the carbon-carbon bond structure in the near surface determines the spectrum of hydrocarbons emitted.

In figures 35 (H⁺) and 36 (D⁺) we have plotted the hydrocarbon yields as a function of energy for the selected isotherms based on the type of carbon-carbon bonds in the molecule. Here the methane yields are shown for comparison. The C₃H₆ molecule, which contains single and double carbon-carbon bonds, has been counted among the doubly bonded carbon molecules. The yields indicated are molecular, that is they are not

multiplied by the number of carbon atoms in the molecules. If amorphization of the implantation zone, resulting in approximately equal concentrations of singly and doubly bonded carbon atoms [16], determines the type of hydrocarbon produced then we would expect to see some sort of transition in the molecular yields in the neighbourhood of 100 eV in figures 35 and 36. There is little or no evidence of such a transition in either of the figures.

All together figures 33 to 36 offer no conclusive evidence that the erosion of various hydrocarbon species from pyrolytic graphite is related solely to their size or their carbon-carbon bond structure. It seems more likely that the mechanism(s) which determines the various concentrations of radicals attached as ligands to the graphitic network (i.e. the same mechanism which determines the constant ratio of sp^3 carbon centers which contain attached methyl groups), which has not been identified, plays a more important role. There is some evidence that σ_E , the cross-section for damage deposition, affects these relative concentrations at higher impact energies and/or that the prefactor for thermal release, k_x , is different for each radical group.

Having examined the various hydrocarbon yields due to H^+ and D^+ on a somewhat separate basis we undertake, in section 7.5, a comparison where these yields are plotted together in order to highlight any isotopic effects in the chemical erosion of pyrolytic graphite.

7.5 ISOTOPIC EFFECTS IN THE CHEMICAL EROSION OF PYROLYTIC GRAPHITE

As discussed in section 2, there has been some discrepancy in the experimental results regarding the magnitude of the isotopic effect on chemical erosion for low-energy hydrogen ion impact. Roth and Bohdansky [22], observed a room temperature total yield for D^+ impact that was more than five times that due to H^+ impact for energies below ~ 100 eV. On the other hand, sniffer probe experiments in TEXTOR [42] and plasma experiments in PISCES [45] have measured isotopic effects closer to a factor of 2.

In the present experiments we have a unique opportunity to determine the isotopic effect on the chemical erosion yield of pyrolytic graphite over a range of impact energies and specimen temperatures. This comparison is undertaken here and will be divided into

discussions on the isotopic effect observed in the methane, heavy hydrocarbon, and total chemical erosion yields.

7.5.1 Isotopic Effects in the Methane Yield of Pyrolytic Graphite

In figure 37, the methane yields for H^+ and D^+ impact are plotted as a function of graphite temperature for impact energies of 10, 15, and 25 eV. For 10 eV impact, we observe that the methane yield for D^+ impact is slightly greater than a factor of 2 at room temperature, but for temperatures greater than, say 350 K, this isotopic difference is less than a factor of ~ 1.7 and, within experimental error the isotopic effect may be considered small. For 10 eV impact we presume that the kinetic ejection of methyl groups attached to the graphite surface as ligands is the principal source of methane production at low temperatures. If we consider the simple case of an elastic head-on collision then the amount of energy transferred from the impacting species (m_1) to the stationary target species (m_2) is equal to $E_1[4m_1m_2/(m_1+m_2)^2]$. Thus a deuterium ion would transfer 36% of its energy to a deuterated methyl group while a protium ion would transfer 23.4% of its energy to a CH_3 radical. Although we have not considered inelastic losses and scattering, this simple approach indicates that the isotopic increase in energy transferred would be a factor of $\sim 1.5/collision$. The reader should be aware that uncertainties involved in the splitting and subsequent interaction of each of the atoms in the molecular ion (H_3^+ and D_2^+), upon striking the graphite surface, may affect this energy transfer. It seems reasonable, however, that based solely on a kinetic low-energy interaction, the methane yield due to D^+ impact should not exceed that due to H^+ impact by more than a factor of 2. At higher temperatures, we expect the isotopic effect to be even smaller, for low-energy impact (< 25 eV), since the thermally induced release of methane is independent of the impacting isotope.

In figure 37b, the methane yields are plotted for H^+ and D^+ impact at 15 eV. Here we note that the deutero-methane yields are uniformly higher than the methane yields due to H^+ impact again by a factor of 1.3 - 1.4 which falls within experimental error. In figure 37c, for 25 eV impact, we note that the methane yield at room temperature is ~ 1.5 times greater for D^+ than for H^+ . This factor gets smaller at higher temperatures where the

thermal release of methane is independent of the impacting species smoothing over kinetic isotopic effects. Given uncertainties in the data, figure 37 seems to indicate that the methane yield due to low-energy impact (≤ 25 eV) exhibits little or no isotopic effect, save perhaps for 10 eV impact at room-temperature.

In figure 38, we compare the two isotopic methane yields in the intermediate ion energy range of 50 to 200 eV. In this case we may expect that damage deposition, which is isotope dependent, will play a more significant role in the methane production. In figure 38a for 50 eV impact, we note that the methane yield due to D^+ impact is still only 1.2 - 1.5 times that due to H^+ impact between 300 and 800 K. Only at higher temperatures do we observe a significant isotopic factor of ~ 3.5 near 1000 K. One explanation may be that the D^+ ions deposit significantly more damage than the H^+ ions and that this may delay the impact of the thermal process (k_H) which reduces the concentration of attached methyl groups in the near surface layer. Alternatively higher temperatures may be required to thermally desorb the deutero-methane but, since T_m is about the same for both species, this is unlikely.

In figure 38b, for 100 eV impact, the deuterio-methane yield is uniformly higher than that induced by H^+ impact by a factor of ~ 1.4 , save perhaps near 1000 K where the curves approach. Similarly in figure 38c, for 200 eV impact, the deuterio-methane yield is a factor of 1.7 to 1.9 higher up to a temperature of ~ 800 K where it begins to get smaller. Although some of these isotopic differences fall outside experimental errors they are still not large. It is likely that the damage deposition, described by σ_E , and the hydrogen abstraction, described by k_D , are isotope dependent leading to enhanced methane yields for D^+ impact, but the experimental evidence indicates that this effect is small.

The energy dependence of the methane yield, due to H^+ and D^+ impact, is shown as a function of energy for the selected temperatures in figure 39. Taken as a whole this figure reaffirms that, though the trends in the isotopic effect on methane production make physical sense, the magnitude of this effect is still small (generally $<$ a factor of 2). For instance, the fact that kinetic ejection principally determines the methane yield at room temperature (fig. 39a) and not damage deposition is reflected in the absence of a

significant rise in the isotopic factor above 50 eV. And for impact at higher temperatures (700 K fig. 39c), where we do expect damage deposition to have an effect, we do see an increase in the isotopic factor above \sim 40 eV. Within experimental errors, however, this evidence is hardly conclusive.

In general, we may say that, within experimental error, the isotopic enhancement in the methane yield of pyrolytic graphite, if it exists, is small.

7.5.2 Isotopic Effects in Heavy Hydrocarbon Erosion Yields

Here we will examine the heavy hydrocarbon erosion yields for H^+ and D^+ impact as functions of temperature on the same scale (figs. 40 and 41) and energy (fig 42).

In figure 40, the heavy hydrocarbon (HHC) yields are plotted for low-energy H^+ and D^+ impact (\leq 25 eV). For 10 eV impact, we note that HHC yield due to D^+ impact exceeds that due to H^+ by a factor of 1.5 to 1.7, up to temperatures of 600 K. The curves cross near 650 K so that the HHC yield for H^+ impact is actually higher than that for D^+ up to 1000 K where this inverse isotopic effect approaches a factor of \sim 3. Still, however the isotopic effect in the HHC yields is negligible within errors. In figure 40 b and c, the HHC yields exhibit similar behaviour. We can offer no viable explanation as to why the H^+ induced hydrocarbon yield should exceed that due to D^+ for any energy and temperature and must conclude that, considering experimental error, there is no isotopic effect in the heavy hydrocarbon production at low impact energies.

In figure 41, similar isotopic comparisons are made in the HHC yield over the energy range of 50 to 200 eV. Here again there is no clear evidence of an isotopic effect in the heavy hydrocarbon yield of pyrolytic graphite at any temperature in the range of 300 to 1000 K.

We can offer several possibilities for a lack of an isotopic effect in the heavy hydrocarbon production due to H^+/D^+ impact in the energy range of 10 to 200 eV. We have already indicated that the experimental evidence suggests that damage deposition may enhance methyl formation more than HHC radicals. So we would expect that any isotopic enhancement in the HHC yield resulting from the increased damage deposition due to D^+ impact over H^+ impact would be modest. We further note that the energy

transfer to the heavier hydrocarbons will be poor and so isotopic effects in this process may also be negligible. The thermal release of the hydrocarbon groups is a chemical process and should be independent of the impacting isotope. Only the abstraction process, which may be isotope dependent for higher impact energies, could lead to a significant isotopic enhancement in the HHC yield and this is evidently not the case.

In figure 42 we show the energy dependence in the HHC yields due to H^+ and D^+ impact for the sake of completeness. The evidence offered in figures 40 to 42 seems to indicate that there is no isotopic effect in the heavy hydrocarbon erosion yield over the energy range of 10 to 200 eV and the temperature range of 300 to 1000 K.

7.5.3 Isotopic Effect on Total Chemical Erosion Yield

Here we collect the data presented in sections 7.5.1 and 7.5.2 to look at the isotopic effect on the total chemical erosion yield of pyrolytic graphite at low energies.

In figure 43 we look at the total chemical erosion yield as a function of temperature for H^+ and D^+ impact at 10, 15, and 25 eV. For 10 eV impact, we observe an isotopic effect of a factor of 1.6 - 2 up to T_m (~ 600 K). Again, this apparent isotopic enhancement generally falls within the error bars and above 700 K there is no apparent isotopic effect on the total chemical yield. This indicates that, while at low temperatures kinetic effects (energy transfer) might lead to a slight isotopic effect, at temperatures where the thermal release of hydrocarbons dominates there is no discernible isotopic effect. For 15 and 25 eV impact we note similar behaviour again, but the isotopic effect at lower temperatures is even smaller and well within experimental error. Figure 43 indicates that, for low-energy ion impact (≤ 25 eV), we may see a slight isotopic effect (< a factor of 2) at low temperatures where energy transfer is important, but not at higher temperatures where thermal release of hydrocarbons dominates.

In figure 44 we examine the temperature dependence of the total chemical yield for H^+/D^+ energies of 50, 100 and 200 eV. For 50 eV impact the two curves are coincident up to 500 K whereafter the yield due to D^+ impact exceeds that due to H^+ by a factor of ~ 1.5 , but the error bars indicate that the two curves are still similar. At 100 eV, we observe a measurable isotopic effect only in the region of T_m and similar behaviour is exhibited for

ion impact proceeding at 200 eV. In general, figure 44 seems to indicate that for ion energies between 50 and 200 eV, if there is any isotopic effect at all it is in the region of T_m . This likely indicates that the isotopic enhancement in damage deposition, and possibly abstraction, only appears when thermal release of the additional hydrocarbon ligands is highest.

In figure 45, the total chemical yield is plotted as a function of H^+/D^+ energy for the four selected temperatures. Taken as a whole this figure indicates only two regions where the measured isotopic effect lies outside of experimental error; 10 eV impact at room temperature, and higher energy (> 100 eV) impact near T_m . Thus we confirm that the energy transfer effect which is evident in the kinetic ejection of hydrocarbons is only weakly dependent on the impinging isotope. Furthermore, we see that the isotopic enhancement in damage deposition for D^+ impact over H^+ , at energies $> - 40$ eV is only evident where thermal release of hydrocarbons is most effective. That is, although the additional damage resulting from D^+ impact leads to a higher concentration of near surface hydrocarbon ligands, there is little isotopic advantage in their kinetic ejection at these energies, and so the thermal release at temperatures around 700 K is higher.

Given the data presented in figure 37 to 45, we conclude that isotopic effect on the chemical erosion is small and generally less than a factor of ~ 1.7 . In many cases, within experimental error, there is no significant isotopic effect in the chemical erosion of pyrolytic graphite. We note that our isotopic effect, for higher energy impact near T_m , of ~ 1.7 agrees well with previously determined values in PISCES [45] and TEXTOR [42], but is significantly lower than that observed by Roth and Bohdansky [22].

7.6 A COMPARISON OF THE PRESENT METHANE AND TOTAL CHEMICAL YIELDS WITH PREVIOUSLY PUBLISHED RESULTS

In this section we compare the methane and total chemical erosion yields determined in the present experiments with previously published erosion data for the low-energy impact regime of 10 - 200 eV. We note that previously published data in this energy range are rather scarce.

In figures 46 to 48 we present data for the methane and total yield of graphite, as a function of energy, due to H^+ impact at 300 K, 500 K, and T_m , where the latter quantity represents the characteristic temperature at which the maximum yield occurs, for impact energies of 100 eV or greater.

For H^+ impact at 300 K (fig. 46), the TEXTOR Sniffer Probe experiment [42] shows very good agreement with the present results for both the methane and total chemical erosion yields. Ion-beam results [64] also agree well with the present methane yield data. Other ion-beam [22] and PISCES results [45] show reasonable agreement for the total yield. Considering the contributions of physical sputtering the total yields measured in PISCES [45] and by Roth and Bohdansky [22] are a factor of 1.5 to 2 times smaller than those observed in the present experiments. The higher fluxes used in both previous experiments may account for some of the discrepancy. Also, uncertainties in determining the ion flux and energy in plasma experiments may account for some of the difference between the PISCES yields and those measured here [7]. Redeposition, however is not a consideration with the PISCES data [45].

For H^+ impact at 500 K (fig. 47), there is good agreement between the present methane yields and those determined in previous ion-beam [11,49] and TEXTOR [42] experiments for energies above 100 eV. Below this energy, the previous results are generally a factor of ~ 1.5 lower than the methane yields determined in the present experiments. Given experimental errors, however, this still represents reasonable agreement. The methane yield data from another ion-beam experiment [64] are lower by a factor of ~ 2.5 which likely falls outside the range of experimental error. For the total chemical yields at 500 K (fig. 47b), only two previous data points exist and these are lower than the present results by a factor of 2 - 3. Again, some of this difference may be attributable to a flux which was ~ 4 orders of magnitude higher in the TEXTOR and PISCES experiments and the inherent difficulties in measuring the ion flux and energy.

For H^+ impact proceeding at T_m (fig. 48), there is excellent agreement between the present methane data and previously published results [11,42,49], except perhaps at 200 eV where the previous results are about a factor of 2 higher [49]. Other ion-beam data at 100 eV [64] are also higher by a similar factor. Again the TEXTOR [42] and PISCES [45]

results for the total chemical yield at T_m are smaller by a factor of 2 - 2.5 than those measured in the present experiments (fig. 48b), but ion-beam data [18,64] agree very well.

Similar data are presented for D^+ impact in figures 49 to 51. For impact proceeding at room temperature (fig. 49), there is excellent agreement between the present data and methane yields observed in a previous ion-beam experiment [21] and in TEXTOR [42]. The methane yields determined by Roth and Bohdansky [22] are, however, higher by up to a factor of ~ 3 or more than the present experimentally determined yields. For the total yield (fig. 49b), some of the previous data includes contributions due to physical sputtering. These contributions are not enough to account for the differences between the present results and those of Roth and Bohdansky [22], below ~ 100 eV. There is good agreement between the present data and the total chemical yields observed in TEXTOR [42] and PISCES [45] below ~ 100 eV, but the PISCES yields at higher energies may be almost entirely due to physical sputtering, and so the total yields are significantly lower than the present values.

For D^+ impact at 500 K (fig. 50), the agreement between the present methane yield data and those determined in TEXTOR [42] is good, although the available data are limited. Again, for the total chemical yield (fig. 50b) the TEXTOR data at 60 eV agrees quite well with the present data.

At T'_m (fig. 51), the methane yields measured in TEXTOR [42] and a previous ion-beam experiment [21] agree well with the values determined in the present experiments. Once again, however, the results of Roth and Bohdansky [22] are higher by a factor of 2 - 2.5. For the total chemical yield, the present results, though consistently higher, agree quite well (within a factor of 2) with yields measured in TEXTOR [42] and PISCES [45]. The ion-beam results of Roth and Bohdansky [22] are higher again by a factor of 1.7 - 3.

In figure 52 the methane yields due to 50 eV D^+ impact are shown as a function of temperature for several experiments. We note that the yields of Roth and Bohdansky [22] are uniformly higher but that there is reasonable agreement between the present results and previous ion-beam [21] and sniffer-probe [42] data, especially for temperatures below T_m . For the all of the previously published data the value of T_m is consistently higher than

that observed in the present experiments by about 100 K. It is likely that this is a consequence of the smaller ion flux employed in the present experiments. We observe further that for temperatures approaching 1000 K the present results agree well with previous ion-beam data [21], but are lower than the methane yields observed in TEXTOR [42] by a factor of ~ 2.5 . It is also possible that this effect is related to the ion flux density."

In general, we can make the following observations. For the methane yields there is good agreement (within a factor of 2) between the present experimentally determined yields and those obtained in TEXTOR [42] and in ion-beam experiments [11,21,49]. The ion-beam results of Roth and Bohdansky, however, are generally too high by a factor which approaches 3 or more. For the total chemical yield the agreement between the present results and the ion-beam results of Roth and Bohdansky [22] is fairly poor with the latter results being significantly higher. It is possible that energetic neutrals created by charge exchange have led to a synergistic enhancement of the D^+ impact induced yields in their experiments. The total chemical yields observed in TEXTOR agree quite well with the present results, while the values measured in PISCES are generally lower. It may be that the significantly higher fluxes of impacting species and difficulties in determining the particle flux and energy may account for some of these differences.

8. FITTING OF THE MODEL FOR METHANE EROSION DUE TO LOW-ENERGY HYDROGEN ION IMPACT TO THE EXPERIMENTAL RESULTS

In this section, we fit the revised model for methane erosion developed in section 4 to the present experimental data obtained for both H^+ and D^+ impact and discuss the essential features. In general, the best fit to each data set was determined using an iterative procedure whereby the free parameters were varied and the model predictions evaluated against a set of criteria. For a more thorough discussion of this fitting process and the model predictions which result from more rigorous regression fitting the reader is referred to Appendix A.

8.1 Results and Energy Dependence of Fitting Parameters

The best fits for the adjustable parameters were determined for each isotope at each of the six selected energies, and the results are presented, along with the experimentally determined methane yields, in figures 53 and 54 for CH_4 , and figures 55 and 56 for CD_4 . In general, the agreement between the model predictions and the experimental results is very good except for low-energy (≤ 25 eV) impact at high temperatures ($> 800K$). For example, for 10 eV H^+/D^+ impact at 1000 K, the model underestimates the methane yield by up to a factor of 10 or more. The reason for this disagreement is not immediately evident and some of the discrepancy may be attributed to experimental error. Specifically, small errors in the correction for the wall contribution to the measured methane signal may lead to large errors in the methane yield at high temperatures. Alternatively, another low-energy process may be occurring which has not yet been identified. Over the rest of the energy and temperature range the agreement may be considered excellent.

Of course, given the set of energy-dependent adjustable parameters such a good fit is likely. The best-fit values for the adjustable parameters along with Y_m and T_m are presented in Table 6 below. A value of E_D normally distributed about 25 kJ/mol with a width of 14 kJ/mol resulted in the best fit for all energies. Thus the activation energy for abstraction was not dependent on ion energy.

In figure 57, the energy dependence of the adjustable fit parameters, for each isotope of hydrogen, is illustrated along with a curve fit. It should be emphasized that these curve fits are not based on any theory, but rather represent simple mathematical fits to the data. As such, extrapolation of these curves outside of the stated energy range (10 - 200 eV) cannot be justified. The equations resulting from these fits are given below.

Table 6. Revised Model Fitting Parameters and predicted Y_m and T_m

Energy (eV)	$\sigma_i (m^2)$	$\sigma_E (m^2)$	$k_D (s^{-1})$	$T_m (K)$	$Y_m (CH_4/H^+)$
10 H ⁺	2.5×10^{-23}	1.0×10^{-17}	.0070	640	.0073
10 D ⁺	5.5×10^{-23}	1.3×10^{-17}	.0075	630	.0093
15 H ⁺	4.8×10^{-23}	2.0×10^{-17}	.0070	650	.0091
15 D ⁺	8.0×10^{-23}	2.0×10^{-17}	.0077	640	.0111
25 H ⁺	7.0×10^{-23}	1.3×10^{-16}	.0073	710	.0129
25 D ⁺	1.1×10^{-22}	1.0×10^{-16}	.0080	690	.0151
50 H ⁺	1.1×10^{-22}	2.4×10^{-16}	.0084	730	.0172
50 D ⁺	1.6×10^{-22}	3.5×10^{-16}	.0095	730	.0217
100 H ⁺	6.0×10^{-23}	3.2×10^{-16}	.0155	740	.0240
100 D ⁺	9.0×10^{-23}	4.0×10^{-16}	.026	720	.0379
200 H ⁺	2.0×10^{-23}	5.0×10^{-16}	.025	740	.0352
200 D ⁺	5.0×10^{-23}	7.0×10^{-16}	.045	730	.0608

$$\sigma_i^H = 1.944 \times 10^{-21} U^{(-8.549 + 4.702 \ln U - 0.9152 (\ln U)^2 + 0.5689 (\ln U)^3)}$$

$$\sigma_i^D = 1.118 \times 10^{-13} U^{(-27.57 + 12.5 \ln U - 2.335 (\ln U)^2 + 0.1536 (\ln U)^3)}$$

$$\sigma_E^H = 5.636 U^{(-55.37 + 26.01 \ln U - 4.987 (\ln U)^2 + 0.3403 (\ln U)^3)}$$

$$\sigma_E^D = 1.457 \times 10^{17} U^{(-96.12 + 41.93 \ln U - 7.67 (\ln U)^2 + 0.5059 (\ln U)^3)}$$

$$k_D^H = 7.701 \times 10^{-3} - 7.988 \times 10^{-5} U + 2.318 \times 10^{-6} U^2 - 7.429 \times 10^{-9} U^3$$

$$k_D^D = 1.001 \times 10^{-2} - 2.538 \times 10^{-4} U + 6.104 \times 10^{-6} U^2 - 1.98 \times 10^{-8} U^3$$

Where U is the hydrogen ion energy and the superscript indicates the hydrogen isotope. It is important to note that, despite using the adjustable terms to determine the best fit, these energy dependent parameters are not randomly distributed with respect to energy. Instead,

they each show a general energy dependence which is consistent with the process they describe.

In figure 57a, σ_i , the cross-section for kinetic ejection of methyl groups rises as the energy increases from 10 to ~ 50 eV after which it falls. This behaviour is a consequence of the experimentally determined methane yields at room-temperature, and confirms that, within our revised model system, kinetic ejection of surface methyl groups is principally responsible for the yield observed at room-temperature. For ion energies below 50 eV, removal of the methyl radical becomes more difficult and the curve appears to be approaching a threshold below 10 eV, while higher energy ions do not effectively remove methyl groups at the immediate (geometrical) surface. Of course, these higher energy ions lead to the formation of methyl groups away from the immediate surface, via energy deposition and subsequent hydrogenation. However, it is likely that the fraction of the ion flux with enough energy to remove these deeper methyl groups is low, leading to the reduction in σ_i . We note further the isotopic effect on σ_i which is about a factor of 1.5 to 2 over most of the energy range. This is a reflection of the ion energy transfer efficiency which is only moderately increased for the heavier deuterium ions.

The energy dependence of σ_E , the cross-section for energy deposition in the form of broken C=C bonds, is shown in figure 57b. The shape of this curve resembles that for physical sputtering of carbon up to 200 eV [6] (with a threshold below 10 eV) which makes sense since they describe similar processes which rely on the breaking of carbon-carbon bonds. Once these bonds are broken they provide sites for hydrogenation and methyl formation which leads to enhanced erosion, under the activated release of these groups, at higher temperatures. Between 10 and ~ 30 eV there is no measurable isotopic effect on σ_E . It is likely that, at these low energies, carbon-carbon bond rearrangement occurs via electronic excitation, not kinetic energy transfer, and so we would not expect an isotopic effect on σ_E for low-energy impact. This would help explain why we can see no isotopic effect in the methane yields at 700 K for low-energy impact below 30 eV. For energies greater than 30 eV there is a small isotopic effect ranging between 1.2 and 1.5 in favour of deuterium, indicating that the heavier ions are more effective at transferring their

energy to break carbon-carbon bonds in the implantation zone, leading to enhanced thermal release.

In figure 57c the energy dependence of k_D , the prefactor for hydrogen abstraction, is shown. This fit parameter is quite level between 10 and 50 eV and then becomes a steadily increasing function of energy over the rest of the range studied implying that the ions with energy in excess of 50 eV may kinetically enhance the abstraction process. Furthermore, in contrast to σ_i , this process does not approach an energy threshold, but instead approaches a constant value at low energies. We observe that, for impact energies above ~ 50 eV, there is an isotopic shift in k_D which is about a factor of 1.8 for ion energies > 90 eV. This may indicate that the abstraction process is kinetically enhanced and that at least some of the attached hydrogen is being removed energetically. This, coupled with damage deposition, helps explain why we see a measurable isotopic effect for higher energy impact near T_m .

The reader should be reminded, that the fraction of carbon in the sp^3 hybridization state with methyl groups attached, f , has been taken to be an unknown constant which was implicitly incorporated into σ_i and k_D during the fitting process. Furthermore, if this constant depends on the ion energy, this information will also be buried in the fit values, and may account for some of the energy dependence observed in figure 57 a and c.

In section 2, we noted that García-Rosales and Roth [21] did not observe a significant reduction in the methane yield, below 600 K, for graphite doped with 15% boron (USB15) over pyrolytic graphite. For higher graphite temperatures there were significant advantages to the doped graphite in terms of a reduced methane yield. The processes incorporated in the revised model offer a reasonable explanation as to why this is so. We have inferred that the methane yield at low temperatures depends directly on kinetic ejection of methyl groups. There is little reason to suspect that dopants would reduce this contribution other than by the extent to which they fill lattice positions (i.e. 15% in the present example). At higher temperatures, however, where the thermal release of methane can be enhanced by damage deposition and abstraction, the effect of the dopants can be much greater if they chemically suppress this release, presumably by

reducing k_s , k_D , or increasing k_H . This may account for the different effects of dopants in different temperature regimes.

Given that the agreement of the model predictions with experimentally determined methane yields is good, and that the behaviour of the fit parameters as a function of energy makes physical sense, it is likely that most of the physical and chemical mechanisms involved in the erosion of pyrolytic graphite by energetic hydrogen ions have been identified. A possible exception may be the existence of a mechanism which might be significant at high temperatures (> 800 K) for ion impact at energies ≤ 25 eV.

8.2 Energy Dependence of the Methane Yield

Using the model described in section 4 and the parameter fits as a function of energy described in 8.1 the methane yield as a function of energy was determined and plotted for the four selected isotherms in figure 58. At room-temperature the agreement is excellent and this is a consequence of the selection of σ_i , a free fitting parameter, which determines the yield here. In the intermediate temperature ranges of 500 and 700 K we again note very good agreement between the model predictions and the experimental results which suggests that the model has incorporated the correct physical and chemical processes. At 1000 K, we observe that the agreement is acceptable only for energies > 50 eV for H^+ and > 100 eV for D^+ . Experimental errors due to small signals and the background correction discussed in 5.2.2 may play a role here, but it is also possible that some process(es) associated with low-energy impact at high temperature is missing from the model, as noted above.

8.3 Flux Dependence of the Methane Yield

The flux used in all of the model calculations was the same as that used in the erosion experiments themselves, $\sim 10^{18} H^+/m^2 s$. The only flux dependence built into the model comes in the cross-sectional terms, in which the flux appears explicitly and so it is possible to check the flux dependence predicted by the model by varying this number. This was done at fluxes of 10^{17} and $10^{19} H^+/m^2 s$ and the values of Y_m and T_m as predicted by

the model at 10 and 200 eV are presented in Table 7 below along with the values at 10^{18} H^+/m^2s :

Table 7: Flux dependence predicted by the Revised Model

Energy (eV)	$\Phi = 10^{17} H^+/m^2s$		$\Phi = 10^{18} H^+/m^2s$		$\Phi = 10^{19} H^+/m^2s$	
	Y_m	T_m	Y_m	T_m	Y_m	T_m
10	.0289	520	.0073	640	.0025	750
200	.151	590	.0352	740	.0082	950

As the ion flux is reduced, the maximum methane yield goes up and the temperature at which this occurs goes down. Such trends have been observed in previous experiments [11]. The absolute level of these shifts predicted by the model, however, is far too large. For example, for 200 eV impact, one would expect Y_m to be reduced by about 10% as the flux was increased by an order of magnitude [11]. The model, however, predicts a reduction by a factor of ~ 4 . Similarly, the predicted shift in T_m is also too large at 200 eV. So, although Y_m and T_m shift in the right direction when the ion flux is varied in the model, it cannot be said that the present methane yield model accurately predicts the dependence of this yield on flux.

It is quite possible that many or all of the parameters used in the model (fitted for a flux of $10^{18} H^+, D^+/m^2s$) depend on the ion flux, or that the effective flux density (nominal flux density divided by the effective surface area), which is dependent on ion energy, should be used in the model, as discussed in section 4.2.3. Since no experimental methane yield data were obtained as a function of ion flux, the extension of the model to include other fluxes was not considered.

8.4 Summary of Methane Yield Model and Possible Improvements

For the ion flux encountered in the present erosion experiments, the methane yield model predictions agree very well with the experimentally determined methane yields except for low-energy impact at high temperature. This suggests that the principal

processes associated with energetic ions, namely kinetic ejection of methyl groups and energy deposition, which we have incorporated into the atom model of Küppers et al. along with other modifications, describe the hydrogen ion/graphite interaction well. The isotopic effect observed in the experimental measurements can be effectively reproduced in this revised model using the parameters which are expected to be dependent on ion mass. The flux dependence of the methane yield, however, is not well described by the revised model.

In principle, this model could be extended to include heavier hydrocarbons simply by considering a different group attached as the ligand to an sp^3 carbon center. This would involve refitting the adjustable parameters to the erosion data for the specific hydrocarbon, since the group mass, bond strength, and the fraction of carbons in the sp^3 hybridization state which contain the group, would all be different. It is also possible that even the parameters determined experimentally by Küppers et al. (σ_H , k_x , k_{Hx} , E_x , E_{Hx}) would have to be changed. Such an extensive application was not undertaken here.

Apart from an accurate accounting of the true flux dependence there are a couple of possible improvements to the model that are immediately evident.

The approach of Wittmann and Küppers [63], whereby the graphite specimen is divided mathematically into discrete layers would be favourable for energetic ion erosion modelling. This presents some challenges, however, since, given an ion energy and flux, one must now consider the flux of atoms (thermalized ions) and the flux of ions to each layer independently. The ion flux to each layer would have to be associated with a mean energy, so that σ_i , σ_E , and k_D could be estimated, which means that these would be free adjustable parameters for each layer. Clearly, the solution set would become very large if some assumption on the energy dependence of these parameters is not made.

Another improvement would be to explicitly include all of the relevant carbon hybridization state concentrations in the differential equations. For example, the hydrogenation of 2 sp^2 centers to an sp^3 and an sp^2H configuration, clearly depends on the square of the concentration of carbon atoms in the sp^2 hybridization state. In order to keep the equations linear such considerations were not made in the present model.

Furthermore, Küppers indicated that the inclusion of such terms did not have a dramatic effect on the predictions of his model [86].

9. CONCLUSIONS

A comprehensive study of the chemical erosion of pyrolytic graphite due to low-energy H⁺ and D⁺ impact has been performed. Experimental measurements were made of the methane and heavier hydrocarbon erosion yields due to protium and deuterium impact in the energy range of 10 to 200 eV/(H⁺ or D⁺) and pyrolytic graphite temperatures in the range of 300 to 1000 K, for fluxes of 10^{18} (H or D)/m²s. The extension of the incident particle energy range down to 10 eV represents a major contribution since impact energies are expected to be in the 10's of eV range for gaseous divertors in next-generation tokamaks. Furthermore, the use of both protium and deuterium as impacting species has allowed for a systematic study of the isotopic effect on chemical erosion of pyrolytic graphite. A model describing the low-energy chemical erosion of pyrolytic graphite has also been presented.

As the incident H⁺ or D⁺ energy is reduced the methane yield as a function of graphite temperature broadens below T_m such that significant yields are observed even for impact at room temperature. Such behaviour has been noted previously [21,22]. This room temperature yield evidently depends on kinetic ejection of near surface methyl radicals and is not energy independent below 100 eV, but instead peaks for impact energies near 50 eV. For the incident H⁺ and D⁺ fluxes employed in the present experiments [10^{18} (H⁺ or D⁺)/m²s] the maximum yield (Y_m) and the temperature at which this occurs (T_m), shift downwards as the impact energy is reduced below 200 eV. For instance, H⁺ impact at 200 eV results in a maximum yield which is about 0.036 CH₄/H⁺ at T_m ~ 710 K, while for 10 eV H⁺ impact, Y_m ~ 7.7×10^{-3} CH₄/H⁺ and T_m ~ 600 K. The downwards shift in Y_m with decreasing ion energy has been observed in several previous experiments [16,21,22,49], but the shift in T_m has only been noted for relatively low incident H⁺ fluxes ($< 5 \times 10^{18}$ H⁺/m²s) [16,49].

As the graphite temperature increases above 300 K, thermally activated chemical processes become important and lead to an enhancement in the methane yield regardless of the incident particle energy. As well, for impact energies in excess of ~ 40 eV, damage deposition resulting in broken carbon-carbon bonds further enhances the methane yields at

higher temperatures. The present methane yields at room temperature (Y_{RT}) and T_m (Y_m) show reasonably good agreement with previously published values, especially when one considers the differences in the incident particle fluxes.

The heavy hydrocarbon (HHC) yields generally exhibit behaviour similar to that of methane except that they are less dependent on incident particle energy. In general, we see a reduction in the maximum heavy hydrocarbon yield as the ion energy is reduced below 200 eV, but it is not clear whether this is accompanied by a shift in T_m . Such a shift was noted for D^+ impact, but not for H^+ . It is not clear, based on the present experimental evidence, that the HHC production is related to molecular size or carbon-carbon bond structure. Instead, it seems more likely that either damage deposition leads to preferential formation of certain ligand groups, or that the thermal release prefactor, k_s , is different for each ligand group.

The total chemical erosion yields of pyrolytic graphite exhibit a gross behaviour which is very much like that due to methane in that the temperature dependence broadens and Y_m and T_m shift downwards with decreasing ion energy. The contribution of the heavy hydrocarbons, however, tends to have a moderating effect on many of the trends observed for methane production. For D^+ impact a maximum yield of ~ 0.089 C/ D^+ was observed for 200 eV impact at $T_m \sim 700$ K and this was reduced to 0.023 C/ D^+ at 10 eV ($T_m \sim 600$ K). The experimentally determined chemical yields agree reasonably well with previously published results. For plasma-facing graphite surfaces in reactors, where we desire low erosion yields, we conclude that it is more important to control graphite temperature (near 300 K or 1000 K) than it is to reduce ion energy, although there is still an advantage to lower energy impact. From an engineering standpoint it may also be desirable to operate at a temperature of ~ 500 K where the total chemical yield is nearly independent of ion energy over the range of 10 to 200 eV.

Within experimental errors, the isotopic effect on the total chemical erosion yield is less than a factor of 2, with yields due to D^+ impact being higher for the most part. The only regimes where the isotopic effect approaches a factor of 2 are for 10 eV impact at room temperature and higher energy (≥ 100 eV) impact near T_m . For all other

temperatures and energies the isotopic effect was < a factor of 1.7. These values agree reasonably well with the factor of ~ 2 observed in TEXTOR [42] and PISCES [45], but are significantly lower than the factor of ~ 5 determined by Roth and Bohdansky [22]. Based on energy transfer and damage deposition considerations we do not expect an isotopic enhancement of greater than a factor of 2 for D⁺ impact over H⁺.

A methane erosion yield model has been developed using the principal reactions outlined by Küppers et al. [54-63], with some modifications and additional terms to account for kinetic ejection and damage deposition associated with energetic particle impact. Fitting of this model to the present methane yield data show excellent agreement, except for low energy (\leq 25 eV) impact at temperatures above \sim 800 K. We have provided a sound physical basis for the behaviour of the free fitting parameters and conclude that most of the processes associated with low-energy impact on pyrolytic graphite leading to methane production have been incorporated.

In summary, the major contributions of this thesis include; i) the extension of the incident H⁺ and D⁺ energy range down to 10 eV where no systematic experimental investigations have been conducted, ii) the determination of individual hydrocarbon and total chemical erosion yields, iii) the use of both protium and deuterium as impacting species in order to determine the isotopic effect on the erosion yields, and iv) the development of a semi-empirical model for the methane yield of pyrolytic graphite due to low-energy hydrogenic impact.

The present experimental results for methane and total chemical yields, as well as the modified chemical erosion model provide useful input for fusion reactor design. They are important in determining component lifetimes and carbon impurity levels. Also, they will contribute to the modelling of the plasma/edge region, where transport and redeposition of impurities are major concerns.

REFERENCES

- [1] T. Dolan, "Fusion Research volume 1", Pergamon Press, 1982.
- [2] W. Fundamenski, *Fusion Tech.*, **29** (3) (1996), 313.
- [3] D. Reiter, "The Edge Plasma" in *Physical Processes of the Interaction of Fusion Plasmas with Solids*, ed., W.O. Hofer and J. Roth, Academic Press, (1996) pp1.
- [4] M. Sessler and H. Stix, *Physics Today*, June 1996, 21.
- [5] J. Roth, in *Sputtering by Particle Bombardment II*, ed., R. Behrish. TAP 52, Springer, Berlin, (1983).
- [6] W. Eckstein, C. García-Rosales , J. Roth and W. Ottenberger, "Sputtering Data", Max-Plank-Institut für Plasmaphysik Report IPP 9/82 (1993).
- [7] J.W. Davis and A.A. Haasz, 12th PSI review, in press.
- [8] W. Eckstein and V. Philipps, "Physical Sputtering and Radiation-Enhanced Sublimation" in *Physical Processes of the Interaction of Fusion Plasmas with Solids*, ed., W.O. Hofer and J. Roth, Academic Press, (1996) pp 93.
- [9] E. Vietzke and A.A. Haasz, "Chemical Erosion" in *Physical Processes of the Interaction of Fusion Plasmas with Solids*, ed., W.O. Hofer and J. Roth, Academic Press, (1996) pp135.
- [10] J. Roth, E. Vietzke, and A.A. Haasz, in *Atomic and Plasma-Material Interaction Data for Fusion*, *Suppl. Nucl. Fusion* **1** (1991), 63.
- [11] J.W. Davis, A.A. Haasz and P.C. Stangeby, *J. Nucl. Mater.* **145-147**, 417 (1987).
- [12] J. Roth, *Topics Appl. Phys.* **52** (1983), 91.
- [13] E. Vietzke, K. Flaskamp, and V. Philipps, *J. Nucl. Mater.* **128-129** (1984), 545.
- [14] S. Chiu and A.A. Haasz, *J. Nucl. Mater.* **208** (1994), 282.
- [15] J. Roth and J. Bohdansky, *Appl. Phys Lett.* **51** (13) (1987), 964.
- [16] J.W. Davis, A.A. Haasz and P.C. Stangeby, *J. Nucl. Mater.* **155-157** (1988), 234.
- [17] R. Yamada, *J. Nucl. Mater.* **145-147** (1987), 359.

- [18] A.A. Haasz and J. W. Davis, *J. Nucl. Mater.* **175** (1990), 84.
- [19] E. Vietzke, KFA Forschungszentrum, Julich, private communication.
- [20] R. Yamada, *J. Nucl. Mater.* **174** (1990), 118.
- [21] C. García-Rosales and J. Roth, *J. Nucl. Mater.* **196-198** (1992), 573.
- [22] J. Roth and J. Bohdansky, *Nucl. Instr. Meth.* **B23** (1987), 549.
- [23] C. García-Rosales , W. Eckstein and J. Roth, *J. Nucl. Mater.* **218** (1994), 8.
- [24] P.C. Stangeby and G. M. McCracken, *Nucl. Fusion* **30** (1990), 1225.
- [25] B. Labombard et al., *J. Nucl. Mater.* **220-222** (1995), 976.
- [26] G. Lieder et al., " Spectroscopic determination of ion temperatures in the divertor of ASDEX-Upgrade", Proc. 22nd EPS Conf. on Contr. Fusion and Plasma Phys., IV-345, Bournemouth (1995).
- [27] R. Yamada and K. Sone, *J. Nucl. Mater.* **98** (1981), 167.
- [28] R. Yamada and K. Sone, *J. Nucl. Mater.* **120** (1984), 119.
- [29] J. W. Davis and A. A. Haasz, *Appl. Phys. Lett.* **57** (1990), 1976.
- [30] J. W. Davis, A.A. Haasz and C.H. Wu, *J. Nucl. Mater.* **196-198** (1992), 581.
- [31] E. Vietzke, K. Fluskamp and V. Philipps, *J. Nucl. Mater.* **111-112** (1982), 763.
- [32] A.A. Haasz and J.W. Davis, *Nucl. Instrum. Methods B* **83** (1993), 177.
- [33] R. Behrisch, in *Atomic and Plasma-Material Interaction Data for Fusion*, Suppl. *Nucl. Fusion* **1** (1991), 3.
- [34] D. Post et al., *ITER Physics*, *ITER Documentation Series 21* (IAEA Vienna, 1991).
- [35] C. García-Rosales , *J. Nucl. Mater.* **211** (1994), 202.
- [36] K. Behringer, *J.Nucl. Mater.* **176-177** (1990), 606.
- [37] A. Kallenbach, R. Neu, W. Poschenrieder et al., *Nucl. Fusion* **34** (1994), 1557.
- [38] W. Poschenrieder et al., *J. Nucl. Mater.*, **220-222** (1995), 36.

- [39] C. S. Pitcher et al. , Nucl. Fusion **26** (1986), 1641.
- [40] A. Pospieszczyk, in “Atomic and Plasma-Material Interaction Processes in Controlled Thermonuclear Fusion,” R.K. Janev and H. W. Drawin ed.. Elsevier, Amsterdam (1993).
- [41] C.C. Klepper et al., J. Nucl. Mater., **220-222** (1995), 521.
- [42] V. Philipps, E Vietzke and M. Erdweg, J. Nucl. Mater. **162-164** (1989), 550.
- [43] Y. Hirooka, D.M. Goebel, R.W. Conn et al., J. Nucl. Mater. **141-143** (1987), 93.
- [44] D.M. Goebel, J. Bohdansky, R.W. Conn et al., Nucl. Fusion **28** (1988),1041.
- [45] D.M. Goebel, J. Bohdansky, R.W. Conn et al., Fusion Tech. **15** (1988), 102.
- [46] J. Bohdansky, R.W. Conn, D.M. Goebel et al., Proc. 14th European Conf. Controlled Fusion and Plasma Physics, Madrid Spain, 1987, Vol. 11D, 794.
- [47] H. Grote et al., 12th PSI, in press.
- [48] B.V. Mech, A.A. Haasz and J.W. Davis, 12th PSI, in press.
- [49] C.H. Wu, J.W. Davis and A.A. Haasz, Proc. 15th Conf. on Controlled Fusion and Plasma Heating, Dubrovnik, May 16-20, 1988, Europhysics Conf. Abstracts Vol 12B Part II, p. 691.
- [50] A.A. Haasz and J.W. Davis, J. Chem. Phys. **85** (1986), 3293.
- [51] A.A. Haasz and J. W. Davis, J. Chem. Phys., **85 (6)** (1986), 3293.
- [52] W. Möller and B.M.U. Scherzer, Appl. Phys. Lett., **50 (26)** (1987), 1870.
- [53] S. K. Erents, et al., J. Nucl. Mater., **63** (1976), 399.
- [54] A. Schenk et al., Appl. Phys. Lett. **61 (20)** (1992), 2414.
- [55] J. Biener, A. Schenk, B. Winter and J. Küppers, J. Elec. Spec. Rel. Phen. **64/65** (1993), 331.
- [56] J. Biener et al., Surf. Sci. Lett. **291** (1993), 725.
- [57] J. Biener et al., J. Chem. Phys. **99 (4)** (1993), 3125.
- [58] J. Biener et al., Surf. Sci. **307-309** (1994), 228.
- [59] C. Lutterloh et al., Surf. Sci. Lett. **312** (1994), L1039.

- [60] A. Horn et al., Chem. Phys. Lett. **231** (1994), 193.
- [61] J. Biener et al., Phys. Rev. B **49** (24) (1994), 17307.
- [62] A. Schenk et al., J. Nucl. Mater. **220-222** (1995), 767.
- [63] M. Wittmann and J. Küppers, J. Nucl. Mater. **227** (1996), 186.
- [64] J. Roth and C. García-Rosales, Nuclear Fusion, **36** (12) (1996), 1647.
- [65] M. Grayson, ed. of “Encyclopedia of Composite Materials and Components”, John Wiley and Sons (1983), pp 155.
- [66] I. W. Drummond, Vacuum **34** (1984), 51.
- [67] E. Harting and F. H. Read, *Electrostatic Lenses*, Elsevier, Amsterda, (1976).
- [68] H. Liebl, J. Bohdansky, J. Roth, and V. Dose, Rev. Sci. Instrum. **58** (1987), 1830.
- [69] Z. Herman, J. D. Kerstetter, T. L. Rose, and R. Wolfgang, Rev. Sci. Instrum. **40** (1969), 538.
- [70] K.K. Foo, R.P.W. Lawson, X. Feng, and W. M. Lau, J. Vac. Sci. Tech. **A9** (2) (1991), 312.
- [71] R. Freeman and E. Jones, “Atomic collision processes in plasma physics experiments”, Culham Laboratory report CLM-R-137, 1974.
- [72] C. Weber in “Focussing of Charged Particles”, ed. A. Septeir, Vol. 1, ch. 1, p. 45, Academic Press, New York (1967).
- [73] S. D. Tanner, Spectrochimica Acta. **47B** (6) (1992), 809.
- [74] A.A. Haasz and I. Youle, Fusion Eng. Des. **12** (1990), 373.
- [75] E. Vietzke, KFA Forschungszentrum, Julich, private communication.
- [76] R. Weast, ed. of “CRC Handbook of Chemistry and Physics - 89th Edition”, section F, p. 176, CRC Press, Florida (1988).
- [77] J. Roth, J. Bohdansky and K.L. Wilson, J. Nucl. Mater. **111-112** (1982), 775.
- [78] R. Yamada, K. Nakamura, K. Sone and M. Saidoh, J. Nucl. Mater. **95** (1980), 278.
- [79] S. Chiu and A.A. Haasz, J. Nucl. Mater. **196-198** (1992), 972.
- [80] E. Vietzke, V. Philipps and K. Flaskamp, J. Nucl. Mater. **162-164** (1989), 898.

- [81] R. Rye, *Surf. Sci.* **69** (1977), 653.
- [82] W. Eckstein, *Supplement to J. Nucl. Mater.*, **1** (1991), 17.
- [83] G. Staudenmaier et al., *J. Nucl. Mater.*, **84** (1979), 149.
- [84] A.A. Haasz and J. W. Davis, *J. Nucl. Mater.*, **232** (1996), 219.
- [85] A.A. Haasz, B.V. Mech and J.W. Davis, *J. Nucl. Mater.*, **231** (1996), 170.
- [86] J. Küppers, Max-Plank-Institut für Plasmaphysik, private communication.

FIGURES

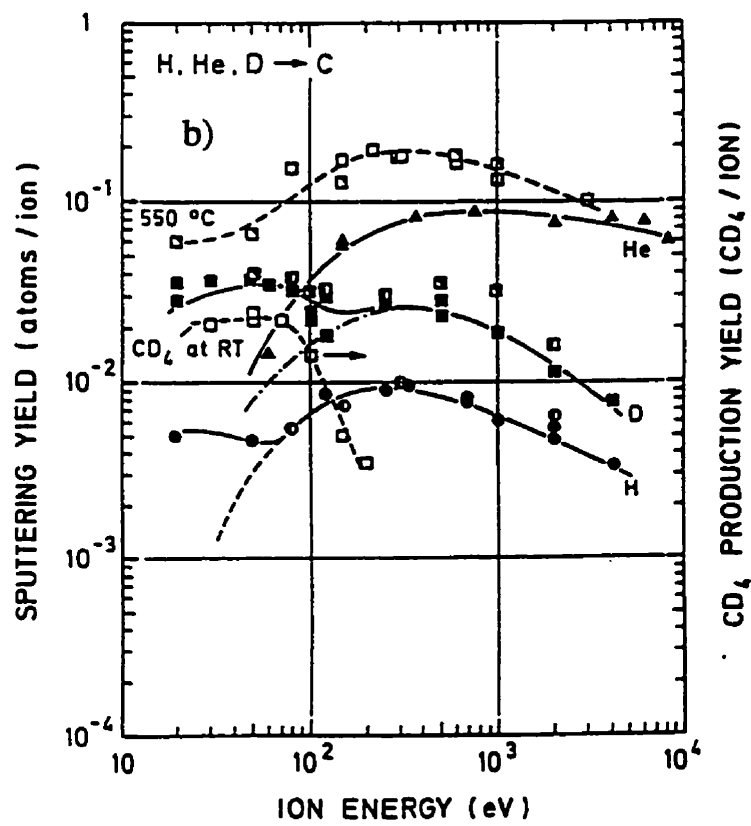
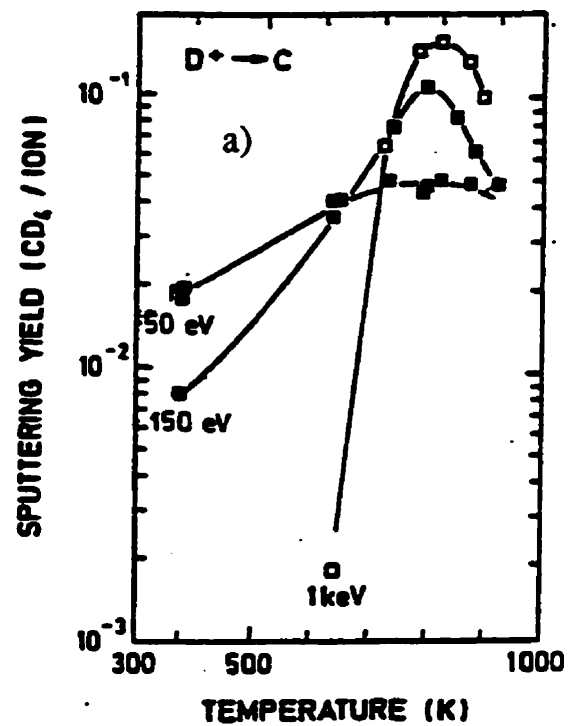


Figure 1: (a) Methane yield of pyrolytic graphite as a function of temperature for D^+ impact at 50, 150 and 1000 eV [22], and (b) the methane yield and total yield of pyrolytic graphite as a function of energy for H^+ , D^+ , and He^+ impact at room temperature (solid symbols) and 820 K (open squares) [22].

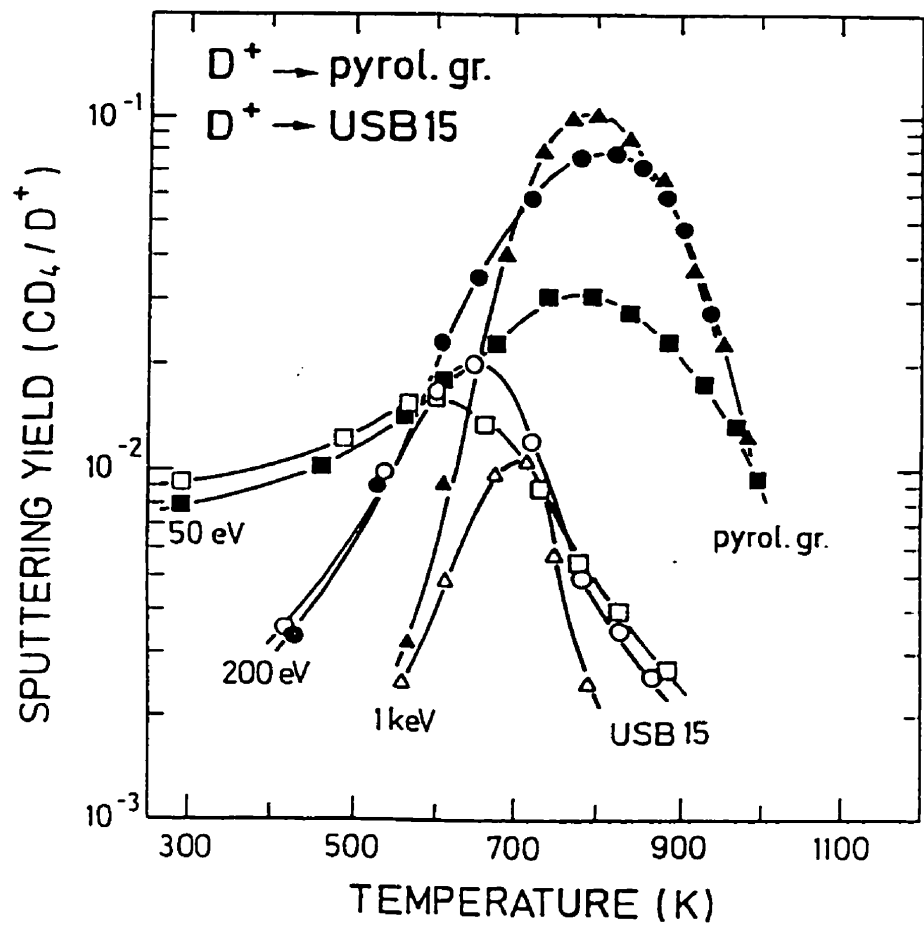


Figure 2: Methane yield of pyrolytic graphite (solid symbols) and USB15 (open symbols) as a function of temperature for D^+ impact at 50, 200, and 1000 eV [21].

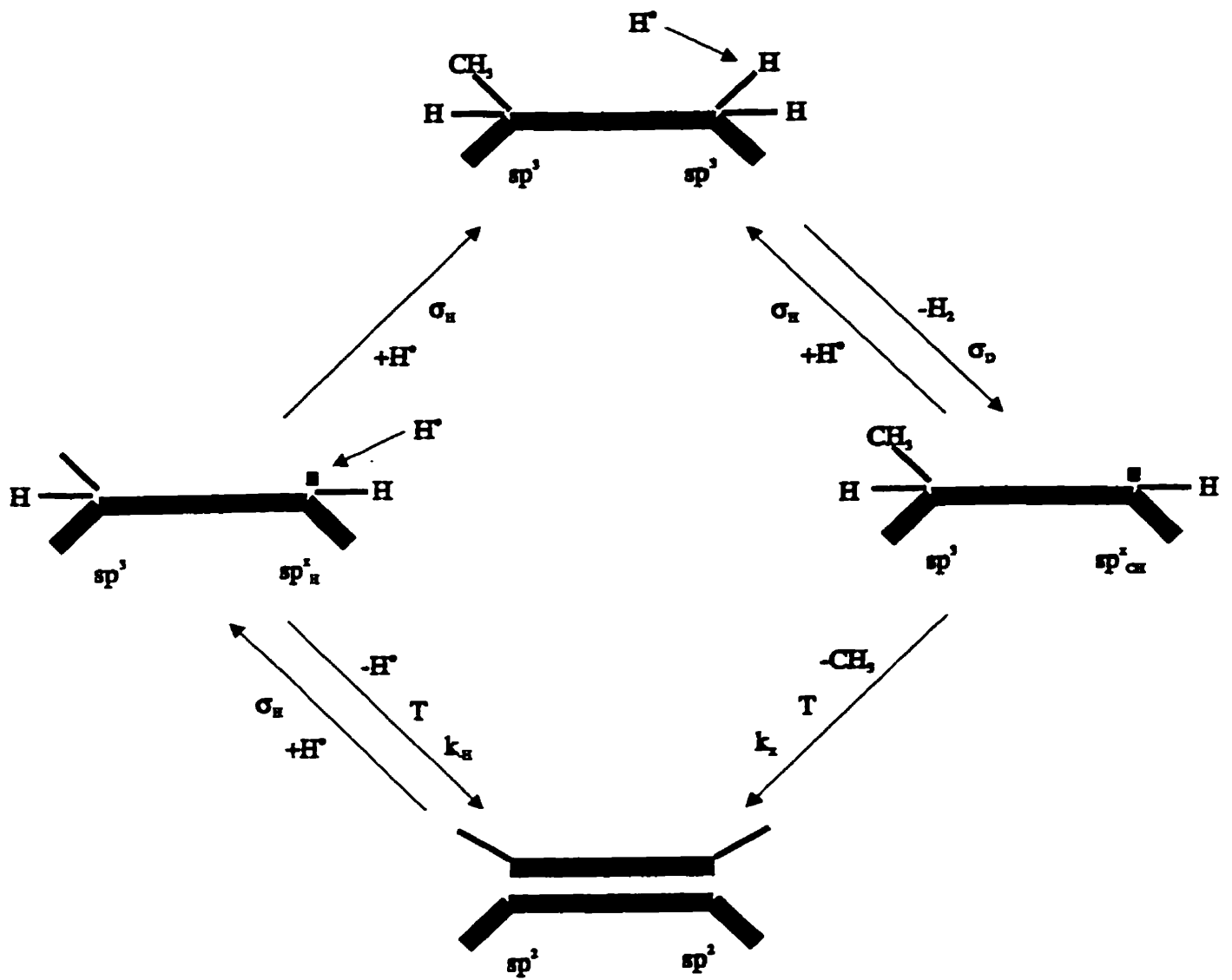


Figure 3: The model of Wittmann and Küppers et al. [54–63] for the erosion of a-C:H films due to thermal hydrogen atom impact.

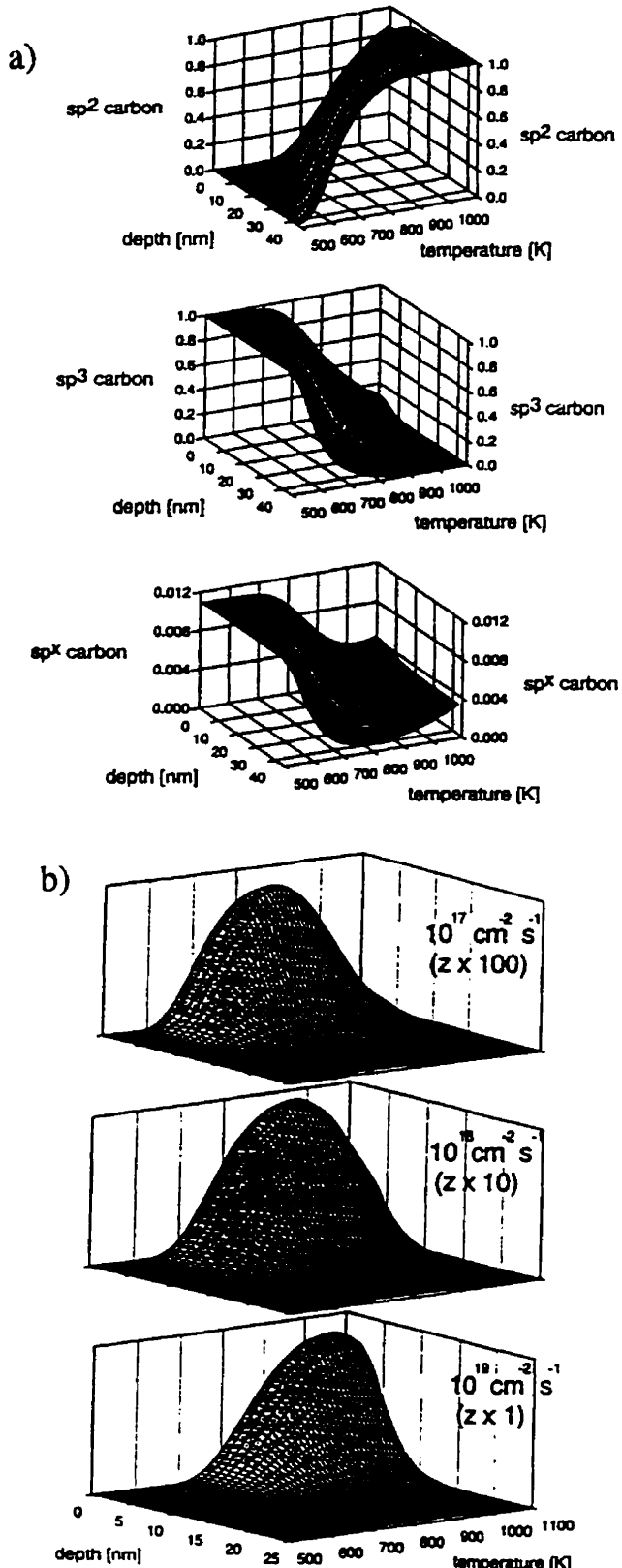


Figure 4: Results of the application of the Wittmann and Küppers atomic model for chemical erosion [63] for an ASDEX-U energy distribution of ions and neutrals. In a) the equilibrium fractions of sp^2 (a), sp^3 (b) and sp^x (c) carbon atoms are shown as a function of depth and temperature. In b) the methyl production rates are shown for 3 total fluxes as a function of depth and temperature. Note that, for a given total flux, the flux as a function of depth varies inversely with depth.

H → C

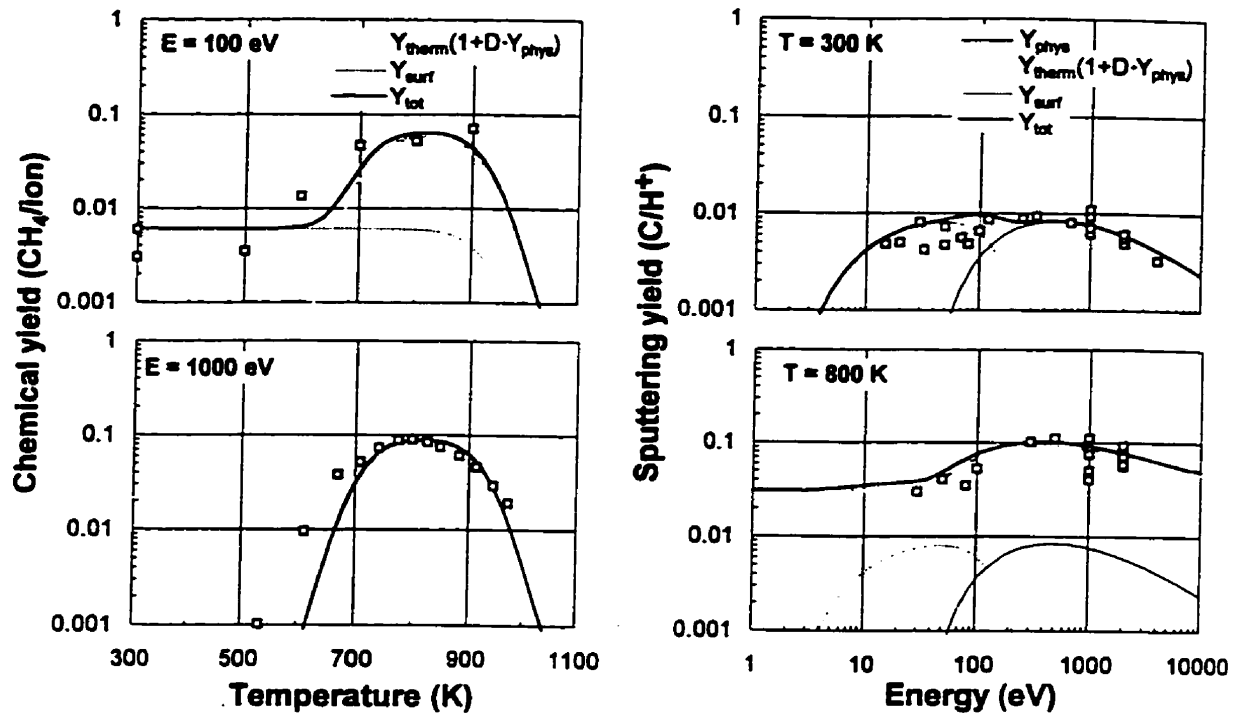


Figure 5: Results of the RG-R model for erosion [64] under mono-energetic ion beam conditions for H^+ impact on carbon. The methane yield is shown as a function of temperature for 100 and 1000 eV impact and the total yield as a function of energy for impact at 300 and 800 K.

$D \rightarrow C$

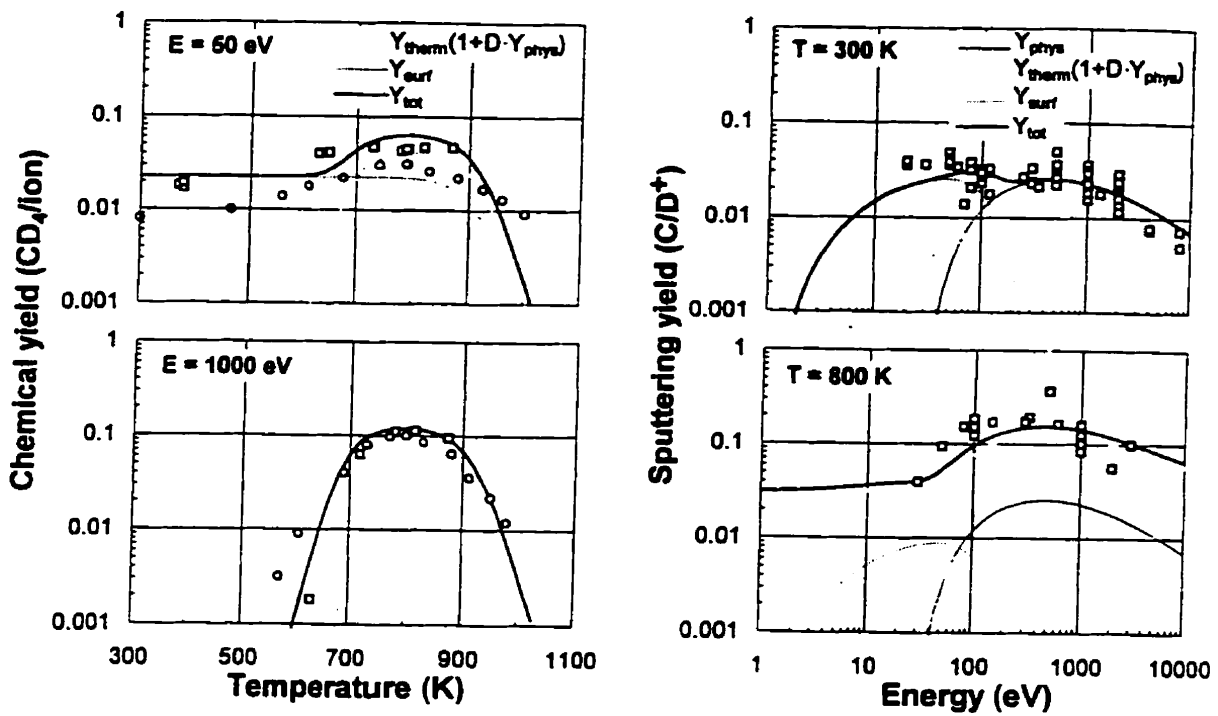


Figure 6: Results of the RG-R model for erosion [64] under mono-energetic ion beam conditions for D^+ impact on carbon. The methane yield is shown as a function of temperature for 50 and 1000 eV impact and the total yield as a function of energy for impact at 300 and 800 K.

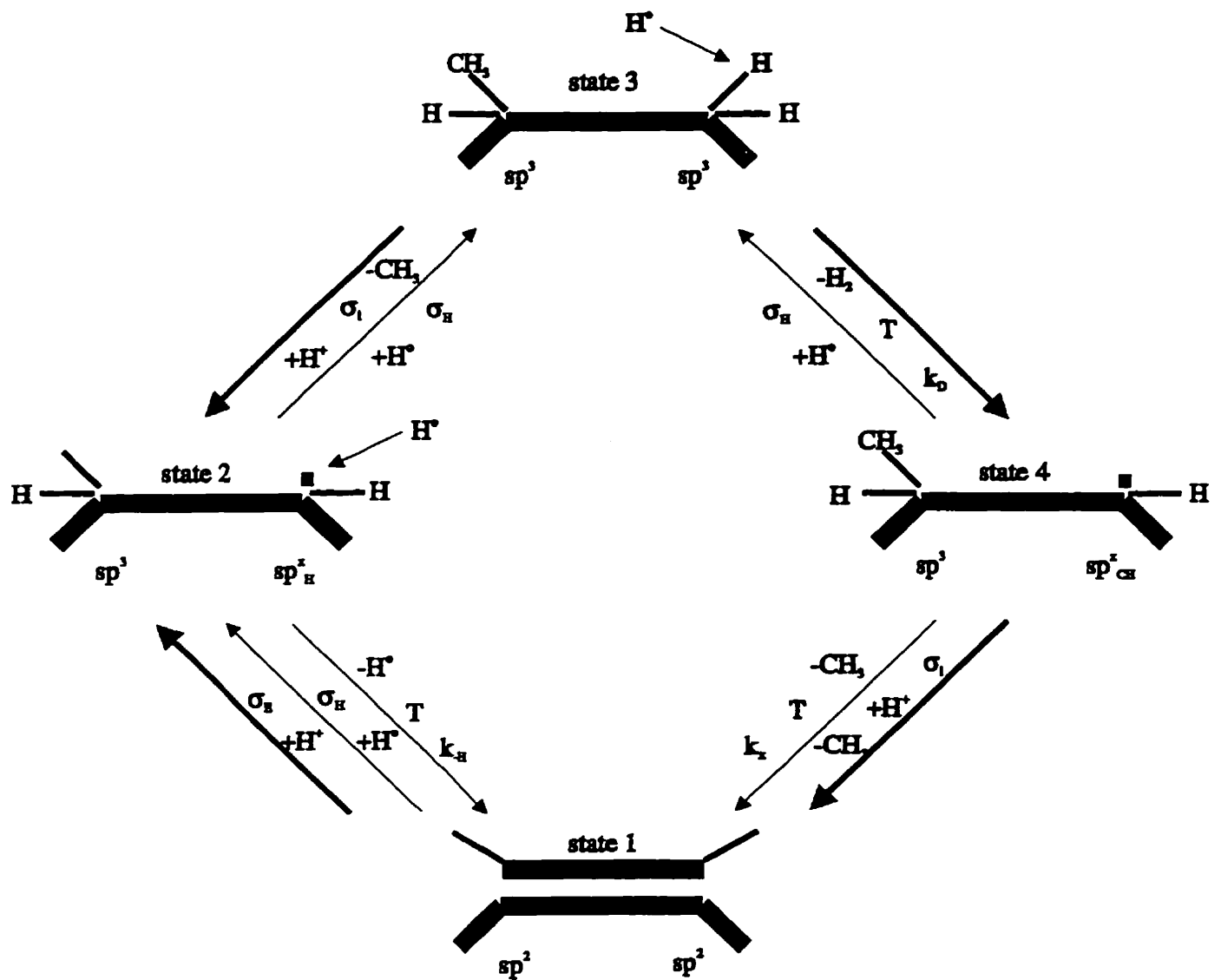


Figure 7: The revised model for chemical erosion due to low-energy ion impact. The thicker arrows represent new or modified processes.

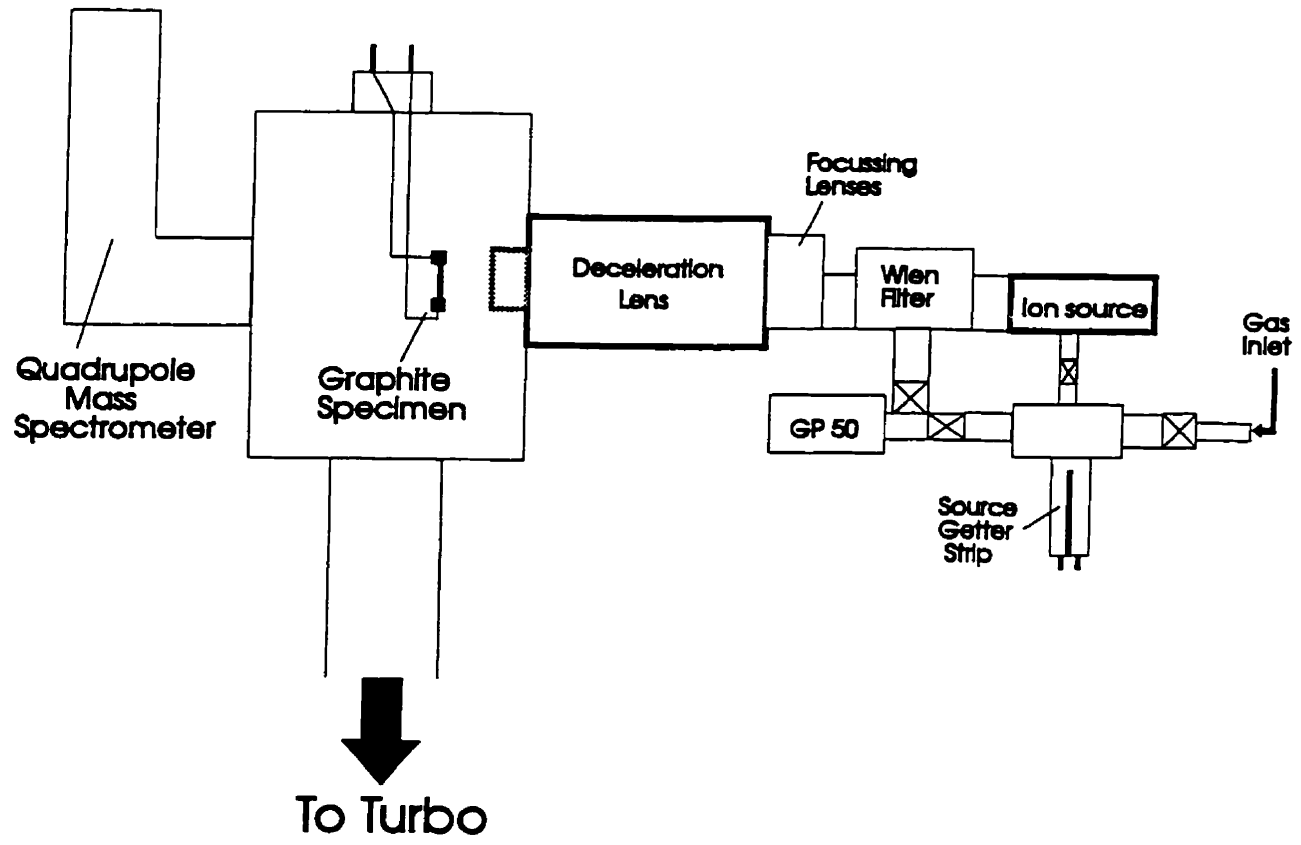


Figure 8: Conceptual drawing of the experimental facility.

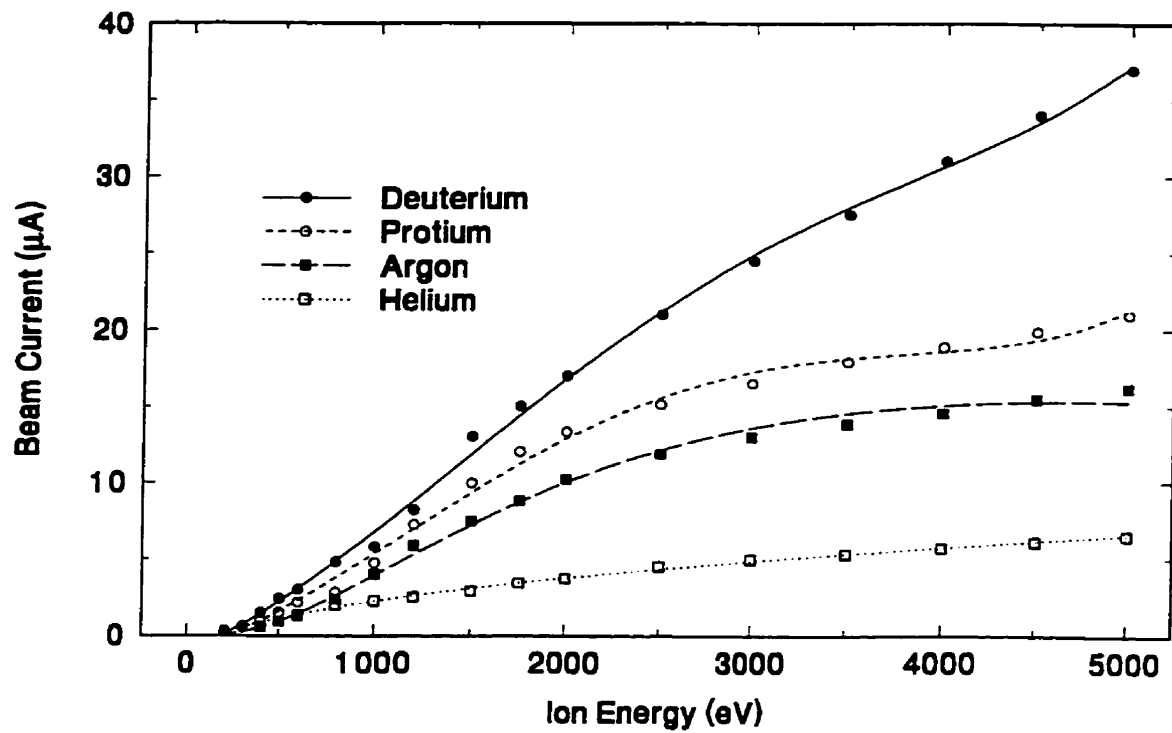


Figure 9: Available ion current for Specs IQE 12/38 ion source as a function of ion energy. Results are shown for protium, deuterium, argon and helium at the optimal ion source pressure for each gas.

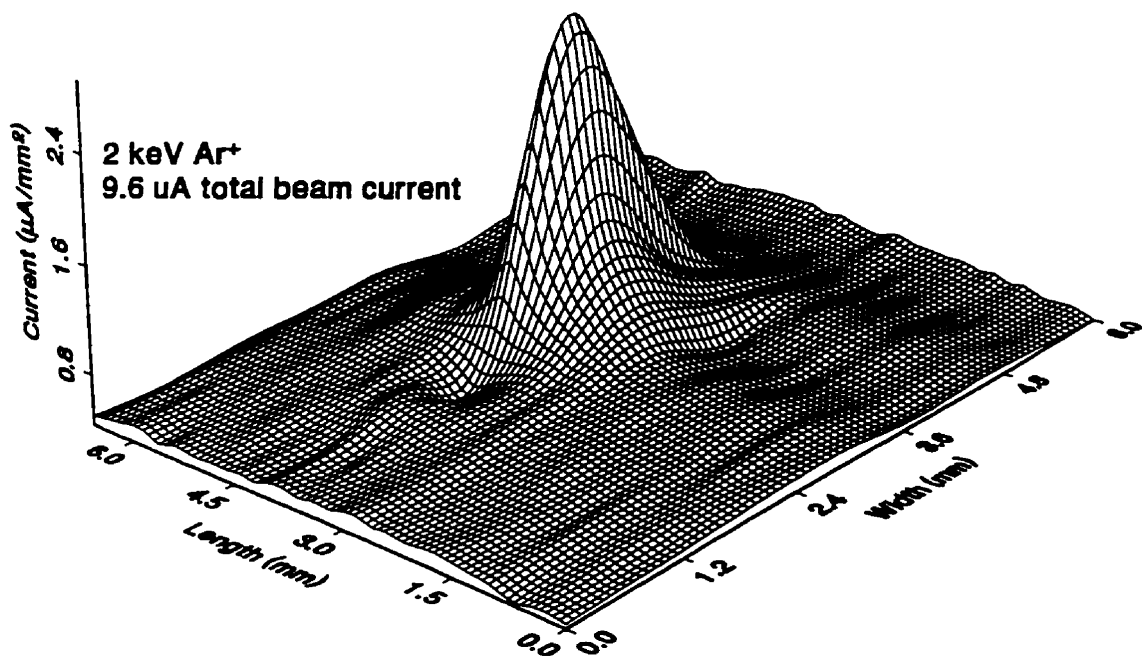


Figure 10: Ion beam profile for 2 keV Argon beam where the 12-pin probe is located 2 cm downstream of the gun exit aperture. The x and y coordinates are in mm.

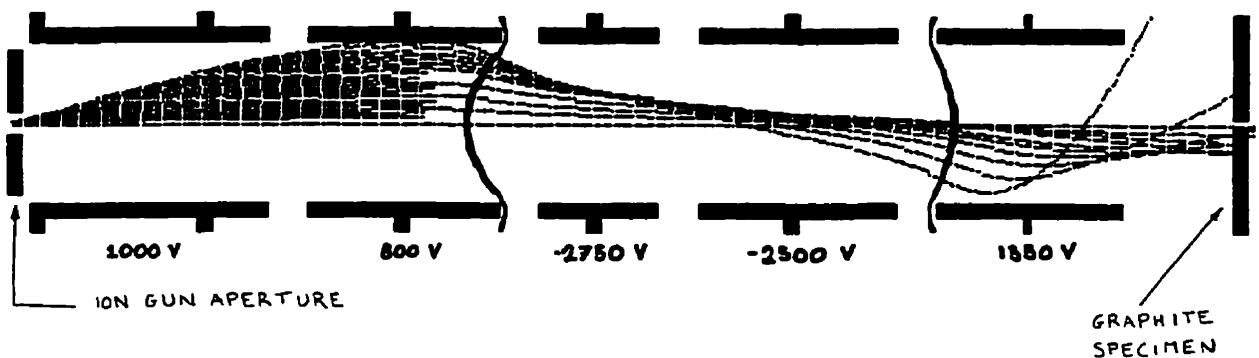


Figure 11: MacSimion ion trajectory calculations for deceleration of T_2^+ from 1.5 keV to 50 eV through 5-element electrostatic lens. Bias voltages are as indicated while the electrode dimensions and lens diameter are described in figure 12.

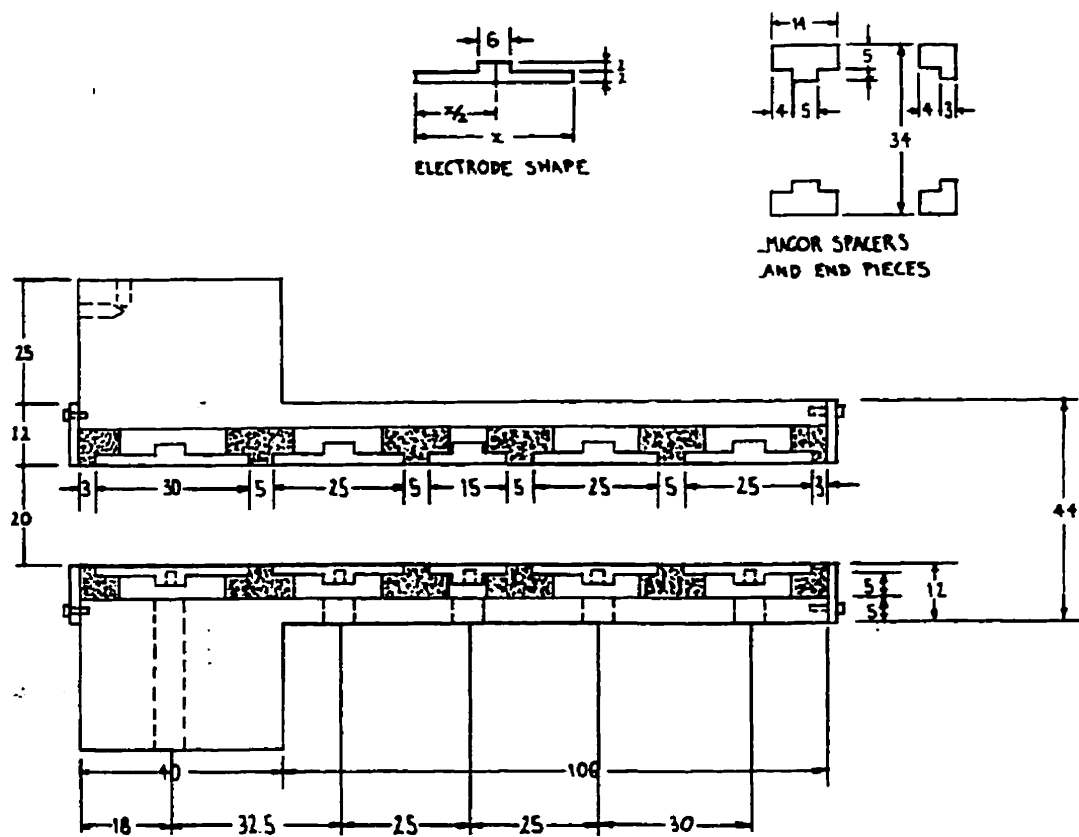


Figure 12: Electrostatic deceleration lens design. Dimensions are in mm.

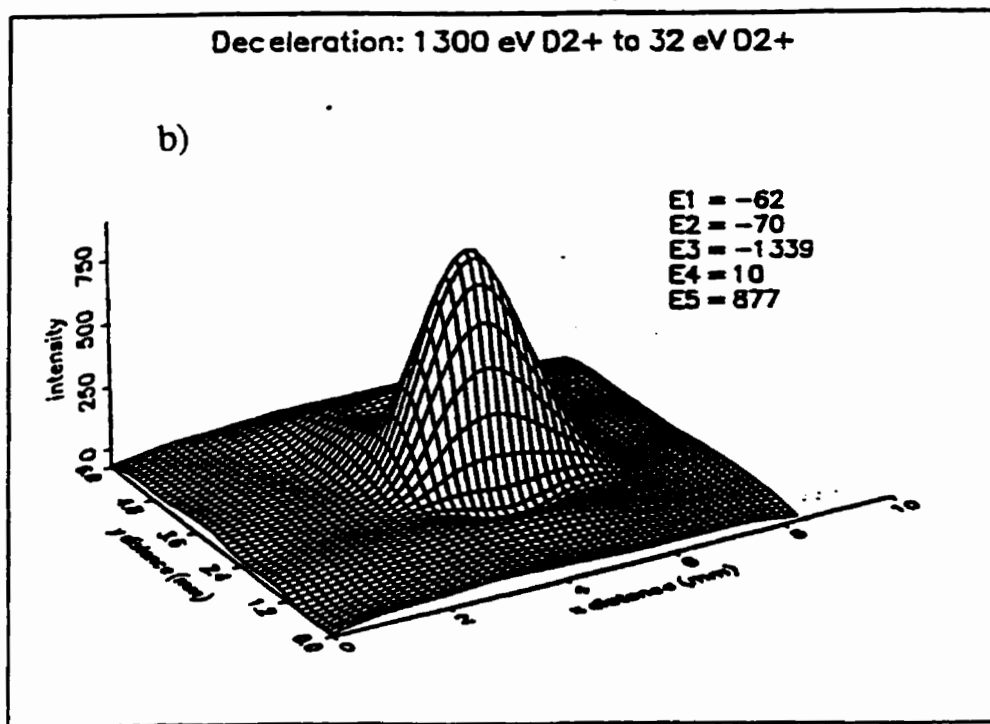
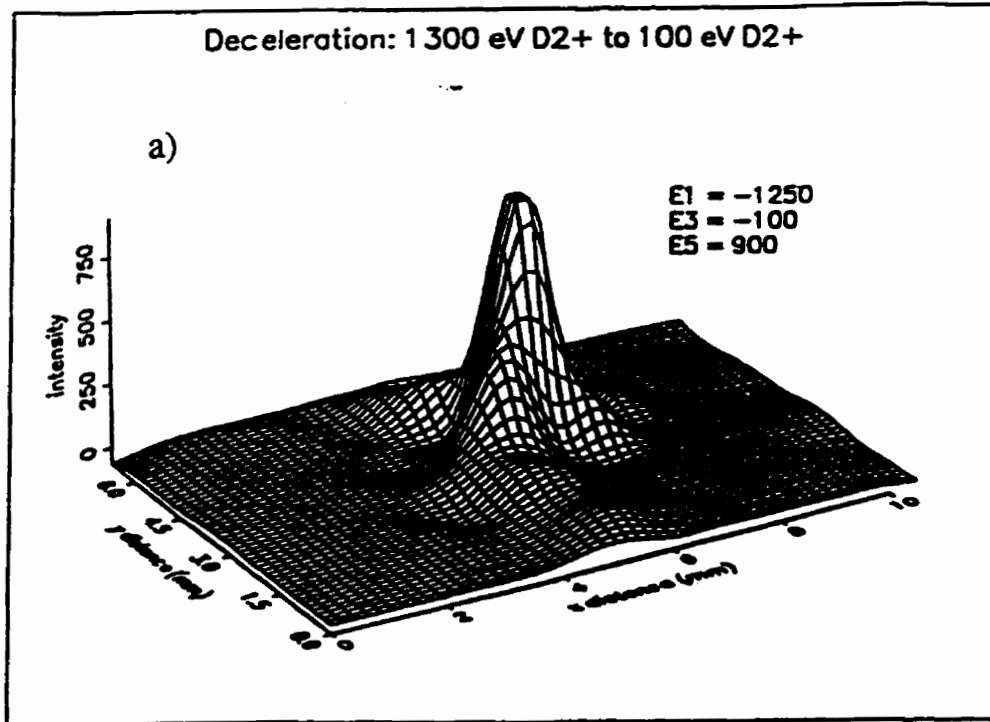


Figure 13: Ion beam profiles for deceleration of 1300 eV D₂⁺ ions to (a) 100 eV (b) and 32 eV. Applied electrode voltages are indicated while the probe bias is the difference between 1300 V and the final molecular ion energy in volts.

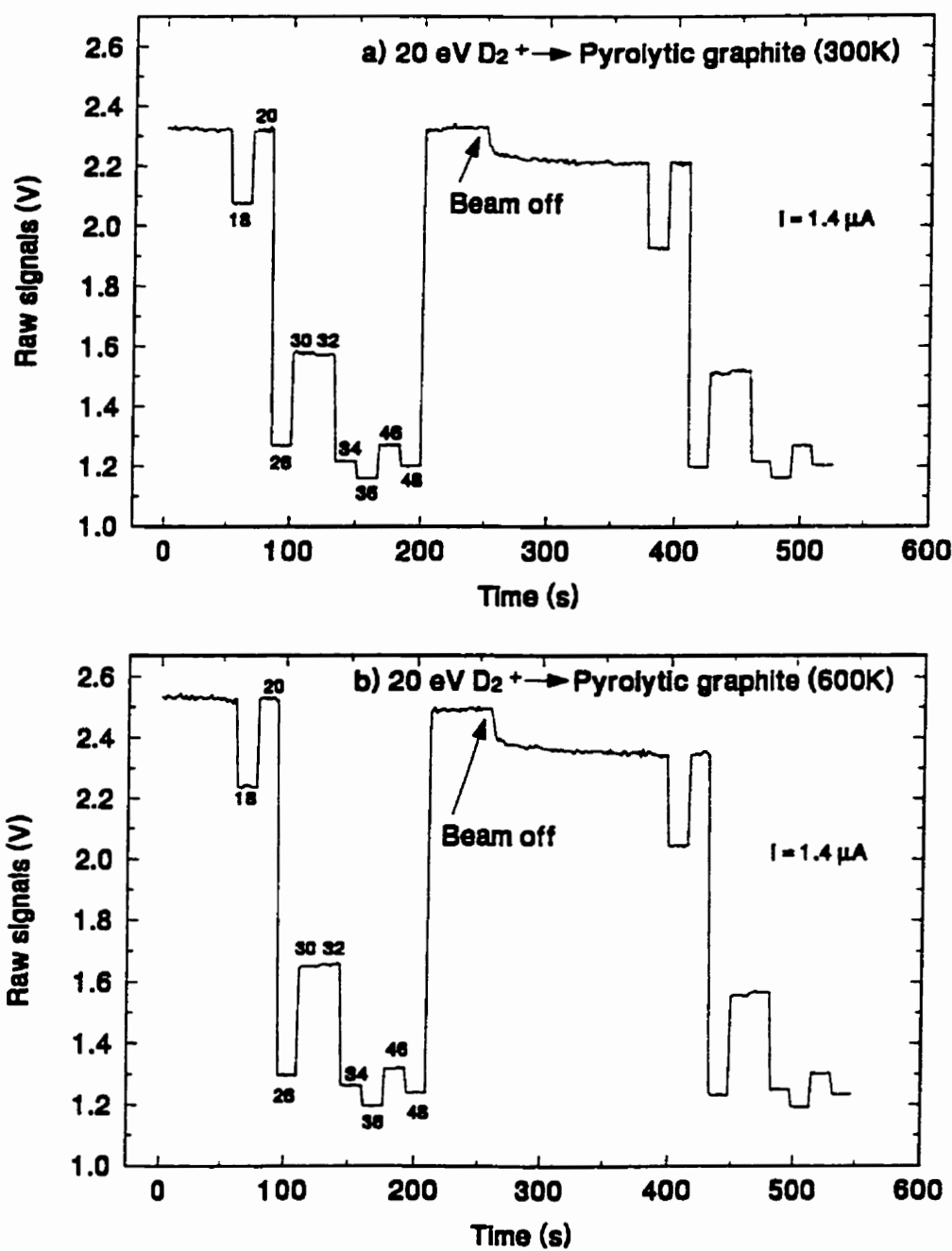


Figure 14: Raw data signals for 20 eV D_2^+ impact at (a) 300 K and (b) 600 K. The number labels indicate the mass monitored by RGA in a.m.u. Each plateau represents the maximum values from ten scans over the mass peak.

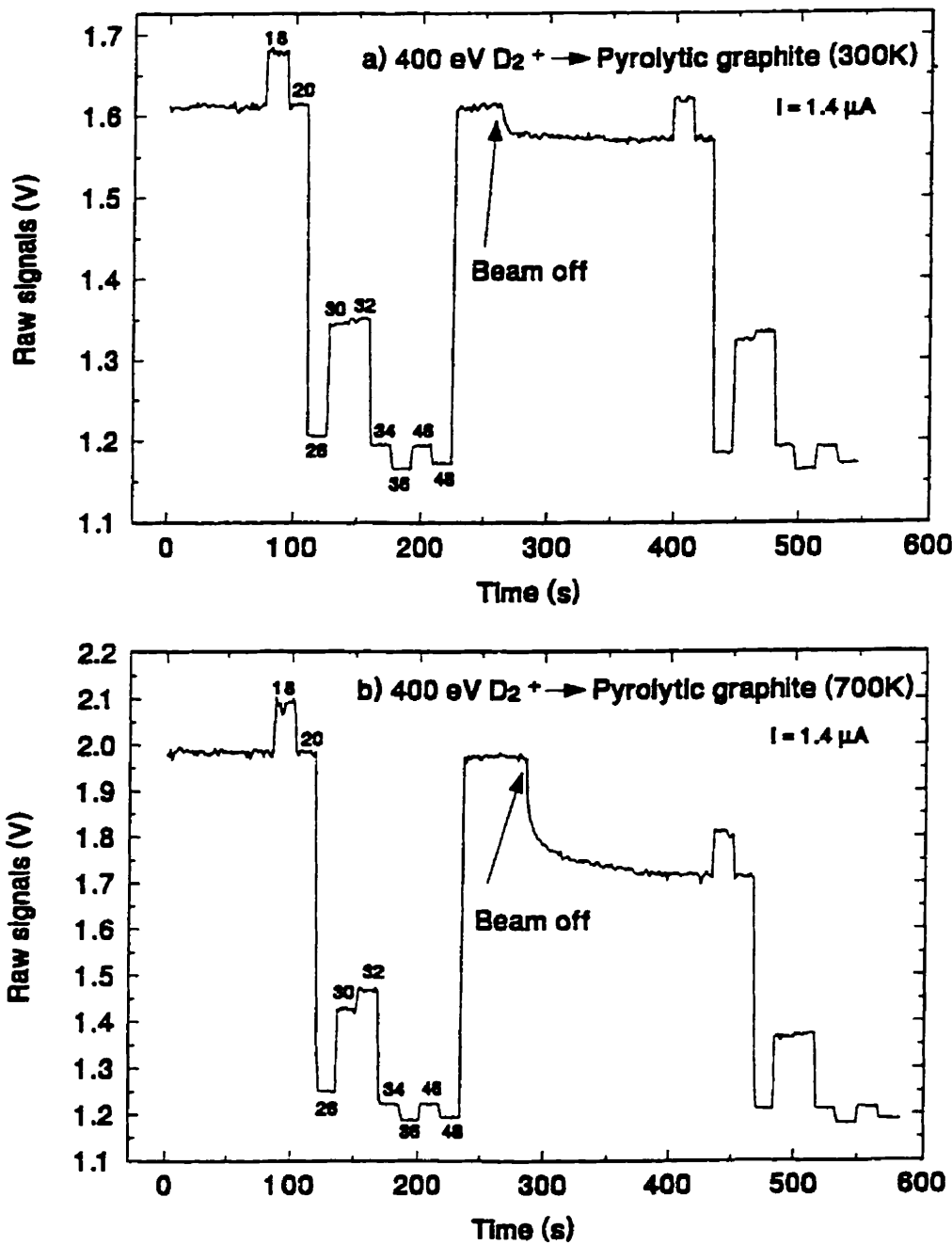


Figure 15: Raw data signals for 400 eV D_2^+ impact at (a) 300 K and (b) 700 K. The number labels indicate the mass monitored by RGA in a.m.u. Each plateau represents the maximum values from ten scans over the mass peak.

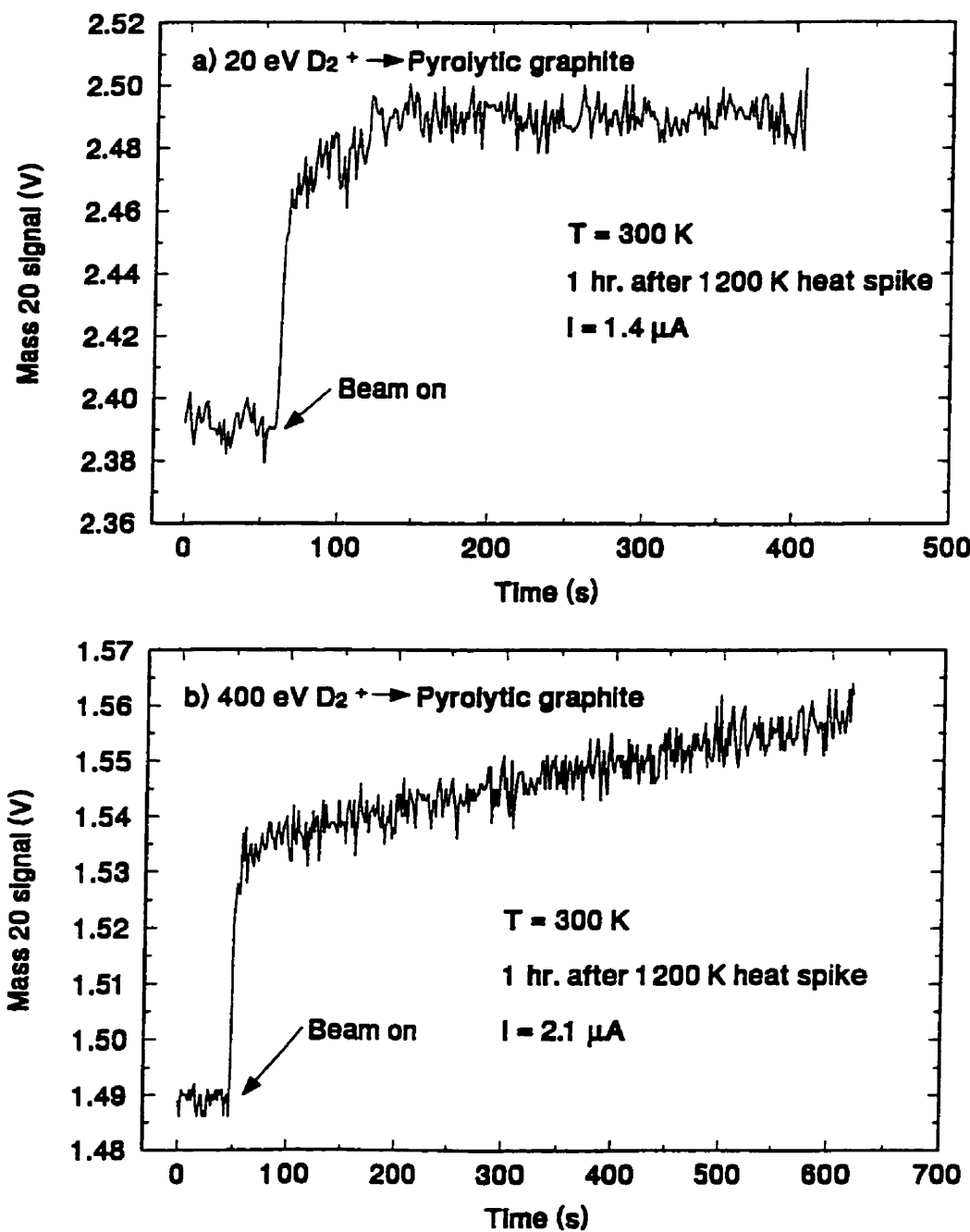


Figure 16: Raw methane signals ($m/e = 20$ a.m.u.) resulting from ion beam incidence at (a) $20 \text{ eV } D_2^+$ and (b) $400 \text{ eV } D_2^+$ for unhydrogenated pyrolytic graphite at 300 K . The intial steep increase is attributed to methane formation on the vacuum walls, while the subsequent slower increase is due to methane orginating from the specimen.

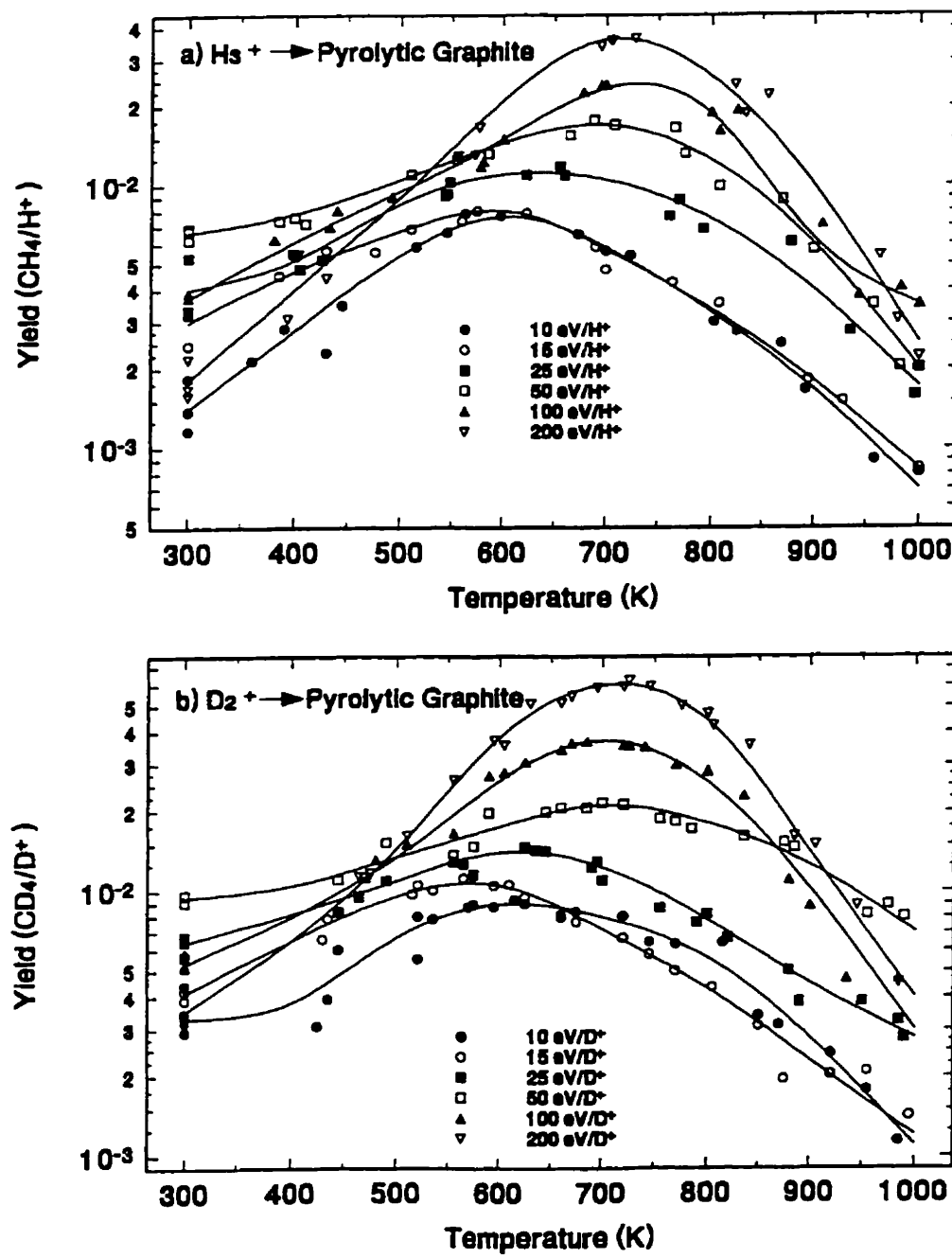


Figure 17: Methane yield of pyrolytic graphite as a function of temperature for (a) H_3^+ and (b) D_2^+ impact at 10, 15, 25, 50, 100 and 200 eV/ion. Spline curves are drawn to aid the reader.

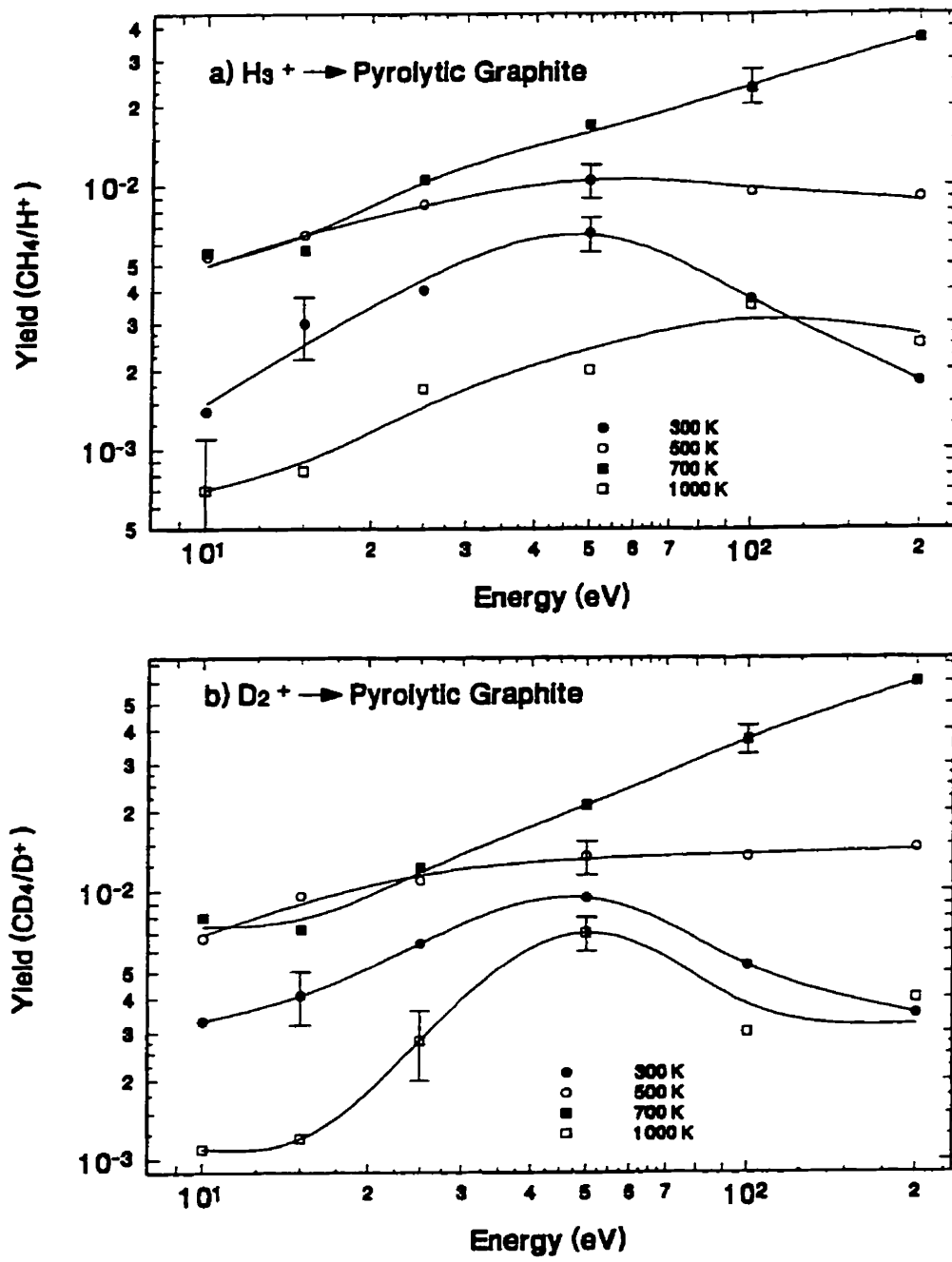


Figure 18: Methane yield of pyrolytic graphite as a function of ion energy for (a) H_3^+ and (b) D_2^+ impact at 300, 500, 700 and 1000 K. Molecular ion energy is divided by the number of atoms in the molecule to arrive at the energy of each atom. Data points are extracted from the spline fits in figure 17. New spline curves are drawn to aid the reader.

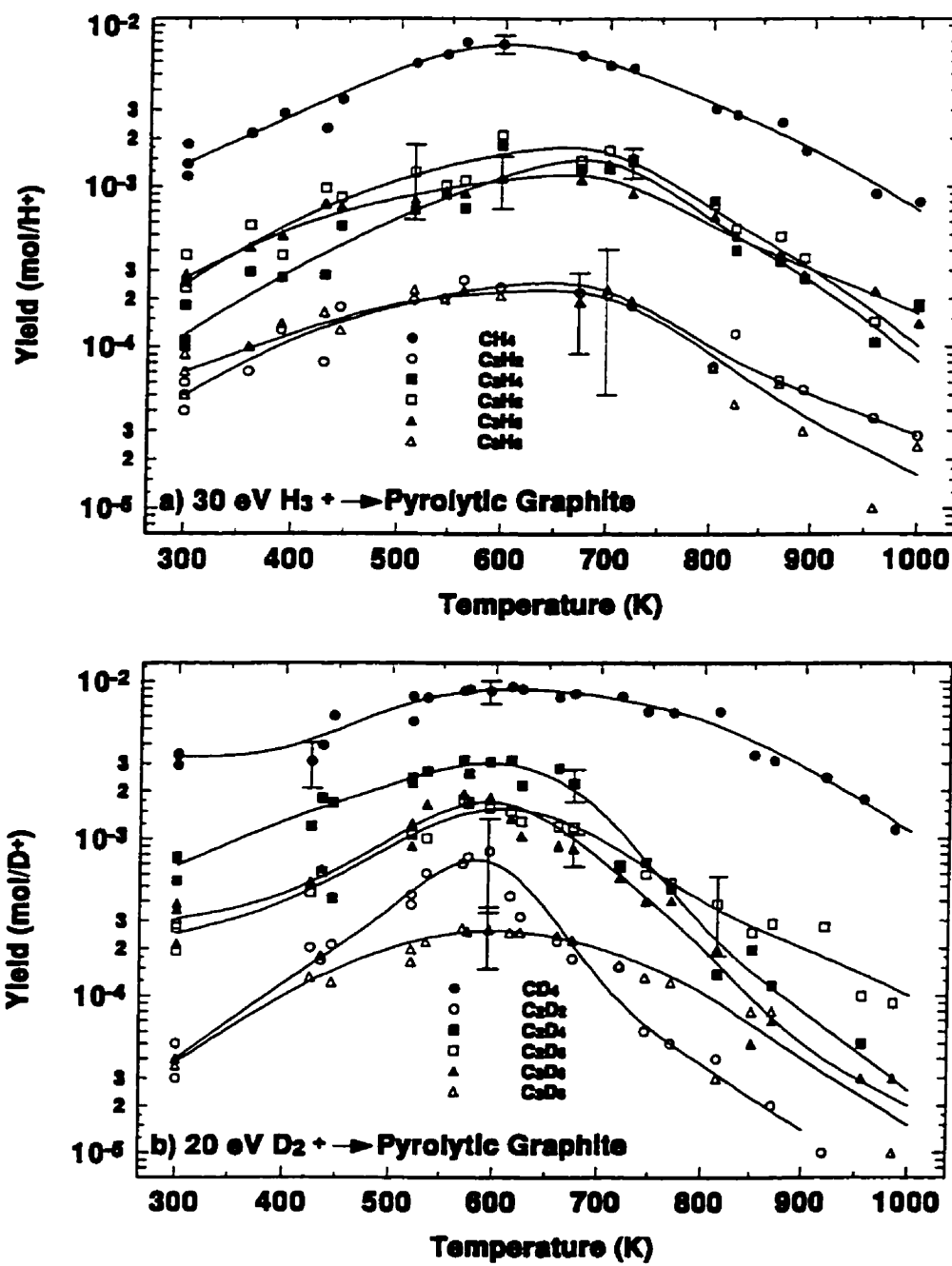


Figure 19: Hydrocarbon spectrum as a function of temperature for (a) 30 eV H_3^+ and (b) 20 eV D_2^+ impact on pyrolytic graphite. Spline curves are drawn to aid the reader.

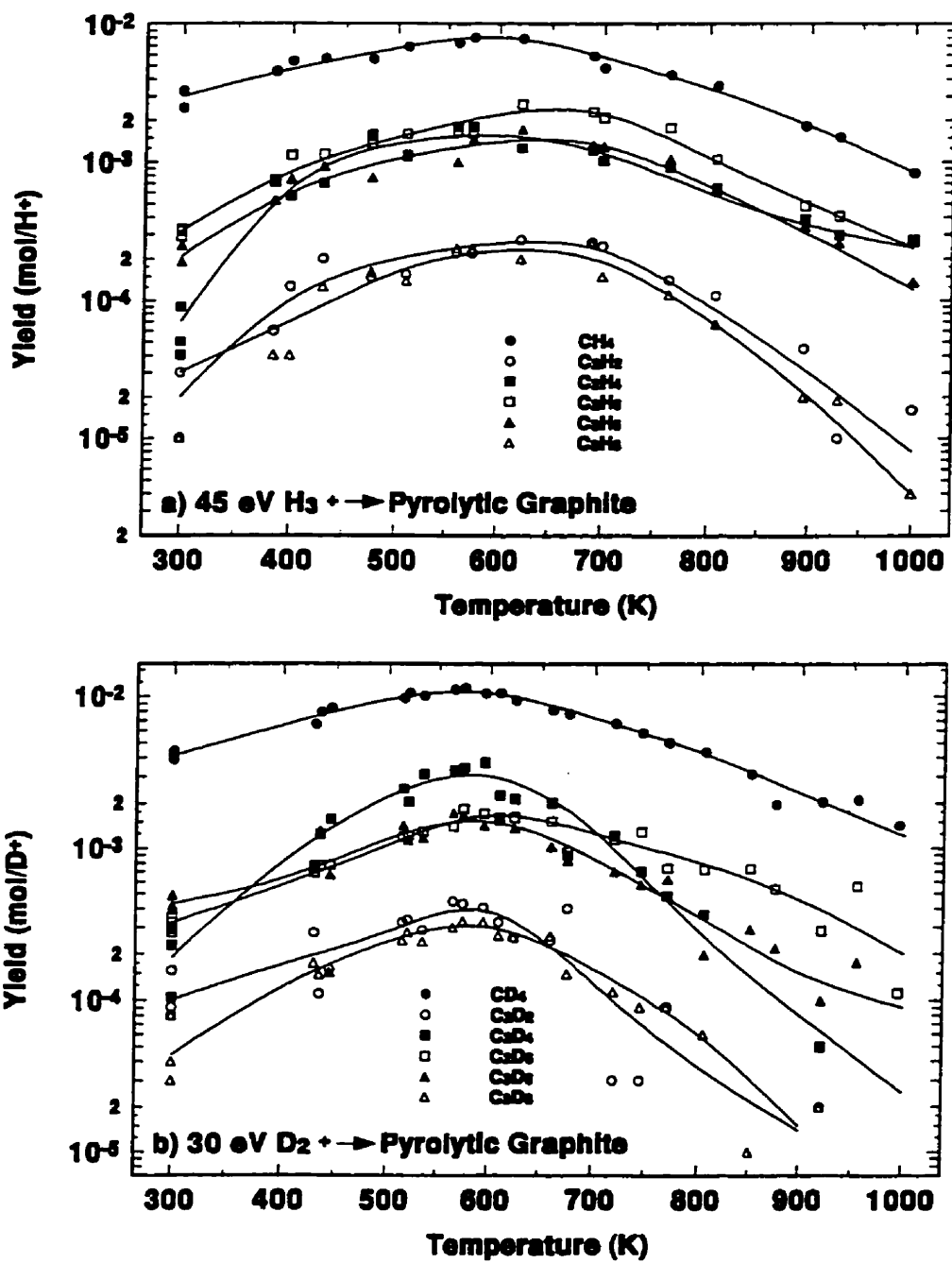


Figure 20: Hydrocarbon spectrum as a function of temperature for (a) 45 eV H_3^+ and (b) 30 eV D_2^+ impact on pyrolytic graphite. Spline curves are drawn to aid the reader.

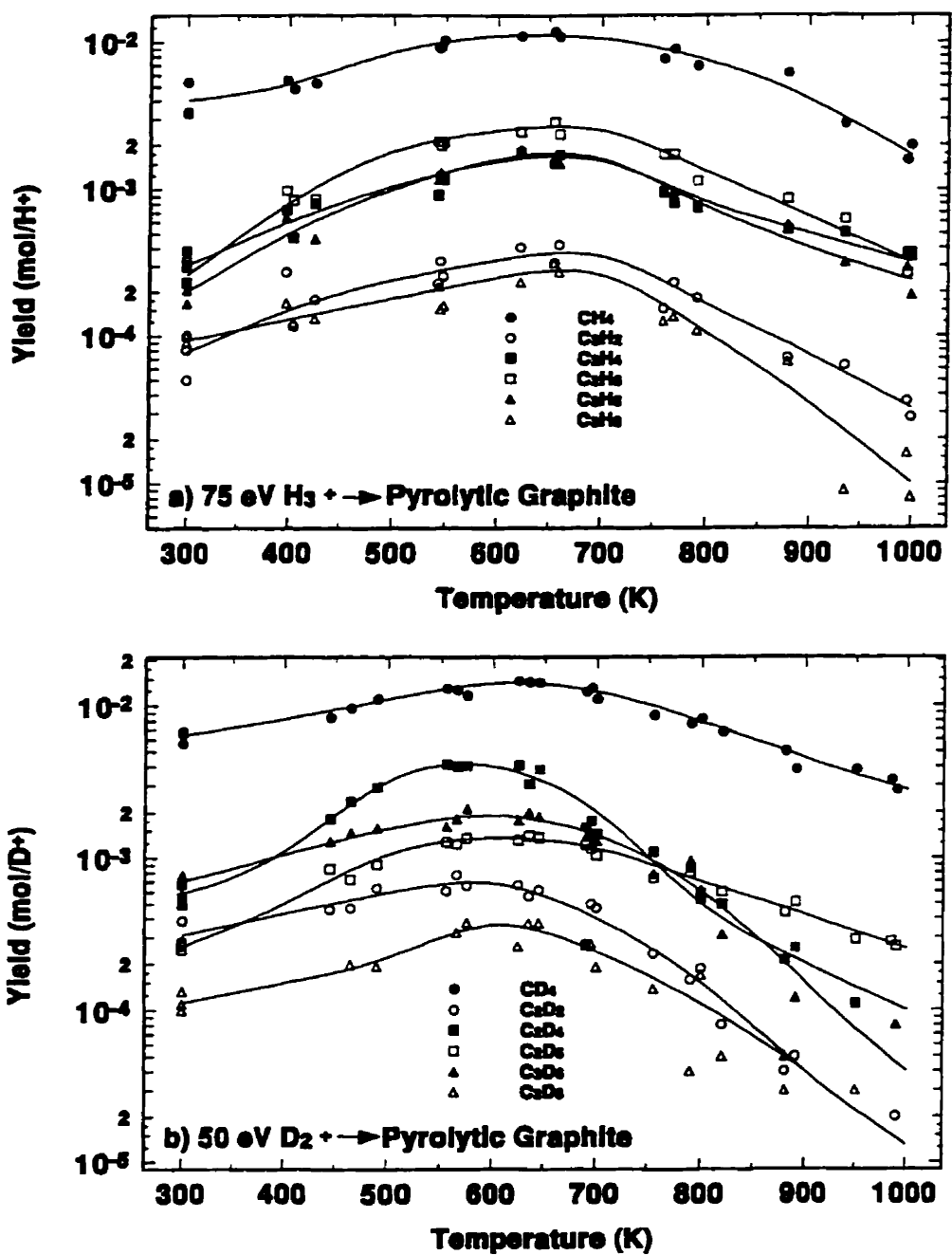


Figure 21: Hydrocarbon spectrum as a function of temperature for (a) 75 eV H_3^+ and (b) 50 eV D_2^+ impact on pyrolytic graphite. Spline curves are drawn to aid the reader.

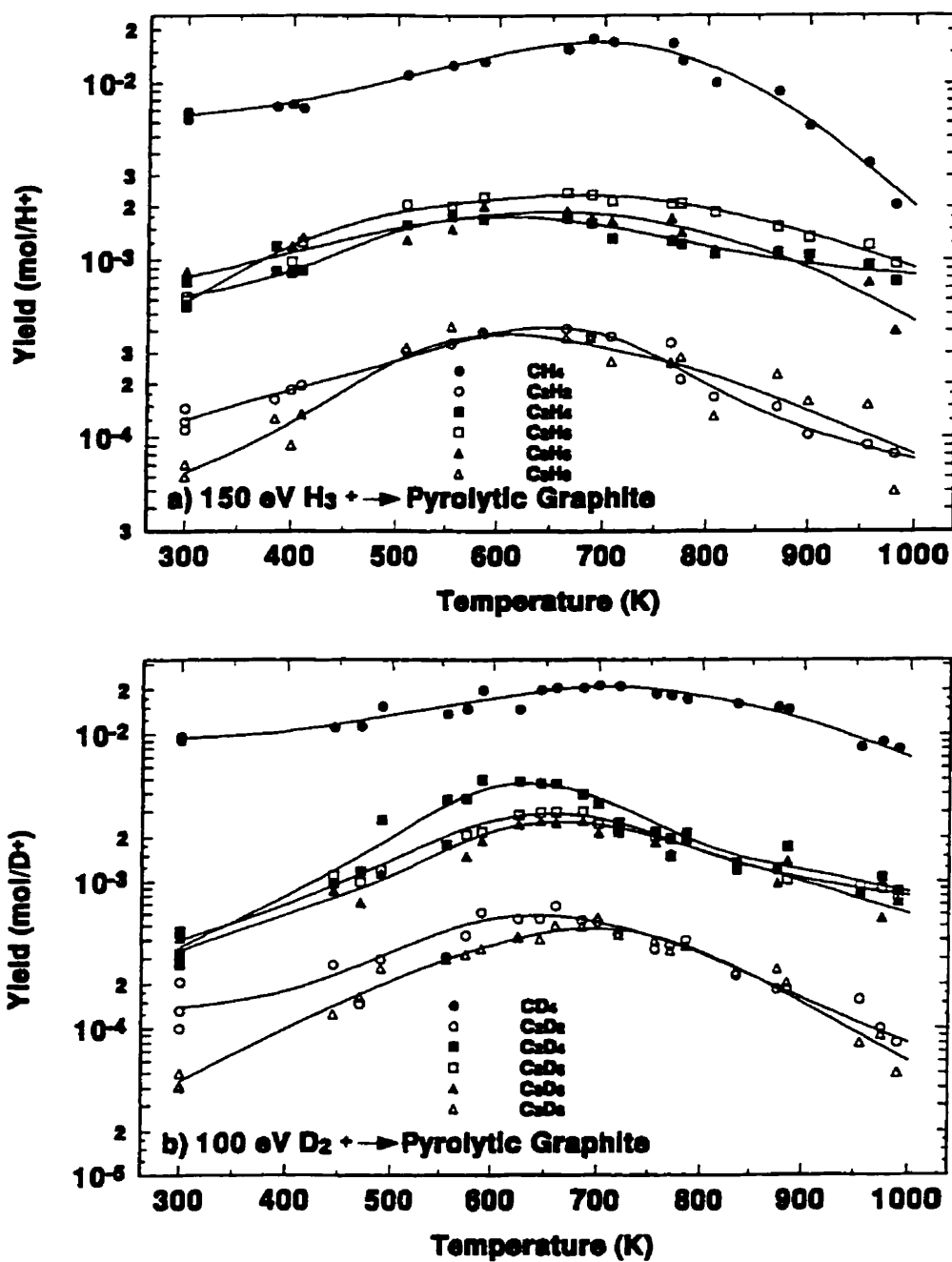


Figure 22: Hydrocarbon spectrum as a function of temperature for (a) 150 eV H_3^+ and (b) 100 eV D_2^+ impact on pyrolytic graphite. Spline curves are drawn to aid the reader.

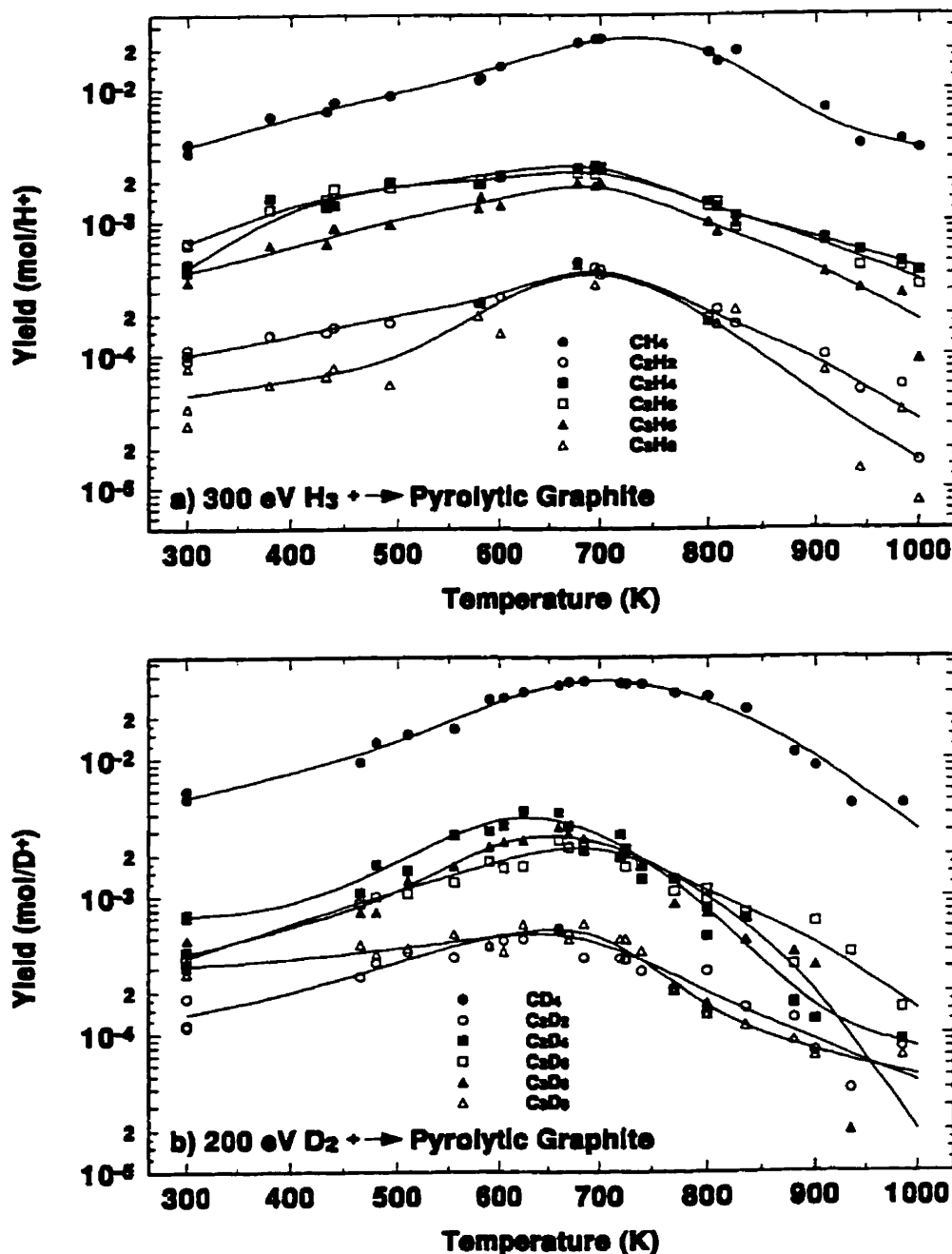


Figure 23: Hydrocarbon spectrum as a function of temperature for (a) 300 eV H_3^+ and (b) 200 eV D_2^+ impact on pyrolytic graphite. Spline curves are drawn to aid the reader.

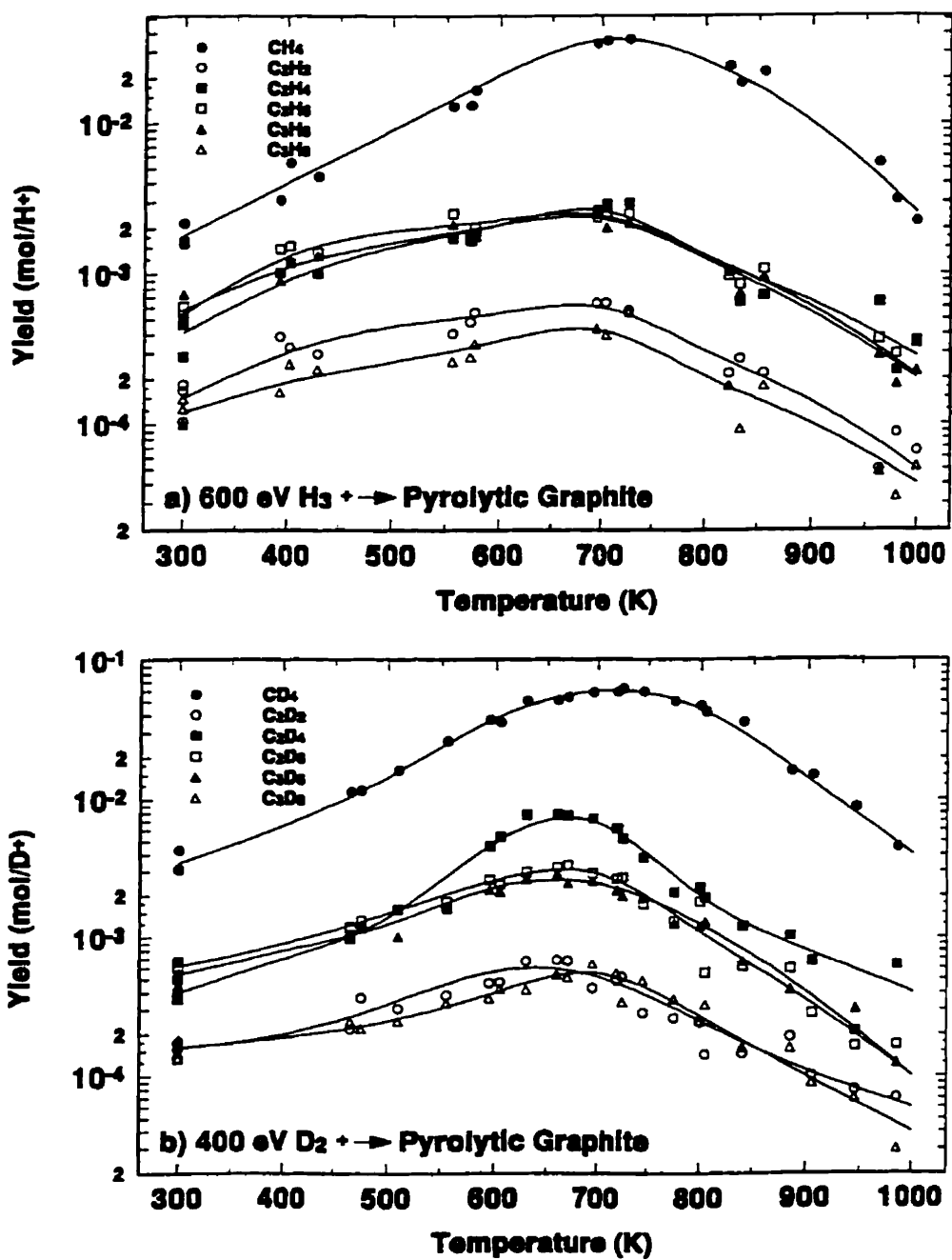


Figure 24: Hydrocarbon spectrum as a function of temperature for (a) 600 eV H_3^+ and (b) 400 eV D_2^+ impact on pyrolytic graphite. Spline curves are drawn to aid the reader.

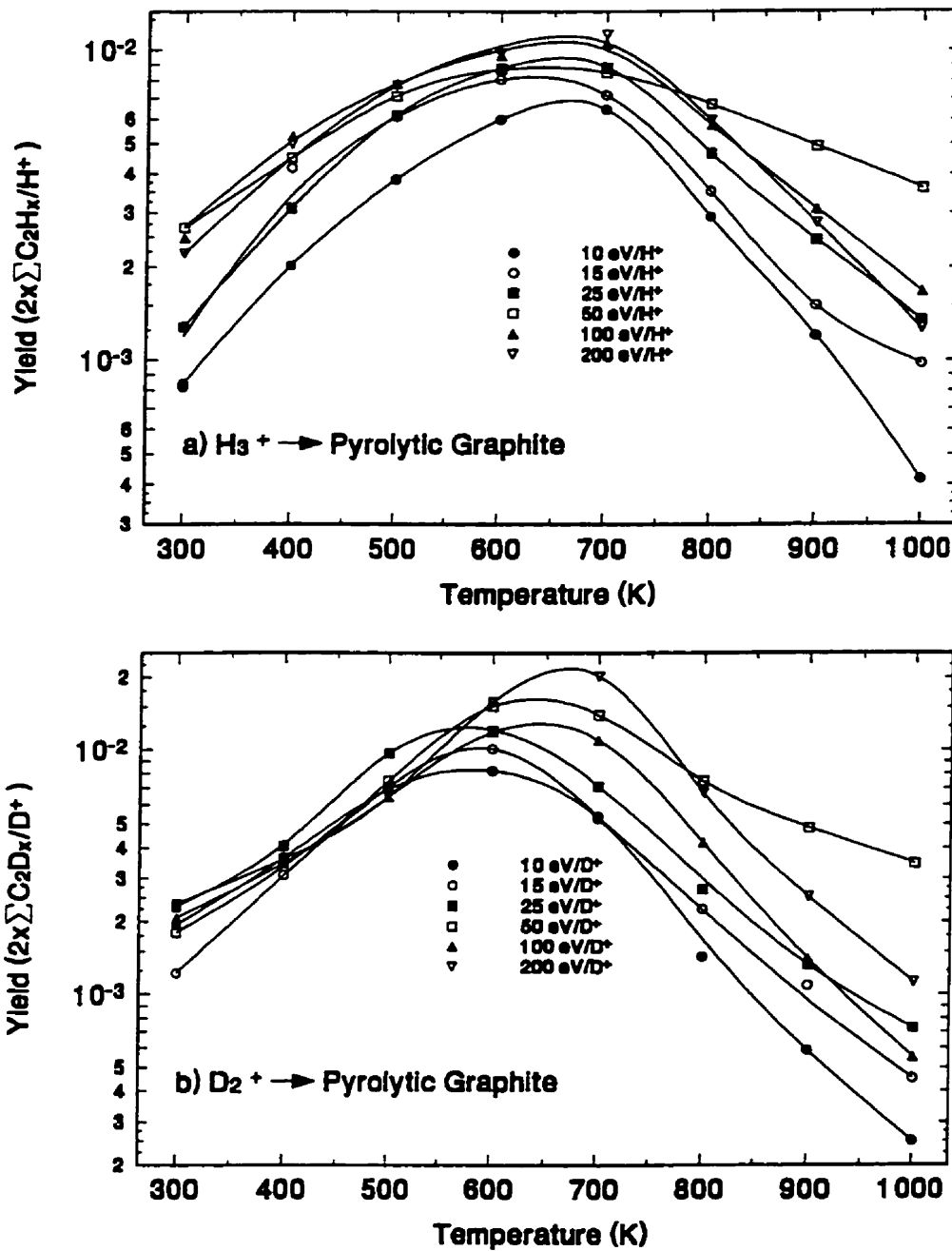


Figure 25: C_2 -containing hydrocarbon yield of pyrolytic graphite as a function of temperature for (a) H_3^+ and (b) D_2^+ impact at 10, 15, 25, 50, 100 and 200 eV/ion. The molecular yield is multiplied by the number of carbon atoms in the molecule (i.e. $2 \times \sum \text{C}_2\text{H}_x/\text{H}^+$). Data points are extracted from spline fits in figures 19 to 24. New spline curves are drawn to aid the reader.

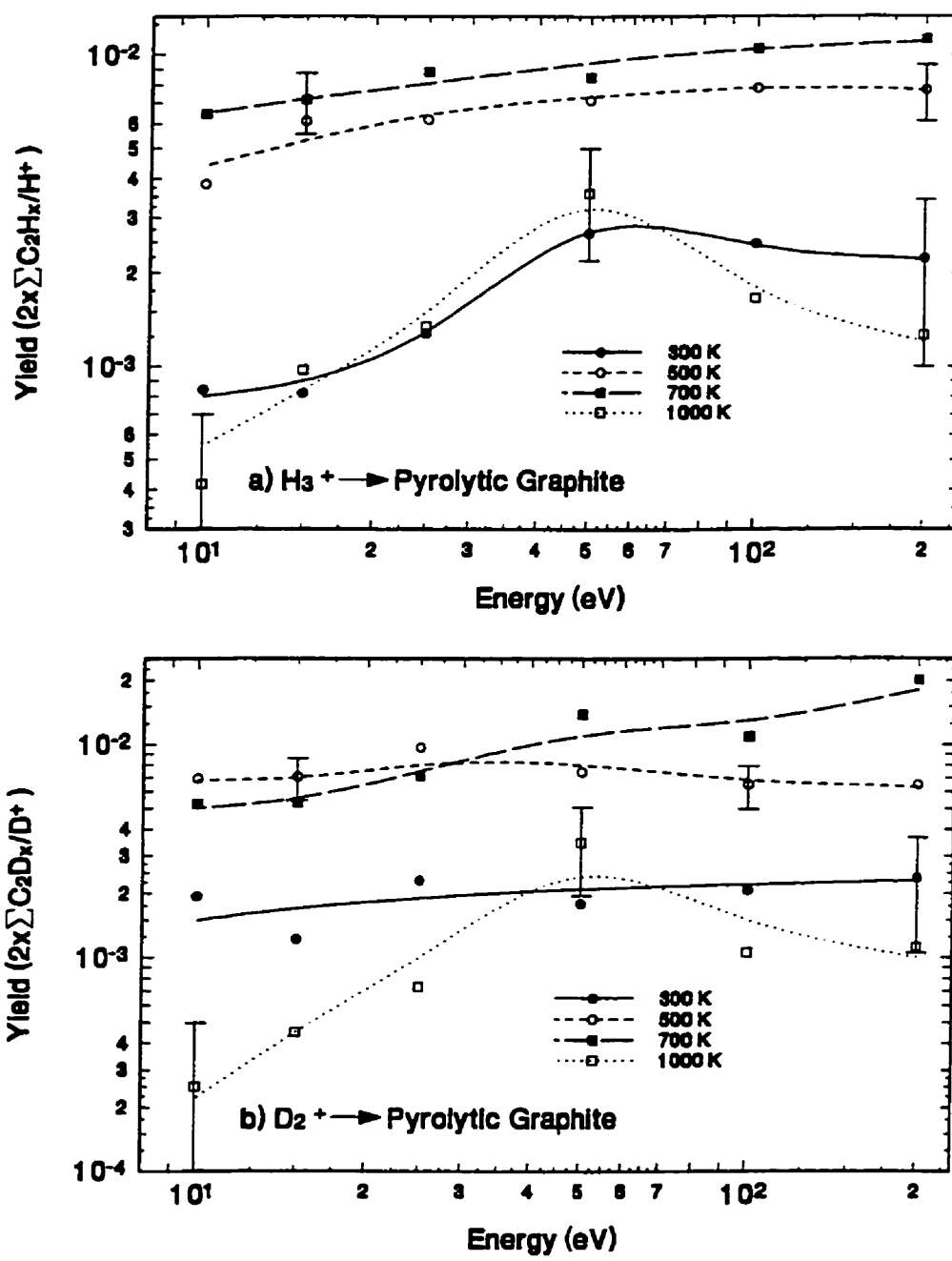


Figure 26: C_2 -containing hydrocarbon yield of pyrolytic graphite as a function of ion energy for (a) H_3^+ and (b) D_2^+ impact at 300, 500, 700 and 1000 K. The molecular yield is multiplied by the number of carbon atoms in the molecule (i.e. $2 \times \sum \text{C}_2\text{H}_x/\text{H}^+$). Data points are extracted from spline fits in figures 19 to 24. New spline curves are drawn to aid the reader.

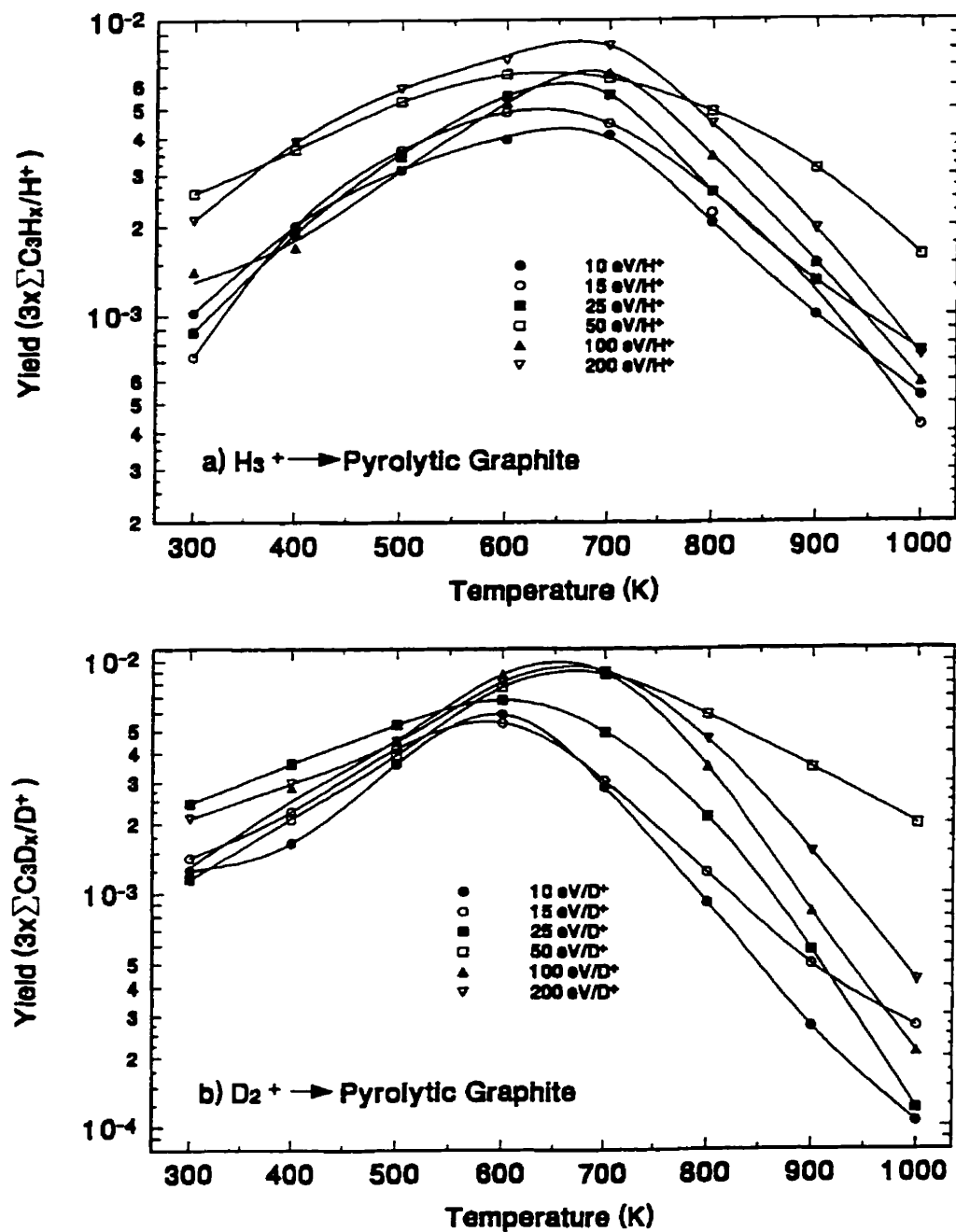


Figure 27: C₃-containing hydrocarbon yield of pyrolytic graphite as a function of temperature for (a) H₃⁺ and (b) D₂⁺ impact at 10, 15, 25, 50, 100 and 200 eV/ion. The molecular yield is multiplied by the number of carbon atoms in the molecule (i.e. 3×ΣC₃H_x/H⁺). Data points are extracted from spline fits in figures 19 to 24. New spline curves are drawn to aid the reader.

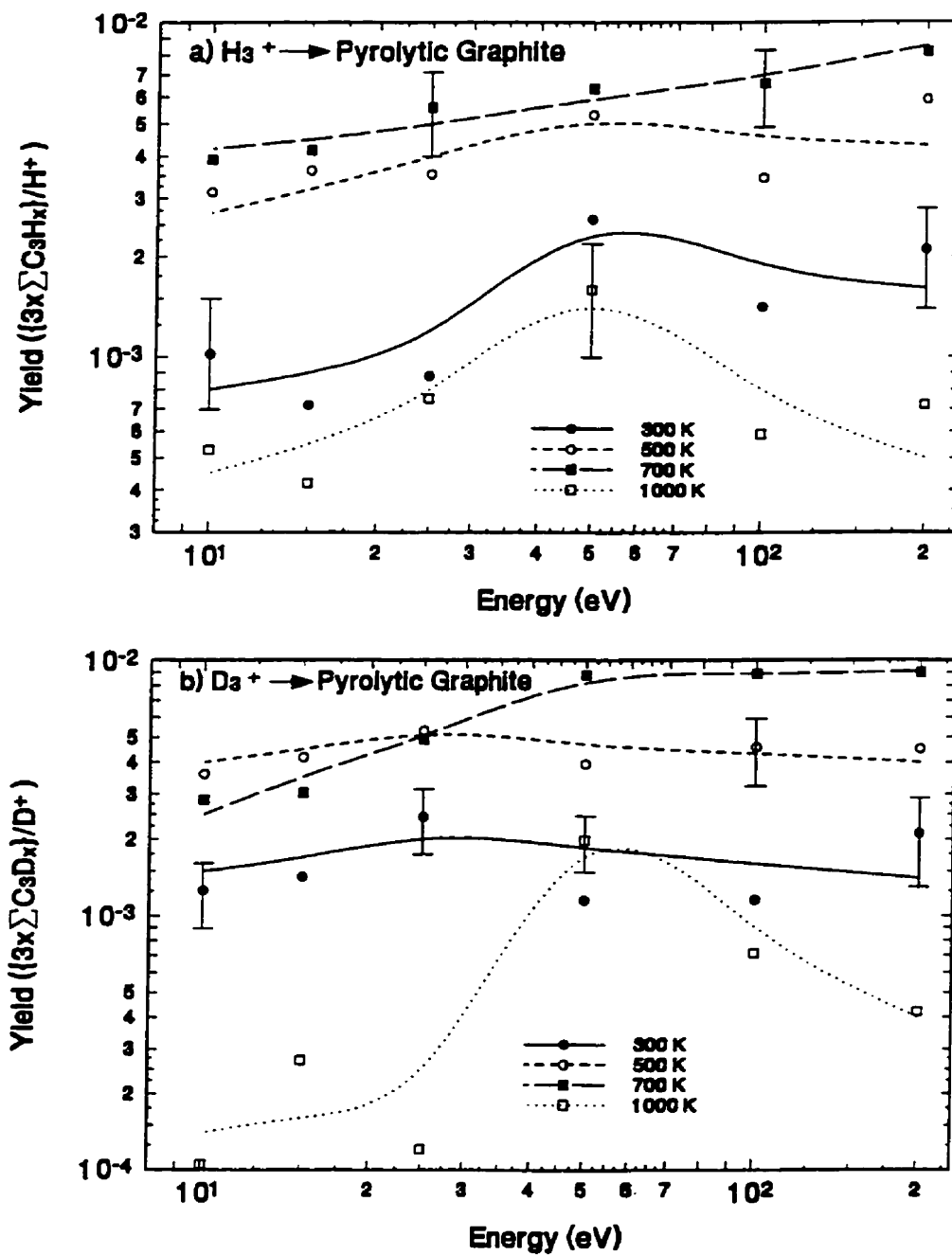


Figure 28: C₃-containing hydrocarbon yield of pyrolytic graphite as a function of ion energy for (a) H₃⁺ and (b) D₂⁺ impact at 300, 500, 700 and 1000 K. The molecular yield is multiplied by the number of carbon atoms in the molecule (i.e. $3 \times \sum C_3H_x/H^+$). Data points are extracted from spline fits in figures 19 to 24. New spline curves are drawn to aid the reader.

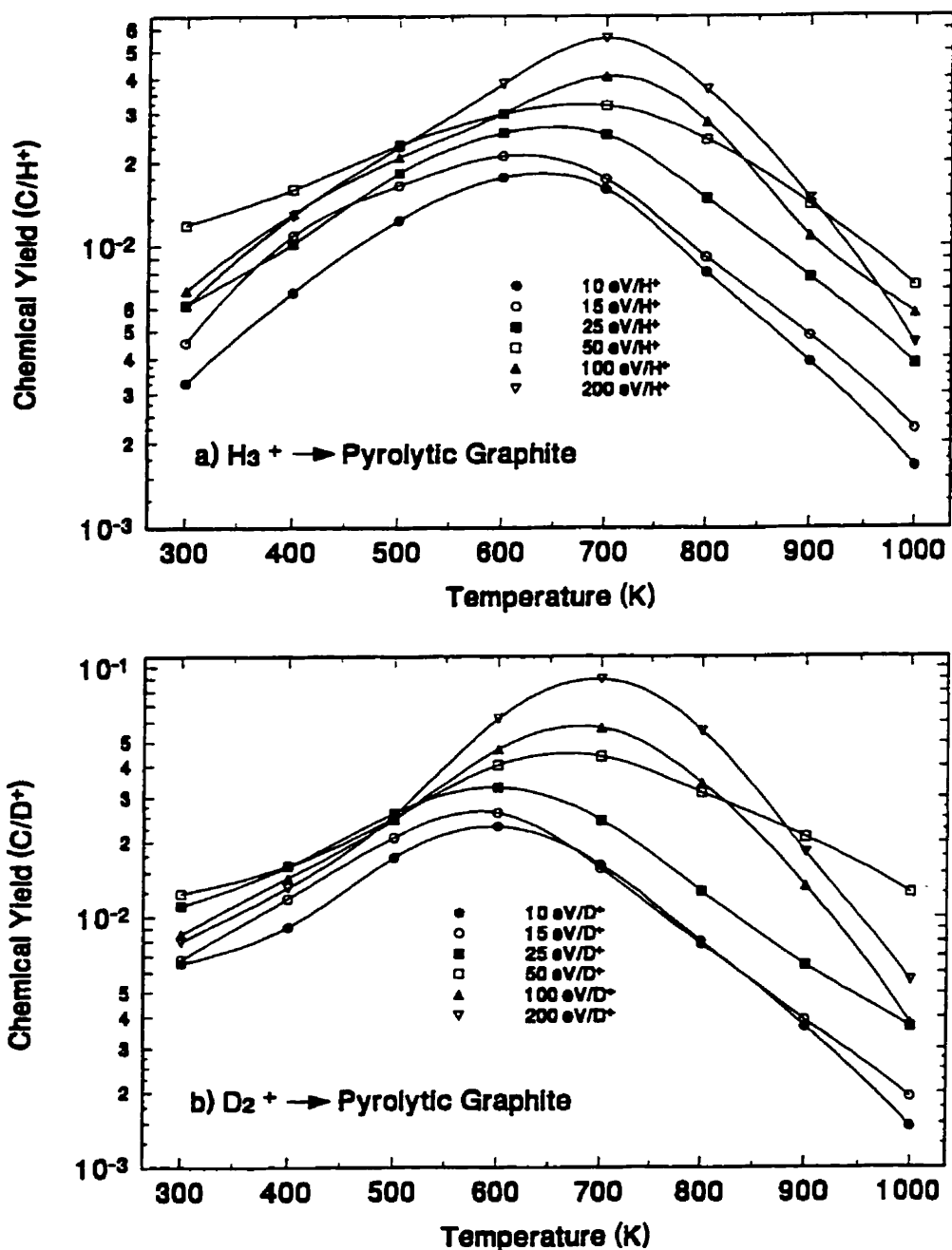


Figure 29: Total chemical yield (i.e. $[\text{CH}_4 + 2 \times \Sigma \text{C}_2\text{H}_x + 3 \times \Sigma \text{C}_3\text{H}_x]/\text{H}^+$) of pyrolytic graphite as a function of temperature for (a) H_3^+ and (b) D_2^+ impact at 10, 15, 25, 50, 100 and 200 eV/ion. The data points are the sum of the spline curves in figures 17, 25 and 27.

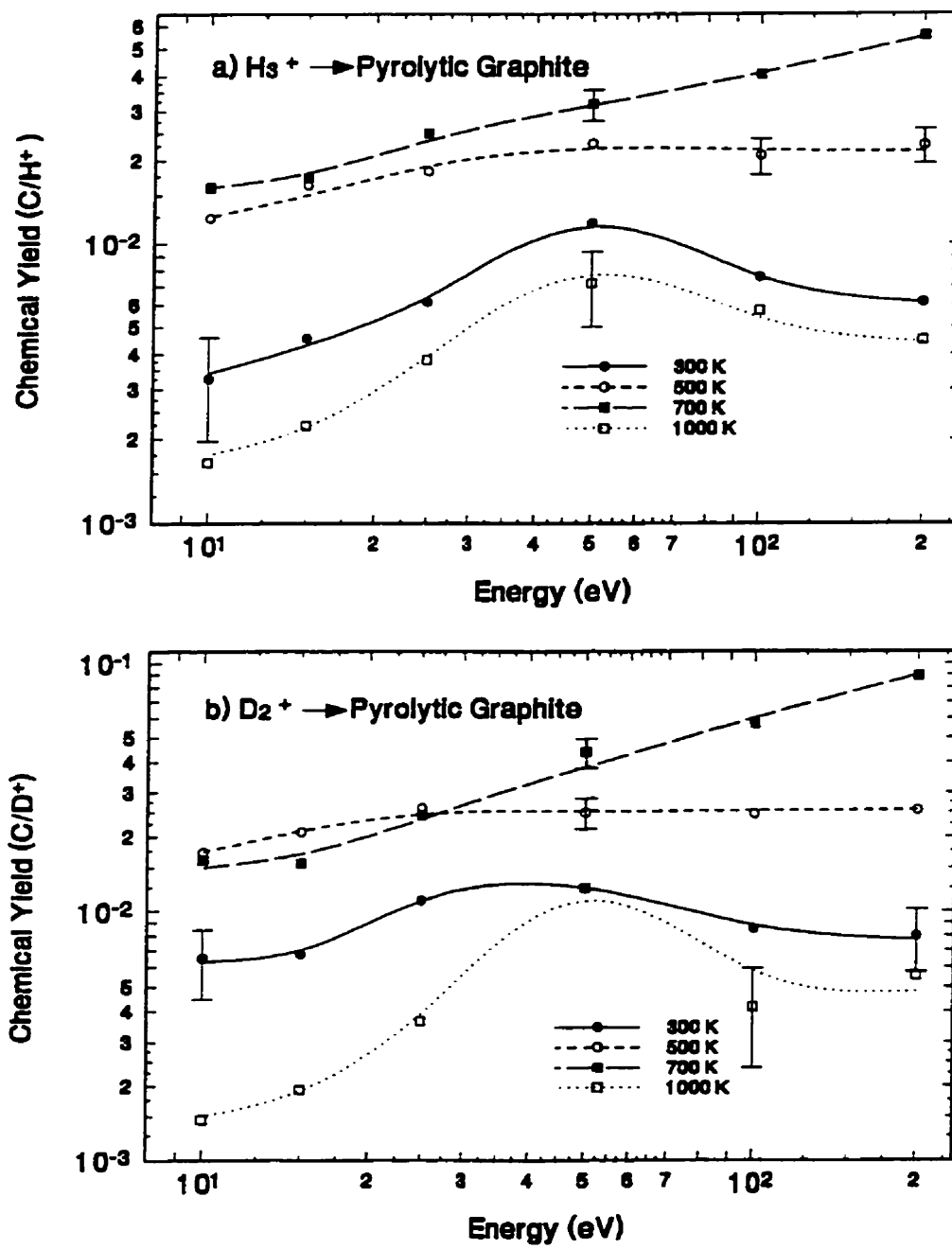


Figure 30: Total chemical yield of pyrolytic graphite as a function of ion energy for (a) H_3^+ and (b) D_2^+ impact at 300, 500, 700 and 1000 K. The data points are the sum of the data points shown in figures 18, 26 and 28.

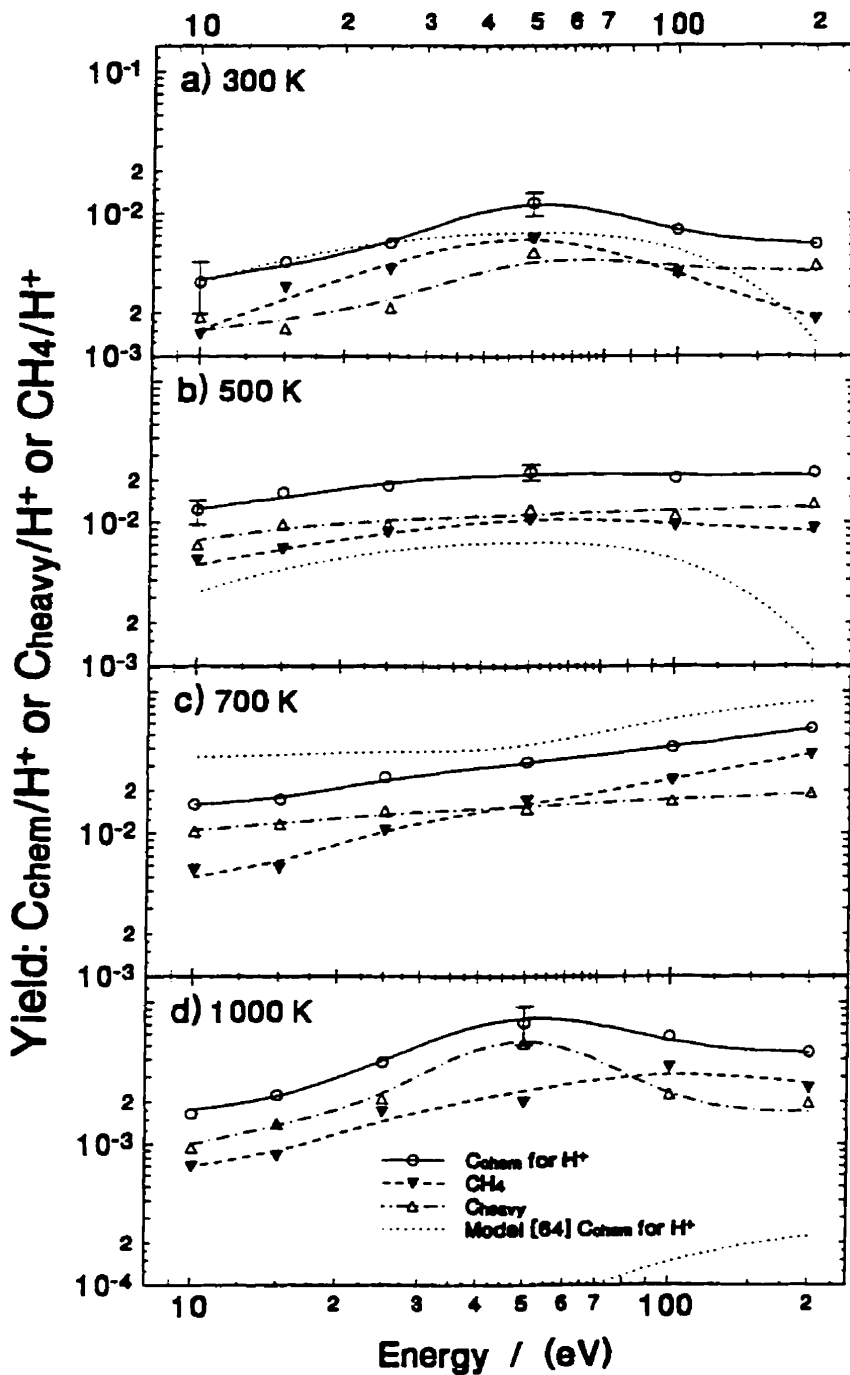


Figure 31: Methane, heavy hydrocarbon, and total chemical yields of pyrolytic graphite as a function of ion energy for H_3^+ impact at (a) 300 K, (b) 500 K, (c) 700 K and (d) 1000 K. The methane and total chemical yield curves are extracted from figures 17a and 29a, respectively. The heavy hydrocarbon yield is the difference between the total chemical and methane yields. In addition, the predictions of the RG-R model [64] for the total chemical yield at a flux of $10^{18} \text{ H}^+/\text{m}^2\text{s}$ are also included.

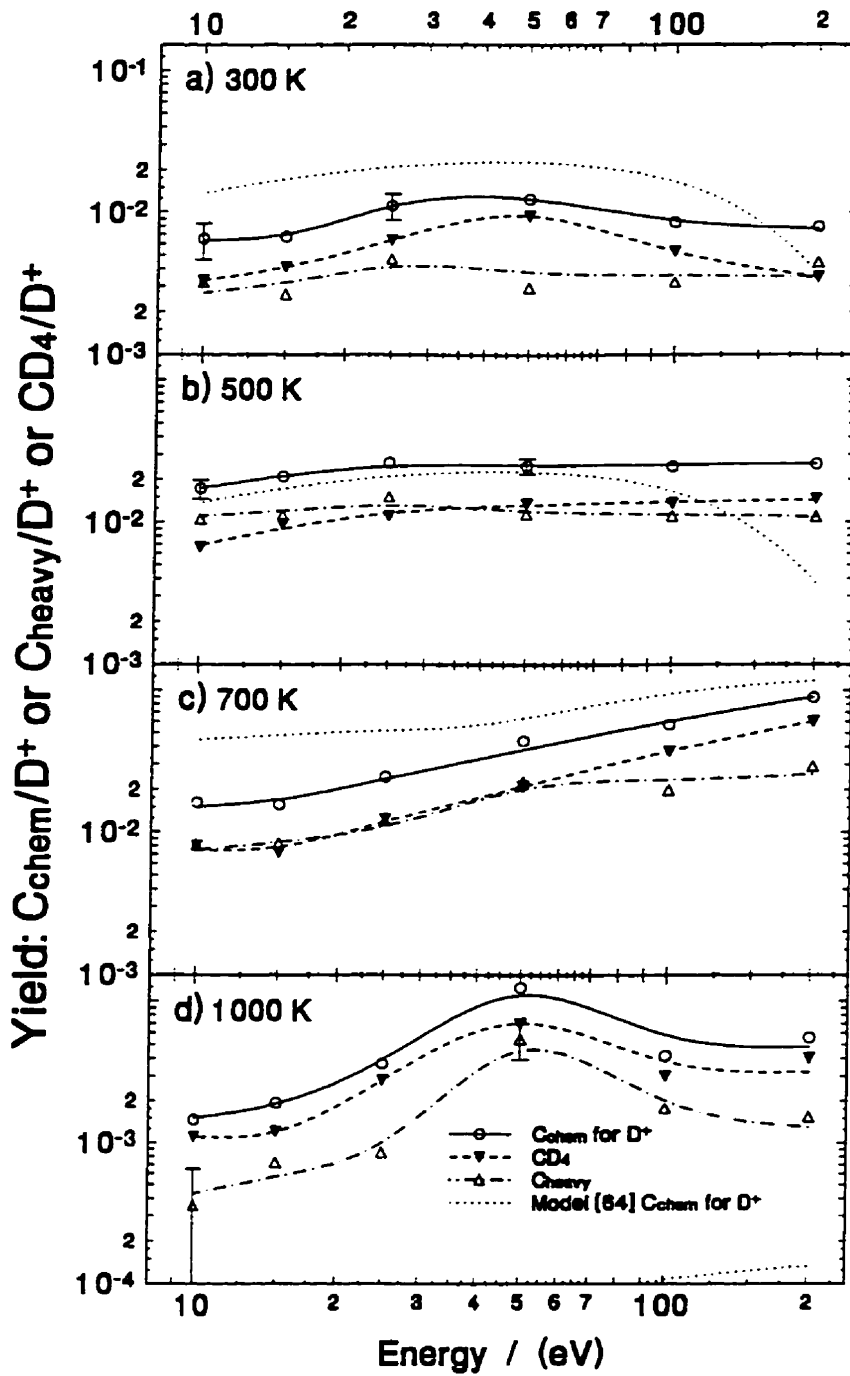


Figure 32: Methane, heavy hydrocarbon, and total chemical yields of pyrolytic graphite as a function of ion energy for D_2^+ impact at (a) 300 K, (b) 500 K, (c) 700 K and (d) 1000 K. The methane and total chemical yield curves are extracted from figures 17b and 29b, respectively. The heavy hydrocarbon yield is the difference between the total chemical and methane yields. In addition, the predictions of the RG-R model [64] for the total chemical yield at a flux of $10^{18} D^+/m^2 s$ are also included.

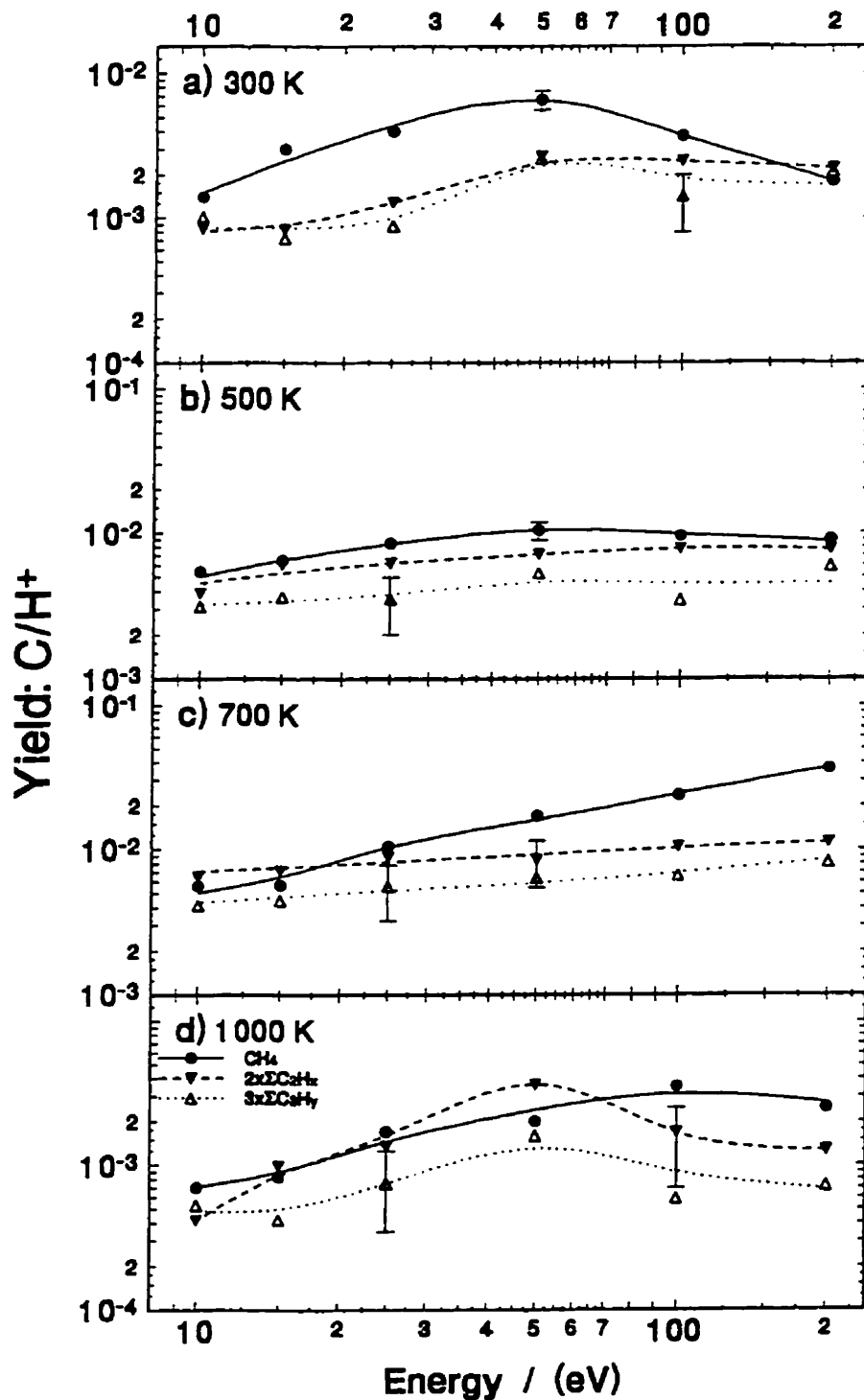


Figure 33: Methane, C_2 - and C_3 - hydrocarbon yields of pyrolytic graphite as a function of ion energy for H_3^+ impact at (a) 300 K, (b) 500 K, (c) 700 K and (d) 1000 K. The methane curves are extracted from figure 18a. The C_2 and C_3 curves are taken from figures 26a and 28a, respectively.

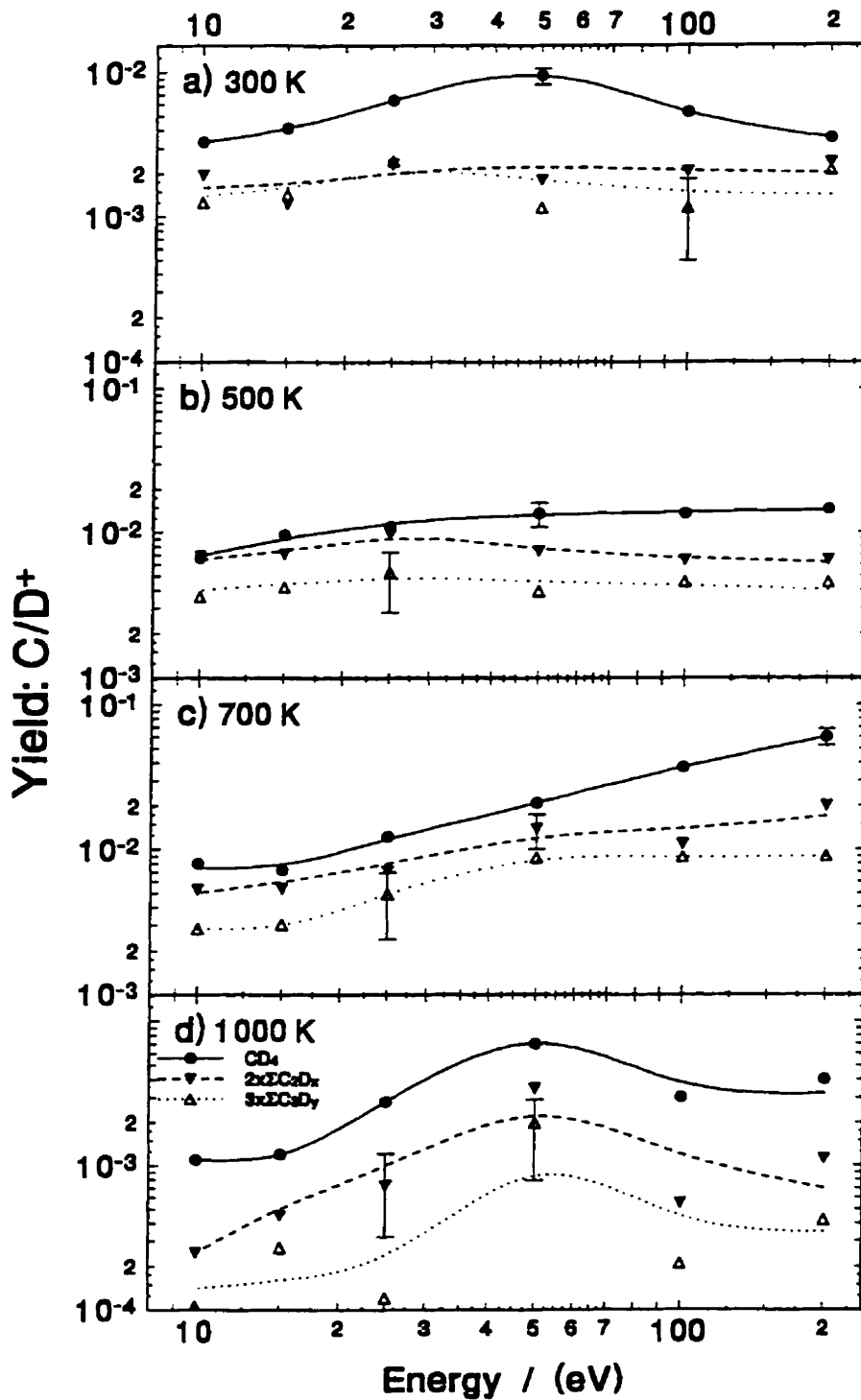


Figure 34: Methane, C₂- and C₃- hydrocarbon yields of pyrolytic graphite as a function of ion energy for D₂⁺ impact at (a) 300 K, (b) 500 K, (c) 700 K and (d) 1000 K. The methane curves are extracted from figure 18b. The C₂ and C₃ curves are taken from figures 26b and 28b, respectively.

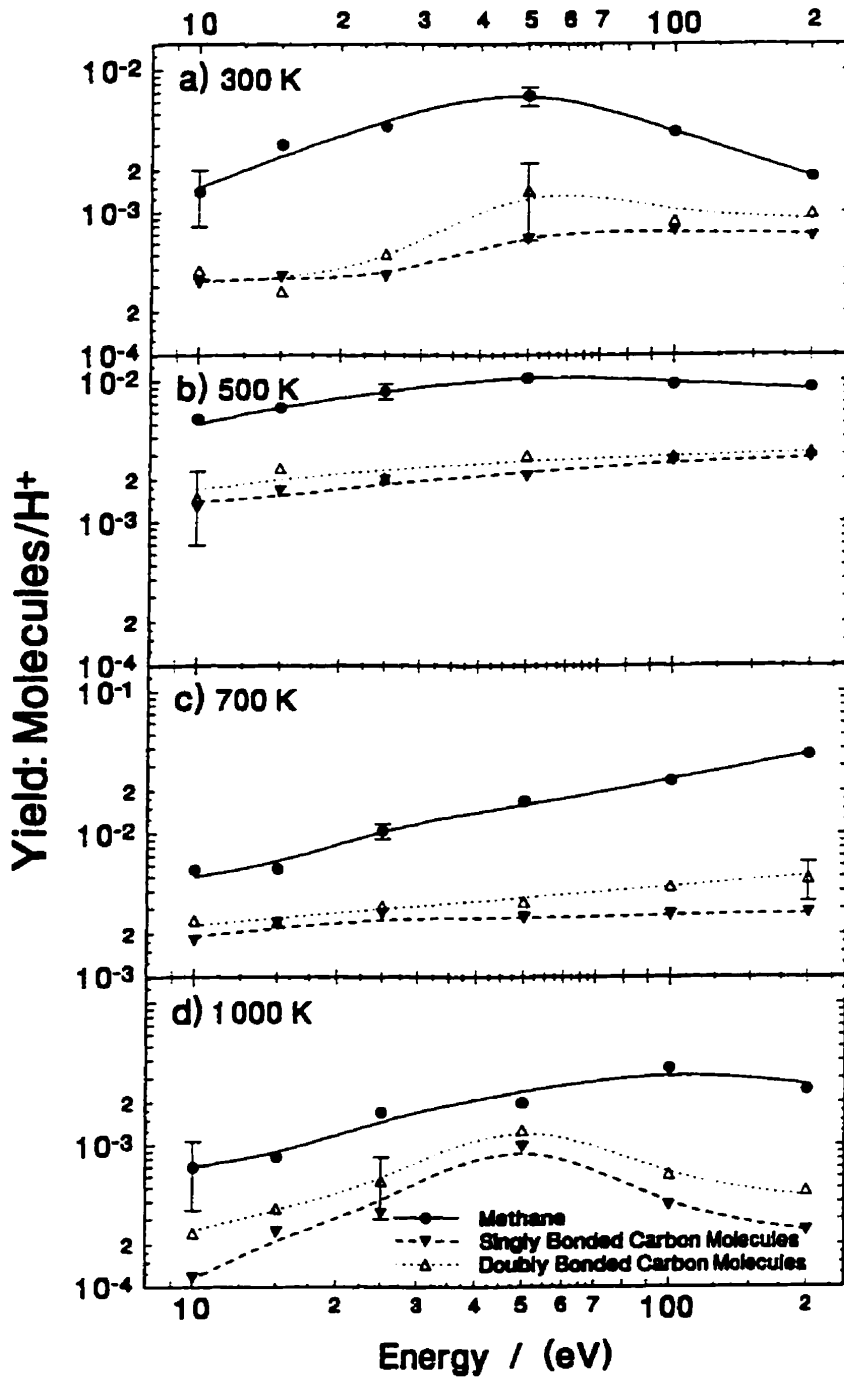


Figure 35: Molecular yields, defined by type of carbon-carbon bond, of pyrolytic graphite as a function of ion energy for H_3^+ impact at (a) 300 K, (b) 500 K, (c) 700 K and (d) 1000 K. The methane curves are extracted from figure 18a. The data points for the singly and doubly bonded carbon atoms are taken from the spline fits to the spectral data in figures 19a to 24a. The sums are linear and are not multiplied by the number of carbon atoms in the molecule. C_2H_6 and C_3H_8 represent the singly bonded carbon molecules while C_2H_4 and C_3H_6 are counted among the doubly bonded carbon molecules even though the latter contains one single and one double C-C bond.

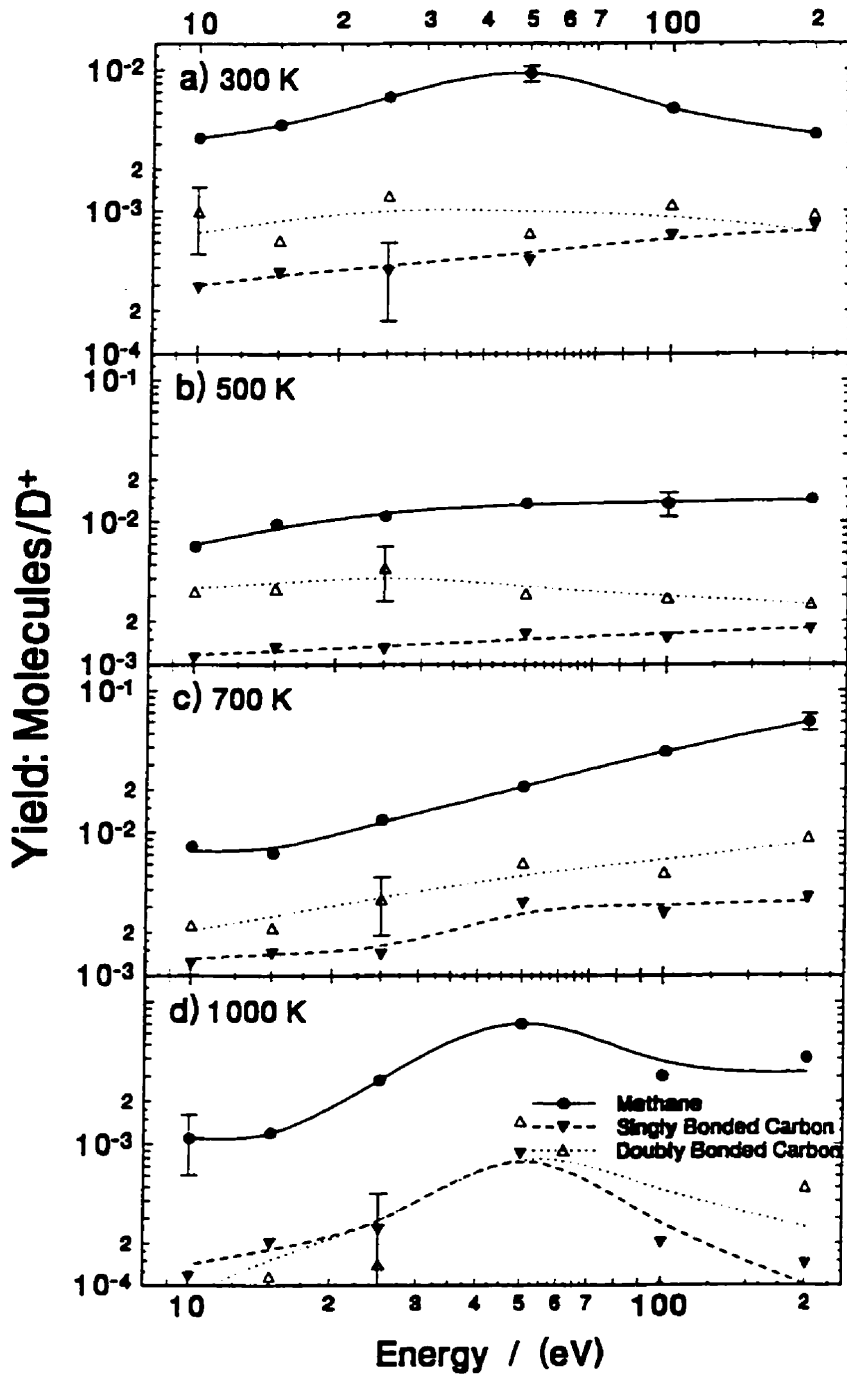


Figure 36: Molecular yields, defined by type of carbon-carbon bond, of pyrolytic graphite as a function of ion energy for D₂⁺ impact at (a) 300 K, (b) 500 K, (c) 700 K and (d) 1000 K. The methane curves are extracted from figure 18b. The data points for the singly and doubly bonded carbon atoms are taken from the spline fits to the spectral data in figures 19b to 24b. The sums are linear and are not multiplied by the number of carbon atoms in the molecule. C₂D₆ and C₃D₈ represent the singly bonded carbon molecules while C₂D₄ and C₃D₆ are counted among the doubly bonded carbon molecules even though the latter contains one single and one double C-C bond.

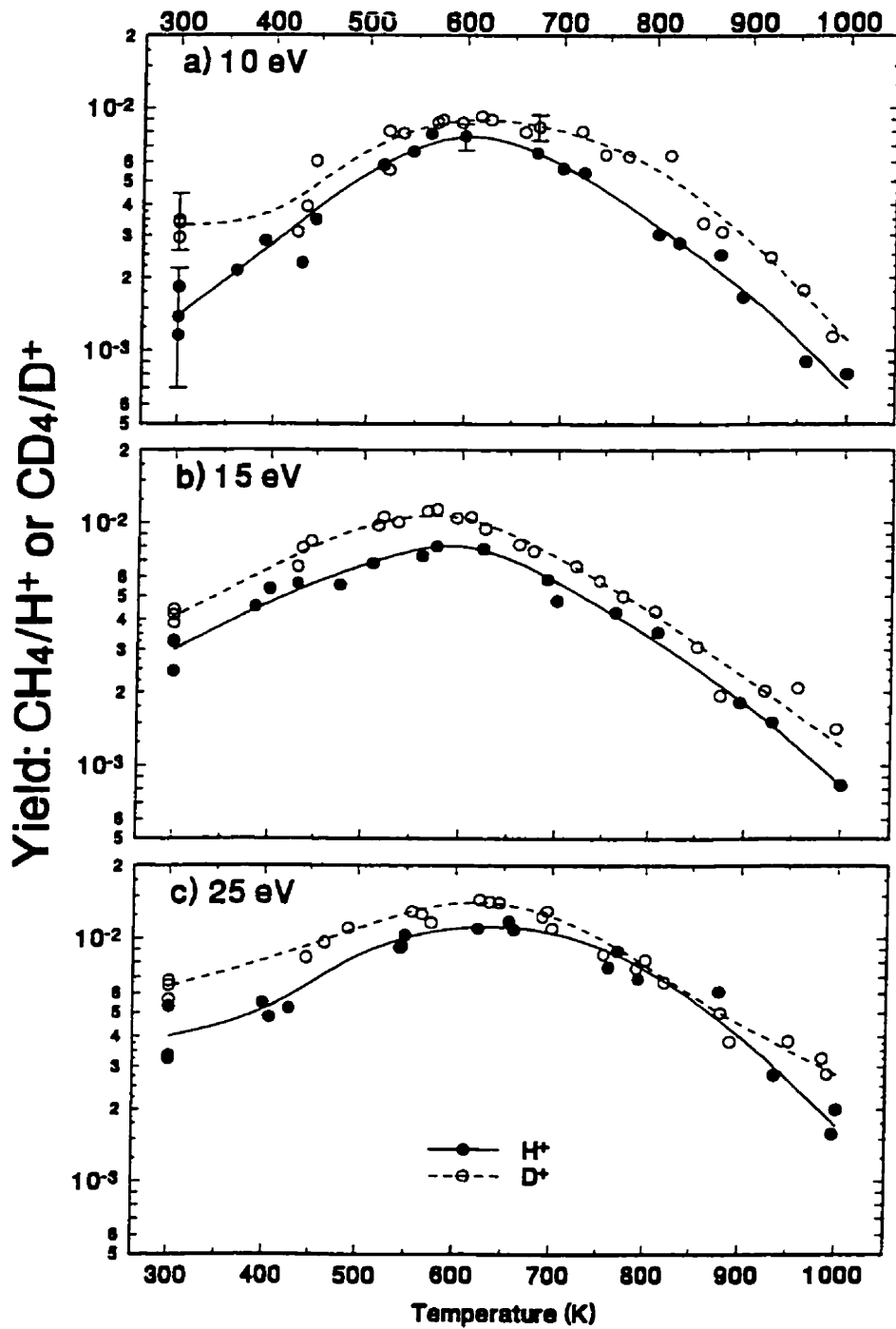


Figure 37: Isotopic comparison of the methane yield of pyrolytic graphite as a function of temperature for ion impact at (a) 10, (b) 15 and (c) 25 eV/ion. The data and curves are taken from figure 17.

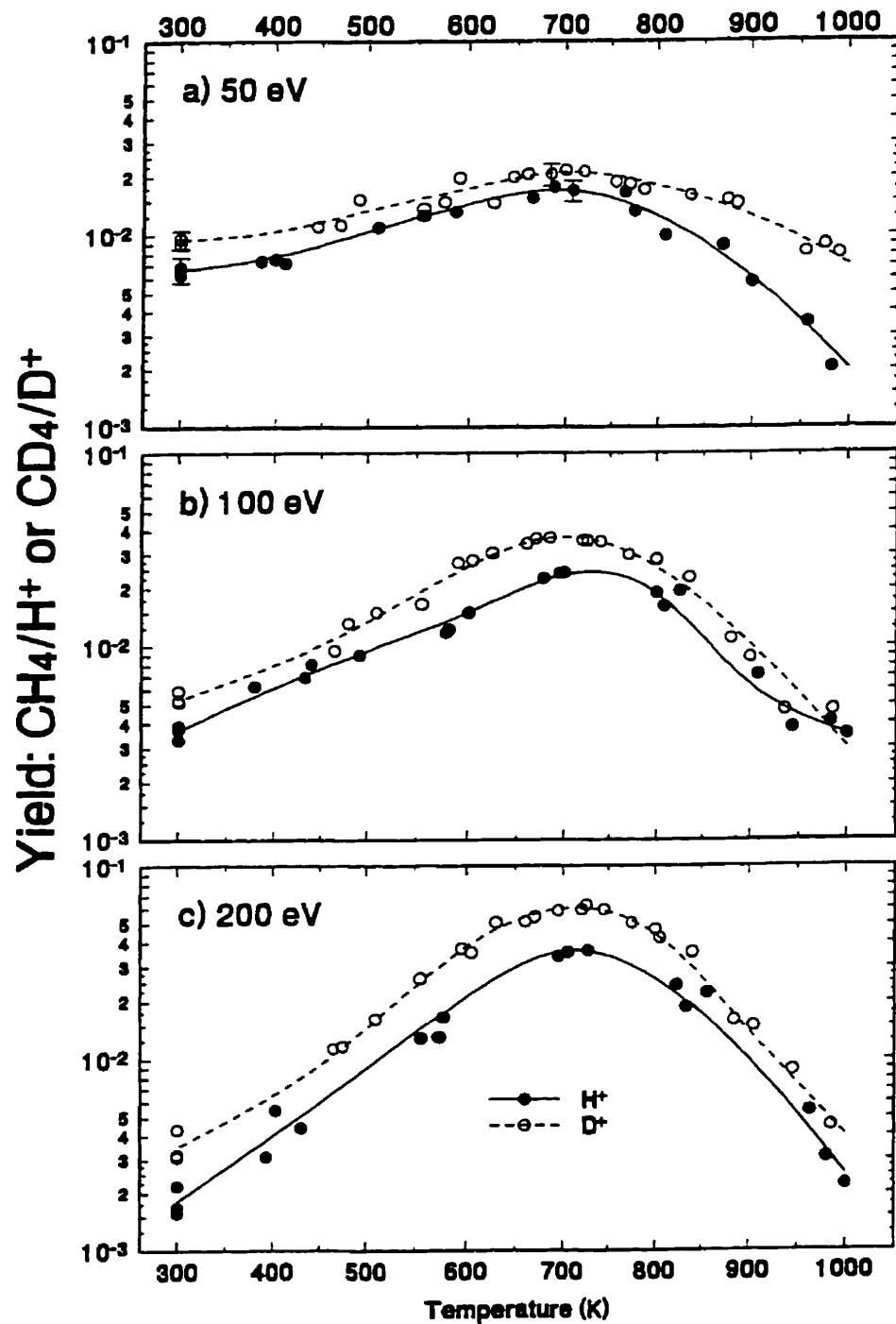


Figure 38: Isotopic comparison of the methane yield of pyrolytic graphite as a function of temperature for ion impact at (a) 50, (b) 100 and (c) 200 eV/ion. The data and curves are taken from figure 17.

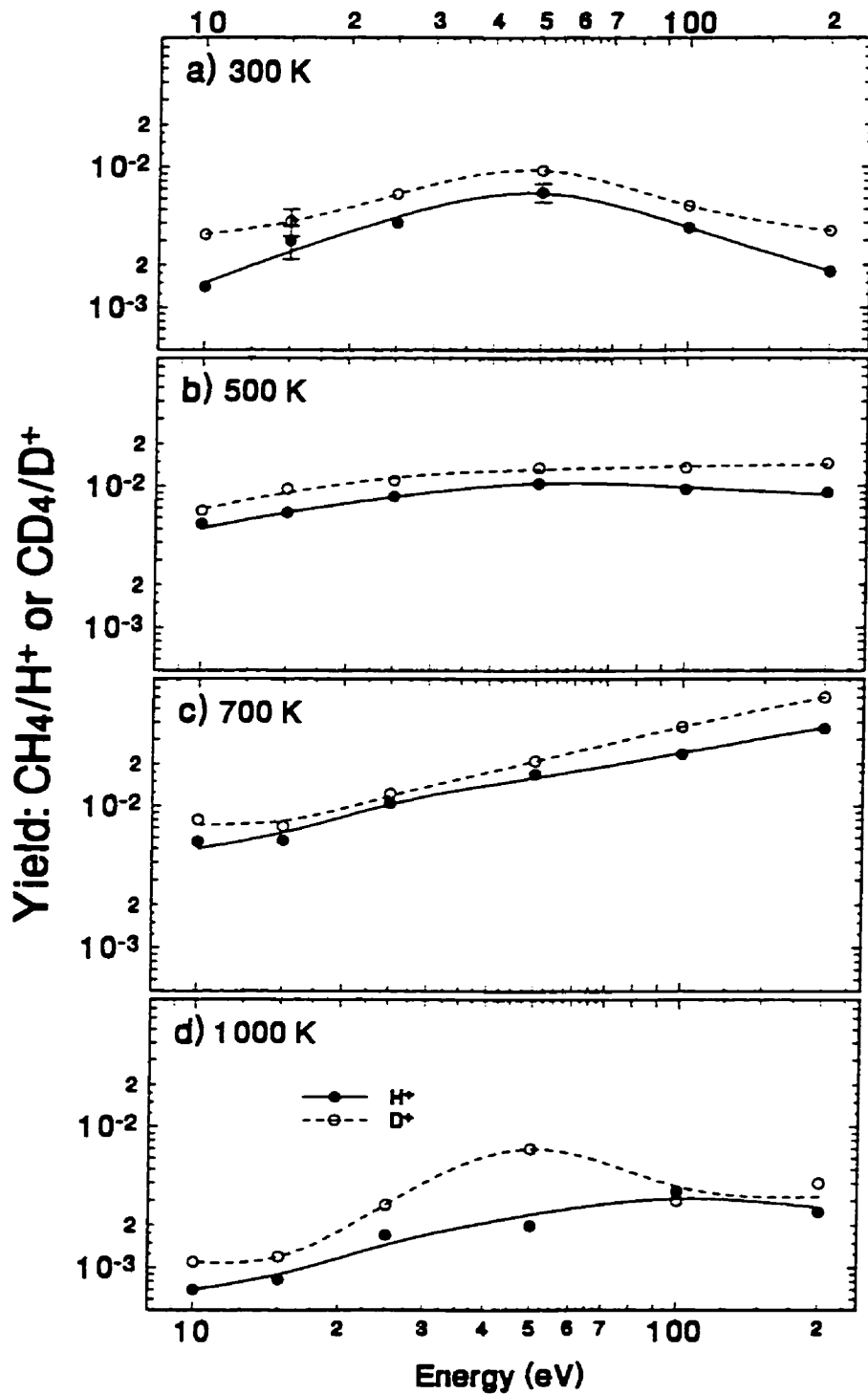


Figure 39: Isotopic comparison of the methane yield of pyrolytic graphite as a function of energy for ion impact at (a) 300 K, (b) 500 K, (c) 700 K and (d) 1000 K. The data and curves are taken from figure 18.

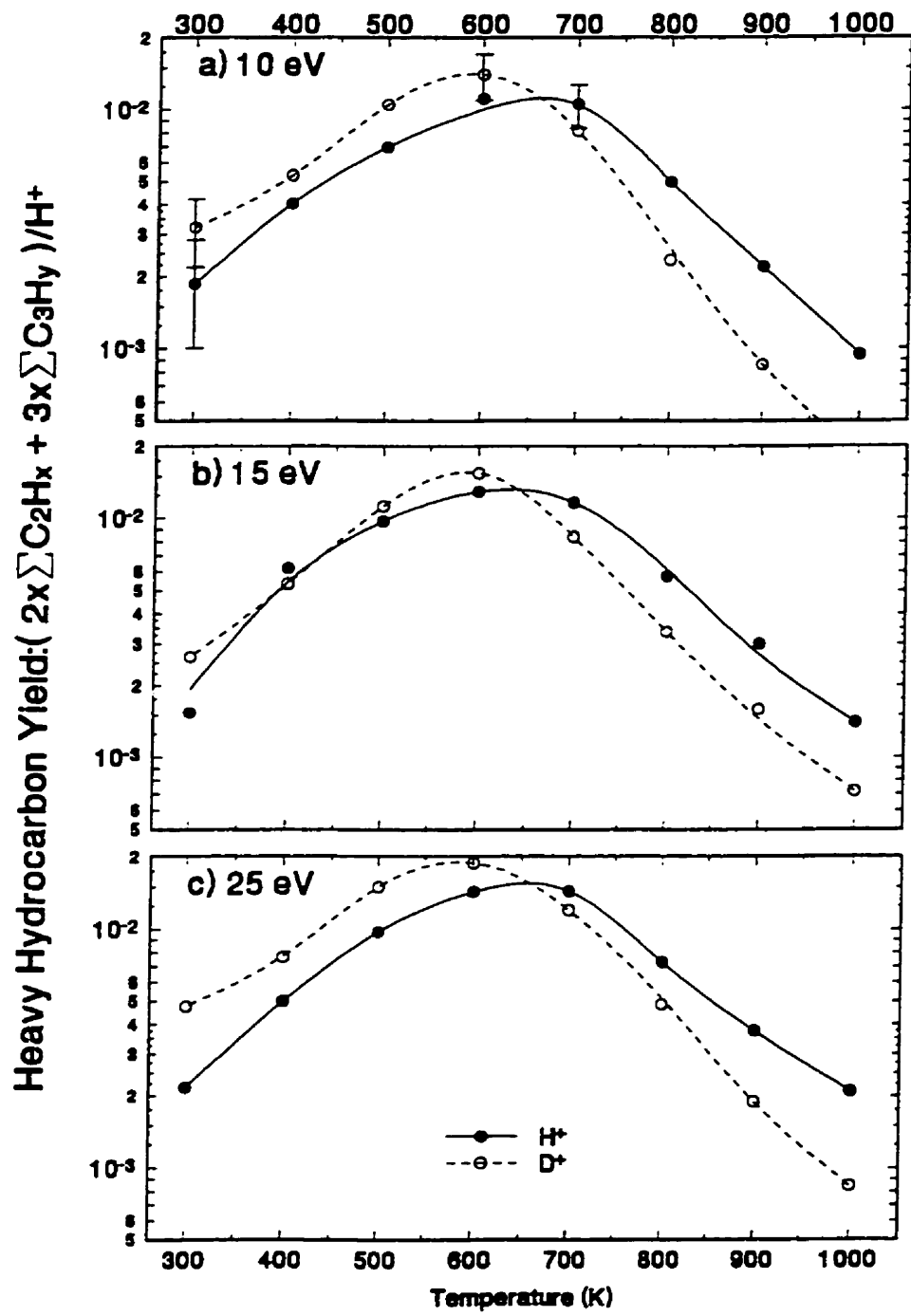


Figure 40: Isotopic comparison of the heavy hydrocarbon yield of pyrolytic graphite as a function of temperature for ion impact at (a) 10, (b) 15 and (c) 25 eV/ion. The data and curves are taken from figures 25 and 27.

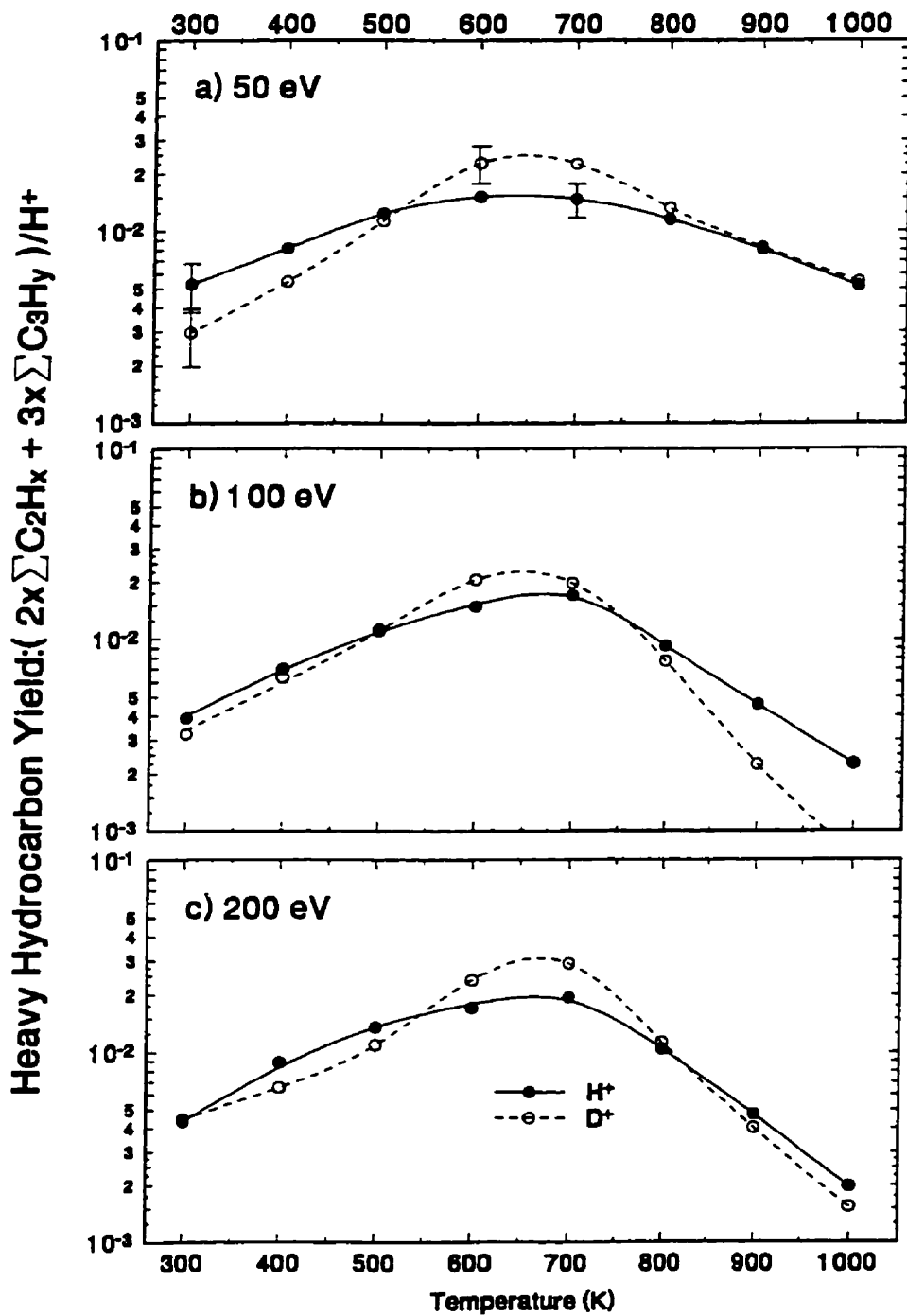


Figure 41: Isotopic comparison of the heavy hydrocarbon yield of pyrolytic graphite as a function of temperature for ion impact at (a) 50, (b) 100 and (c) 200 eV/ion. The data and curves are taken from figures 25 and 27.

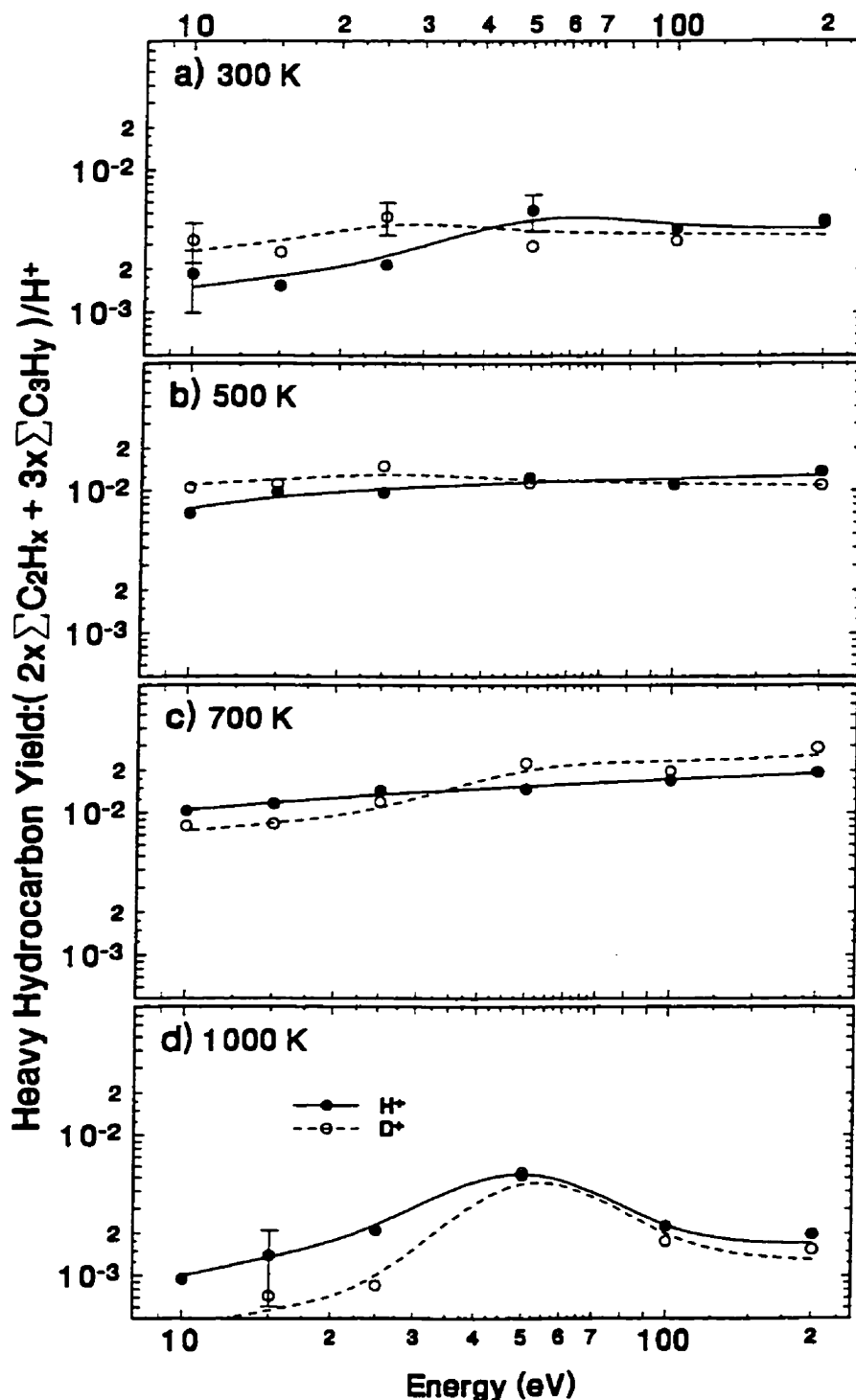


Figure 42: Isotopic comparison of the heavy hydrocarbon yield of pyrolytic graphite as a function of energy for ion impact at (a) 300 K, (b) 500 K, (c) 700 K and (d) 1000 K. The data and curves are taken from figures 31 for H^+ impact and 32 for D^+ impact.

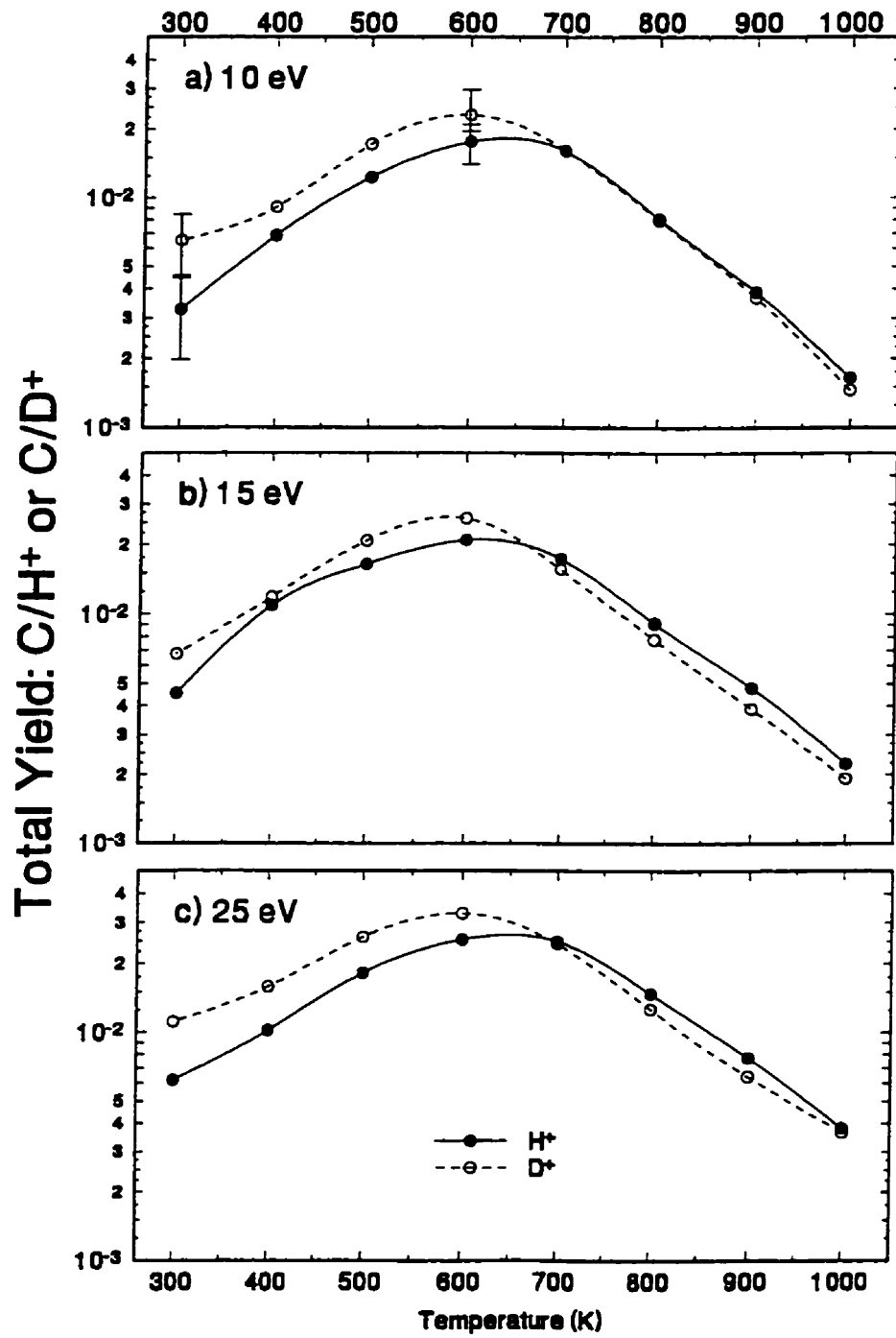


Figure 43: Isotopic comparison of the total chemical yield of pyrolytic graphite as a function of temperature for ion impact at (a) 10, (b) 15 and (c) 25 eV/ion. The data and curves are taken from figure 29.

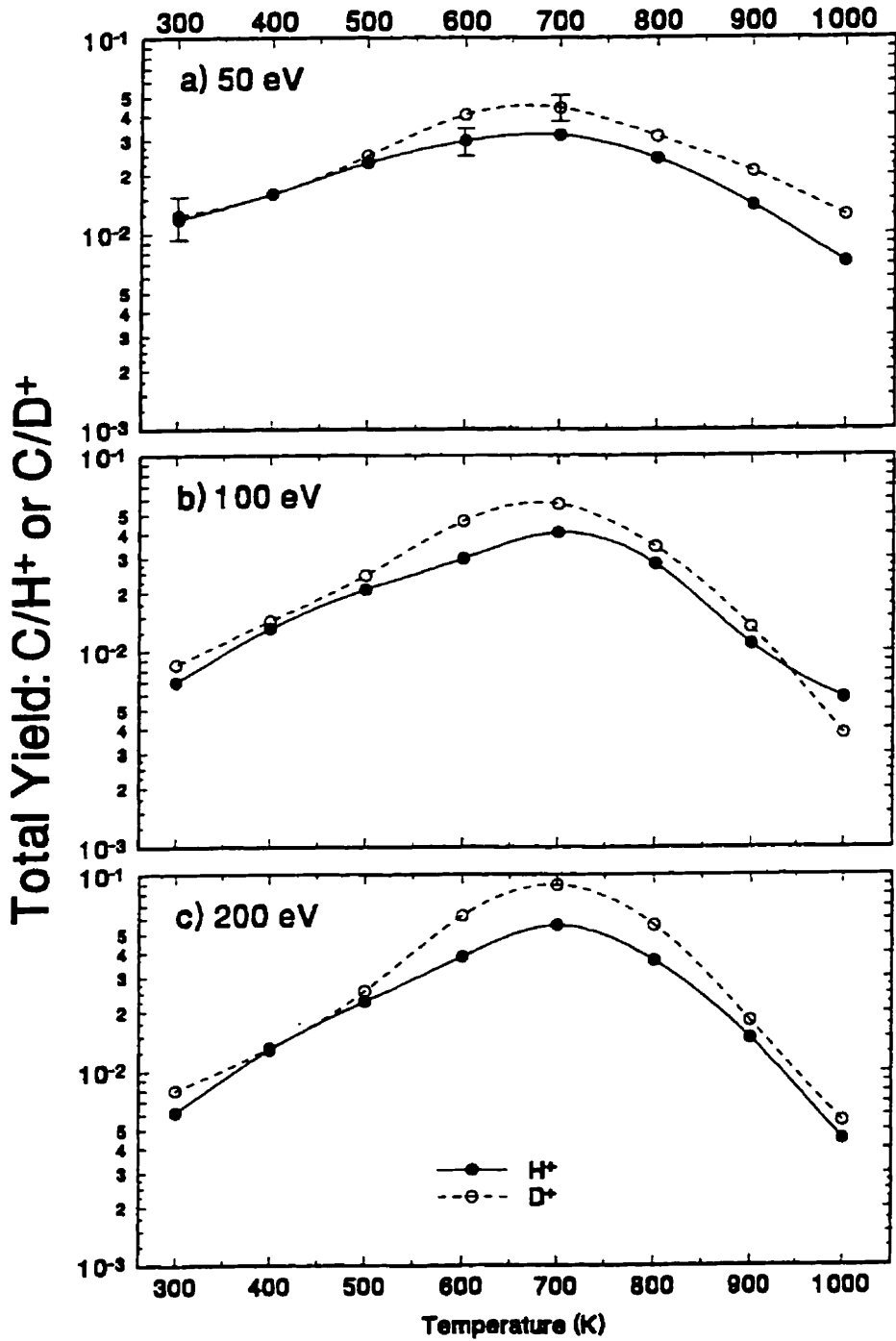


Figure 44: Isotopic comparison of the total chemical yield of pyrolytic graphite as a function of temperature for ion impact at (a) 50, (b) 100 and (c) 200 eV/ion. The data and curves are taken from figure 29.

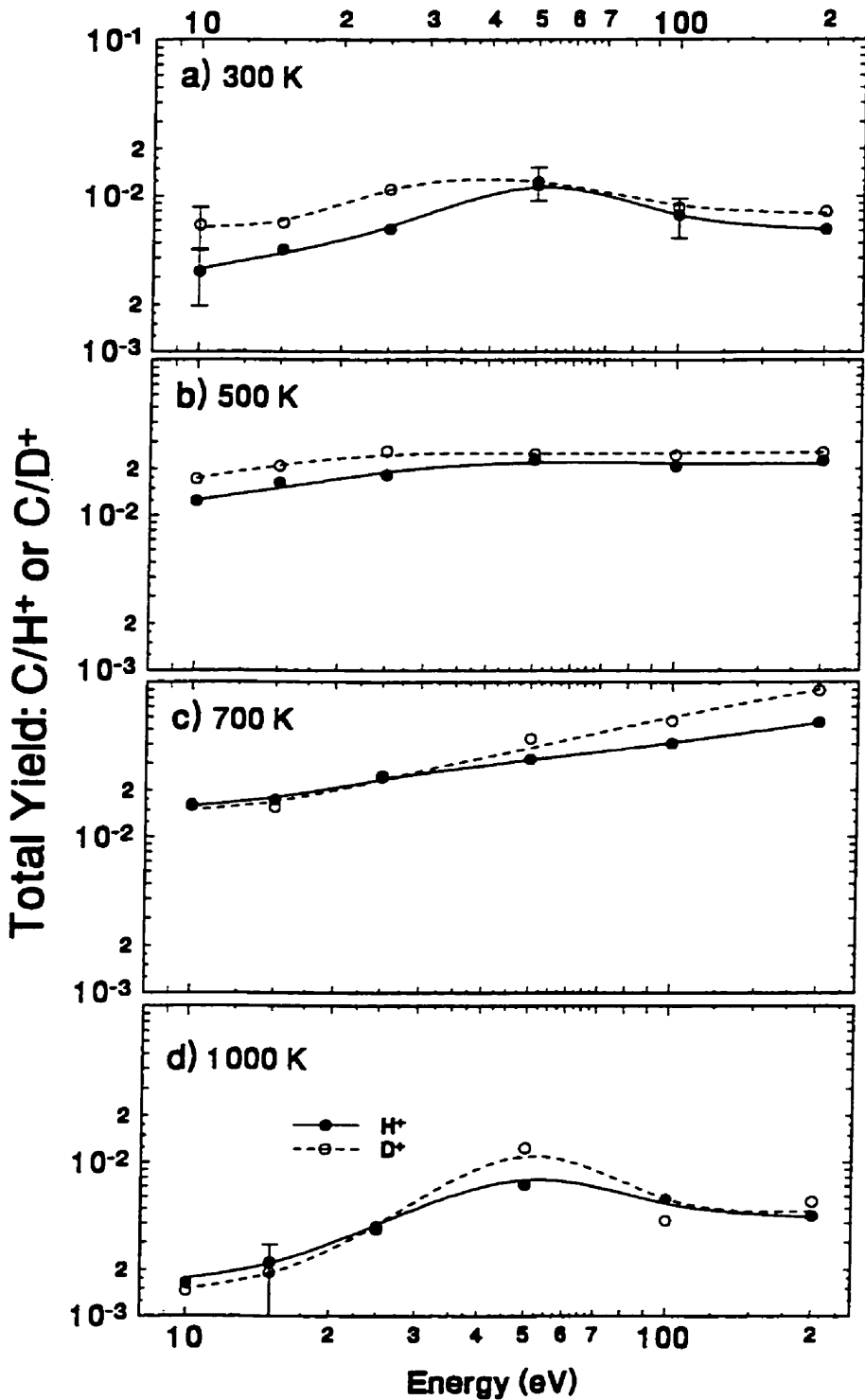


Figure 45: Isotopic comparison of the total chemical yield of pyrolytic graphite as a function of energy for ion impact at (a) 300 K, (b) 500 K, (c) 700 K and (d) 1000 K. The data and curves are taken from figure 30.

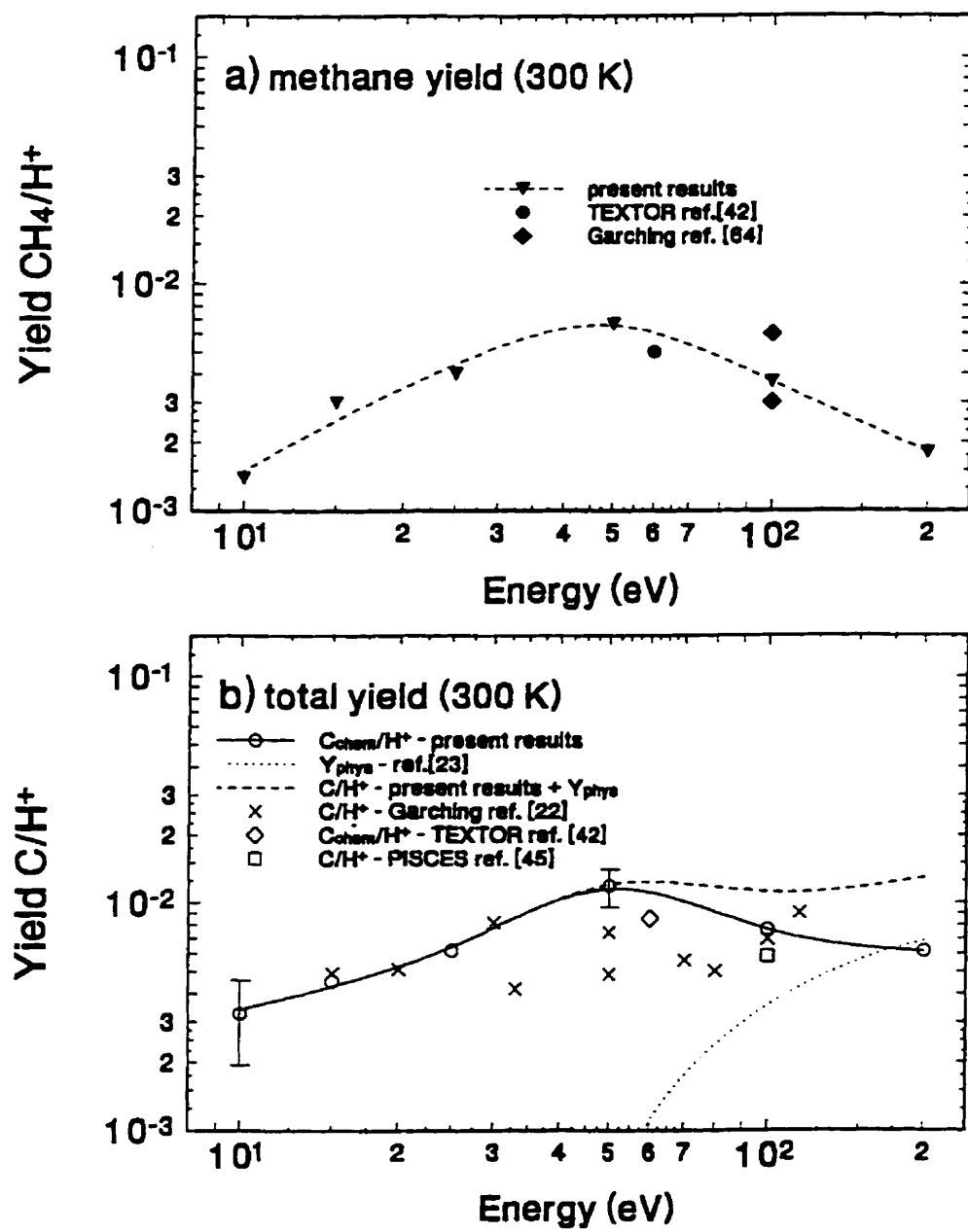


Figure 46: The (a) methane yield and (b) total yield of pyrolytic graphite, as a function of energy, due to H^+ impact at 300 K. The methane yield data are from [42] ($\Phi = 5 \times 10^{21} \text{ H}^+/\text{m}^2\text{s}$) and [64] ($\Phi = 10^{20} \text{ H}^+/\text{m}^2\text{s}$). The total yield data are from [22] ($\Phi = 5 \times 10^{19} \text{ H}^+/\text{m}^2\text{s}$), [42] ($\Phi = 5 \times 10^{21} \text{ H}^+/\text{m}^2\text{s}$) and [45] ($\Phi = 2 \times 10^{22} \text{ H}^+/\text{m}^2\text{s}$). The total yield data from [22,42] include physical sputtering. In (b) the physical sputtering contribution [23] is shown and summed with the present results to give the total yield (C/H^+).

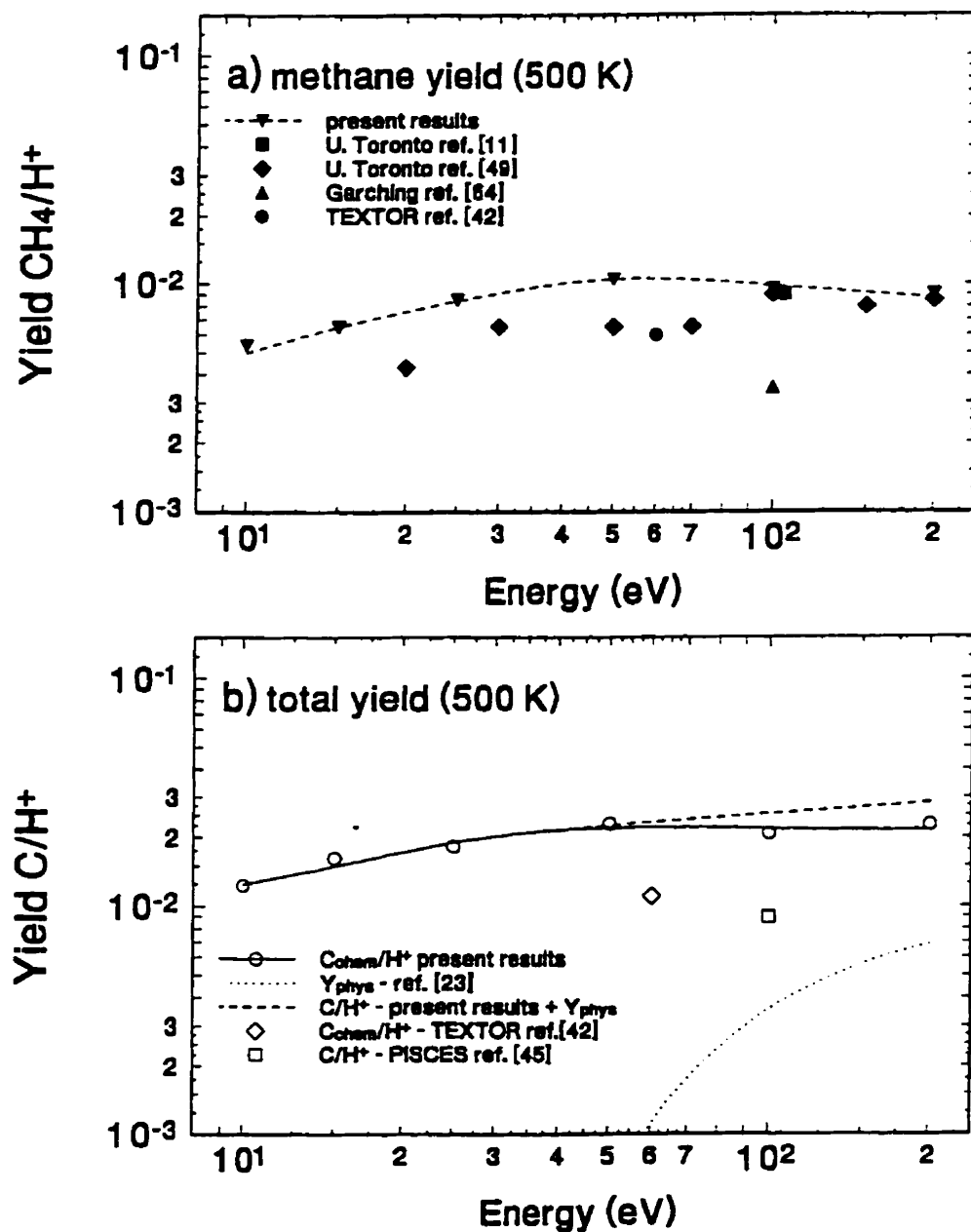


Figure 47: The (a) methane yield and (b) total yield of pyrolytic graphite, as a function of energy, due to H^+ impact at 500 K. The methane yield data are from [11,49] ($\Phi = 3-30 \times 10^{17} \text{ H}^+/\text{m}^2\text{s}$), [64] ($\Phi = 10^{20} \text{ H}^+/\text{m}^2\text{s}$), and [42] ($\Phi = 5 \times 10^{21} \text{ H}^+/\text{m}^2\text{s}$). The total yield data are from [42] ($\Phi = 5 \times 10^{21} \text{ H}^+/\text{m}^2\text{s}$) and [45] ($\Phi = 2 \times 10^{22} \text{ H}^+/\text{m}^2\text{s}$) which includes contributions from physical sputtering. In (b) the physical sputtering contribution [23] is shown and summed with the present results to give the total yield (C/H^+).

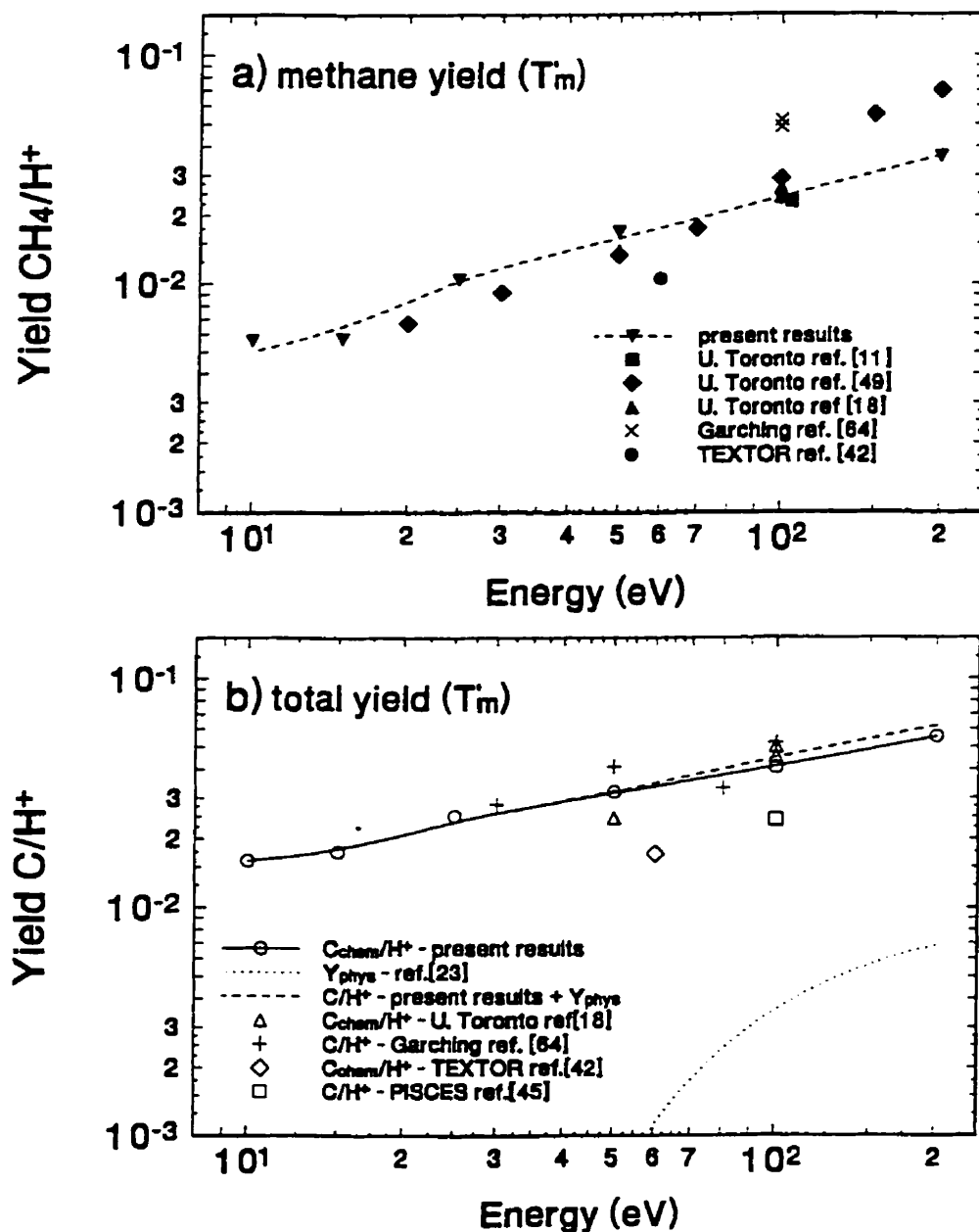


Figure 48: The (a) methane yield and (b) total yield of pyrolytic graphite, as a function of energy, due to H^+ impact at T_m , the temperature of maximum yield for impact energies ≥ 100 eV (~ 700 K in the present results, ~ 750 K in [11,18,42,49] and ~ 820 K in [45,64]). The methane yield data are from [11,18,49] ($\Phi = 3-30 \times 10^{17} H^+/m^2 s$), [64] ($\Phi = 10^{20} H^+/m^2 s$), and [42] ($\Phi = 5 \times 10^{21} H^+/m^2 s$). The total yield data are from [18] ($\Phi = 3 \times 10^{18} H^+/m^2 s$), [42] ($\Phi = 5 \times 10^{21} H^+/m^2 s$), [64] ($\Phi = 10^{20} H^+/m^2 s$), and [45] ($\Phi = 2 \times 10^{22} H^+/m^2 s$). The total yield data from [45,64] include contributions from physical sputtering. In (b) the physical sputtering contribution [23] is shown and summed with the present results to give the total yield (C/H^+).

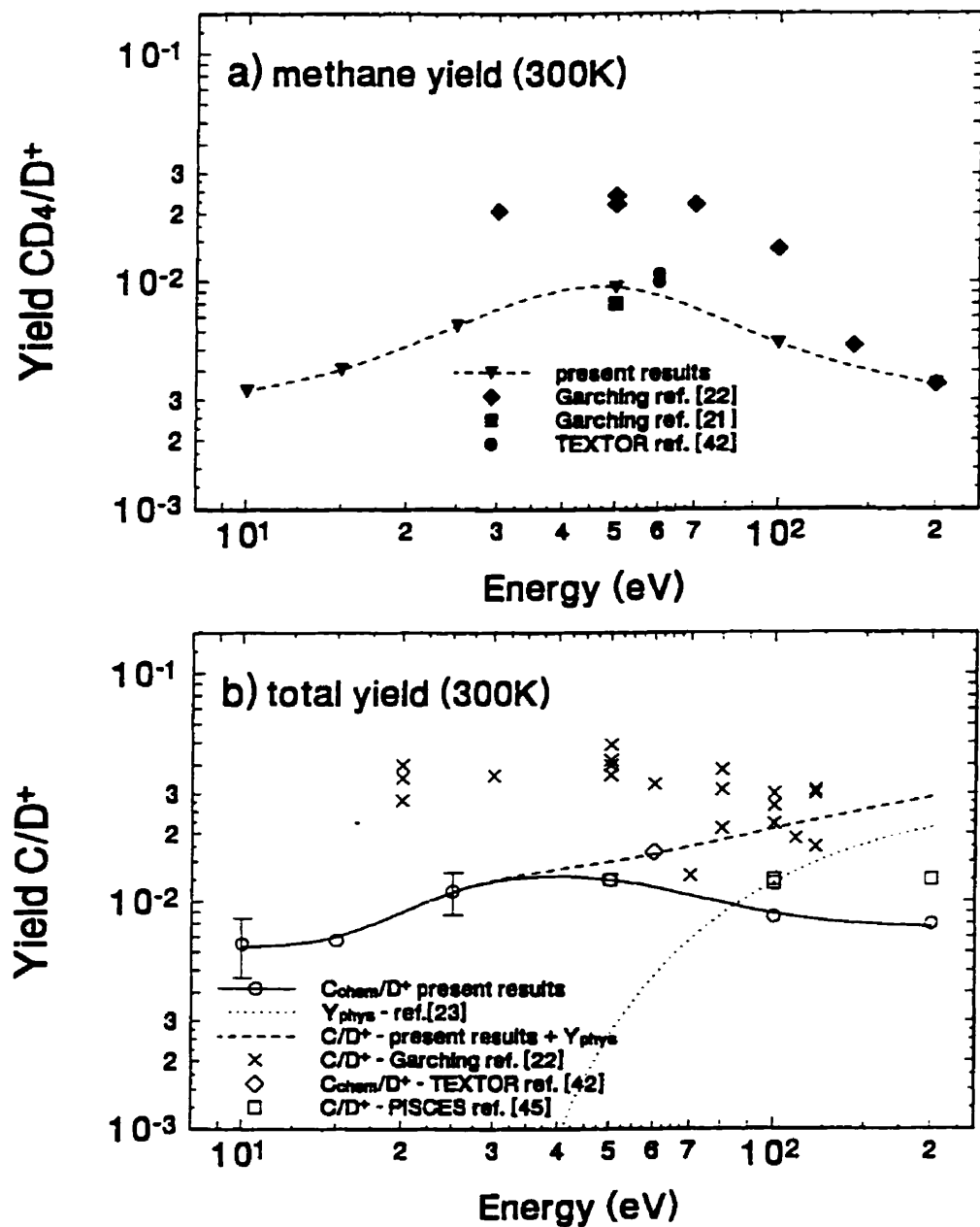


Figure 49: The (a) methane yield and (b) total yield of pyrolytic graphite, as a function of energy, due to D^+ impact at 300 K. The methane yield data are from [21,22] ($\Phi = 2.8\text{-}5 \times 10^{19} \text{ H}^+/\text{m}^2\text{s}$) and [42] ($\Phi = 5 \times 10^{21} \text{ H}^+/\text{m}^2\text{s}$). The total yield data are from [42] ($\Phi = 5 \times 10^{21} \text{ H}^+/\text{m}^2\text{s}$), [22] ($\Phi = 5 \times 10^{19} \text{ H}^+/\text{m}^2\text{s}$) and [45] ($\Phi = 2 \times 10^{22} \text{ H}^+/\text{m}^2\text{s}$). The total yield data from [22,45] include contributions from physical sputtering. In (b) the physical sputtering contribution [23] is shown and summed with the present results to give the total yield (C/D^+).

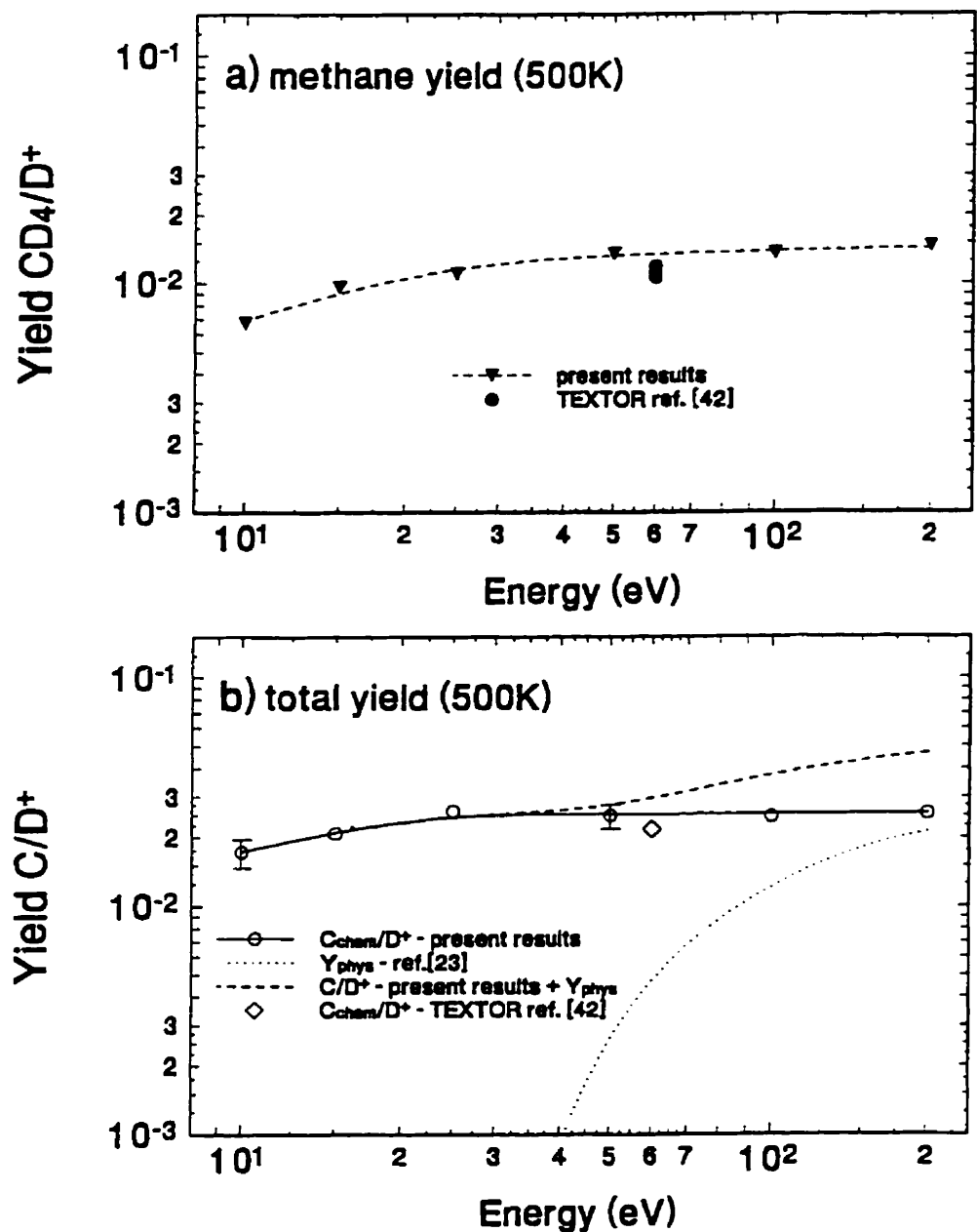


Figure 50: The (a) methane yield and (b) total yield of pyrolytic graphite, as a function of energy, due to D⁺ impact at 500 K. The methane and total yield data are from [42] ($\Phi = 5 \times 10^{21} \text{ H}^+/\text{m}^2\text{s}$). In (b) the physical sputtering contribution [23] is shown and summed with the present results to give the total yield (C/D⁺).

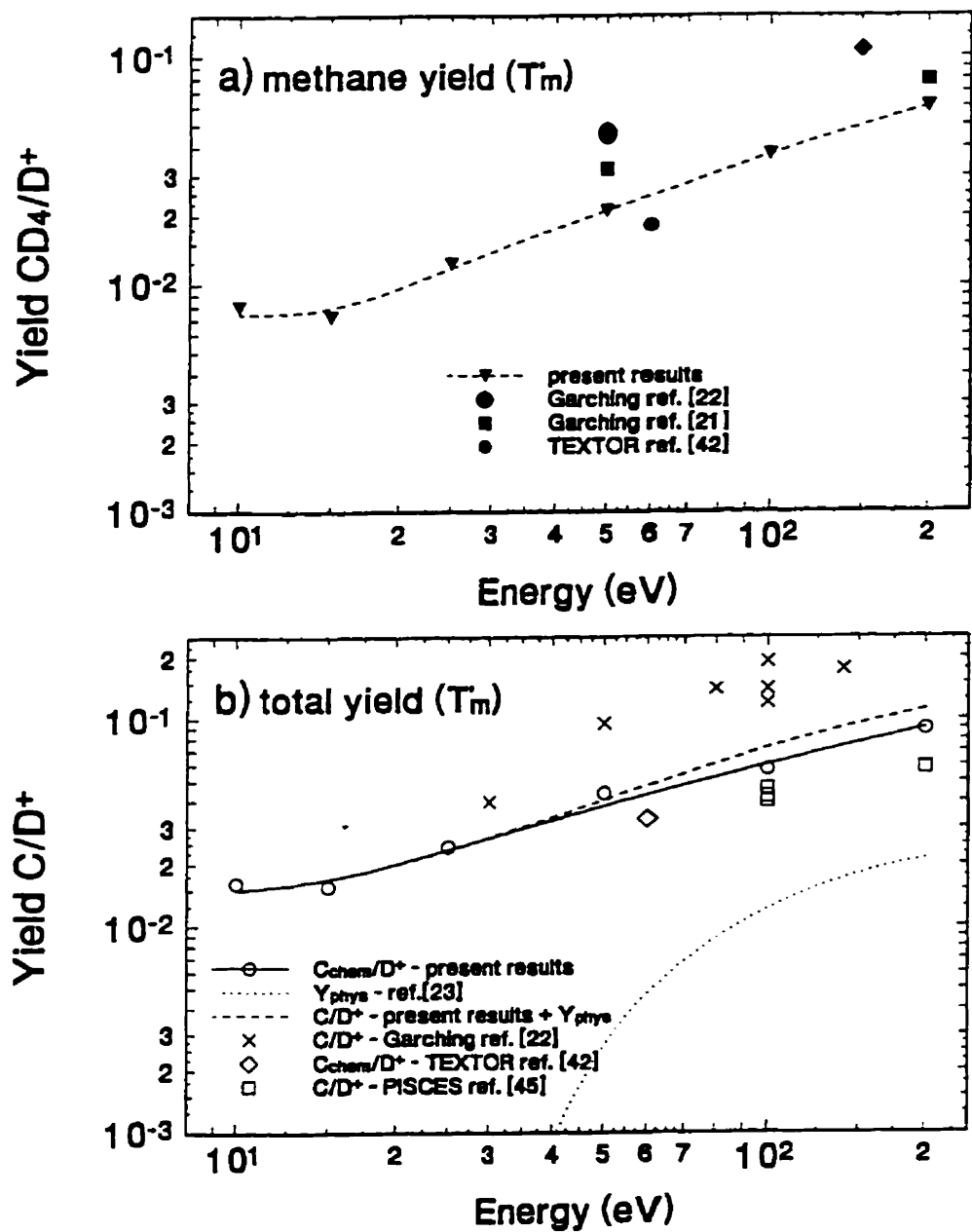


Figure 51: The (a) methane yield and (b) total yield of pyrolytic graphite, as a function of energy, due to D^+ impact at T_m , the temperature of maximum yield for impact energies ≥ 100 eV (~ 700 K in the present results, ~ 760 K in [42] and ~ 820 K in [21,22,45]). The methane yield data are from refs. [21,22] ($\Phi = 2.8\text{--}5 \times 10^{19} H^+/m^2 s$). The total yield data are from [42] ($\Phi = 5 \times 10^{21} H^+/m^2 s$), [22] ($\Phi = 5 \times 10^{19} H^+/m^2 s$) and [45] ($\Phi = 2 \times 10^{22} H^+/m^2 s$). The total yield data from [22,45] include contributions from physical sputtering. In (b) the physical sputtering contribution [23] is shown and summed with the present results to give the total yield (C/D^+).

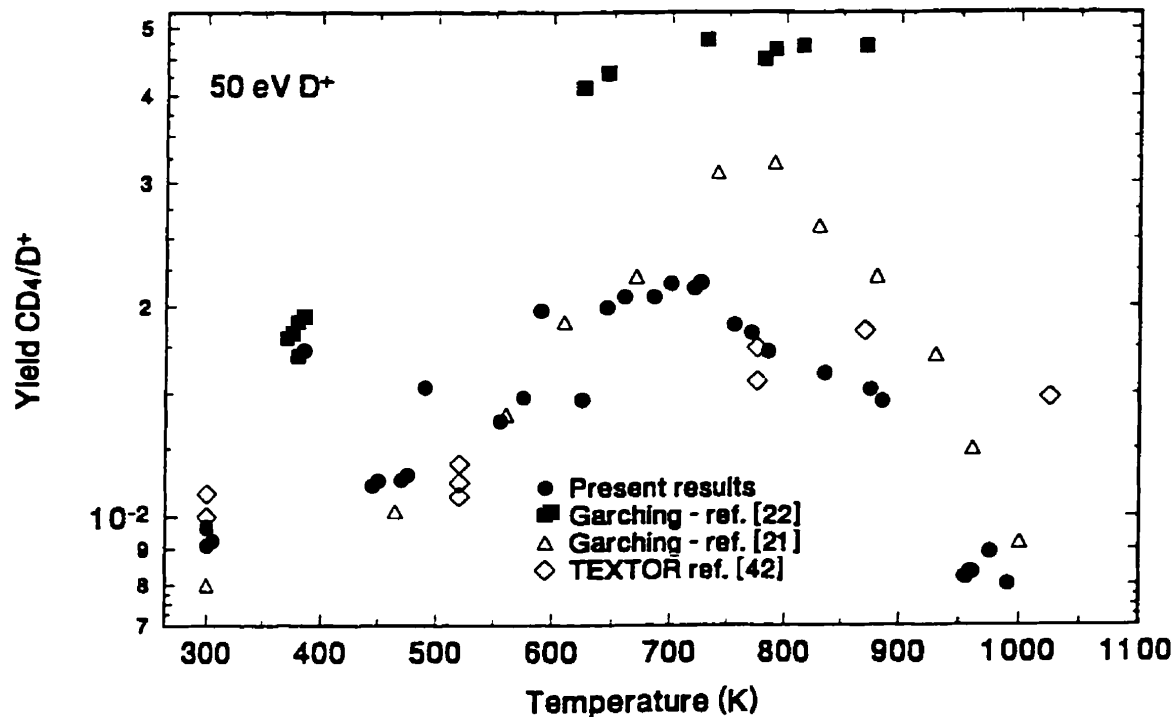


Figure 52: The methane yield of pyrolytic graphite as a function of temperature for 50 eV D⁺ impact. The present results are compared to data taken from [21,22] ($\Phi = 2.8\text{--}5 \times 10^{19} \text{ H}^+/\text{m}^2\text{s}$) and [42] ($E \sim 60 \text{ eV}, \Phi = 5 \times 10^{21} \text{ H}^+/\text{m}^2\text{s}$).

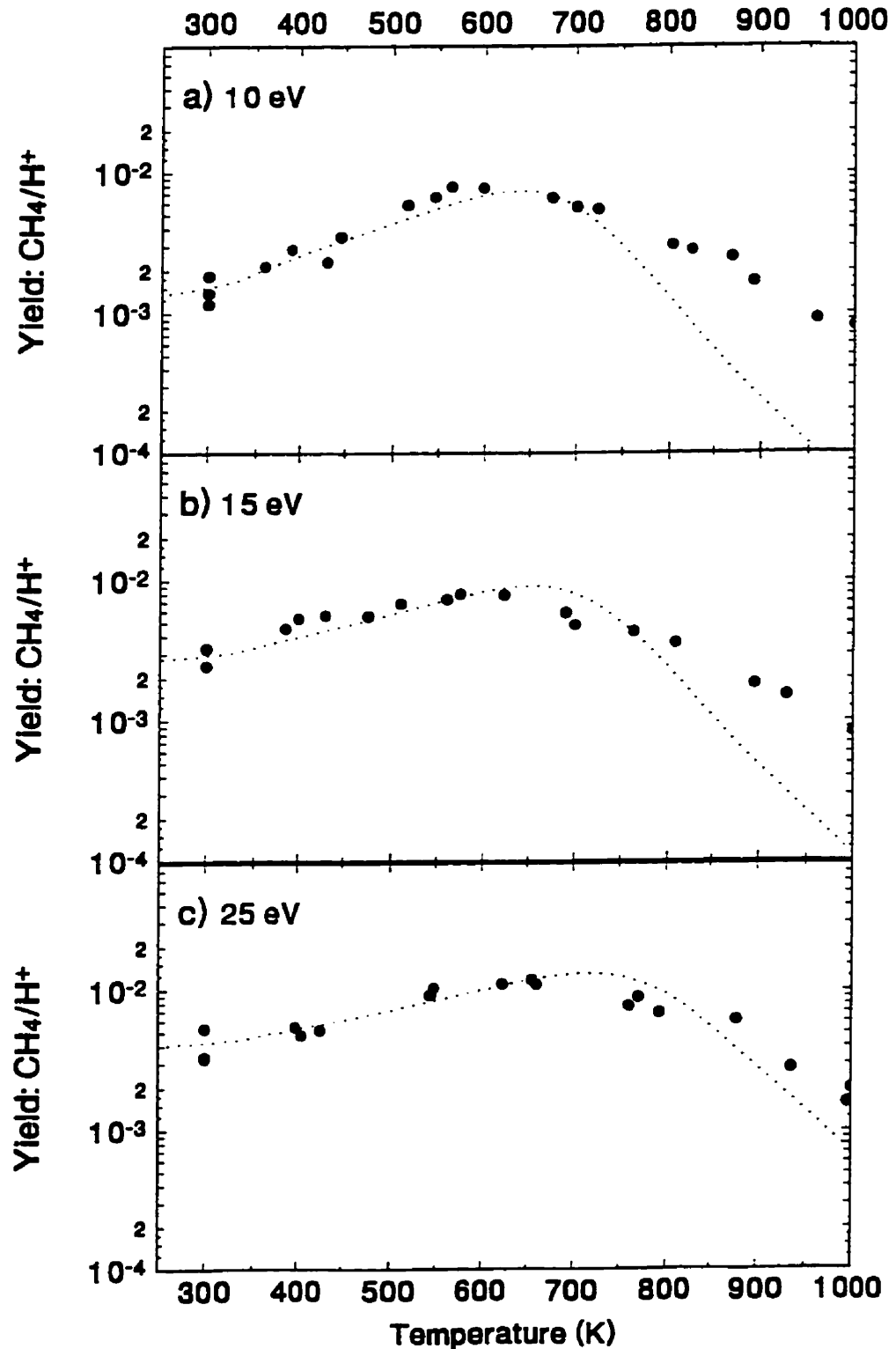


Figure 53: The revised model predictions for the methane yield of pyrolytic graphite due to H^+ impact at (a) 10, (b) 15 and (c) 25 eV. Data from the present experiments (figure 17a) is shown for comparison.

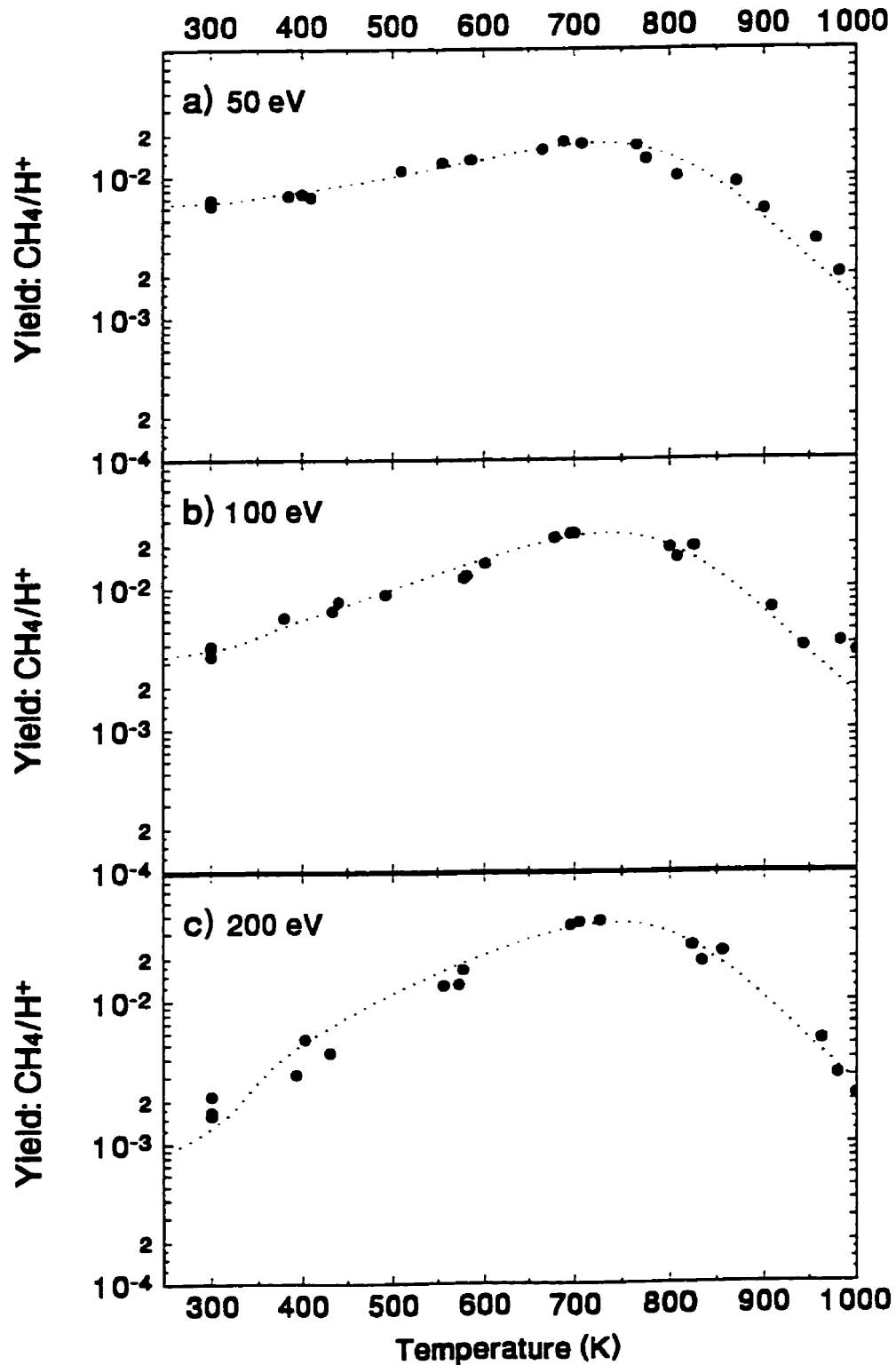


Figure 54: The revised model predictions for the methane yield of pyrolytic graphite due to H⁺ impact at (a) 50, (b) 100 and (c) 200 eV. Data from the present experiments (figure 17a) is shown for comparison.

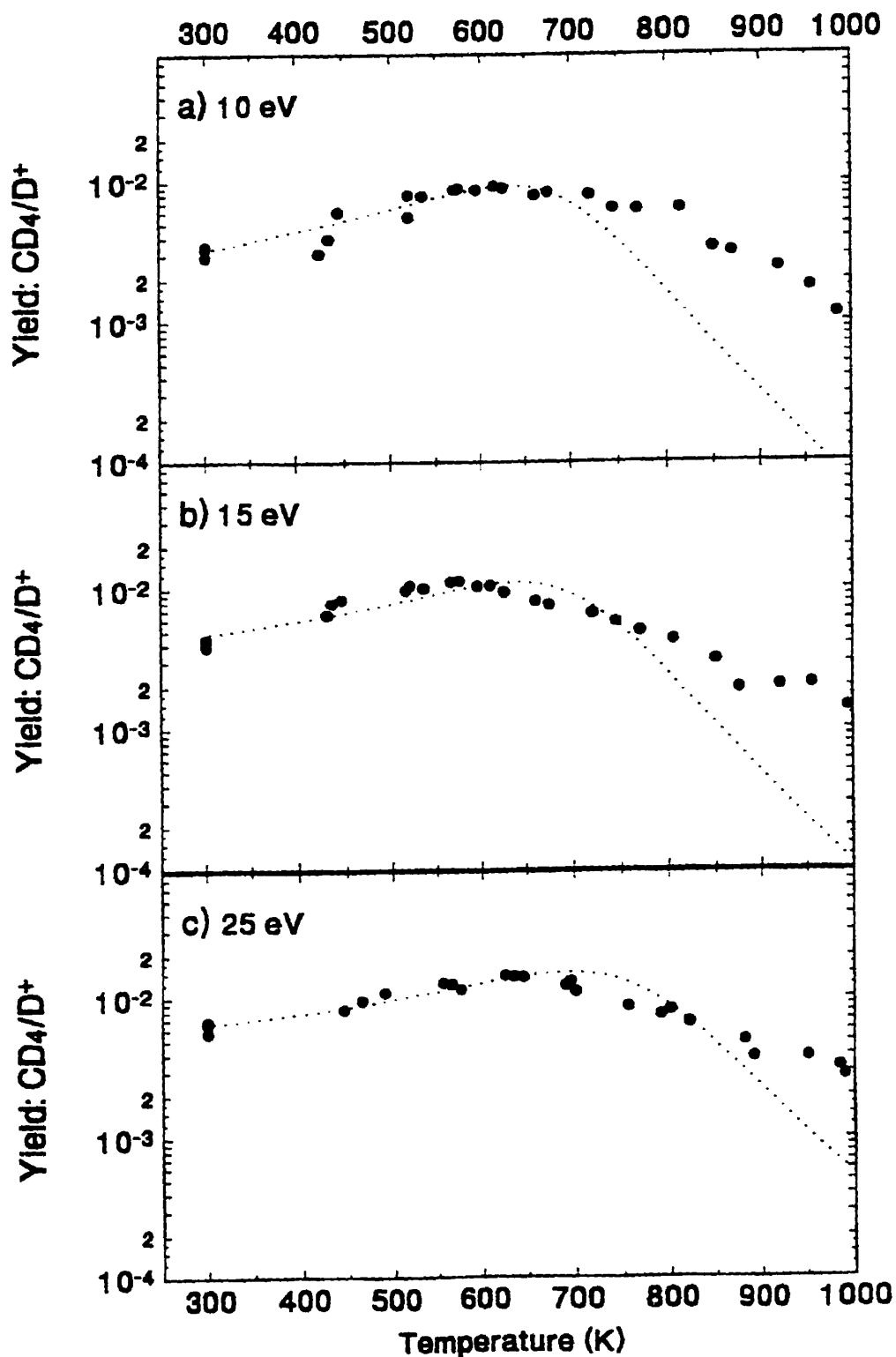


Figure 55: The revised model predictions for the methane yield of pyrolytic graphite as a function of temperature due to D^+ impact at (a) 10, (b) 15 and (c) 25 eV. Data from the present experiments (figure 17b) is shown for comparison.

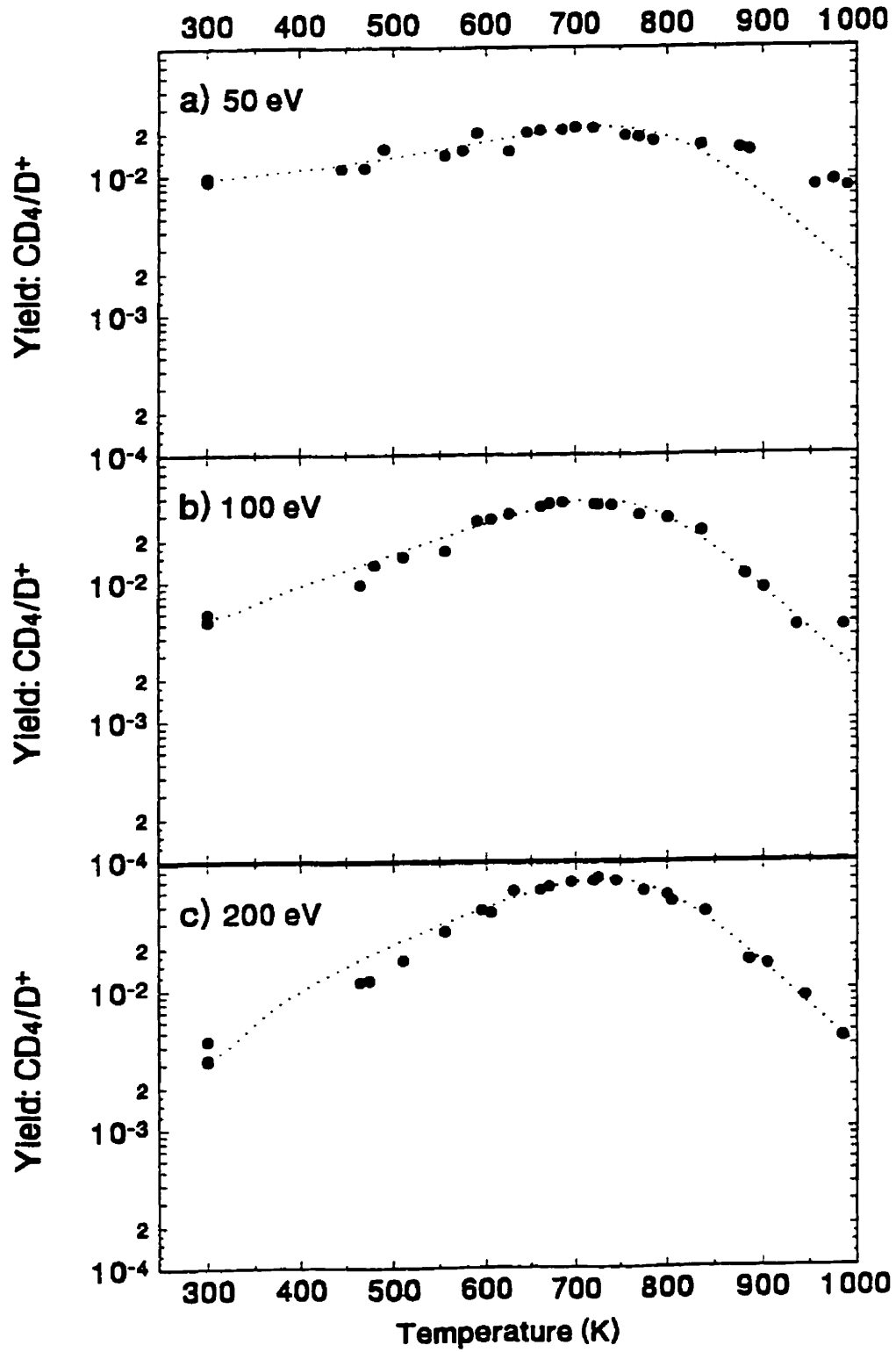


Figure 56: The revised model predictions for the methane yield of pyrolytic graphite as a function of temperature due to D^+ impact at (a) 50, (b) 100 and (c) 200 eV. Data from the present experiments (figure 17b) is shown for comparison.

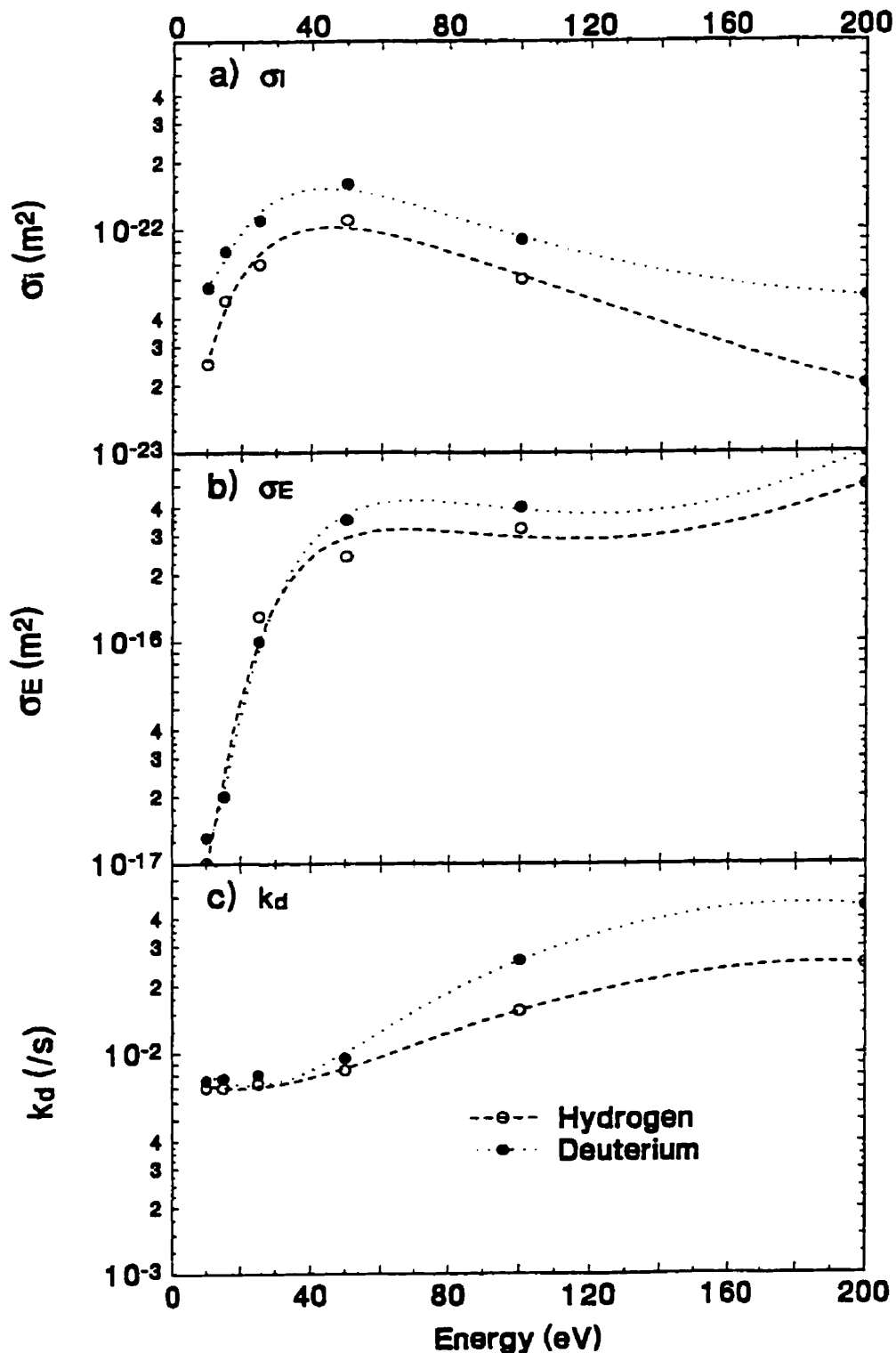


Figure 57: Energy dependence of the revised model fitting parameters for low-energy H^+ and D^+ impact.

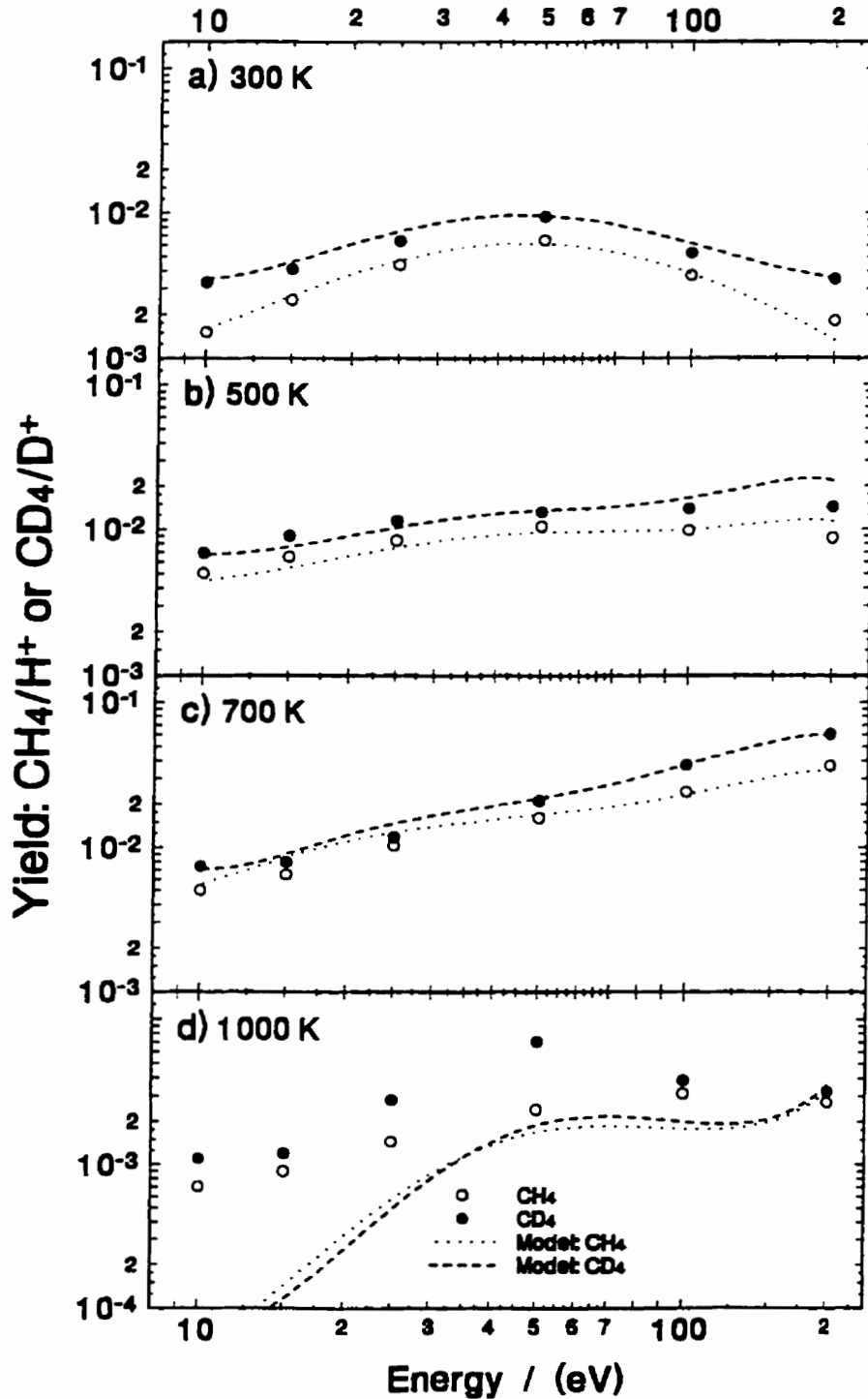


Figure 58: The revised model predictions for the methane yield of pyrolytic graphite as a function of ion energy for H^+ and D^+ impact at (a) 300 K, (b) 500 K, (c) 700 K and (d) 1000 K. Data form the present experiments (figure 18) are shown for comparison.

APPENDIX A

MODEL FITTING

INTRODUCTION

In this appendix we will examine the sensitivity of the model predictions to the free parameters, and discuss the criteria used to arrive at the model fits described in section 8. The attempt here is to provide more insight into the effects of the individual processes incorporated into the model on the predicted yields and the constraints employed in arriving at the derived parameter values.

We will first discuss the three terms which directly contribute to the methane yield in terms of their importance and region of influence. We then investigate the effects of varying the free parameters on such important quantities as the yield at room temperature (Y_{RT}), the maximum yield (Y_m), the yield at 1000 K (Y_{1000}), and T_m . A discussion of the criteria and technique employed in the present fitting of the model will ensue along with a presentation of more rigorous regression curves resulting from a least squares fit and a logarithmic least squares fit. In addition we will present and discuss the best fit curves which result from allowing almost all of the parameters, even those determined by Küppers et al., to be free fitting parameters. And finally, we will summarize our findings and present some conclusions.

A.1 Contributing terms

In the revised model there are three terms which contribute directly to the release of methyl groups; the atom-induced thermal release, the kinetic ejection of methyl groups attached to sp^3 carbon centers neighboured by a radical sp^x carbon configuration, and the kinetic ejection of methyl groups attached to sp^3 carbon centers neighboured by another sp^3 carbon center. The contributions of each of these terms to the methane yield are shown in fig. A.1a and the relative contributions of each term as a percentage of the methane yield are shown in fig. A.1b, as a function of temperature for 10 eV H^+ impact.

It is clear from figure A.1 that the contribution from kinetic ejection of methyl groups neighboured by a radical sp^x carbon configuration is insignificant. The other kinetic

ejection term leads to a methane contribution which is essentially constant between 300 and 550 K after which the thermal reduction in the concentration of sp^3 carbon centers leads to a reduction in this contribution. The atom-induced thermal release of methyl leads to a methane contribution which is increasing with temperature to a peak near 650 K after which the contribution from this term decreases. From plots of the methane yield fractions in fig. A.1b, it is clear that kinetic ejection dominates the methane yield at room temperature, but the fraction of the methane yield due to the thermal contribution steadily increases with temperature so that this term dominates for temperatures above ~ 500 K. We conclude then that the methane yield at room temperature is controlled by the kinetic ejection parameter σ_i , but thermal processes (abstraction and thermal release) dominate for higher temperatures.

A.2 Model sensitivity to free fitting parameters

In this section we will vary the free fitting parameters (σ_i , σ_E , k_D , E_D), one at a time for 10 eV H^+ impact, and discuss their effect on the methane yield as a function of temperature as predicted by the model. We examine only the case of 10 eV H^+ impact here since the same general observations will apply for all of the other cases.

A.2.1 Model sensitivity to σ_i

In figure A.2 we show the model predictions for 10 eV H^+ impact for three different values of the kinetic ejection parameter, σ_i , the value determined in section 8 (fig. A.2b), 50% of that value (fig. A.2a) and 150% of that value (fig. A.2c). We note that the value of σ_i has little discernible affect on the methane yield for temperatures above T_m and that the value of T_m is only weakly dependent on σ_i . As expected, based on figure A.1, σ_i has the greatest effect for lower temperatures, and this is especially true at room-temperature where the methane yield is almost completely determined by this parameter. Increasing the value of σ_i by 50% increases the absolute methane yield by nearly 50% at room-temperature (48.7%), but this effect weakens with increasing temperature so that the maximum yield is increased by only 7.5% and the yield at 1000 K is unaffected.

The ability of the parameter to pin the methane yield at room-temperature is the main reason why the model gives such good agreement with the experimental results at this temperature.

A.2.2 Model sensitivity to σ_E

In figure A.3 the model predictions are shown for 10 eV H⁺ impact for three values of the damage deposition parameter, σ_E , the value determined in section 8 (fig. A.3b) and 50% and 150% of this value (fig. A.3a and A.3c, respectively). Here we note that, in contrast to σ_i , the damage parameter has the greatest effect for higher graphite temperatures. Decreasing the value of σ_E by 50% has no effect on Y_{RT} , but reduces Y_m by 9.5% and Y_{1000} by 49.8%. Furthermore, there is a reduction in T_m by ~ 20 K. From a fitting perspective this is the only free parameter which can change the slope of the temperature profile above T_m . For 10 eV impact, where we desire a smaller slope in order to obtain better agreement however, this requires a significant increase in the value of σ_E which results in a value of T_m which is much too large. This is discussed further in section A.3.

A.2.3 Model sensitivity to k_D

In figure A.4 the model predictions for 10 eV H⁺ impact are shown for three values of k_D , the abstraction prefactor. Again, these values represent 50% (fig. A.4a), 100% (fig. A.4b) and 150% (fig. A.4c) of the value determined in section 8. Here we observe that k_D has the greatest effect on the methane yield for graphite temperatures near T_m where the thermal contribution to the release of methane is at its highest. For an increase in k_D of 50%, Y_{RT} increases by 1.1%, Y_m increases by 33.9%, Y_{1000} is unaffected and T_m is reduced by ~ 10 K. So, when fitting the model to experimental data, the abstraction prefactor is most effective at determining the value of Y_m and, to a lesser degree, T_m .

A.2.4 Model sensitivity to E_D

Figure A.5 shows the model predictions for 10 eV H⁺ impact for three values of the abstraction activation energy, E_D . Since this parameter appears in an exponential term it has more of an effect on the methane yield and therefore smaller variations of 80% (fig. A.5a), 100% (fig. A.5b) and 120% (fig. A.5c) of the value determined in section 8 have been used. The effect of varying this activation energy is nearly inverse to that of varying k_D , except that it shows more of an influence on the methane yield over the temperature range of 350 to 700 K. For example, if E_D is reduced by 20% this increases the values of Y_{RT} and Y_m by 14.8% and 107%, respectively, while reducing T_m by ~ 30 K. Variations of this parameter by 20%, however, have no effect on the yield at 1000 K.

A.2.5 Summary of model sensitivities

The effects of varying the free fitting parameters on the quantities of Y_{RT} , Y_m , Y_{1000} , and T_m are summarized in Table A.1 below.

Table A.1 Sensitivity of model predictions to parameter variations

Parameter	% change in Y_{RT}		% change in Y_m		% change in Y_{1000}		abs. change in T_m (K)	
Variation	+50%	-50%	+50%	-50%	+50%	-50%	+50%	-50%
σ_i (m ⁻²)	+48.7	-48.9	+7.5	-7.5	nil	nil	-10	nil
σ_E (m ⁻²)	nil	nil	+6.0	-9.5	+49.5	-49.5	+10	-20
k_D (s ⁻¹)	+1.1	-1.2	+34	-37	nil	nil	-10	+10
Variation	+20%	-20%	+20%	-20%	+20%	-20%	+20%	-20%
E_D (kJ/mol)	-2.0	+15	-45	+107	nil	nil	+20	-30

We conclude that, of the free fitting parameters, the kinetic ejection parameter, σ_i , is almost solely responsible for the model prediction at room-temperature, while the damage deposition parameter, σ_E , determines the methane yield predicted by the model at higher

temperatures ($> \sim 700$ K). In the intermediate range, it is largely the thermal abstraction process, described by k_D and E_D , that determines the model predictions.

A.3 Fitting the model to the experimental results

The model fits presented in section 8 are based on a set of analytic criteria developed to ensure better agreement in certain temperature regimes where we have more confidence in the experimentally determined methane yields. A list of these criteria, in order of importance, is presented here.

<u>Rank</u>	<u>Criterion</u>
1.	The predicted maximum yield could not be more than 10% off that determined experimentally.
2.	T_m could not be more than 40 K off that determined experimentally.
3.	Where possible, a smooth transition is preferable to one with kinks.

These criteria do not represent a rigorous regression fitting criterion based on the minimization of some quantity. Instead, a certain amount of judgment has been exercised in arriving at the present fits. For the balance of this discussion such fits will be referred to as the nominal curve fits.

In the interest of completeness we present here model fits arrived at in a more rigorous manner, employing strict regression criteria. These model fits are based on i) the least squares method, $\min\{\sum(Y_{exp} - Y_{pred})^2\}$, and ii) the logarithmic least squares method, $\min\{\sum(1 - Y_{exp}/Y_{pred})^2\}$. Using these criteria, the free fitting parameters σ_i , σ_E , k_D and E_D were varied to arrive at the optimal fit for 10 eV H⁺ and 200 eV D⁺ impact and the results are presented in figures A.6 and A.7.

In figure A.6, where the fits for 10 eV H⁺ impact are presented, we observe that the nominal fit (fig. A.6a) is very similar to the least squares fit for $T > T_m$, while it is closer to the logarithmic least squares fit for $T < 600$ K. This reflects the criteria that T_m , as predicted by the model, cannot be more than 10% off that observed experimentally. The

values of the fitting parameters and their effect on Y_{RT} , Y_m , Y_{1000} and T_m for the three fits are presented in table A.2 below.

Table A.2 Parameters and model predictions for 3 fit criteria and 10 eV H^+ impact.

Curve Fit	Fitting Parameters				Model Predictions			
	σ_i m ²	σ_E m ²	k_D s ⁻¹	E_D eV/mol	Y_{RT} (CH ₄ /H)	Y_m (CH ₄ /H)	Y_{1000} (CH ₄ /H)	T_m (K)
nominal	2.5	1.0	7.0	25	.0015	.0073	5.6x10 ⁻⁵	640
Least sqr.	3.1	1.4	7.2	25	.0019	.0081	7.8x10 ⁻⁵	650
Log. least sqr.	2.8	9.9	6.5	25	.0017	.0098	5.4x10 ⁻⁴	720

We note that the least squares fitting criterion does not lead to parameter values which are very different from those determined in section 8. The logarithmic least squares fit, however, results in a value of σ_E which is ~ an order of magnitude higher than the nominal value. This leads to better agreement with the experimental data at higher temperatures (> 800 K) at the expense of an overestimate of the maximum yield and the temperature at which it occurs. Since we have the most confidence in the experimentally determined values of Y_m and T_m , where the methane yields are largest, this logarithmic fit is not acceptable.

In figure A.7 we present the curve fits which emerge from the three fit criteria as applied to the case of 200 eV D^+ impact. We observe that there is little to choose between the three curves save for the sharper kink present at about 380 K for the least squares curve fit. See Table A.3 for a summary of the fitting parameters and model predictions for the three fit criteria.

The smaller value of σ_i required by the least squares criterion results in the sharper kink at low temperature as predicted by the model. We note that the value of E_D is independent of the criteria used for both impact energies. This is a consequence of the sensitivity of the model predictions to this parameter.

Table A.3 Parameters and model predictions for 3 fit criteria and 200 eV D⁺ impact.

Curve Fit	Fitting Parameters				Model Predictions			
Criteria	σ_0 (m ²) ($\times 10^{-16}$)	σ_H (m ²) ($\times 10^{-16}$)	k_D (s ⁻¹) ($\times 10^3$)	E_D kJ/mol	X_m (CD ₂ /D)	Y_m (CD ₂ /D)	Y_{1000} (CD ₂ /D)	T_m (K)
nominal	5.0	7.0	4.5	25	.0032	.061	.0038	730
Least sqr.	2.1	7.1	4.5	25	.0015	.060	.0038	730
Log. least sqr.	5.6	7.8	4.1	25	.0035	.057	.0041	740

We conclude that for low-energy impact, where there is poor agreement between the nominal fit and the experimentally determined methane yields at high temperatures (> 750 K), better agreement can be obtained for $T > 800$ K if the logarithmic least squares fit criterion is employed, but this results in values of Y_m and T_m which are too high. For 200 eV D⁺ impact, however, the fitting criteria do not produce very different results, suggesting that the experimental results are well modelled by the nominal fit at this energy.

A.4 Optimal model fits

Here we relax the constraints imposed on the reaction parameters σ_H , k_x , and k_H as determined by Küppers et al, and on the Gaussian distributions employed for E_x , E_H , and E_D in section 8 to see how much the fit can be improved. This was done since it is possible that the energy of the incident ions could affect some of the previously determined parameters based on sub-eV H,D results, as well as the energy distributions employed. If so, we should find that the curve fits can be dramatically improved. This investigation is undertaken for both 10 eV H⁺ and 200 eV D⁺ impact and the results are presented in figure A.8 and A.9, respectively.

In figure A.8 the optimal least squares and logarithmic least squares fits for 10 eV H⁺ impact are shown. Here we have allowed all of the parameters employed in the model to be free fitting parameters, except the activation energies E_x and E_H which should not depend on incident ion energy. The values of the parameters and important model predictions are presented for the two fits in table A.4. From this table it is clear that optimization does not lead to any significant changes in either the model parameter values

or the model predictions. In fact, the model predictions for the optimal least squares and the optimal logarithmic least squares fits hardly differ at all from those developed in section A.3 where only four free parameters were used. This gives us some confidence that the parameters determined by Küppers et al. (σ_H , k_x , k_H) do not differ significantly for energetic impact.

Table A.4 Optimal curve fits for 10 eV H⁺ impact.

Parameter	LSF	LLSF	NOMINAL
σ_H (m ²) $\times 10^{-20}$	4.4	4.5	4.5
k_x (s ⁻¹) $\times 10^{12}$	9.8	7.0	10
k_H (s ⁻¹) $\times 10^{13}$	1.0	1.0	1.0
σ_i (m ²) $\times 10^{-23}$	3.0	2.6	2.5
σ_E (m ²) $\times 10^{-17}$	1.4	9.8	1.0
k_D (s ⁻¹) $\times 10^{-3}$	7.3	6.0	7.0
E_D (kJ/mol)	25	25	25
W_D (kJ/mol)	14	15	14
W_x (kJ/mol)	37	40	40
W_H (kJ/mol)	50	50	50
Y_{RT} (CH ₄ /H)	.0018	.0016	.0015
Y_m (CH ₄ /H)	.0081	.0097	.0073
Y_{1000} (CH ₄ /H)	7.6×10^{-5}	5.4×10^{-4}	5.6×10^{-5}
T_m (K)	640	720	640

The optimal least squares and optimal logarithmic least squares fits for 200 eV D⁺ impact (see fig. A.9 and Table A.5) again show that optimization does not lead to any significant changes in either the model parameter values or the model predictions. Even for k_x , which is increased by a factor of 2 or more for the optimal fits, the changes in the model predictions are minimal. We conclude again that the parameters determined by Küppers et al. (σ_H , k_x , k_H), for atomic impact, do not differ significantly for energetic impact.

Table A.5 Optimal curve fits for 200 eV D⁺ impact.

Parameter	LSF	LLSF	NOMINAL
$\sigma_H (m^2) \times 10^{-20}$	4.4	4.5	4.5
$k_x (s^{-1}) \times 10^{13}$	2.0	2.3	1.0
$k_H (s^{-1}) \times 10^{13}$	1.0	1.0	1.0
$\sigma_i (m^2) \times 10^{-23}$	1.3	5.3	5.0
$\sigma_E (m^2) \times 10^{-16}$	7.2	7.8	7.0
$k_D (s^{-1}) \times 10^{-2}$	4.6	4.1	4.5
$E_D (kJ/mol)$	25	25	25
$W_D (kJ/mol)$	14	14	14
$W_x (kJ/mol)$	53	40	40
$W_H (kJ/mol)$	50	50	50
$Y_{RT} (CH_4/H)$.0021	.0036	.0032
$Y_m (CH_4/H)$.060	.058	.061
$Y_{1000} (CH_4/H)$.0038	.0036	.0038
$T_m (K)$	730	740	730

A.5 Summary

We conclude that of the three terms which lead directly to the release of a methyl group only two are important. The first, kinetic ejection of a methyl group attached to a sp³ carbon center neighboured by another carbon atom in the sp³ hybridization state, is a constant between room temperature and ~ 550 K which controls the erosion behaviour at low temperatures. The second, atom-induced thermal release of methyl, increases steadily between 300 and 650 K and dominates the gross erosion behaviour for temperatures above ~ 500 K.

The four free fitting parameters σ_i , σ_E , k_D , and E_d affect the model in different ways and in different temperature regimes. The kinetic ejection parameter, σ_i , affects the methane yields at low temperatures. At room-temperature the yield is nearly directly

proportional to this parameter. The damage deposition parameter, σ_E , dominates for temperatures approaching 1000 K where the predicted yield is again nearly directly proportional to this parameter. The abstraction prefactor, k_D , tends to control the model predictions in the intermediate temperature range. The predicted value of Y_m increases and T_m decreases for an increase in k_D . All of the model predictions are quite sensitive to changes in E_D , the activation energy for abstraction, and it was found that this parameter should be kept always at 25 kJ/mol for the best agreement between the model predictions and the experimentally determined methane yields.

We have presented the criteria used to arrive at the nominal model fits, using the four free fitting parameters, discussed in section 8. In addition, we have presented the curves which result from a more rigorous application of least squares and logarithmic least squares regression fitting. We found that for low-energy impact (10 eV H^+) there are differences between the three curves, but these differences are much smaller for more energetic impact (200 eV D^+). We further presented the optimal curves which can be generated by using the least squares and logarithmic least squares fit criteria and allowing all of the parameters to be free, except for the activation energies for the atom-induced thermal release of hydrogen and methyl. It was found that the improvements in these fits were marginal compared to those obtained using only the four free fitting parameters. This gives us confidence that the parameters determined by Küppers et al. for atomic impact (σ_H , k_s , k_H) are not functions of ion energy, and that the activation energy distributions employed in the revised model are also relatively independent of ion energy.

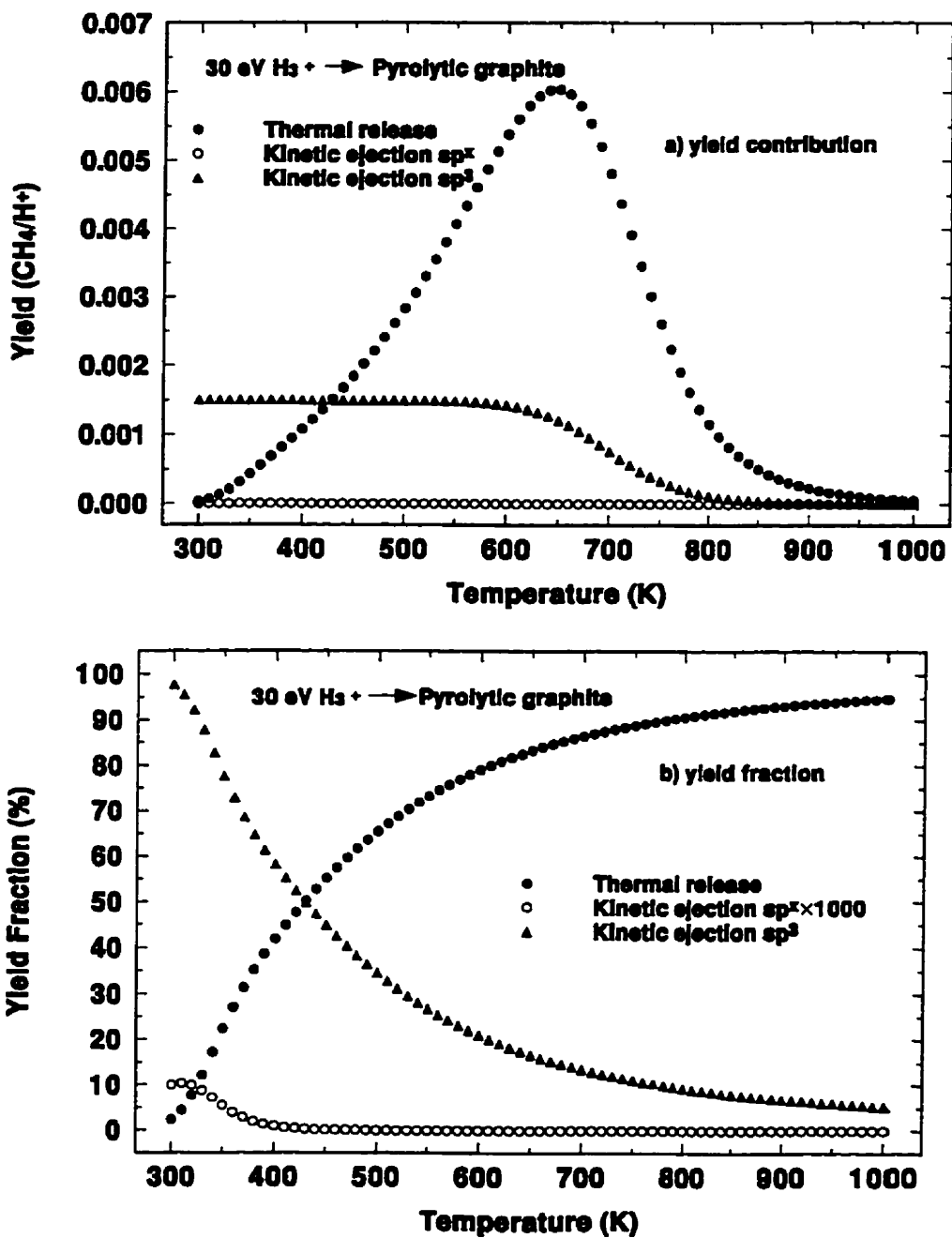


Figure A.1: The contributions of the thermal release and two kinetic ejection processes to methane production as a function of temperature for 10 eV H⁺ impact. In (a) the absolute contributions are shown while, in (b), the relative contributions are shown.

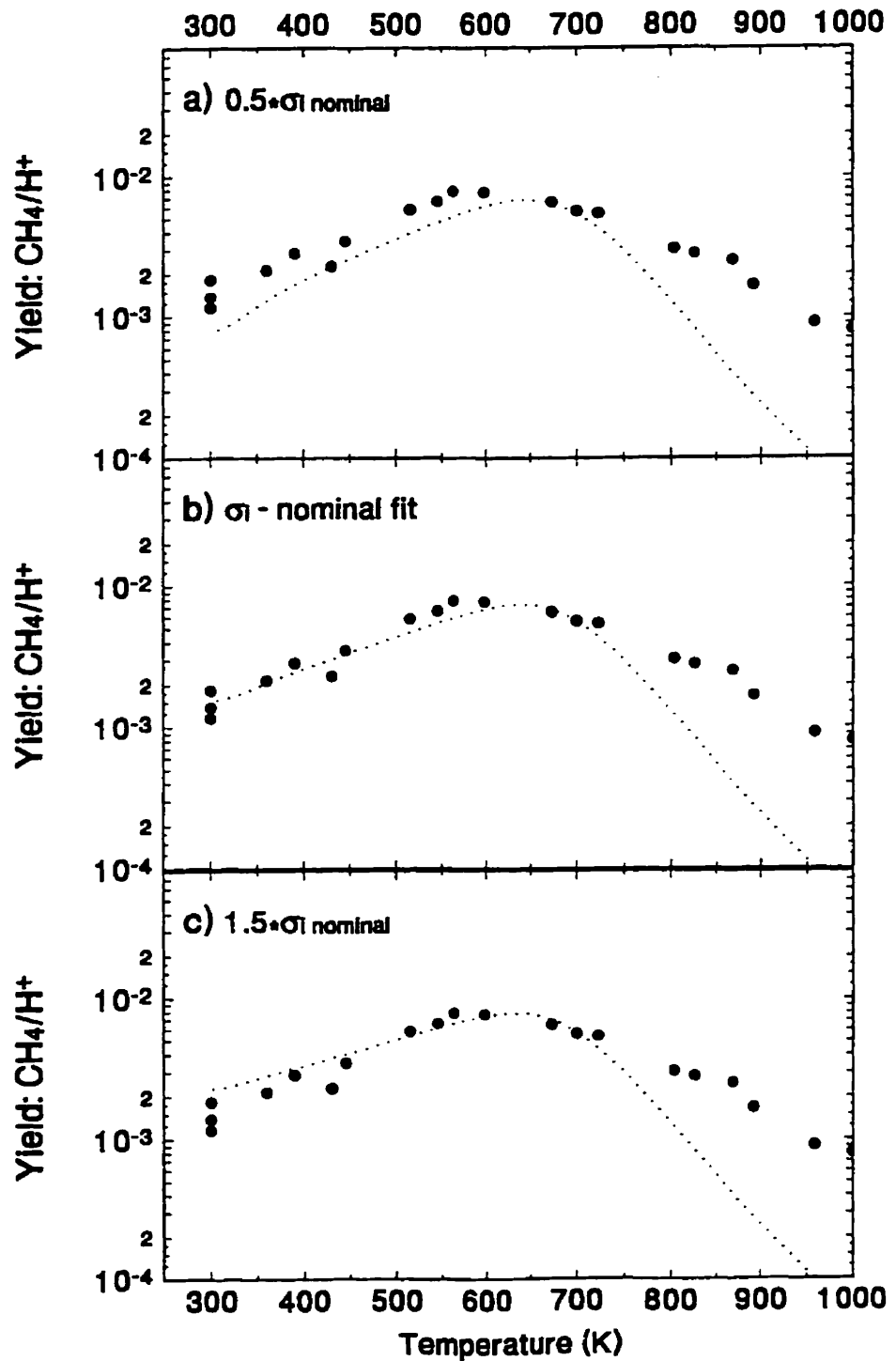


Figure A.2: The effects of a variation in σ_i on methane yield predictions. The nominal case is shown in (b), while the a +50% variation is shown in (a) and a -50% variation is shown in (c). Data shown are for 10 eV H^+ impact.

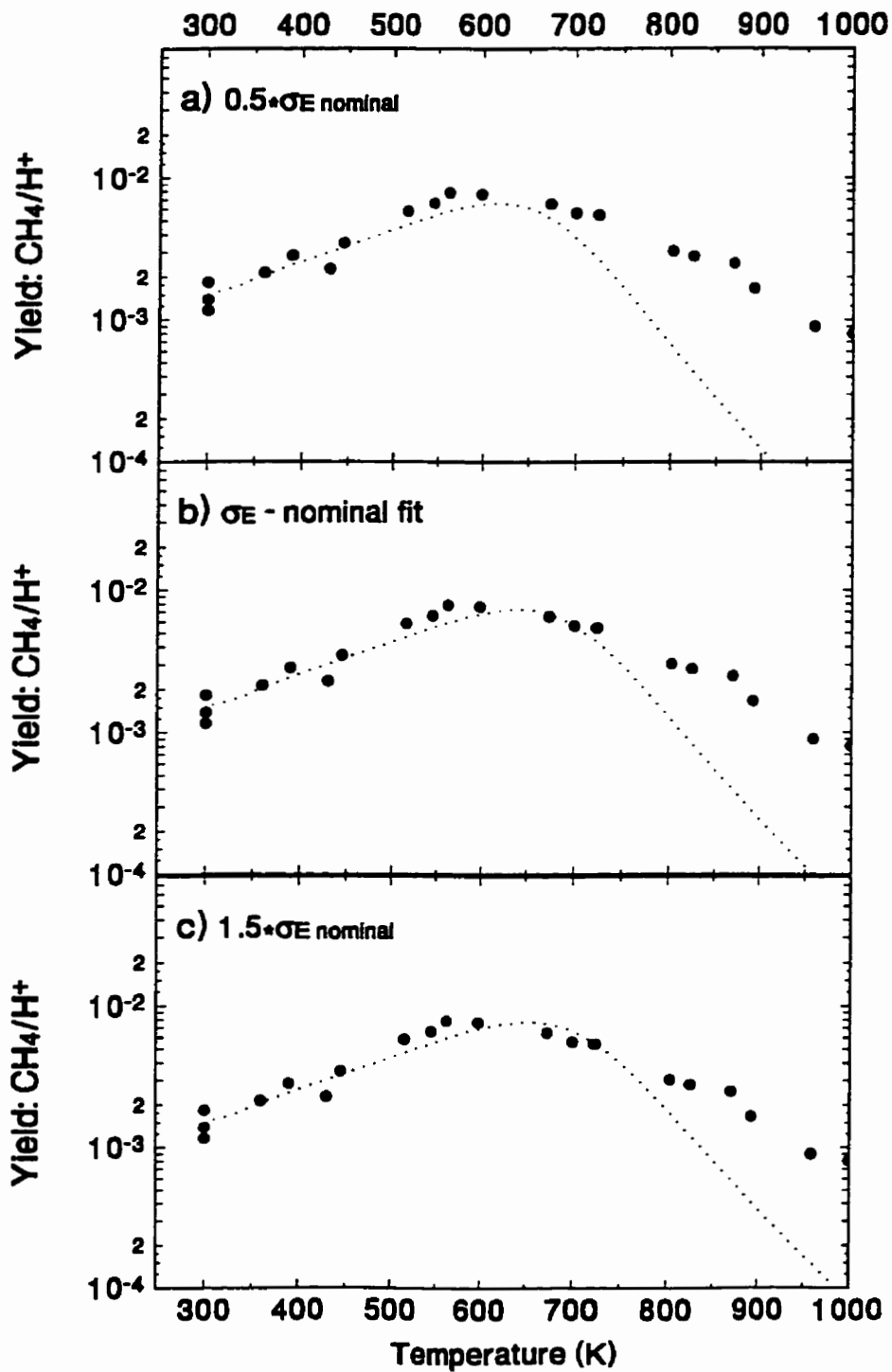


Figure A.3: The effects of a variation in σ_E on methane yield predictions. The nominal case is shown in (b), while the a +50% variation is shown in (a) and a -50% variation is shown in (c). Data shown are for 10 eV H^+ impact.

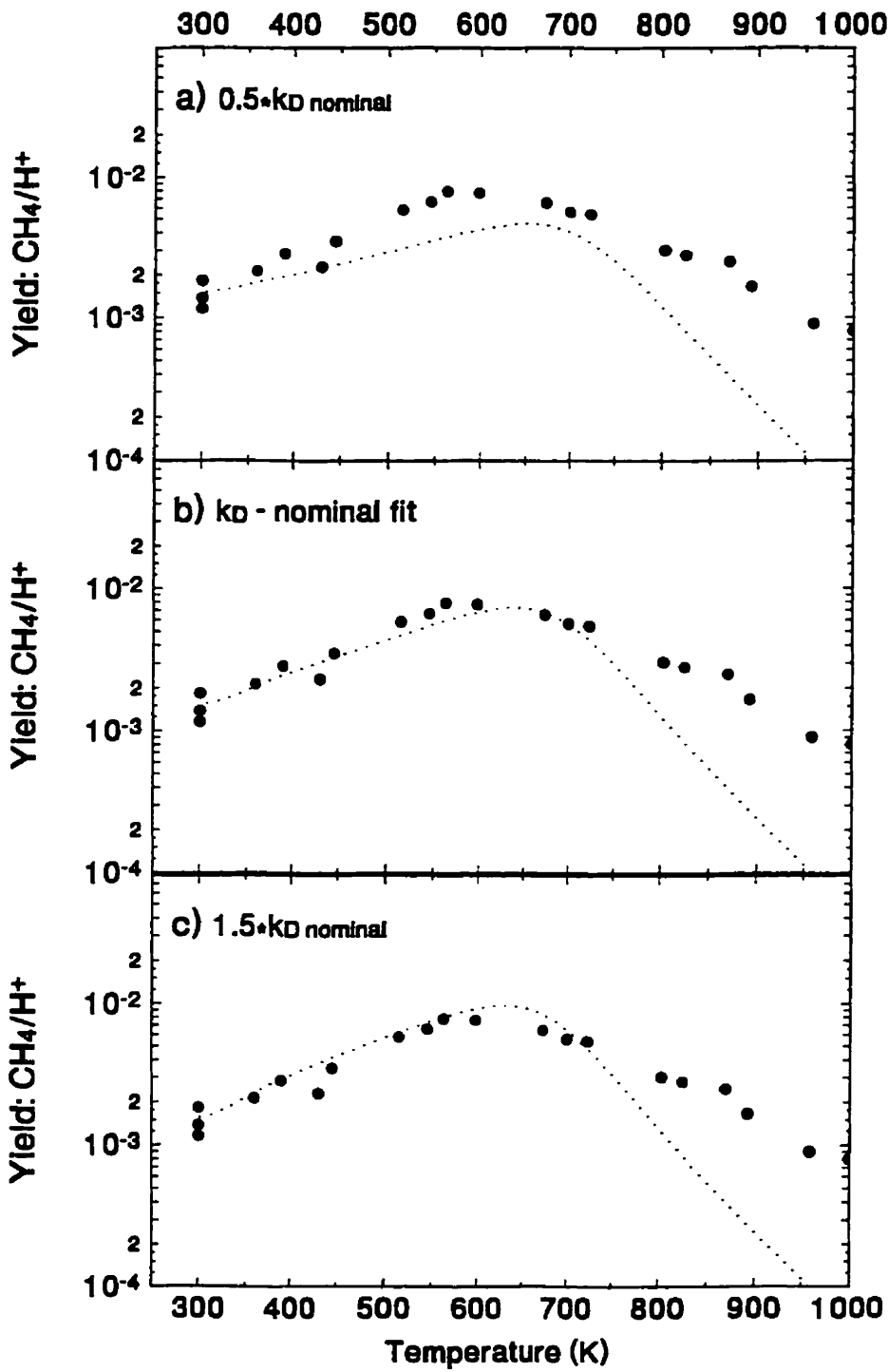


Figure A.4: The effects of a variation in k_D on methane yield predictions. The nominal case is shown in (b), while the a +50% variation is shown in (a) and a -50% variation is shown in (c). Data shown are for 10 eV H^+ impact.

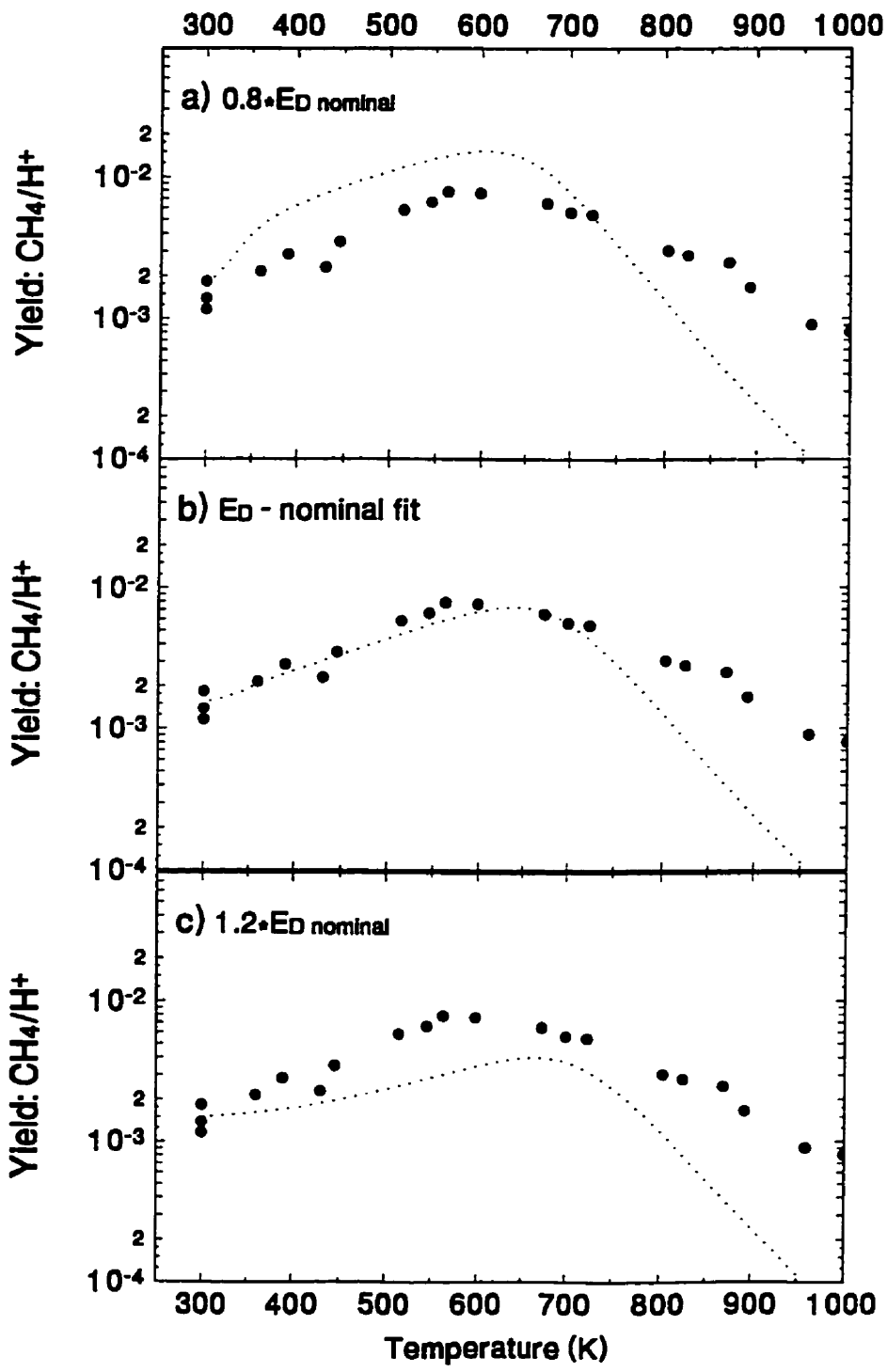


Figure A.5: The effects of a variation in E_D on methane yield predictions. The nominal case is shown in (b), while the a +20% variation is shown in (a) and a -20% variation is shown in (c). Data shown are for 10 eV H^+ impact.

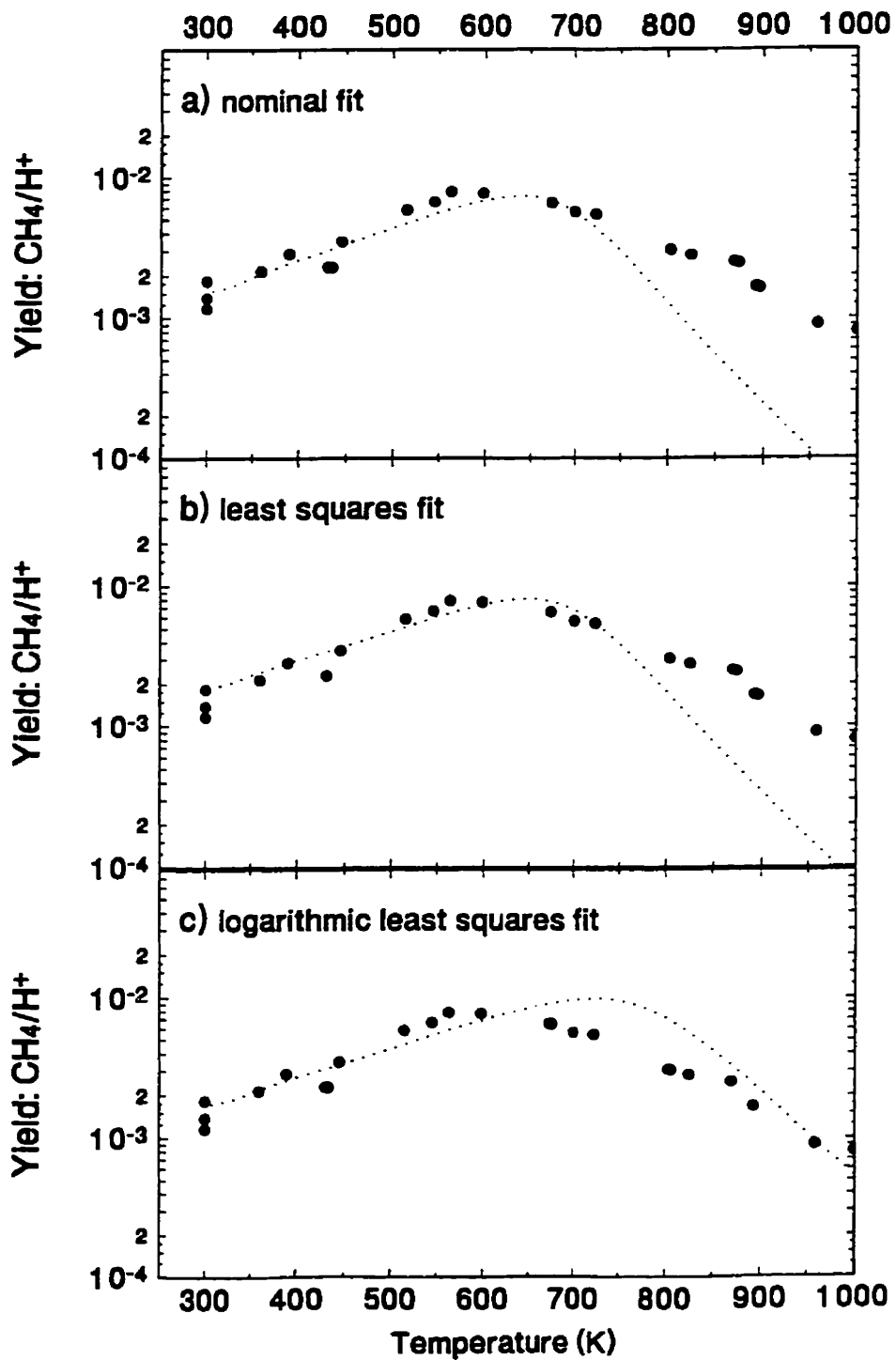


Figure A.6: Model predictions, for the methane yield as a function of temperature due to 10 eV H^+ impact, resulting from regression fitting using (b) least squares and (c) logarithmic least squares criteria. The nominal fit (a) is shown for comparison.

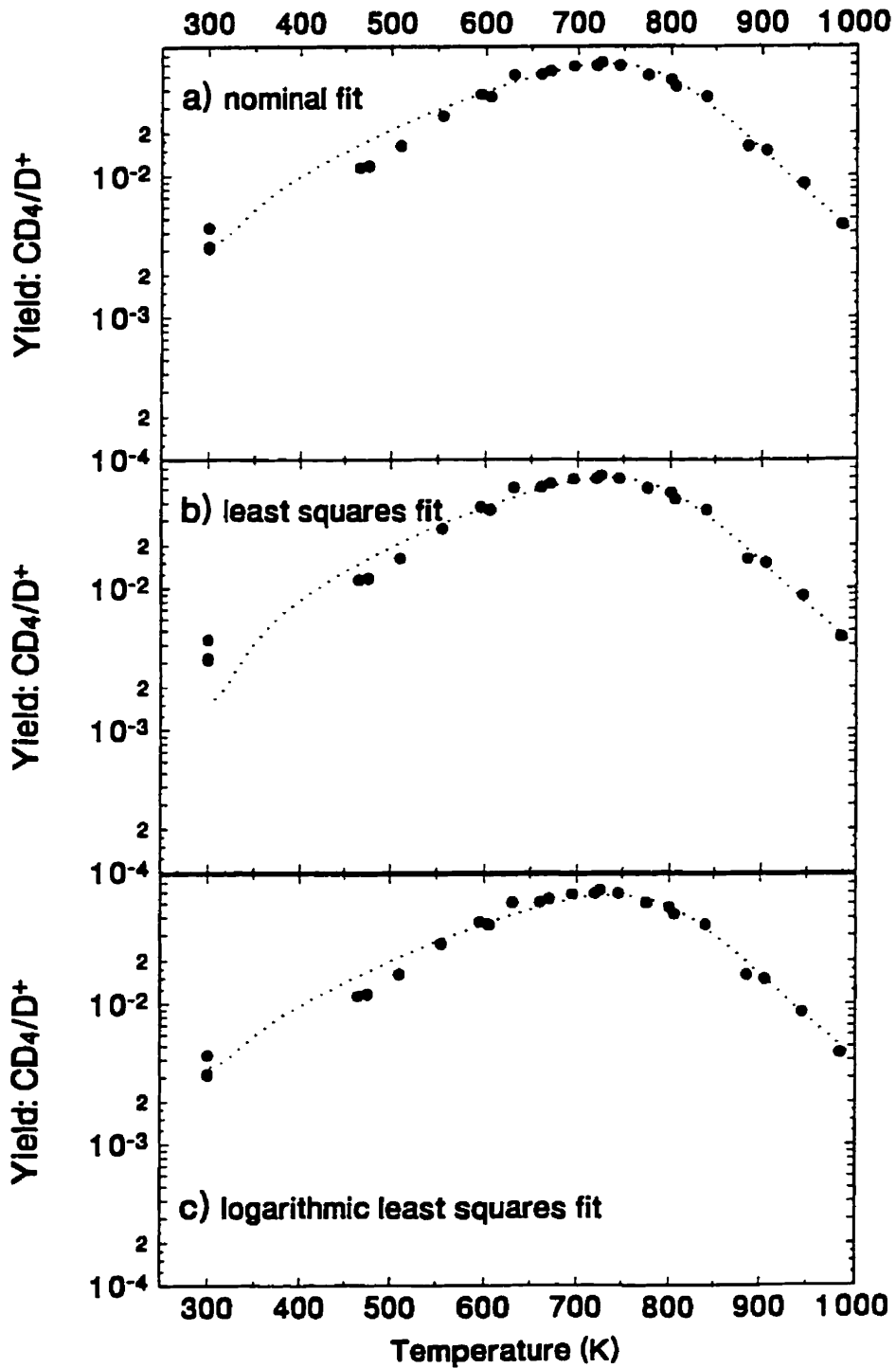


Figure A.7: Model predictions, for the methane yield as a function of temperature due to 200 eV D^+ impact, resulting from regression fitting using (b) least squares and (c) logarithmic least squares criteria. The nominal fit (a) is shown for comparison.

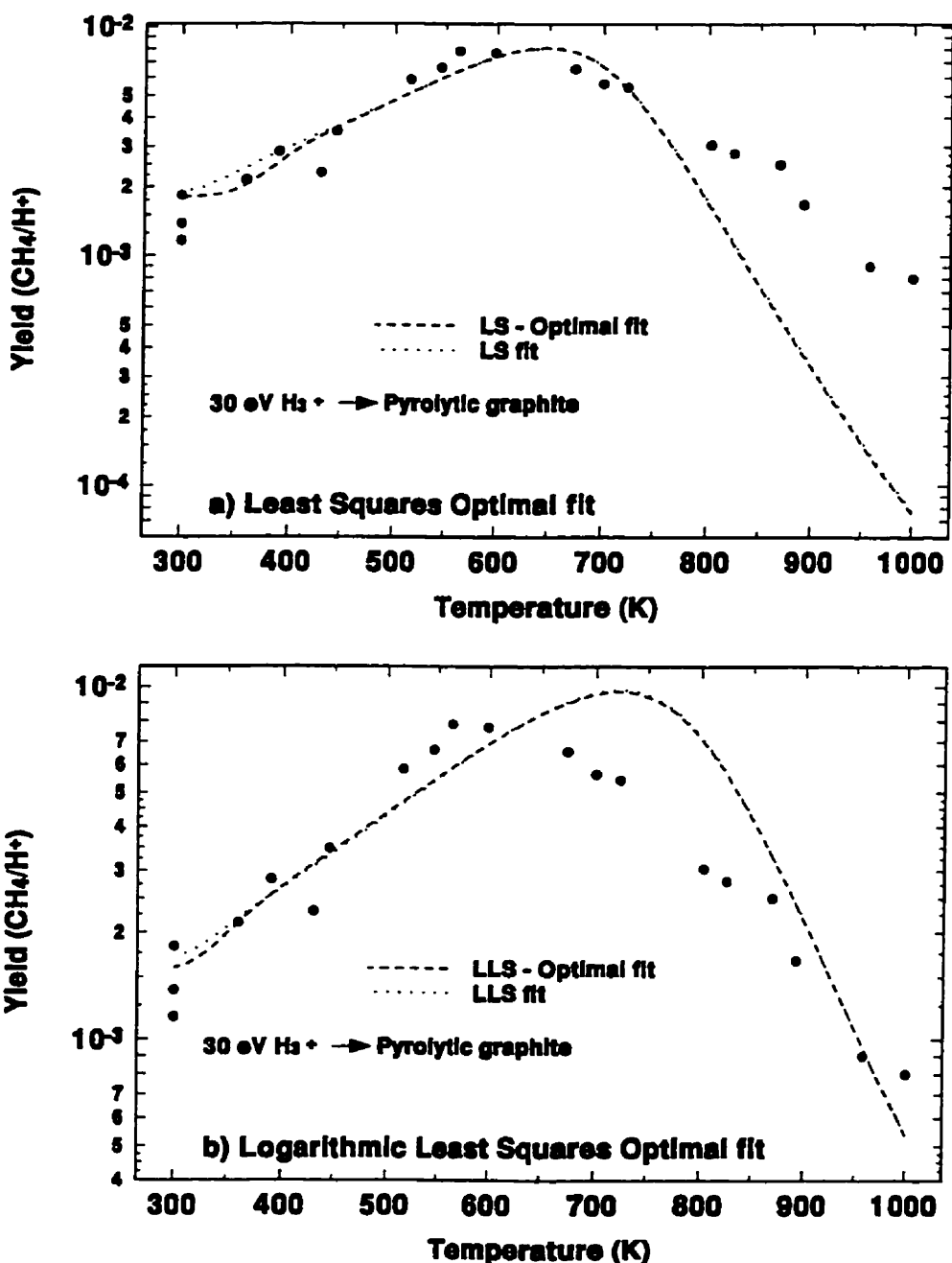


Figure A.8: Optimized model predictions, for the methane yield as a function of temperature due to 10 eV H^+ impact, resulting from applying (a) least squares and (b) logarithmic least squares regression criteria and using all of the model parameters (except E_x and E_H) as free fitting parameters. The curves from fig. B.6 b and c, where only four free parameters were used, are shown for comparison.

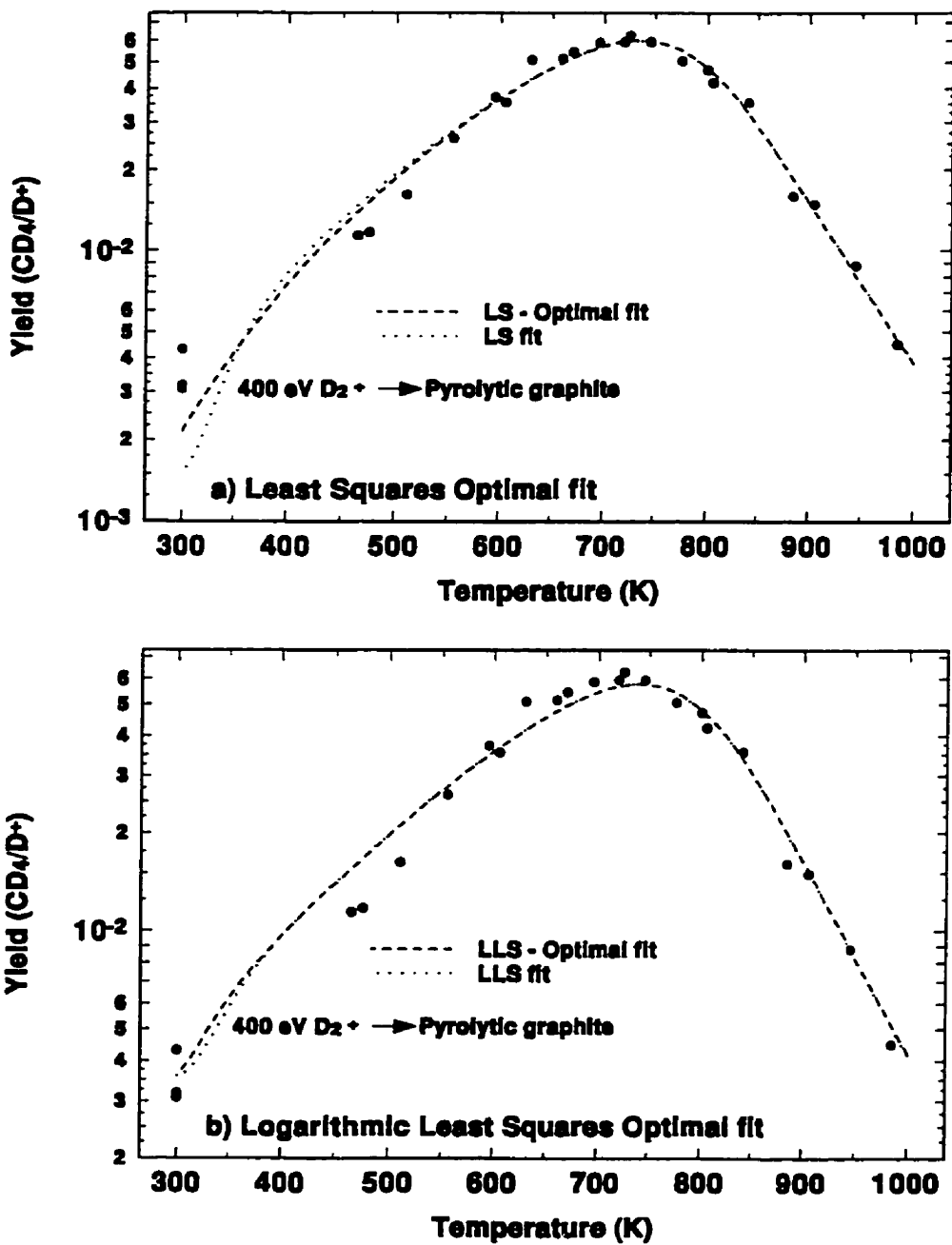
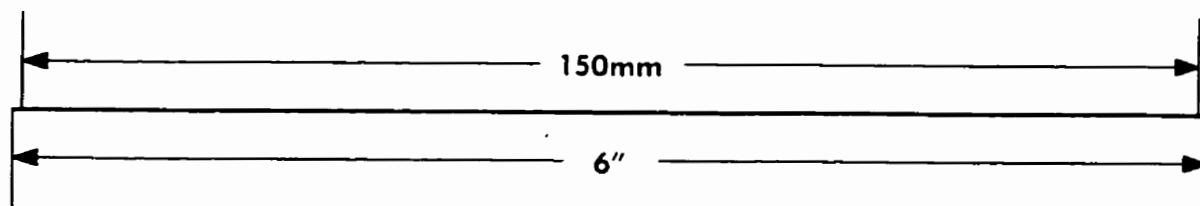
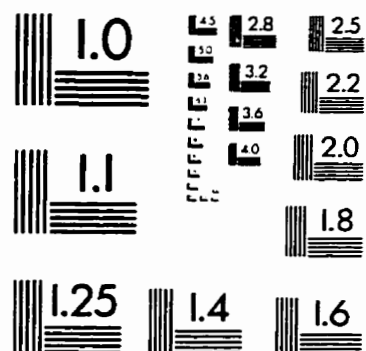
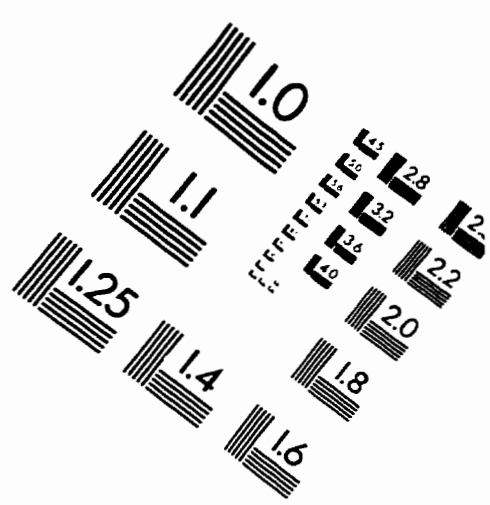
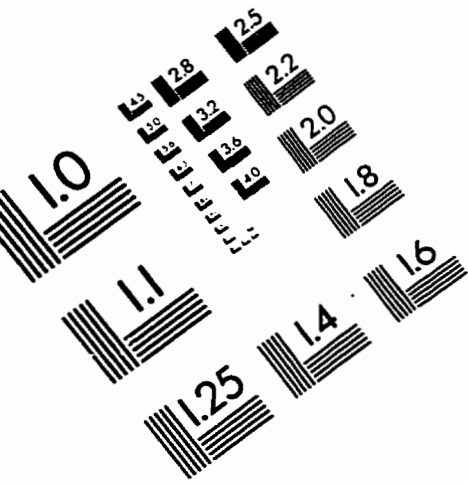


Figure A.9: Optimized model predictions, for the methane yield as a function of temperature due to 200 eV D⁺ impact, resulting from applying (a) least squares and (b) logarithmic least squares regression criteria and using all of the model parameters (except E_x and E_H) as free fitting parameters. The curves from fig. B.7 b and c, where only four free parameters were used, are shown for comparison.

IMAGE EVALUATION TEST TARGET (QA-3)



APPLIED IMAGE, Inc
1653 East Main Street
Rochester, NY 14609 USA
Phone: 716/482-0300
Fax: 716/288-5989

© 1993, Applied Image, Inc., All Rights Reserved

